A Gluon Transverse Momentum Dependent Parton Distributuon Function Analysis Using a $J/\psi + \gamma$ Final State at $\sqrt{s} = 13$ TeV With ATLAS

Amy Tee

Department Of Physics

Lancaster University

A thesis submitted to Lancaster University for the degree of Doctor of Philosophy in the Faculty of Science and Technology

September 2020

Declaration

I hereby declare that this thesis is my own work and effort and that it has not been submitted anywhere for any award. Where other sources of information have been used, they have been acknowledged.

Amy Moira Selvi Tee
September 2020

Acknowledgments

This is for you.

For my supervisor, Vakhtang Kartvelishvili, who took a chance on someone with no experimental particle physics knowledge, and provided more guidance than he probably should have. I am indebted for all the help you have given over the last four years. Thank you.

For James Walder, who provided help and support with the technical side of the thesis, creating ntuples, helping with code, and answering all my emails including the ridiculous ones which I can only presume tested his professionalism at times. Thank you.

For Dwayne Spiteri, who saved me, who has been my rock, and who has listened to me with so much kindness and patience everyday. Thank you.

For Izaac Sanderswood and Ben Whitmore, who were amazing CERN officemates in B40-4-C08, providing so many laughs and interesting discussions.

For Adam Parker, a wonderful guy with a huge heart, who helped me with many silly coding issues and was at times awake into the early hours trying to come up with solutions to my coding problems. Thank you.

For Jean-Philippe Lansberg, who provided the inspiration for this thesis, and as such would not exist without him.

For the staff and academics at Lancaster University, who provided me with help, guidance, and support throughout the course of this thesis, especially in the last year. Thank you.

For my friends at CERN and elsewhere, who have provided many laughs, good times, and who were there when I needed them. Thank you.

For Paula Tee, the big sister I wish I had. You have helped me navigate through life, always supporting my choices, and beng a source of guidance. Thank you.

For Nathan Ybanez, one of the most interesting people I know, who first sparked my interest in particle physics when he told me about the Pauli Exclusion Principle.

For my brother, who took on so many burdens to ensure I could write this thesis. Thank you.

For my parents, who adopted me, who sacrificed so much so that I would never go without, who did everything they could so that I would have a good life. Thank you.

For 'my little girl', who taught me about unconditional love. There are no words which convey how much I love and miss you. Thank you for everything you gave me.

Thank you for being part of my journey in life.

This is for you.

"For God so loved the world that He gave His only begotten Son,
so that whoever believes in Him shall not perish but have everlasting life"
John 3:16

Abstract

This thesis describes a study into Transverse-Momentum-Dependent (TMD) distributions of gluons inside a proton, through a J/ψ meson plus γ final state. The analysis was performed using 2.57 fb^{-1} of data collected by the ATLAS detector in proton-proton collisions at a centre-of-mass energy of 13 TeV in 2015.

A measurement of the continuum J/$\psi + \gamma$ cross section is carried out, in order to give access to the TMD function $f_1^g(k_{\mathrm{T}}^2)$, which describes the distribution of unpolarised gluons in an unpolarised proton. Assuming a Gaussian shape of the TMD distribution, with dependence on the intrinsic transverse momentum of a gluon, k_{T}, a measurement of the mean transverse momentum was achieved at three different invariant mass ranges, Q, of the J/$\psi - \gamma$ system. The invariant mass ranges, and measured values of $\sqrt{\langle k_{\mathrm{T}}^2 \rangle}$ are summarised in the table:

Q (GeV)	$\sqrt{\langle k_{\mathrm{T}}^2 \rangle}$ (GeV)
$15 \leq Q < 22$	1.99 $\pm$ 0.25
$22 \leq Q < 31$	3.63 $\pm$ 0.41
$31 \leq Q < 44$	4.08 $\pm$ 0.74

It is shown that between the lowest and highest invariant mass ranges considered, the intrinsic mean transverse momentum of gluons inside an unpolarised proton increases by a factor of 2.

The second measurement was an attempt to measure the contribution of the TMD function $h_1^{\perp g}(k_{\mathrm{T}}^2)$, which describes the distribution of linearly polarised gluons inside an unpolarised proton. By measuring the induced angular azimuthal modulations expected from interacting polarised gluons no statistically significant modulation was found with the dataset used.

Contents

Chapter 1

Introduction

Knowledge of the internal structure of hadrons in terms of its constituent partons (comprised of quarks, gluons, and anti-quarks) is described by the parton model, initially understood through deep-inelastic scattering (DIS) experiments. Our understanding of the proton's structure is continuously improving well into the Large Hadron Collider (LHC) era, where the majority of hard reactions are initiated from the fusion of two gluons from colliding protons.

The picture of a rich 'sea' of interacting partons allows one to factorise hadronic cross sections into a partonic-scattering amplitude squared and collinear parton distribution functions (PDFs). Collinear PDFs describe the longitudinal momentum distribution of the constituent partons within a proton.

Factorisation is central to the computation of hadronic cross sections, and in recent years theorists have sought to refine the parton picture by considering partons that carry a momentum component transverse to their parent hadron momentum. Usually, the transverse momentum in colliding partons is assumed negligible, it is safely neglected, or integrated over, thus current factorisation schemes lose all knowledge of initial transverse momenta. However, one must consider reactions where the overall transverse momenta remains small, but not negligible, which could affect the observed dynamics of final state particles. These processes would be sensitive to the intrinsic transverse momentum of partons, and can therefore serve as a microscope on parton behaviour in the transverse plane.

Factorisation may be generalised to include transverse parton dynamics, with one method being transverse-momentum-dependent PDFs (or TMDs) applicable in low transverse momentum reactions. It is then expected that the transverse momentum spectra of such reactions will be influenced by the partonic transverse momentum, also giving rise to azimuthal asymmetries in multi particle final states. This framework has held for a handful of processes for the extraction of quark TMDs from data, however, very little is known about gluon TMDs, mainly due to the lack of good probes at hadron colliders.

At the LHC, gluons are the dominant contribution to parton densities, therefore an understanding of gluon densities inside the proton is vital to make accurate and reliable theoretical predictions for process cross sections. Quarkonium production can serve as a tool to access gluon TMDs in proton collisions at the LHC, as perturbative Quantum Chromodynamics (QCD) can be safely used to describe partonic subprocesses. Quarkonium production can originate from gluon-gluon fusion, where low transverse momentum events should be sensitive to the intrinsic momentum of gluons and the possibility of extracting gluon TMDs. These two topics are the subject of this thesis. Additionally, as a result of studies into TMDs, the first differential continuum cross section measurement of $g + g \rightarrow J/\psi + \gamma$ is performed.

The second chapter details the CERN accelerator complex with attention paid to the ATLAS detector where data collected during Run II at 13 TeV in 2015 offering an effective integrated luminosity of 2.57 fb^{-1} is used in the analysis described within this thesis.

In the third chapter, the theoretical TMD framework is established, which discusses the advantages of selecting a $\text{g} + \text{g} \rightarrow J/\psi + \gamma$ final state, for the first dedicated measurement of the distribution of the intrinsic transverse momentum of gluons inside an unpolarised proton. Presented is the TMD cross section for this particular process and how its manipulation can be used to give information on gluon TMDs through azimuthal modulation.

The fourth chapter begins the analysis description, describing the data sample and the three Monte Carlo (MC) samples, along with the variable selections applied to each. The description encompasses how the analysis is divided into two branches, one concerning the properties of the intrinsic transverse momentum distribution of unpolarised gluons in an unpolarised proton, and the other, an attempt to extract the polarised gluon TMD component in an unpolarised proton.

Chapters five and six outline the data-driven analysis strategy and steps to separate out the signal and background events in data through a multi-variate analysis technique, background subtraction methods and a statistical tool, to allow the determination of the continuum cross section for $g + g \to J/\psi + \gamma$ presented in chapter seven.

Chapter eight describes the various systematics in the analysis encompassing four areas: event selections, efficiency corrections, pileup, and resolution.

Chapters nine and ten present the final results incorporating systematics, and the conclusions.

The author joined the experimental particle physics group at Lancaster University in Autumn 2016, shortly afterwards joining the ATLAS collaboration. Throughout the PhD qualification the author has been the main contributor towards the analysis described in this document for its entirety, writing the majority of the code required. As expected with any analysis, numerous studies have been undertaken to build up the analysis framework, and only the successful parts of said framework are presented here.

The analysis is motivated by theoretical studies conducted by Maddie Smith as part of her Master's project at Lancaster University under the supervision of Professor Vakhtang Kartvelishvili. The author wishes to thank her for her work, and credits her with Figure 3.11. All other plots contained within are the author's creation. The author would like to express gratitude towards James William Walder who provided numerous sources of help throughout this analysis, preparing the ntuples, assisting with efficiency systematics, and assisting with a lot of technical problems. As mentioned, part of the analysis strategy involved the use of a multivariate technique (TMVA), which utilised code from the $VH(b\bar{b})$ group at ATLAS, and thanks them for their assistance in moulding the framework to this thesis's needs. Finally, the author would like to thank Tamar Zakareishvili who performed the modelling for the mass background systematics.

As part of the ATLAS community, the author has undertaken service work within the B-physics trigger group, focusing on investigations into partial event building triggers. Within that group, additional work to produce public plots and investigations into low purity yields from a trigger were conducted. Although these activities helped the author gain invaluable experience and better understanding of the ATLAS trigger system, its description was not directly relevant for this thesis and hence is not described.

Chapter 2

The Large Hadron Collider And The ATLAS Detector

In this chapter an introduction to the LHC is presented, housed at the Centre Européanne pour la Recherche Nucléaire (CERN). Section 2.1 describes the LHC, with one of the four detectors, A Toroidal LHC ApparatuS (ATLAS), outlined in some detail in Section 2.2.

2.1 The Large Hadron Collider

The LHC is a 26.7 km superconducting ring accelerator located approximately 100 m underground, predominantly focusing on proton-proton (pp) collisions [1].

The ring is designed to accelerate protons in two counter rotating beam lines, at a operational frequency of 40 MHz (25 ns bunch spacing) [2], which interact at four main experiments located around the ring: ATLAS[1], CMS [3], LHCb [4], and ALICE [5].

During pp collisions, proton beams are accelerated through several stages inside the CERN accelerator complex [6], emerging from the Super Proton Synchroton (SPS) with an average beam energy of 450 GeV. Beams injected into the LHC ring are then brought to a beam energy of 6.5 TeV [7]. Collisions occur at precise points within each detector, where the two counter rotating beam intersect - the crossing point.

During the data taking periods of 2015 - 2018, referred to as Run II, each beam was built from approximately 2600 - 2800 proton bunches spaced at 25(50) ns intervals for the

2016(2015) periods [8]. Each bunch contained approximately 1.15 $\times 10^{11}$ protons, yielding an instantaneous luminosity of L $\simeq 10^{34}$ cm^2 s^{-1} [9, 10].

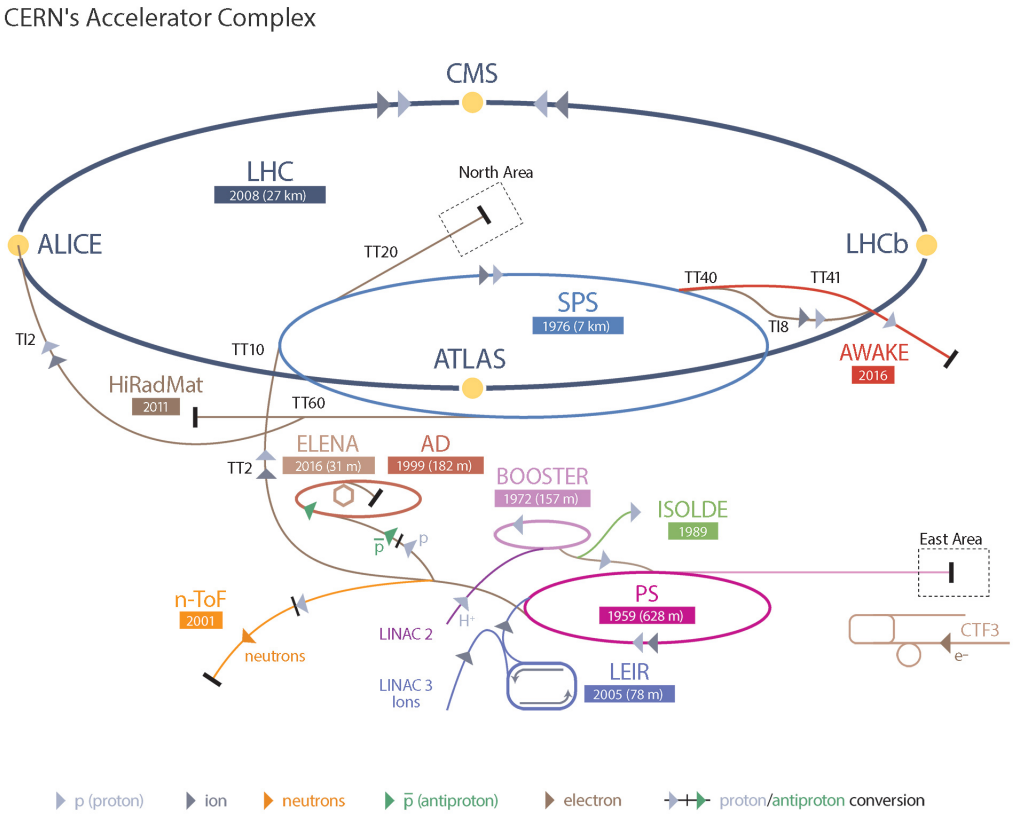

Figure 2.1: CERN accelerator complex showing the main experiments on the LHC ring, and the accelerator chain [6].

2.2 The ATLAS Detector

The ATLAS detector [1], has an approximately cylindrical forward-backward symmetric design. The detector comprises a number of subdetectors assembled in concentric cylindrical layers, centred around the Interaction Point (IP) where the LHC beams collide, as illustrated in Figure 2.2.

The detector is divided into four main components described in various Sections of this chapter: the magnet system (Section 2.3), the Inner Detector (ID) (Section 2.4), the electromagnetic and hadronic calorimeters (Section 2.5), and the Muon Spectrometer (MS) (Section 2.6). Particle trajectories emerging from the IP are reconstructed with the ID

tracking system, which consists of a Silicon Pixel Detector (Section 2.4.1), a Semiconductor Tracker (SCT) (Section 2.4.2), and a Transition Radiation Tracker (TRT) (Section 2.4.3).

ATLAS utilises a two stage trigger system to decide and record various processes of interest by the Trigger and Data Acquisition (TDAQ) system developed for the Run II setup (Section 2.7).

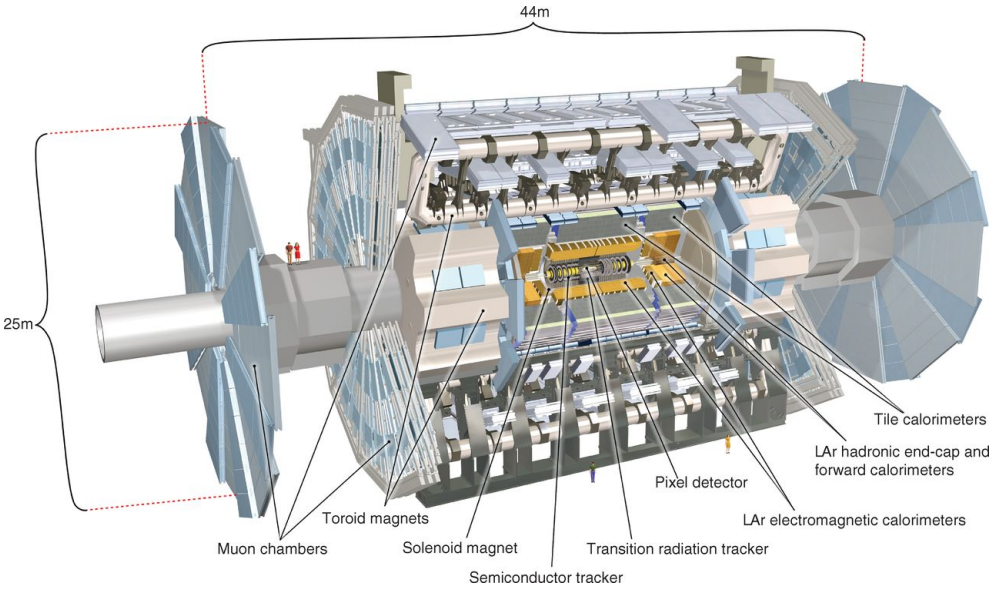

Figure 2.2: Cutaway view of the ATLAS detector and its various components [1].

2.2.1 The ATLAS Coordinate System

A common right-handed coordinate system, with reference to the LHC ring, is used throughout ATLAS. It describes the orientation of particles produced from collisions with respect to the detector, using the IP to define the origin, and the beam line to define the z-axis. The x-axis points towards the centre of the LHC ring, and the y-axis points towards the surface [1].

The coordinates to describe particles are based on a cylindrical system with the transverse plane often described in terms of r and ϕ. The azimuthal angle, ϕ, is measured around the z-axis in the x–y plane, and the polar angle θ defines the angular separation from the beam line (z-axis) [1].

The kinematics of objects are commonly expressed in the x–y plane of the detector, where the momentum, p, and energy, E, of objects can be defined as variables transverse to the

beam line. The transverse momentum, p_{T}, and transverse energy, $\mathrm{E_T}$, are given by:

$$\begin{aligned} p_{\mathrm{T}} &= |\vec{p}| \sin\theta \\ E_{\mathrm{T}} &= E \sin\theta. \end{aligned} \tag{2.1}$$

The rapidity, y, is defined relative to the beam axis:

$$y = \frac{1}{2} \ln\left(\frac{E + p_z}{E - p_z}\right), \tag{2.2}$$

where $p_{\mathrm{z}} = |\vec{p}| \cos\theta$ is the component of momentum along the beam line.

Rapidity simplifies to the pseudo-rapidity, η, describing the angle of a particle relative to the beam axis, provided $m \ll |\vec{p}|$ and $E \approx |\vec{p}|$:

$$\eta = \lim_{E \to |\vec{p}|} \frac{1}{2} \ln\left(\frac{E + |\vec{p}| \cos\theta}{E - |\vec{p}| \cos\theta}\right) = \frac{1}{2} \ln\left(\frac{1 + \cos\theta}{1 - \cos\theta}\right) = -\ln\left(\tan\frac{\theta}{2}\right). \tag{2.3}$$

The distance ΔR in the pseudo-rapidity - azimuthal angle space, describing angular separation between particles within the detector is given by:

$$\Delta R = \sqrt{\Delta\eta^2 + \Delta\phi^2}. \tag{2.4}$$

2.3 The Magnet System

The ATLAS detector uses four large superconducting magnet systems [11]: a Central Solenoid (CS) magnet to provide a magnetic field for the ID, an air-core Barrel Toroid (BT), and two air-core End-Cap Toroids (ECTs) providing a toroidal field configuration for the MS [11]. The magnetic system provides the bending power for the momentum measurement of charged particles. The magnetic system extends 26 m in length, and 22 m in diameter storing 1.6 GJ of energy [12]. The magnetic fields are generated by aluminium stabilised NbTi superconducting coils, and cooled by a liquid He system. Each coil is housed inside a mechanical structure, with cryostats for thermal insulation [12].

The CS magnet wound from a single coil shares the cryostat of the Liquid Argon (LAr) calorimeter, spans 5.3 m in length and 2.4 m in diameter, immerses the ID in a 2 T nearly uniform magnetic field [12].

The two ECTs, each with 8 coils in the same cryostat, are inserted in the BT at each end, covering the region $1.6 < |\eta| < 2.7$. Spanning 5 m, they have an inner(outer) diameter of 1.65(10.7) m. The BT has an inner(outer) diameter of 9.4(20.1) m and spans 25.3 m. The BT (consisting of 8 coils) and ECTs are arranged in a racetrack shape, as illustrated in Figure 2.3, providing a magnetic field of approximately 4 T [12]. Each ECT coil system is rotated in the azimuthal angle ϕ by 22.5° to the BT coils, in order to produce radial overlap in the magnetic field between the two coil systems. However the bending power in the transition regions ($1.4 < |\eta| < 1.6$) is lower where the two magnets overlap [1].

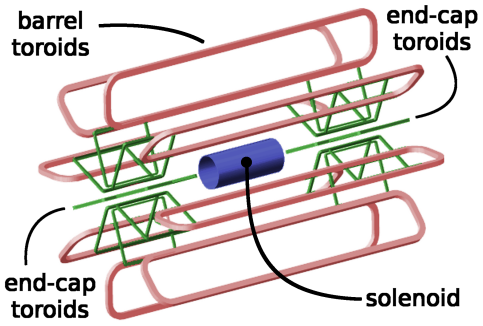

Figure 2.3: A schematic of the ATLAS magnet system highlighting the Central Solenoid, Barrel Toroid, and End-Cap Toroids components [13].

2.4 The Inner Detector

The ATLAS ID [1] is designed to provide hermetic coverage of the beam line, in order to measure the trajectory of incident charged particles traversing the early stages of the detector. The ID is enclosed by the 2 T magnetic field of the CS [11], with the subdetectors and their distances to the beam line outlined in Figure 2.4.

The ID provides high momentum resolution, primary/secondary vertex determination of charged particles with $p_{\mathrm{T}} > 0.5$ GeV in the region $|\eta| < 2.5$, and electron/pion identification over $|\eta| < 2.0$.

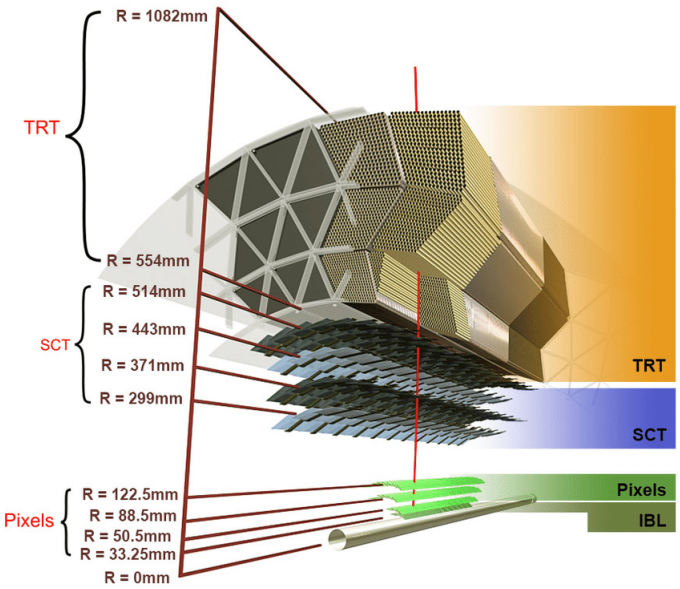

Figure 2.4: Sketch of the ATLAS Inner Detectors, highlighting the distances between the Interaction Point (R = 0) and the various layers of each subdetector component [1].

2.4.1 The Silicon Pixel Detector

The Silicon Pixel Detector [14] sits closet to the beam pipe, designed to detect short-lived particles that decay close to the beam pipe. Constructed from four layers of silicon pixels there is: the Insertable B-layer (IBL) [15], and three concentric cylindrical pixel layers in the region $|\eta| < 1$, and three discs perpendicular to the beam axis in the end-cap regions.

There are 80 M pixels, and each pixel sensor has size (R-$\phi \times z$) = (50 $\times$ 400) μm^2 with a resolution 14 $\times$ 115 μm^2 [1, 16]. The high granularity of the subdetector's layers gives high precision measurements.

2.4.2 The Silicon Semiconductor Tracker

The SCT [1] forms the second layer of the ID, arranged in four concentric cylinders in the central barrel region and nine discs perpendicular to the beam direction in each end-cap, and is composed of silicon microstrip modules (sensors). Each module in the barrel region runs parallel to the beam axis, and is composed of two 6.4 cm silicon sensors rotated around the geometric centre by $\pm$20 mrad, and is divided longitudinally into silicon strips with an average separation of 80 μm. The strips on each side of the module have a small 40 mrad

angle between them to perform a stereo-angle measurement [17].

The SCT provides four measurements per reconstructed track, contributing to both momentum measurement and vertex positioning. The resolution of each module is (R-$\phi \times z$) = (17 $\times$ 580) μm in the barrel and (R-$\phi\times$ R) = (17 $\times$ 580) μm in the end-caps [17].

2.4.3 The Transition Radiation Detector

The TRT [1] is the outermost component of the ID, consisting of 300,000 Monitored Drift Tubes (MDTs). Tubes of length 1.5 m are arranged parallel to the beam axis in the barrel region, whilst 0.4 m long tubes are arranged radially in the end-caps, offering track coverage up to $|\eta| < 2.0$. Each tube is 4 mm in diameter, with 3.5 μm thick kapton walls [18]. The walls are kept at a voltage of -1.5 kV [1]. Each straw is filled with 70% Xe, 27% CO_2 and 3% O_2 gas mixture[1]. An anode wire, kept at ground potential, and made from gold-plated tungsten runs through the centre. The gas mixture is ionised when charged particles pass through, creating negative charges that drift towards the wire, providing a measurement with a spatial resolution of 130 μm. The space between straws contain polymer fibres, causing charged particles to radiate photons as they traverse the material boundary. The transition radiation produced from different massive charged particles can be used to distinguish pions from electrons for instance [18].

2.5 The Calorimeters

The ATLAS calorimeters [1] are situated outside the solenoid magnet, providing fine-grained measurements of charged and neutral particle energies originating from the IP, covering $|\eta| < 4.9$ and offering hermetic coverage in ϕ. The calorimeter system consists of an inner electromagnetic (ECAL) and an outer hadronic (HCAL) calorimeter, with their positions shown in Figure 2.5.

Termed sampling calorimeters, the detector system is composed of alternating elements of active and passive material, where the passive material is designed to initiate a particle shower, whilst the active material measures the resulting energy deposits [19].

[1] During Run II several leaks were found, some tubes now contain an Ar-based gas mixture

The ECAL is suited towards electron and photon precision measurements, whilst the coarser granularity of the hadronic calorimeter is suited towards jet reconstruction from hadrons and missing transverse momentum, E_T^{miss}, measurements.

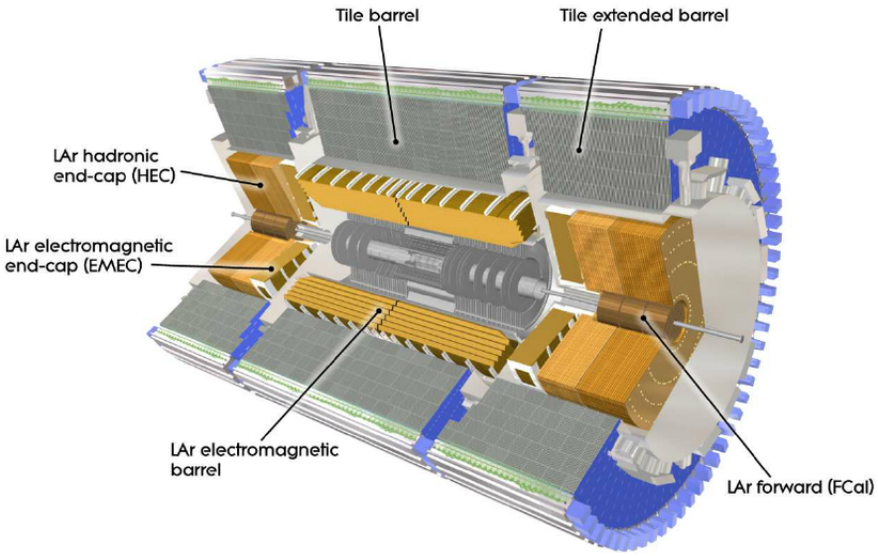

Figure 2.5: Schematic view of the ATLAS Electromagnetic and Hadronic Calorimeters [1].

2.5.1 The Liquid Argon (LAr) Electromagnetic Calorimeter

The ECAL [1] is formed from two half barrel components covering $|\eta| < 1.475$, separated by a 4 mm gap at $z = 0$. Each barrel is 3.2 m in length with an inner(outer) radius of 2.8(4) m. The calorimeter provides fine granularity ranging from $\Delta\eta \times \Delta\phi = 0.0031 \times 0.0245$ to $\Delta\eta \times \Delta\phi = 0.05 \times 0.0245$ in the back layer, with a thickness between 24 – 33 radiation lengths, X_0, depending on $|\eta|$ [20].

Two coaxial wheels make up the end-caps with the outer wheel covering $1.375 < |\eta| < 2.5$, and an inner wheel covering $2.5 < |\eta| < 3.2$ [1]. The thickness of the end-caps to incident particles ranges from 24 – 38 X_0, as $|\eta|$ increases [20].

The ECAL uses lead and steel as the absorbing material that interacts electromagnetically with incident electrons and photons, resulting in an electromagnetic cascade of particles. The cascade ionises liquid argon that is used as the sampling material between alternating layers of absorbing material and electrodes, arranged in an accordion shape to provide full ϕ symmetry without azimuthal cracks. The electrodes consist of three copper layers separated

by polyimide insulating sheets. The energy deposition in the calorimeter is determined from the measured voltage due to the ionised active material [21].

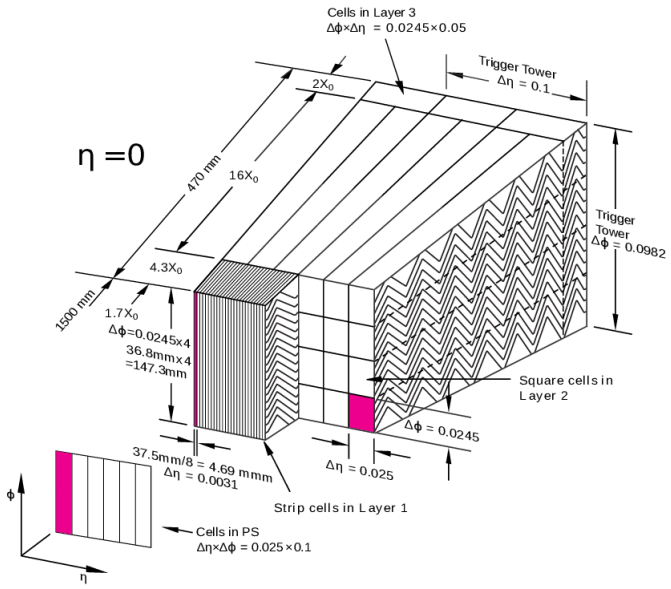

Figure 2.6: Sketch of the lateral and longitudinal segmentation of the ATLAS Electromagnetic Calorimeter around $\eta = 0$. Illustrated is the lead absorber plate geometry and liquid argon active material for the barrel sections [20].

2.5.2 The Hadronic Calorimeters

Tile Calorimeter

The tile calorimeter [1] is composed of three components, a 5.8 m long barrel in the region $|\eta| < 1.0$, and two 2.6 m long barrels covering $0.8 < |\eta| < 1.7$. Each barrel contains 64 steel-scintillator modules, divided longitudinally into three layers of varying interaction lengths. Steel is used as the absorber material, whilst the scintillator acts as the active medium, with the signal read out through fibre optic cables into photo-multiplier tubes [22]. The inner layers have a resolution of $\Delta\eta \times \Delta\phi = 0.1 \times 0.1$ while the outer layer has slightly poorer granularity with $\Delta\eta \times \Delta\phi = 0.2 \times 0.1$ [1, 23].

LAr Hadronic End-cap Calorimeter

Two parallel plate copper-LAr hadronic end-caps are positioned either side of the tile barrels, covering the region $1.5 < |\eta| < 3.2$. Each wheel is constructed from 32 identical wedge

shapes, sharing the LAr cryostats. The inner wheels are made from 24 parallel, 25 mm thick copper plates with a radius of 0.475 m. The rear wheels use 16 copper plates of 50 mm thickness. The copper plates are separated by 8.5 mm LAr copper gaps, and act as the active medium for the calorimeter [24]. The size of the readout cell is $\Delta\eta \times \Delta\phi = 0.1 \times 0.1$ for $|\eta| < 2.3$ and $\Delta\eta \times \Delta\phi = 0.2 \times 0.2$ for $|\eta| > 2.3$ [1].

Forward LAr End-cap Calorimeter

The forward calorimeter (FCAL) [25] provides coverage of the region $3.1 < |\eta| < 4.9$, and is divided into three 45 cm deep modules. Each cylindrical module is comprised of stacked plates parallel to the beam axis with rod electrodes inside.

- The first module, FCAL1, is optimised for electromagnetic measurements using copper as the absorbing material, with 269 μm LAr gaps.
- The second (FCAL2) and third (FCAL3) modules, are optimised for hadronic activity using tungsten as the main absorbing material which limits the lateral spread of a hadronic shower. FCAL2 and FCAL3 have LAr gaps of 376 μm and 508 μm respectively.

Each module is constructed from stacked copper plates with electrodes running parallel to the beam axis through the plates.

2.6 The Muon Spectrometer

The MS [26] is the outermost ATLAS detector, containing a system of three large air-core superconducting toroid magnets to provide a 0.5 T magnetic field in the central barrel region ($|\eta| < 1.05$) and end-caps ($1.05 < |\eta| < 2.4$) to deflect muon tracks in the high precision tracking chambers [1]. Four types of detection element are present, as can be seen in Figure 2.7:

- Monitored Drift Tubes (MDTs): MDTs perform the primary momentum measurement in the precision tracking system of the MS. MDTs measure muon momentum in the barrel and end-cap regions up to $|\eta| < 2.0$, and correspond to the tracking chamber of the MS. Modules are constructed from three to eight layers of drift tubes. Each

tube is approximately 30 mm in diameter and filled with Ar/CO_2 at a pressure of 3 bar with a 50 μm diameter tungsten-rhenium wire running down the middle. Incident muons liberate charge in the MDT gas mixture, which drift toward the wire. The precise muon position can be determined from the drift time which is proportional to drift distance. Each tube has a resolution of 80 μm [27].

- Cathode Strip Chambers (CSCs): Placed closed to the beam pipe ($2.0 < |\eta| < 2.7$) CSCs have superior timing resolution and rate capability. Each tracking chamber contains 4 layers of CSC multi-wire anode planes sandwiched by segmented orthogonal cathode planes. The position of the muon is determined from charge depositions on adjacent cathode strips [28].
- Resistive Plate Chambers (RPCs): Gaseous detectors based on the ionisation produced by charged particles, provide a coordinate measurement in the non-bending direction of the barrel region. RPCs provide information to the muon trigger in the barrel. [29].
- Thin Gap Chambers (TGCs): Give a coordinate measurement in the non-bending region and provide information to the muon trigger in the end-cap regions [29].

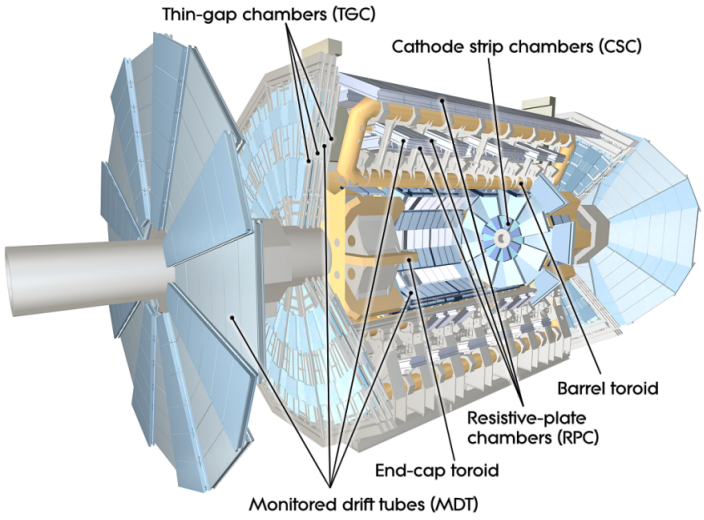

Figure 2.7: Illustration of the four types of component that make up the Muon Spectrometer: Monitored Drift Tubes (MDTs), Thin Gap Chambers (TGCs), Cathode Strip Chambers (CSCs), and Resistive Plate Chambers (RPCs) [7].

2.7 The Trigger and Data Acquisition

The LHC operates at 40 MHz bunch crossing rate to produce high statistics, which provides ATLAS with the challenge of recording processes of interest. The ATLAS detector must compromise between filtering out events for an acceptable rate of storage, whilst also capturing the most important physics processes [30].

The ATLAS Trigger and Data Acquisition system (TDAQ), Figure 2.8, works in real time to reduce data to a feasible storage size. Decision making and reconstruction at the triggering stage is known as online, whereas general ATLAS reconstruction is referred to as offline. The TDAQ consists of two levels: A hardware based Level 1 (L1), followed by a software based Higher Level Trigger (HLT). The HLT is split in two, the Level 2 (L2) and Event Filter (EF) [1].

The L1 trigger decision, which first encounters all pp collisions, creates Regions of Interest (RoIs) in η-ϕ space for each event if they pass certain threshold requirements. It is then passed to the Central Trigger Processor (CTP) which relies on inputs from the L1 Calorimeter (L1Calo) and the L1 Muon (L1Muon) triggers, the LUCID Cherenkov Counter and Zero-Degree Calorimeter (ZDC). The L1 trigger is based on identifying high p_T objects of events using calorimeter clustering and track information from the MS. In the interests of speed, detector performance is ignored, granularity of the ECAL is reduced, and only certain components of the muon system are used for read out [1].

The HLT receives the RoIs from L1, which is then stored in the Read Out System (ROS), and then L2 performs regional object reconstruction using additional detector information. These objects determine whether full event reconstruction should take place at the EF stage, after which a hypothesis test on the full event takes place to see whether it should be recorded. A passed event is then stored locally to the experiment and then exported to the Tier-0 facility at CERN for offline reconstruction. The HLT reduces the event rate to around 700 - 1000 Hz [1].

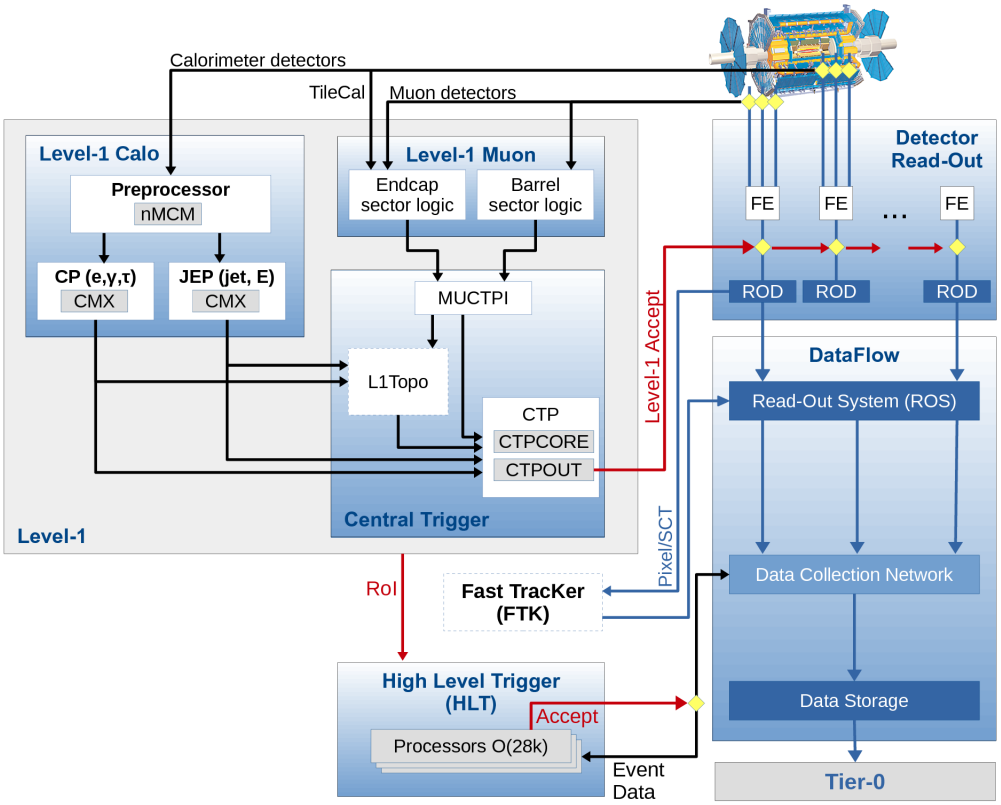

Figure 2.8: The ATLAS Trigger and Data Acquisition system in place during Run II [31].

Chapter 3

Theoretical Framework

This chapter introduces the concept of transverse-momentum-dependent parton distribution functions (TMD PDFs or TMDs), but begins with a brief introduction to the Standard Model (SM) of particle physics in Section 3.1, focusing on QCD (Section 3.1.1). The chapter then moves onto parton distribution functions (PDFs) in Section 3.2 as a prelude to TMDs. Section 3.3 describes the extension of collinear PDFs to include the transverse dynamics of partons inside protons, leading to TMDs. One promising subprocess for gluon TMD measurements is $\mathrm{g} + \mathrm{g} \to \mathrm{J}/\psi + \gamma$ production, with its advantages explored in Section 3.3.3. With this in mind, the cross section for this subprocess, within the TMD factorisation framework, is presented in Section 3.3.5, which allows for a measurement of the transverse motion of gluons inside a proton. The chapter concludes with two Monte Carlo (MC) studies: i) Section 3.3.6, which emulates gluon polarisation effects to perform a TMD measurement, and ii) Section 3.3.7, which models a differential cross section as a means to extract the average transverse momentum of a gluon.

3.1 The Standard Model

The SM [32, 33] is a non-abelian quantum field theory, based on an $SU(3)_c \otimes SU(2)_L \otimes U(1)_Y$ gauge symmetry [34], which is currently the most successful theory in describing how subatomic particles behave and their interactions through the electromagnetic, weak, and strong interactions. The $SU(3)_c$ group describes QCD, whilst Quantum Electrodynamics

(QED) and the Weak force are embedded in the chiral weak $SU(2)_L$ and hyper-charge $U(1)_Y$ sectors [32].

The fundamental particles which make up matter in the Universe are considered to be point-like and elementary, with an intrinsic spin used to further categorise particles. Particles with integer spin are known as bosons, whilst those with half-integer spin are known as fermions. Each elementary particle has its own duplicate particle known as an anti-particle, which has the same mass but opposite electric charge [35].

Fermions, summarised in Table 3.1, can be further sub-divided into quarks and leptons. Quarks, q, have only been observed in bound states, for instance, as mesons ($q\bar{q}$ - a quark anti-quark state), baryons (qqq) [36] and the newly discovered tetraquarks [37, 38] and pentaquarks [39].

Leptons which exist freely, interact via the electromagnetic and weak forces of the SM in the case of charged leptons, and via the weak force for neutrinos [35].

	Leptons			Quarks		
Gen.	Particle	Mass	Charge	Particle	Mass	Charge
I	electron e	0.511 MeV	-1	Up u	2.3 MeV	$+\frac{2}{3}$
I	e neutrino ν_e	< 2 eV	0	down d	4.8 MeV	$-\frac{1}{3}$
II	muon μ	105.658 MeV	-1	charm c	1.275 GeV	$+\frac{2}{3}$
II	μ neutrino ν_μ	< 2 eV	0	strange s	95 MeV	$-\frac{1}{3}$
III	tau τ	1776.82 MeV	-1	top t	173.07 MeV	$+\frac{2}{3}$
III	τ neutrino ν_τ	< 2 eV	0	bottom b	4.18 GeV	$-\frac{1}{3}$

Table 3.1: Table detailing the Standard Model fermions which are divided generationally into quarks and leptons with their corresponding masses and electric charge [40].

The interactions between fermions are governed by three aforementioned fundamental forces mediated by integer spin gauge bosons and are summarised in Table 3.2. The massless gluons and photons govern the strong and electromagnetic forces respectively, whereas the massive Z and $W^{\pm}$ bosons govern the weak interactions [35]. A fundamental force not part of the SM is gravity which is many orders of magnitude lower than the strong, electromagnetic and weak forces, and has no practical effect in pp collisions.

Particle	Mass	Charge	Spin
γ	0	0	1
$W^{\pm}$	80.385 ± 0.015 GeV	±1	1
Z^0	91.1876 ± 0.0021 GeV	0	1
Gluon	0	0	1
Higgs	125.09 ± 0.24 GeV	0	0

Table 3.2: The Standard Model bosons with their corresponding masses, electric charge, and spin. [40]

Particles acquire mass in the SM by spontaneous symmetry breaking through the Brout-Englert-Higgs mechanism, which requires a Higgs boson [41, 42]. This particle, completing the SM, was discovered jointly by the ATLAS and CMS experiments in 2012 [43, 44].

3.1.1 Quantum Chromodynamics

QCD is the description of the strong interaction between quarks and gluons described by the non-abelian special unitary (SU) colour symmetry group, $SU(N_c)$, where $N_c = 3$ [32]. The simplest representation of the theory allows for triplets of quarks of each flavour with $(N_c^2-1) = 8$ massless gluons carrying colour charge, which correspond to the eight generators of the $SU(3)$ symmetry group [45]. QCD proposes that when gluons mediating the strong force interact with quarks they rotate the quark's colour in $SU(3)$ space through the three 'colour' orthogonal states of QCD: red, green, and blue. Gluon interaction vertices preserve colour.

One might expect nine possible combinations of colour and anti-colour in gluons (i.e. $r\bar{r}$, $r\bar{g}$, $r\bar{b}$, $g,\bar{r}$, $g\bar{g}$, $g\bar{b}$, $b\bar{r}$, $b\bar{g}$, $b\bar{b}$), but these are not actual colour states. All stable strongly interacting particles observed in nature are 'colourless', namely in a colour singlet state composed of $(r\bar{r}+b\bar{b}+g\bar{g})/\sqrt{3}$ [35], which leaves eight remaining independent colour states. There are numerous ways of presenting the remaining eight colours of gluons, with one possibility: $(r\bar{b}+b\bar{r})/\sqrt{2}$, $(r\bar{g}+g\bar{r})/\sqrt{2}$, $(b\bar{g}+g\bar{b})/\sqrt{2}$, $(r\bar{r}+b\bar{b})/\sqrt{2}$, $-i(r\bar{b}-b\bar{r})/\sqrt{2}$, $-i(r\bar{g}-g\bar{r})/\sqrt{2}$, $-i(b\bar{g}-g\bar{b})/\sqrt{2}$, and $(r\bar{r}+b\bar{b}-2g\bar{g})/\sqrt{6}$ [35].

The self coupling of gluons, due to gluons themselves carrying colour, leads to two important properties of QCD, namely asymptotic freedom and confinement [32]. Confinement concerns why quarks and gluons are not observed as states which propagate over macroscopic

distances. Asymptotic freedom allows for methods of perturbation at high energies, and why the coupling constant is said to 'run' [46].

3.1.1.1 Asymptotic Freedom

A consequence of gluon self interactions can be seen in $gg \to gg$, whose matrix element can be expanded in terms of the strong coupling constant, α_s, which leads to an infinite number of terms:

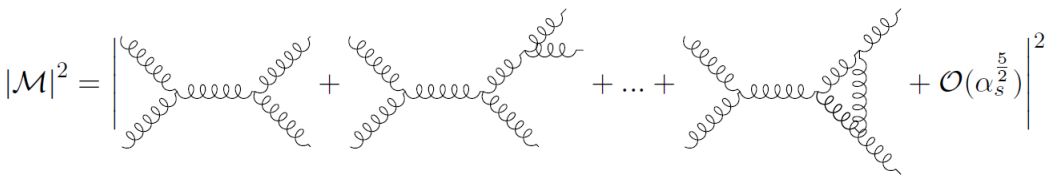

Figure 3.1: Expansion of the matrix element in terms of Feynman diagrams for the process $gg \to gg$ [47].

Virtual terms in the series involve loop integrals of four-momenta that often diverge (become infinite). Fortunately, higher order terms ($\mathcal{O}(\alpha_s^{\frac{5}{2}})$), cancel out these infinite loops, yielding a finite result. However, when truncating the series at a given order in perturbation theory, e.g next-to-leading order (NLO) in QCD, the loop integrals are no longer cancelled out by higher order terms, leading to ultraviolet divergences. This is overcome by renormalising the theory.

A renormalisation scale, μ_R, not predicted by QCD is introduced. The parameter controls how much of a calculation stems from non-loop Feynman diagrams versus the remaining finite components of loop Feynman diagrams [46, 48]. No physical parameter must ever depend on μ_R, so α_s absorbs this parameter; $\alpha_s \to \alpha_s(\mu_R^2)$ such that is now runs with the choice of scale.

The evolution of $\alpha_s(\mu_R^2)$ can be expressed via the renormalisation group equation [40, 46, 48]:

$$\mu_R \frac{\partial \alpha_s}{\partial \mu_R^2} = \beta(\alpha_s(\mu_R^2)). \tag{3.1}$$

Known as the beta function, $\beta(\alpha_s)$, encodes higher order loop corrections to the bare QCD vertices, which has a perturbative expansion:

$$\beta(\alpha_s) = -b\alpha_s^2 + b'\alpha_s^3 + b''\alpha_s^4 + \mathcal{O}(\alpha_s^5). \tag{3.2}$$

The coefficients of the beta function are extracted from higher order corrections to the bare vertices of QCD theory [40]. At leading order (LO), $b = 11 - \frac{2}{3}f$, where f is the number of quark flavours, which in the SM is six. $\alpha_s(\mu_R^2)$ can be expressed as:

$$\alpha_s(\mu_R^2) = \frac{\alpha_s(\mu_0^2)}{1 + \alpha_s(\mu_0^2) b \ln(\frac{\mu_R^2}{\mu_0^2})} \tag{3.3}$$

The strong coupling constant decreases as the scale of the interaction increases. The renormalisation scale can be equated to the scale of the physical process ($\mu_R = Q$), as the choice of renormalisation scale is not defined [40, 46, 48]. The running of the strong coupling constant, such that $\alpha_s \to 0$ at small distances, is referred to as asymptotic freedom.

3.1.1.2 Colour Confinement

Gluon self interactions are believed to give rise to colour confinement, such that colour-charged particles cannot be isolated and are never observed in nature. Coloured quarks are confined inside hadrons, limiting the range of the strong interaction to roughly the size of the atomic nucleus. If one tries to separate two coloured objects, a flux tube of interacting gluons with an approximately constant energy density of 1 GeV/fm forms. If two coloured particles are separated far enough, the flux tube contains enough energy to split to produce a new quark anti-quark pair rather than extending the tube further, as shown in Figure 3.2.

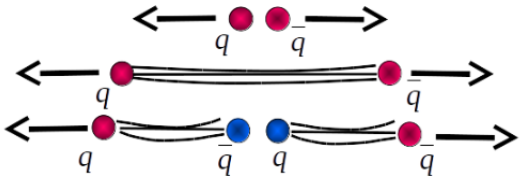

Figure 3.2: Drawing of a $q\bar{q}$ pair splitting to form two pairs of $q\bar{q}$ states [49].

To summarise, QCD is studied by using the fact that α_s is small in high energy, or short distance interactions, allowing perturbation techniques to be applied. Testable predictions with QCD are extremely difficult due to the infinite number of topologically inequivalent interactions. Over short distances the coupling is small enough that an infinite number of terms can be approximated accurately by a finite number of terms. Most strong processes cannot be calculated directly with perturbative QCD, since one does not observe free quarks and gluons due to colour confinement. QCD factorisation separates the cross section into a process dependent perturbatively calculable short distance parton cross section and parton distribution functions (PDFs) addressed in Section 3.2.

3.2 Parton Distribution Functions

The 'collinear' parton model [50], proposed by Richard Feynman (1969), describes how the proton is a dynamic system consisting of three valence quarks and a virtual 'sea' of interacting gluons and quark anti-quark pairs. Collinear PDFs describe the probability of finding partons (quarks and gluons) inside a hadron as a function of x – the fraction of a proton's momentum carried by a particular parton, or simply how the overall proton's longitudinal momentum is distributed amongst it's partons. The model considers partons to have negligible transverse momentum [51].

PDFs are non-perturbative objects traditionally obtained through DIS experiments, which describes the electromagnetic interaction between a charged lepton and nucleon such as one shown in Figure 3.3. PDFs depend on the variables $Q^2 = -q^2$, where q^2 is the four-momentum transfer of the interaction and Q^2 is the hard scale of the process. PDFs are expressed through the term $f_q^A(x, Q^2)dx$, which describes the probability of probing a hadron A at a hard scale Q^2, and finding a parton q carrying a fraction of the hadron's momentum in the range $x \to x + dx$ [51].

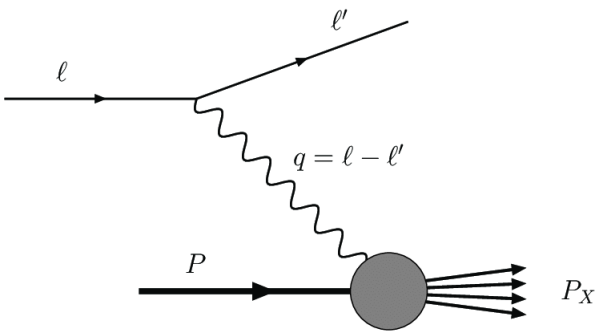

Figure 3.3: Feynman diagram of a deep-inelastic scattering Process. l is the incoming 4-momentum of the lepton which interacts electromagnetically with a parton coming from a hadron P which then fragments into several particles denoted P_X. The 4-momentum carried by the photon is $q = l - l'$ where l' is the 4-momentum of the outgoing lepton [52].

The 4-momentum exchange in DIS interactions determines whether the lepton scatters elastically or inelastically. In the low energy regime the scattering is elastic and the nucleon remains intact. In the high energy regime, scattering is inelastic and the nucleon breaks apart in a process called fragmentation [53]. The energy dependence of PDFs can be demonstrated by an electron electromagnetically scattering off a proton via photon exchange. The 4-momentum square of the photon is Q^2 and as this increases, the photon's wavelength decreases giving the photon greater resolving power. If $Q \leq 1$ GeV, the photon's wavelength is larger than the diameter of the proton, and the electron scatters elastically off the proton as a whole. Beyond 1 GeV, the photon is able to 'see' the proton's constituents, and the electron scatters of a constituent parton forcing the nucleon to break apart. As the photon's energy is increased it is able to 'see' quark - anti-quark loops which appear in NLO interactions. The number of loops 'seen' by the photon increases with photon energy. To sum up, the probability of a photon scattering off a parton which carries a small fraction of a parent hadron's momentum increases with the hard scale. The types of partons seen will differ at different energy scales.

The success of the parton model allows for interactions to be decomposed into short and long distance parts, according to collinear factorisation theorems. Long distance behaviours are folded into PDFs which describes the non-perturbative initial and final state interactions. Cross sections can then be written in terms of a 'hard' part containing the short distance parton subprocess cross section $d\sigma$, and a 'soft' part containing the long distance behaviour,

with a two hadron collision cross section taking the form [51]:

$$d\sigma \sim \sum_{\mathrm{a,b}} \int dx_{\mathrm{A}}\, dx_{\mathrm{B}}\, \underbrace{f_{\mathrm{a/A}}(x_{\mathrm{A}})\, f_{\mathrm{b/B}}(x_{\mathrm{B}})}_{\text{soft}}\, \underbrace{d\hat{\sigma}}_{\text{hard}}. \tag{3.4}$$

One can arbitrarily take hadron A to contain a quark and hadron B to contain an anti-quark. $x_{\mathrm{A}}(x_{\mathrm{B}})$ is a fraction of the linear momentum held by a quark(anti-quark) inside hadron A(B). These have collinear PDFs denoted $f_{\mathrm{a/A}}(x_{\mathrm{A}})$ and $f_{\mathrm{b/B}}(x_{\mathrm{B}})$ for partons a(b) inside their parent hadron A(B) respectively. $d\hat{\sigma}$ is the subprocess cross section, where the initial state consists of the two colliding partons, and the integration covers all contributing phase space configurations.

The factorisation theorem considers PDFs to be universal and therefore process independent. Theoretically PDFs only need to be measured once in order to predict the cross section of many other processes, provided they do not violate the appropriate factorisation theorem.

PDF sets can only be obtained by fitting a large number of cross section data points in a grid of Q^2 and x values obtained experimentally. It is common to parameterise parton distributions in terms of x at a low level of $Q^2 = Q_0^2$, and evolve them up to Q^2 through the Dokshitzer–Gribov–Lipatov–Altarelli–Parisi (DGLAP) equation [54]. PDF sets are a valuable tool needed for Monte Carlo generation which assumes a process is described by a PDF. An example of a commonly used PDF set (CTEQ6L1) within the ATLAS experiment is shown in Figure 3.4, which is applied to Monte Carlo simulations. The figure shows how the proton structure varies at differing values of x at a scale given by $\mathrm{Q}^2 = 100\ \mathrm{GeV}^2$.

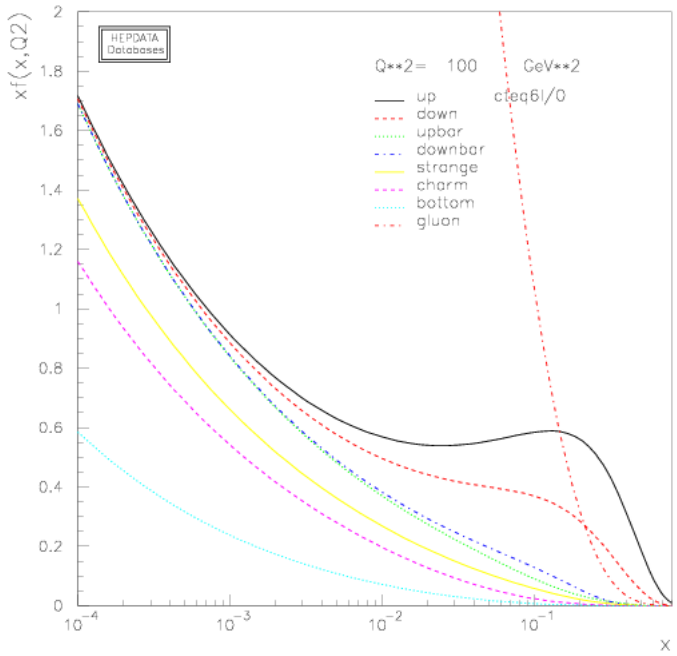

Figure 3.4: Figure of the CTEQ6L1 PDF set at fixed $Q^2 = 100$ GeV^2. The CTEQ6L1 PDF set is commonly used for B-physics analyses on the ATLAS experiment for Run II analyses, which is obtained from Run I data. This type of PDF set is applied to Monte Carlo simulations [55].

3.3 Transverse-Momentum-Dependent Parton Distribution Functions

Despite the longitudinal dimension of the parton model phase space being more important to collider physics, with PDFs accurately describing the distribution of longitudinal momentum, they do not describe internal proton dynamics in three dimensions. Drell-Yan studies ($q + \bar{q} \rightarrow l^+l^-$) have found that the produced dilepton pair have a non-zero distribution in transverse momentum which cannot be explained by the 'naive' parton model [56], which suggests that transverse momentum must be included for a complete hadronic description.

Spin also appears to play an important role in QCD, with QCD spin physics driven by DIS experiments [57–59]. The results showed that quark and anti-quark spins (when summed over all flavours) account for about a quarter of a nucleon's spin according to the proton

helicity sum rule [60–62]. It has been suggested that gluons could significantly contribute to the proton's spin through the assumption gluons are polarised [63], with some experimental evidence supporting this [64].

Collinear factorisation may be extended to incorporate the internal transverse dynamics of the proton, by considering the individual partonic transverse momenta. One scheme is TMD factorisation, where the individual transverse motion of partons within a proton is parameterised through TMD PDFs [65]. TMD phenomenology and derivations can be read in Refs [66, 67]. Some experiments have attempted to understand the transverse motion of partons and extract TMD PDFs [68–70].

3.3.1 Current Experimental Landscape

Presently, only the transverse structure of the quark component of the proton has been studied experimentally [71], with a first determination of unpolarised quark TMDs in 2018 [72]. Interacting quarks can produce a virtual gauge boson such as γ^*, or a Z boson, which is not strongly interacting, that is then a courier of information regarding parton transverse momenta from the initial to the final state of the interaction. Should the gauge boson decay into a lepton anti-lepton pair, the dilepton transverse momentum enables the transverse momentum of the gauge boson to be determined. Indeed, the first measurement was through the simultaneous analysis of DIS, Drell-Yann and Z boson hadroproduction processes at LO perturbative QCD, determining the average transverse momentum of a parton, and the unpolarised quark TMD function f_a^1 [72]. Further discussion of experimental efforts to extract quark TMDs can be reviewed in Ref [71].

Little is known about gluon TMD PDFs as studying them is more challenging [65] due to few 'clean' probes, such as $\gamma^* + \mathrm{g} \to c + \bar{c}$ in DIS shown in Figure 3.5. In this interaction the photon's transverse momenta is the difference between the initial and final momentum of the interacting electron. Ideally, one should be capable of performing a measurement of the transverse momentum of the $c\bar{c}$ system, providing information on the initial gluon transverse momentum. However, in this process $c\bar{c}$ pairs are not easily produced [73]. Furthermore, in this scenario, the transverse momentum of the $c\bar{c}$ pair is not measured directly, but rather the transverse momenta of two mesons. The complication is that some meson transverse momenta would have been created during hadronisation, and therefore

not first hand information regarding the transverse momentum of the initial gluon. As such, DIS is not a clean process for the determination of gluon TMDs [73]. At the LHC, an ideal candidate, produced in abundance at the LHC in gluon-gluon collisions, and does not interact strongly with hadronic matter produced in a collisions, is the Higgs boson. However, Higgs production suffers from large backgrounds, and in fact knowledge of gluon TMDs is necessary to determine certain properties of Higgs production in the first place [73].

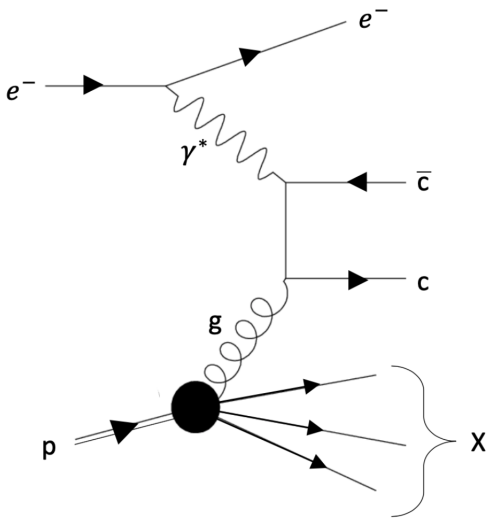

Figure 3.5: Feynman diagram of photon-gluon fusion into a $c\bar{c}$ pair. A gluon from a proton interacts with a photon emitted from an electron producing a $c\bar{c}$ pair [73].

3.3.2 Transverse Momentum Dependent Factorisation

The TMD picture can give rise to the appearance of azimuthal modulations in gluon-gluon scatterings [74–76] originating from the polarisation of partons with non-zero transverse momenta, k_{T}, even when colliding protons are unpolarised. The distribution of gluons with non-zero transverse momenta inside an unpolarised proton is parameterised by two TMD PDFs. TMD PDF f_1^g describes the distribution of unpolarised gluons inside an unpolarised proton, whilst TMD PDF $h_1^{\perp g}$ describes the distribution of linearly polarised gluons inside an unpolarised proton [65].

The linearly polarised distribution is the difference between gluon states with $+1$ and -1 helicity which would be suppressed if gluons had zero transverse momentum [74], and leads to angular distributions being modulated by a $\cos(2\phi_{\mathrm{CS}})$ term and a $\cos(4\phi_{\mathrm{CS}})$ term in the

Collins-Soper frame (see Section 3.3.4). Polarised gluons interact with each other, creating a preferred angular direction which manifests itself as azimuthal modulations.

Drell-Yan studies indicated that dilepton transverse momentum distributions within a TMD parameterisation can only be accounted for in the region of low transverse momenta (whose magnitude is in comparison to the hard scale of the process), which restricts the kinematical regime for TMD factorisation to apply [46]. For the cross section of a subprocess to be factorised according to the TMD framework, the overall transverse momentum of the final state, q_{T}, has to be small compared to the invariant mass, Q, of that system, i.e. $Q^2 \gg q_{\mathrm{T}}^2$. In QCD, a cross section can be separated into its long and short distance parts (see Eqn. 3.4), where there is just one scale, Q^2, which must be larger than Λ_{QCD} as this is the point where separation occurs. For TMD factorisation, two scales are required: Q, and q_{T} which must also be larger than Λ_{QCD}. In particular, for gluon TMD studies a subprocess must satisfy the following criteria:

- The initial state of the subprocess, at leading order, must have a two-gluon structure.
- In the final state, the objects must be colour singlets, so that the final state interactions (FSI) are suppressed.

For TMD factorisation to hold, at most, either initial state interactions (ISI) or FSI can be present, which limits interactions to either a colourful initial or final state [75]. Unfortunately, there currently exists no experimental programme in which to explore colourful final states. Therefore, only processes with a colourful initial but colourless final state can be explored.

3.3.3 Associated J/$\psi + \gamma$ Production In pp Collisions

Several subprocesses have been proposed for the measurement of the transverse momentum of gluons inside the proton, [65, 76–79], one of which is pursued here.

To explore gluon TMDs at the LHC in pp collisions, a subprocess must fulfil the two aforementioned criteria such that the produced particles directly carry the information from the initial to the final state.

Several papers [65, 75] advocate the extraction of gluon TMD PDFs in an unpolarised proton through the production of quarkonium states in pp collisions. In particular, it is

proposed that a suitable process is the associated production of a ${}^3S_1$ quarkonium, $\mathcal{Q}$, such as the J/ψ meson with a photon, $pp \to \mathcal{Q} + \gamma + X$, whose Feynman diagram at LO is given by Figure 3.6. In the loop are charm quarks, with the two forming the J/ψ on shell, whilst the other two are real charm propagators whose mass is not fixed.

Although QCD corrections to inclusive production of a J/ψ are known to be large, this does not translate to the J/$\psi + \gamma$ final state production. Selecting an appropriate energy scale also leaves the process free of large logarithmic divergences. The J/ψ is produced via the colour-singlet production mechanism, dominating at leading order [65], with the $c\bar{c}$ bound state consisting of two heavy quarks which have their interaction with hadronic matter suppressed. The J/ψ decays, on a relatively short timescale, into muons approximately 6% of the time. The photon is produced even more cleanly and does not interact. Electromagnetic scattering of the photon can be safely ignored as it is outside the level of sensitivity for the analysis due to the electromagnetic coupling constant, α_{em}, suppression. If gluons are radiating from the loop, it is heavily suppressed by the charm quark propagators, and does not need to be considered for this analysis.

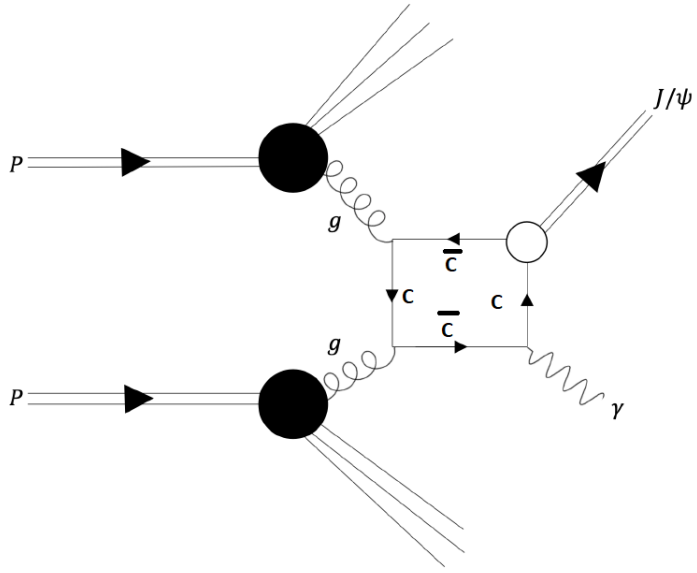

Figure 3.6: Feynman diagram of the associated production of a g + g $\to$ J/$\psi + \gamma$ in pp collisions [73].

In this subprocess, for TMD factorisation to apply, the final state transverse momentum imbalance, $\boldsymbol{q_T} = \mathbf{P}_{\mathrm{T}}^{\mathcal{Q}} + \mathbf{P}_{\mathrm{T}}^{\gamma}$, must be small compared to the invariant mass of the J/$\psi + \gamma$ system [65], which is achieved when a J/ψ and γ are produced back to back.

In conclusion, a measurement of the continuum cross section of the associated production of a J/ψ and an isolated photon represents a good process for the extraction of gluon TMDs at LO. Information on the initial transverse momentum of gluons is directly accessible from the J/$\psi + \gamma$ system, any gluon radiation is suppressed, both the J/ψ and γ are produced as colour singlets, with the J/ψ interacting little with hadronic matter and quickly decaying to a muon pair, with electromagnetic scattering of the photon outside the level of sensitivity of the analysis.

3.3.4 Collins-Soper Frame

The Collins-Soper (CS) frame is a convenient frame in which to make measurements of angular dependencies (azimuthal modulations), which would otherwise be smeared (appear flat) in the laboratory frame. In the CS frame, the J/$\psi - \gamma$ system is at rest, and angular dependencies look distinct. An illustration of this frame for the subprocess considered in this thesis is shown in Figure 3.7

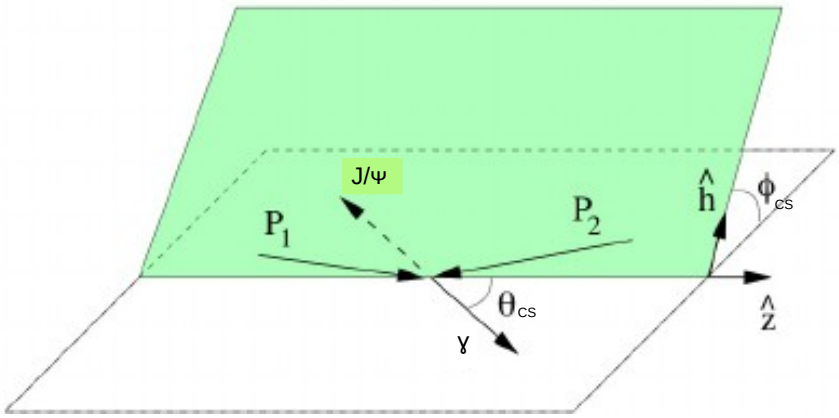

Figure 3.7: Illustration of the Collins-Soper frame, defining the angles θ_{CS} and ϕ_{CS}, which are measured in this frame [80].

Boost from the laboratory frame to the CS frame, which is the rest frame of the J/$\psi + \gamma$ system. In the boosted frame, the incoming proton momenta P_1 and P_2 are not aligned along the same line, defining the green plane in Figure 3.7. The z-axis is chosen to be along

the line bisecting the angle between the incoming protons, i.e the z-axis forms the same angle with both proton momenta. The polar angle ϕ_{CS} is defined between the green plane and the plane formed by the momenta of the J/ψ and γ. Only the momenta of the outgoing J/ψ and γ, and the incoming proton directions are needed. An indepth examination of this frame can be found in Appendix A.

3.3.5 Gluon TMD Study With A J/$\psi + \gamma$ Final State

Within the TMD approach, the relevant cross section for any process initiated by gluon-gluon scattering can be written (up to $\mathcal{O}(\frac{q_T^2}{Q})$ corrections) as the convolution of the short distance subprocess matrix element, $\mathcal{M}_{\mu\rho}$, with two TMD correlators. For the associated production of a J/ψ and isolated photon sub-process, the cross section is given by [65]:

$$d\sigma = \frac{(2\pi)^4}{8s^2} \int d^2\boldsymbol{k}_{1\mathrm{T}}\, d^2\boldsymbol{k}_{2\mathrm{T}}\, \delta^2(\boldsymbol{k}_{1\mathrm{T}} + \boldsymbol{k}_{2\mathrm{T}} - \boldsymbol{q}_{\mathrm{T}})\, \mathcal{M}_{\mu\rho}(\mathcal{M}_{\nu\sigma})^*\, \Phi_q^{\mu\nu}(x_1, \boldsymbol{k}_{1\mathrm{T}})\, \Phi_q^{\rho\sigma}(x_2, \boldsymbol{k}_{2\mathrm{T}})\, d\mathcal{R}, \tag{3.5}$$

where $\boldsymbol{q_T}$ represents the transverse momentum imbalance of the J/$\psi - \gamma$ system, namely $\boldsymbol{q_T} = \mathbf{P}_{\mathrm{T}}(\mathrm{J}/\psi) + \mathbf{P}_{\mathrm{T}}(\gamma)$. The individual transverse momenta of the two gluons are given by $\boldsymbol{k}_{1\mathrm{T}}$ and $\boldsymbol{k}_{2\mathrm{T}}$, the hadronic centre of mass (C.o.M) energy squared is $s = (\mathrm{P}_1 + \mathrm{P}_2)^2$, and d$\mathcal{R}$ denotes the phase space element of the outgoing particles [65].

The gluon correlator for an unpolarised proton can be parameterised in terms of two gluon TMD PDFs, namely f_1^g and $h_1^{\perp g}$:

$$\Phi_g^{\mu\nu}(x, \boldsymbol{k}_{\mathrm{T}}) = -\frac{1}{2x}\left\{ g_{\mathrm{T}}^{\mu\nu} f_1^g - \left(\frac{\boldsymbol{k}_{\mathrm{T}}^{\mu}\boldsymbol{k}_{\mathrm{T}}^{\nu}}{m^2} + g_{\mathrm{T}}^{\mu\nu} \frac{\boldsymbol{k}_{\mathrm{T}}^2}{2m^2} \right) h_1^{\perp g} \right\} + \text{suppr.} \tag{3.6}$$

where $g_{\mathrm{T}}^{\mu\nu} = g^{\mu\nu} - (P_1^{\mu}P_2^{\nu} + P_2^{\mu}P_1^{\nu})/P_1 \cdot P_2$. Terms of higher orders in $\boldsymbol{k}_{\mathrm{T}}^2$ are suppressed in the high energy limit. The proton mass is given by m [65]. $\boldsymbol{k}_{\mathrm{T}}^{\mu}$ are the transverse components of the gluon's momentum. For the subprocess $g(k_1) + g(k_2) \to \mathrm{J}/\psi(P^{\mathrm{J}/\psi}) + \gamma(P^{\gamma})$, the cross

section takes the form [65]:

$$\begin{aligned}\frac{d\sigma}{dQ\,dY\,d^2\boldsymbol{q}_{\mathrm{T}}\,d\Omega_{\mathrm{CS}}} = \frac{C_0(Q^2-M^2)}{sQ^3D}\Big\{ & F_1\mathcal{C}\Big[f_1^g f_1^g\Big] \\ & + F_3\cos(2\phi_{\mathrm{CS}})\mathcal{C}\big[w_3 f_1^g h_1^{\perp g}\big] + F_3'\cos(2\phi_{\mathrm{CS}})\mathcal{C}\big[w_3' f_1^g h_1^{\perp g}\big] \\ & + F_4\cos(4\phi_{\mathrm{CS}})\mathcal{C}\Big[w_4 h_1^{\perp g} h_1^{\perp g}\Big]\Big\} + \mathcal{O}\Big(\frac{\boldsymbol{q}_T^2}{Q^2}\Big),\end{aligned} \tag{3.7}$$

where the solid angle $d\Omega_{\mathrm{CS}} = d\cos\theta_{\mathrm{CS}}\,d\phi_{\mathrm{CS}}$ is given in terms of the CS angles [81], which describe the spatial orientation of the J/$\psi-\gamma$ pair in the CS frame. M is the J/ψ mass, Q is the invariant mass of the J/$\psi+\gamma$ system, $\lambda \equiv Q^2/M^2$, and the remaining symbols are defined as follows:

$$\begin{aligned} C_0 &= \Big(4\,\alpha_s^2\,\alpha_{\mathrm{em}}\,e_c^2\,|R_0(0)|^2\Big)/(3M^3), \\ D &= \Big((\lambda+1)^2-(\lambda-1)^2\cos^2\theta_{\mathrm{CS}}\Big)^2, \\ F_1 &= 1+2\lambda+9\lambda^2+(6\lambda^2-2)\cos^2\theta_{\mathrm{CS}}+(\lambda-1)^2\cos^4\theta_{\mathrm{CS}}, \\ F_3 &= 4\lambda\sin^2\theta_{\mathrm{CS}}, \\ F_4 &= (\lambda-1)^2\sin^4\theta_{\mathrm{CS}}, \\ w_3 &= \frac{\boldsymbol{q}_{\mathrm{T}}^2\,\boldsymbol{k}_{2\mathrm{T}}^2-2(\boldsymbol{q}_{\mathrm{T}}\cdot\boldsymbol{k}_{2\mathrm{T}})^2}{2m^2\boldsymbol{q}_{\mathrm{T}}^2}, \\ w_4 &= 2\Big[\frac{\boldsymbol{k}_{1\mathrm{T}}\cdot\boldsymbol{k}_{2\mathrm{T}}}{2m^2}-\frac{(\boldsymbol{k}_{1\mathrm{T}}\cdot\boldsymbol{q}_{\mathrm{T}})(\boldsymbol{k}_{2\mathrm{T}}\cdot\boldsymbol{q}_{\mathrm{T}})}{m^2\boldsymbol{q}_{\mathrm{T}}^2}\Big]^2-\frac{\boldsymbol{k}_{1\mathrm{T}}^2\,\boldsymbol{k}_{2\mathrm{T}}^2}{4m^4}. \end{aligned} \tag{3.8}$$

α_{em} is the fine structure constant, denoting the strength of the electromagnetic interaction, e_c^2 is the heavy quark charge (for c quarks it is $+\frac{2}{3}$), and $R_0(0)$ is the quarkonium wave function evaluated at the origin.

The convolution, $\mathcal{C}$, is defined as:

$$\mathcal{C}[w\,f\,g] \equiv \int d^2\boldsymbol{k}_{1\mathrm{T}}\int d^2\boldsymbol{k}_{2\mathrm{T}}\delta^2(\boldsymbol{k}_{1\mathrm{T}}+\boldsymbol{k}_{2\mathrm{T}}-\boldsymbol{q}_{\mathrm{T}})w(\boldsymbol{k}_{1\mathrm{T}},\boldsymbol{k}_{2\mathrm{T}})f(x_1,\boldsymbol{k}_{1\mathrm{T}}^2)g(x_2,\boldsymbol{k}_{2\mathrm{T}}^2), \tag{3.9}$$

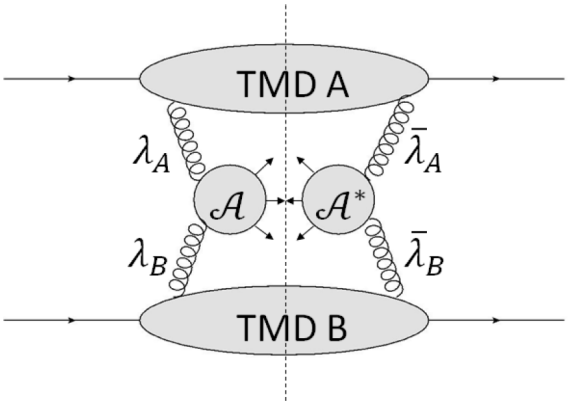

Figure 3.8: Diagram of a two gluon process in the TMD formalism. The amplitude $\mathcal{A}$ corresponds to the left of the split, whilst the conjugate amplitude $\mathcal{A}^*$ corresponds to the right. $\lambda_{A,B}$ is the helicity amplitude of the interacting gluon from hadron A and B respectively [84].

with transverse weights $w_1 = 1$ and $w_{3,4}$ defined above. A convolution is a mathematical function which operates on two functions to produce a third. The chosen definitions for f_1^g and $h_1^{\perp g}$ are substituted for f and g in Eqn. 3.9, with transverse weight w, to produce the relevant convolutions seen in Eqn. 3.7. The convolutions contain the intrinsic transverse momentum dependence and are process independent.

The $F_{1,3,3',4}$ are the short distance coefficients, which contain the kinematics of the process. The factors F_i are calculable process by process, and details on how to obtain them can be reviewed in Ref [82]. The F factors defined in Eqn. 3.8, are expressed in terms of λ, and kinematical configurations where TMD factorisation is expected to hold, i.e. $Q^2 \gg q_{\mathrm{T}}^2$ [83]. An F_2 term would be present if the final state particles were both massive.

The short distance coefficients can be understood in terms of gluon helicity λ, with values $\pm$ 1. The calculation of the gluon-gluon fusion subprocess, represented in Figure 3.8, involves multiplying the helicity amplitude $\mathcal{A}_{\lambda_A \lambda_B}$ by it's conjugate amplitude. Each hadron contributes a gluon TMD to the cross section resulting in distinct convolutions of f_1^g and $h_1^{\perp g}$. The function f_1^g conserves helicity, whilst h_1^g flips it. The amplitude products can be seen in Table 3.3. F_3 considers the case where one gluon is polarised and the other is not, so only one gluon's helicity is flipped. F_4 corresponds to the case where both gluon helicities are opposite, and the helicity of each gluon is flipped. These terms introduce azimuthal asymmetries to angular distributions.

Coefficient	Helicity Contribution	TMD	Helicity Flip	Azimuthal Asymmetry
F_1	$\sum_{\lambda_A,\lambda_B} \mathcal{A}_{\lambda_A,\lambda_B}\mathcal{A}^*_{\lambda_A,\lambda_B}$	$\mathcal{C}[f_1^g f_1^g]$	None	None
F_3	$\sum_{\lambda_A,\lambda_B} \mathcal{A}_{\lambda_A,\lambda_B}\mathcal{A}^*_{-\lambda_A,\lambda_B}$	$\mathcal{C}[w_3 h_1^{\perp g} f_1^g]$	Single	$\cos(2\phi_{\mathrm{CS}})$
$F_{3'}$	$\sum_{\lambda_A,\lambda_B} \mathcal{A}_{\lambda_A,\lambda_B}\mathcal{A}^*_{\lambda_A,-\lambda_B}$	$\mathcal{C}[w_{3'} h_1^{\perp g} f_1^g]$	Single	$\cos(2\phi_{\mathrm{CS}})$
F_4	$\sum_{\lambda} \mathcal{A}_{\lambda,-\lambda}\mathcal{A}^*_{-\lambda,\lambda}$	$\mathcal{C}[w_4 h_1^{\perp g} h_1^{\perp g}]$	Double	$\cos(4\phi_{\mathrm{CS}})$

Table 3.3: Table outlining each helicity contribution to a gluon-gluon fusion cross section. Each contribution is represented by a short distance coefficient and associated TMD convolution [75].

In the field of TMD studies it is usually assumed that [74, 75], f_1^g has to be of the form

$$f_1^g(x, k_{\mathrm{T}}^2) = \frac{G(x)}{\pi\langle k_{\mathrm{T}}^2\rangle} \exp\left(-\frac{k_{\mathrm{T}}^2}{\langle k_{\mathrm{T}}^2\rangle}\right), \tag{3.10}$$

a simple Gaussian with dependence on the intrinsic transverse momentum of the gluon, k_{T}^2, where the collinear gluon distribution is given by $G(x)$ and $\langle k_{\mathrm{T}}^2\rangle$ is expected to be of order of $\mathcal{O}(10\ \mathrm{GeV}^2)$ [75]. Substituting Eqn. 3.10 into the convolution $\mathcal{C}[f_1^g f_1^g]$, seen in Eqn. 3.7, and following the definition for a convolution (see Eqn. 3.9 and using $w = 1$), then $\mathcal{C}[f_1^g f_1^g]$ can be calculated analytically:

$$\mathcal{C}[f_1^g f_1^g] = \frac{G(x_1)G(x_2)}{2\pi\langle k_{\mathrm{T}}^2\rangle} \exp\left(-\frac{\boldsymbol{q}_{\mathrm{T}}^2}{2\langle k_{\mathrm{T}}^2\rangle}\right) \tag{3.11}$$

where x_1, x_2 denote the collinear momentum of the two gluons respectively.

If $h_1^{\perp g} = 0$, or the azimuthal distribution (ϕ_{CS}) of the differential cross section is integrated over (see Eqn. 3.7), then direct access to the gluon TMD distribution $f_1^g(x, k_{\mathrm{T}}^2)$ through the measurement of the dependence of the differential cross section as a function of q_{T}^2 is possible.

For the experimental extraction of gluon TMDs in a gluon induced process, with a J/$\psi + \gamma$ colourless final state, within the TMD framework, the J/ψ and γ need to be produced from Single Parton Scattering (SPS) and produced back-to-back, to give a balanced $q_{\mathrm{T}} \sim 0$ final state [65]. The lowest possible threshold on the transverse momentum of muons on the ATLAS experiment in 2015 was $p_{\mathrm{T}}(\mu^{\pm}) > 4$ GeV, implying a J/ψ with $p_{\mathrm{T}}(\mathrm{J}/\psi) > 8$ GeV. This is balanced by a γ with $p_{\mathrm{T}}(\gamma) > 8$-9 GeV produced at the same space point but flying in the opposite direction to give $q_T \sim 0$ and $Q \sim 16$ GeV. Larger Q is less probable, requiring

harder gluons to collide to create a larger invariant mass. In this configuration, in part due to the ATLAS trigger constraints, $\lambda \sim 20$, hence $\lambda \gg 1$. It is reasonable to simplify the cross section keeping only terms with the highest order in λ. The factor F_3 vanishes, and the remaining F factors simplify to:

$$F_1 = 9\lambda^2 + 6\lambda^2 \cos^2\theta_{\rm CS} + \lambda^2 \cos^4\theta_{\rm CS}$$

$$F_4 = \lambda^2 \sin^4\theta_{\rm CS}$$

The cross section can be re-written as

$$\frac{d\sigma}{dQ\ dY\ d^2q_{\rm T}\ d\Omega_{\rm CS}} = \frac{C_0(Q^2 - M^2)}{s\,Q^3 D} F_1 \mathcal{C}[f_1^g f_1^g] \left\{ 1 + \frac{F_4}{F_1} \cos(4\phi_{\rm CS}) \frac{\mathcal{C}[w_4 h_1^{\perp g} h_1^{\perp g}]}{\mathcal{C}[f_1^g f_1^g]} \right\}. \tag{3.12}$$

Here the first term in the curly brackets corresponds to the unpolarised gluon contribution, since it's only governed by the convolution of two f_1^g TMD functions. The second term corresponds to corrections due to the presence of linearly polarised gluons described by $h_1^{\perp g}$, and some extra dependence on the CS polar angle $\cos\theta_{\rm CS} \equiv z$, present in the ratio:

$$\frac{F_4}{F_1} = \frac{\sin^4\theta_{\rm CS}}{9 + 6\cos^2\theta_{\rm CS} + \cos^4\theta_{\rm CS}} = \frac{(1 - z^2)^2}{9 + 6z^2 + z^4}. \tag{3.13}$$

The second term in Eqn. 3.12 also contains some azimuthal modulation due to the dependence on $\cos(4\phi_{\rm CS})$. If one were to integrate over $\phi_{\rm CS}$, the cross section is reduced to the collinear result. A study [73], addressed in Section 3.3.6, has shown that this term is enhanced at small values of $|z|$, and a cut at $z^2 = 0.1$ separates the low z^2 area where $\cos 4(\phi_{\rm CS})$ modulation is enhanced from the high z^2 area where it is suppressed. This property will be used later for attempts at the extraction of azimuthal $\phi_{\rm CS}$ modulation arising from interacting polarised gluons.

3.3.6 Simulating Gluon Polarisation Effects

This section reports on a study conducted by M.Smith [73] which emulates the effects of the presence of $h_1^{\perp g}$ in a $\mathrm{g} + \mathrm{g} \to \mathrm{J}/\psi + \gamma$ subprocess. The aim was to produce a model for $h_1^{\perp g}$ and induce modulation in $\cos 4(\phi_{\rm CS})$ and determine it's size.

The process of J/ψ + γ production via gluon-gluon fusion was simulated with the MC generator `PYTHIA 8` [85], with $h_1^{\perp g}$= 0. The signal MC sample corresponds to an integrated luminosity of approximately 60 fb^{-1} at 13 TeV, with no accounting for detector efficiency. To induce azimuthal modulation, equivalent to a MC sample generated with a non-zero gluon TMD $h_1^{\perp g}$, each event needs to be assigned a weight equal to the $h_1^{\perp g}$-dependent part of Eqn. 3.12, given by the term inside the curly brackets, which needs to be determined. As such, the ratio of the two convolutions $\mathcal{C}[w_4 h_1^{\perp g} h_1^{\perp g}]$ and $\mathcal{C}[f_1^g f_1^g]$ is required. f_1^g is given by Eqn. 3.10, but little is known about the magnitude of $h_1^{\perp g}$ [75]. A model-independent positivity bound to restrict possible parameterisations for $h_1^{\perp g}$ [86] has been derived:

$$\frac{\boldsymbol{k}_{\mathrm{T}}^2 |h_1^{\perp g}(x, \boldsymbol{k}_{\mathrm{T}}^2)|}{2M^2} \leq f_1(x, \boldsymbol{k}_{\mathrm{T}}^2). \tag{3.14}$$

which holds for any value of x and $\boldsymbol{k}_{\mathrm{T}}$.

The aim of the study [73] was to obtain numerical estimates based on two models of $h_1^{\perp g}$. Following [74, 75], 'Model 1' is defined by:

$$h_1^{\perp g}(x, k_{\mathrm{T}}^2) = \frac{M^2 G(x)}{\pi \langle k_{\mathrm{T}}^2 \rangle^2} \exp\left(1 - \frac{k_{\mathrm{T}}^2}{r\langle k_{\mathrm{T}}^2 \rangle}\right), \tag{3.15}$$

where $r = 2/3$ [74, 75].

A second possible form of $h_1^{\perp g}$ [75], gives 'Model 2', where the function $h_1^{\perp g}(x, k_{\mathrm{T}}^2)$ saturates the positivity bound in equation 3.14, i.e. the inequality becomes an equality:

$$\frac{\boldsymbol{k}_{\mathrm{T}}^2 |h_1^{\perp g}(x, \boldsymbol{k}_{\mathrm{T}}^2)|}{2M^2} = f_1(x, \boldsymbol{k}_{\mathrm{T}}^2). \tag{3.16}$$

For Model 1, $\mathcal{C}[f_1^g f_1^g]$ is given by Eqn. 3.11 and calculating $\mathcal{C}[w_4 h_1^{\perp g} h_1^{\perp g}]$ analytically gives:

$$\mathcal{C}[w_4 h_1^{\perp g} h_1^{\perp g}] = \frac{G(x_1)G(x_2)(\boldsymbol{q}_{\mathrm{T}}^2)^2}{192\pi \langle k_{\mathrm{T}}^2 \rangle^3} \exp\left(2 - \frac{3\boldsymbol{q}_{\mathrm{T}}^2}{4\langle k_{\mathrm{T}}^2 \rangle}\right). \tag{3.17}$$

Thus the required convolution ratio is given by:

$$\frac{\mathcal{C}[w_4 h_1^{\perp g} h_1^{\perp g}]}{\mathcal{C}[f_1^g f_1^g]} = \frac{(\boldsymbol{q}_{\mathrm{T}}^2)^2}{96\langle k_{\mathrm{T}}^2 \rangle^2} \exp\left(2 - \frac{\boldsymbol{q}_{\mathrm{T}}^2}{4\langle k_{\mathrm{T}}^2 \rangle}\right). \tag{3.18}$$

For Model 2 analytical methods are incapable of computing the convolutions, but can be solved numerically as exhibited in the reference material [75] to give:

$$\frac{\mathcal{C}[w_4 h_1^{\perp g} h_1^{\perp g}]}{\mathcal{C}[f_1^g f_1^g]} = 1 - \exp\left(- \frac{\boldsymbol{q}_{\mathrm{T}}^2}{2\langle k_{\mathrm{T}}^2 \rangle} \right). \tag{3.19}$$

These two convolution ratios, Eqns. 3.17 and 3.19, are used to derive model-dependent expressions for the Model 1 and Model 2 weights. Substituting the convolutions into the term inside the curly brackets in Eqn 3.12, for Model 1:

$$W_1 = 1 + \frac{(\boldsymbol{q}_{\mathrm{T}}^2)^2}{96\langle k_{\mathrm{T}}^2 \rangle^2} \exp\left(2 - \frac{\boldsymbol{q}_{\mathrm{T}}^2}{4\langle k_{\mathrm{T}}^2 \rangle} \right) \frac{(1-z^2)^2}{(9+6z^2+z^4)} \cos(4\phi_{\mathrm{CS}}) \tag{3.20}$$

and for Model 2:

$$W_2 = 1 + \left[1 - \exp\left(- \frac{\boldsymbol{q}_{\mathrm{T}}^2}{2\langle k_{\mathrm{T}}^2 \rangle} \right) \right] \frac{(1-z^2)^2}{(9+6z^2+z^4)} \cos(4\phi_{\mathrm{CS}}). \tag{3.21}$$

The weighting functions W_1 and W_2 are dependent on the transverse momentum of the J/$\psi-\gamma$ pair, given by $\mathbf{q}_{\mathrm{T}}$ and the CS angles θ_{CS} and ϕ_{CS}, which describe the spatial orientation of the pair in their CS rest frame. It is expected that some $\cos(4\phi_{\mathrm{CS}})$ modulation is induced when a weight is applied to the MC events. As can be seen in Figure 3.9 for the unweighted distributions, using a sample with no generator level cuts, $\cos\theta_{\mathrm{CS}}$ has sharp peaks at $\pm$ 1. The distribution of the variable $|\phi_{\mathrm{CS}}|$ is flat, hence no visible modulation. However, this sample cannot be used in the analysis, as applying event selection cuts drastically reduces the number of statistics available. Hence the alternative sample with generator level cuts, $p_{\mathrm{T}}(\mu^+) > 4$ GeV, $p_{\mathrm{T}}(\mu^-) > 4$ GeV, and $p_{\mathrm{T}}(\gamma) > 5$ GeV ('445'), is used.

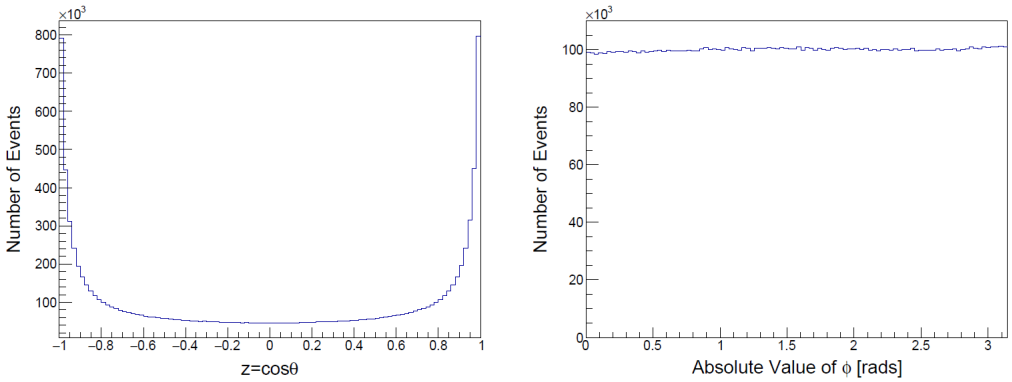

Figure 3.9: Plots of the variables (a) $z = \cos\theta_{CS}$ and (b) $|\phi_{\mathrm{CS}}|$ from a sample produced with no generator level cuts on the muons and photons [73].

The transverse momentum distribution, q_{T}, for the J/ψ + γ system, the unweighted distribution of $|\phi_{\mathrm{CS}}|$, and the unweighted distribution $z = \cos\theta_{\mathrm{CS}}$ are shown in Figure 3.10 with generator level '445' cuts applied to the muons and photons for the signal sample used in the analysis.

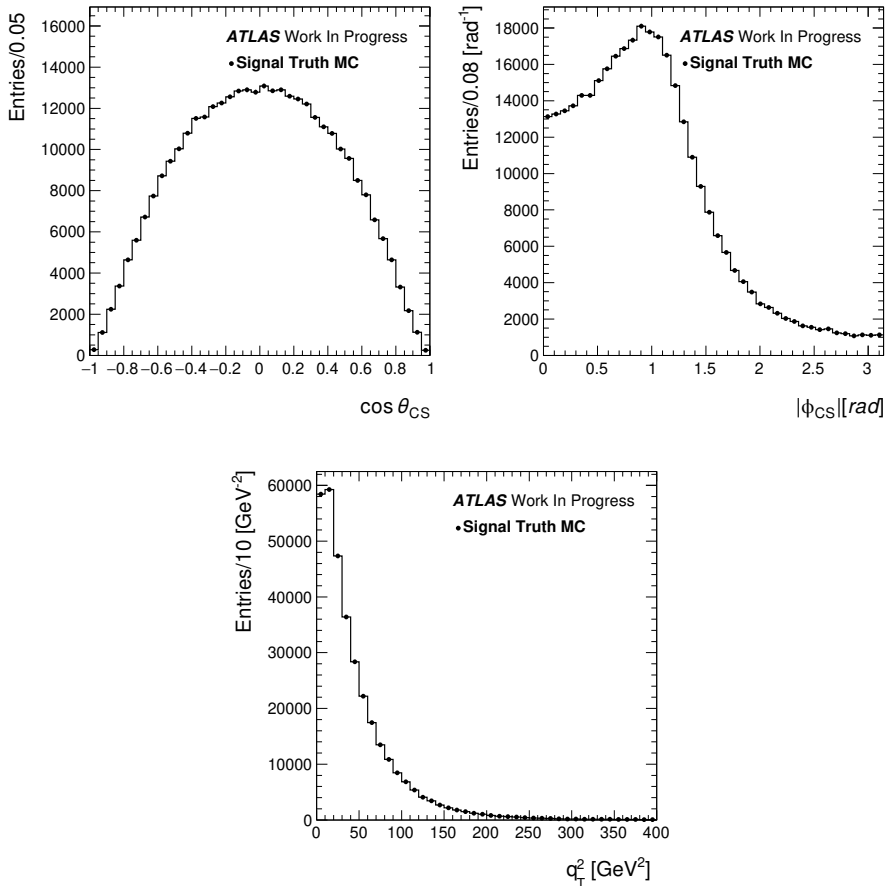

Figure 3.10: Plots of the truth variables (a) q_{T}, (b) $|\phi_{\mathrm{CS}}|$ and (c) $z = \cos\theta_{CS}$ with $p_{\mathrm{T}}(\mu^+) > 4$ GeV, $p_{\mathrm{T}}(\mu^-) > 4$ GeV, and $p_{\mathrm{T}}(\gamma) > 5$ GeV generator level event selection cuts applied to the muons and photons.

In an ideal experiment, with full acceptance, the dependence on ϕ_{CS} in the absence of gluon polarisation is expected to be flat with some $\cos(4\phi_{\mathrm{CS}})$ modulation appearing proportionally to the magnitude of $h_1^{\perp g}$. Unfortunately, kinematical cuts produce a non-negligible distortion of the observed ϕ_{CS} distributions (see Figure 3.10), which complicates the extraction of ϕ_{CS} modulated terms. However, these effects are almost independent of $\cos\theta_{\mathrm{CS}}$, and can be suppressed by taking ratios of differential cross sections for the low and high $\cos^2\theta_{\mathrm{CS}}$ regions to enhance any modulation, which the study advises. A cut at $z^2 = 0.1$ is selected to approximately divide the data sample roughly in half, whilst retaining the statistical significance of any possible signal from polarised gluons.

The events are weighted with a value of $\langle k_{\mathrm{T}}^2 \rangle = 1$ GeV^2, for different values of $\mathbf{q}_{\mathrm{T}}$, and the ratio of the low and high $\cos^2\theta_{\mathrm{CS}}$ distributions can be seen in Figure 3.11 for Model

1 and Model 2 for the MC sample created with '445' generator level cuts. However, as the minimum p_{T} of a muon is 4 GeV suggesting the $p_{\mathrm{T}}(\mathrm{J}/\psi) > 9$ GeV, in order to have a balanced $\mathrm{J}/\psi - \gamma$ system a $p_{\mathrm{T}}(\gamma) > 9$ GeV cut is applied. In order to make the induced modulation effects more visible the ratio of the $|\phi_{\mathrm{CS}}|$ distributions with and without the additional weighting are shown, and both fitted with a Fourier decomposition, $p_0 \times (1 + \sum_{n=1}^{4} p_n \cos(n\phi_{\mathrm{CS}}))$, truncated at $\cos(4\phi_{\mathrm{CS}})$. If gluons are polarised, it is expected that there will be significant enhancement of the $\cos(4\phi_{\mathrm{CS}})$ term, which describes the amplitude of any induced modulation. The cosines in the fitting function are orthogonal to each other, hence their coefficients are independent and removing odd cosine terms will not change the results. The ratios for both models, compared to the unweighted case, are plotted in Figure 3.11.

Model 1 shows little deviation from the unweighted distribution, which is to be expected as all fit parameters, excluding p_4, are consistent within σ of the two distributions, and no significant $\cos(4\phi_{\mathrm{CS}})$ in either case. Clearly, the weighting of the distribution according to Model 1 has little effect, as $p_4 = 0.009 \pm 0.005$, corresponding to 1% amplitude, but is consistent with 0 within 2σ. In comparison, there is clear modulation in Model 2 in comparison to the unweighted case, with $p_4 = 0.049 \pm 0.005$. The LHC may in the future offer the integrated luminosity needed to reach the sensitivity needed for Model 1.

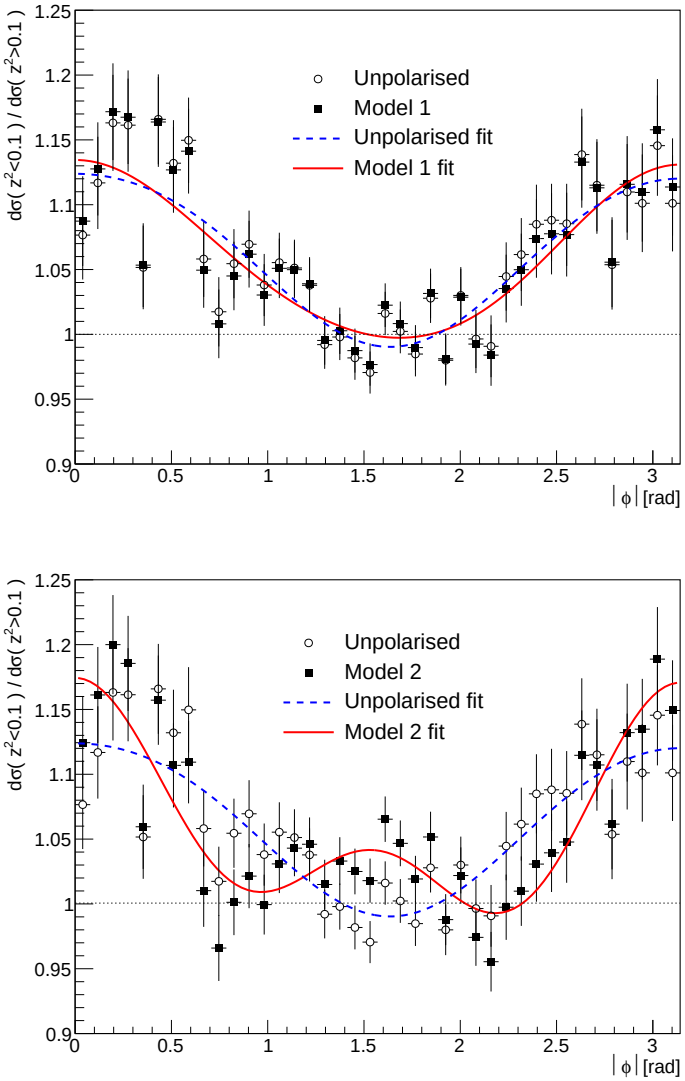

Figure 3.11: The ratios of differential cross sections for events with $z^2 < 0.1$ over the events with $z^2 > 0.1$, for Model 1 (top) and Model 2 (bottom) described in the text. On both plots, open points describe the unweighted distribution, corresponding to $h_1^{\perp g} = 0$, with the fit shown as dashed blue lines. The solid squares describe the weighted distributions, with the fits shown as solid red lines. Details of the origin of these plots can be reviewed in Ref. [73].

To conclude, the study [73] advises that in order to access the linearly polarised gluon TMD $h_1^{\perp g}$, the sample should be separated into two regions of $z^2 \equiv \cos^2\theta_{\mathrm{CS}}$, with the low-to-high z^2 ratio of the differential distributions in $|\phi_{CS}|$ be fitted with a truncated Fourier series: $p_0 \times (1 + \sum_{n=1}^{4} p_n \cos(n\phi_{\mathrm{CS}}))$, as terms beyond $n = 4$ are negligible. The coefficient of $\cos(4\phi_{\mathrm{CS}})$ in the series will give the relative magnitude of the $4\phi_{\mathrm{CS}}$ modulated term seen in

Eqn. 3.12.

3.3.7 Simulating The Average Transverse Momentum of Gluons

The study described in Section 3.3.6 took $\langle k_{\mathrm{T}}^2 \rangle$ to be 1 GeV^2, but the size of this term can be measured for the $\mathrm{g} + \mathrm{g} \to \mathrm{J}/\psi + \gamma$ subprocess, through the measurement of the F_1 term in Eqn. 3.12, where the $\mathcal{C}[f_1^g f_1^g]$ can be expressed as Eqn. 3.11, and f_1^g is assumed to be a Gaussian of the form shown in Eqn. 3.10. The cross section is directly proportional to the $\mathcal{C}[f_1^g f_1^g]$ term once the cross section is integrated over ϕ_{CS}, rapidity, and the angular degrees of freedom, leaving only a q_{T}^2 dependent term.

A measurement of the differential cross section as a function of q_{T}^2 is a measurement of the $\mathcal{C}[f_1^g f_1^g]$ convolution, which is taken to be Gaussian. The distribution can then be fitted with an exponential to measure the average k_{T} of an unpolarised gluon which is proportional to f_1^g (see Eqn. 3.11).

The events in the truth signal sample have the cuts $p_{\mathrm{T}}(\mu^+) > 4$ GeV, $p_{\mathrm{T}}(\mu^-) > 4$ GeV, and $p_{\mathrm{T}}(\gamma) > 9$ GeV ('449') applied. The increased photon cut from generator level ('445') leaves only events with $\lambda > \ 25$. The differential cross section as a function of q_{T}^2 is plotted in Figure 3.12 for three λ regions with edges $25 - 50 - 100 - 200$. The differential cross sections were obtained by dividing the number of events in each q_{T}^2 bin by that bin's bin width and dividing by the estimated integrated luminosity of the MC sample, about 60 fb^{-1}.

To measure the average k_{T} of a gluon in each λ region, the distributions are fitted with a double exponential function: $F(q_T^2) = p_0 \cdot \exp\left(-\frac{q_T^2}{2p_1^2}\right) + p_2 \cdot \exp\left(-\frac{q_T^2}{2p_3^2}\right)$, as can be seen in Figure 3.12. TMD theory [75] suggests that the narrower term, described by p_3, depends on the intrinsic k_{T} of a gluon and this is not perturbative. Hence, p_3 is a measure of the average transverse momentum of gluons inside an unpolarised proton. As can be seen in Figure 3.12, as λ increases the values p_1 and p_3 increase. The parameter of interest is p_3 which results summarised in Table 3.4.

lambda Region	$\sqrt{\langle k_{\mathrm{T}}^2 \rangle}$ (GeV)
$25 \leq \lambda < 50$	1.83 ± 0.01
$50 \leq \lambda < 100$	2.91 ± 0.02
$100 \leq \lambda < 200$	3.41 ± 0.06

Table 3.4: Table of results for the instrinic mean gluon transverse momentum, $\sqrt{\langle k_{\mathrm{T}}^2 \rangle}$, measured at three different truth λ regions.

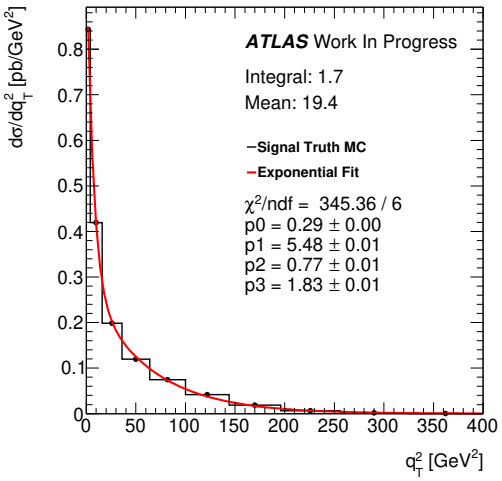

(a) λ slice 3: $25 \leq \lambda < 50$

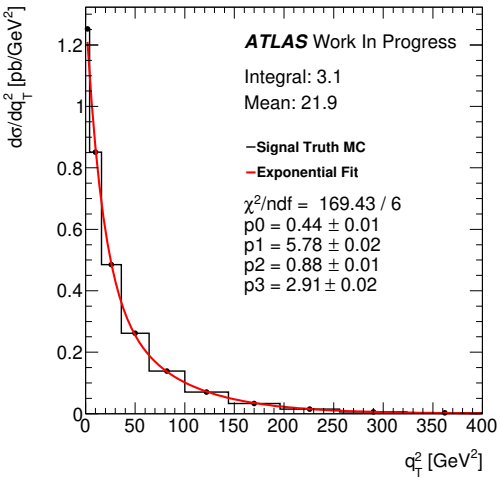

(b) λ slice 4: $50 \leq \lambda < 100$

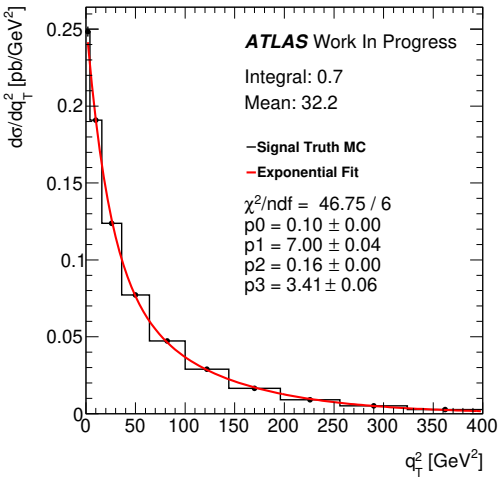

(c) λ slice 5: $100 \leq \lambda < 200$

Figure 3.12: Differential distributions as a function of q_{T}^2 for three different λ regions.

This study which indicates that measuring the q_{T}^2 distribution integrated over the angular variables (see Eqn. 3.12) allows to determine the shape of the unpolarised distribution

f_1^g. The parameter p_1, describing the wider component of the q_T^2 distribution, thus corresponds to the additional transverse momentum smearing which is due to higher-order gluon radiation corrections, which are expected to be concentrated mainly in the initial state of the subprocess $g + g \to J/\psi + \gamma$.

To conclude the studies presented in this section and Section 3.3.6, two measurements concerning TMD studies can be performed. Eq. (3.12) forms the basis of this analysis. Two types of differential cross sections are being studied. First, the angular degrees of freedom are implicitly integrated, thus effectively eliminating the second term in the curly brackets. Rapidity dependence is also integrated out, and the cross section, differential in q_T^2, is measured in several bins ('slices') of the variable λ. This will give a measurement of the average k_T of a gluon inside an unpolarised proton.

In the second part of the analysis, rapidity, λ, and q_T^2 are implicitly integrated, and the distribution in ϕ_{CS} is measured for two slices of z^2: $z^2 < 0.1$ and $z^2 > 0.1$. The ratio of these two distributions is used in an attempt to assess the presence of the polarised TMD function $h_1^{\perp g}$.

Although the sensitivity required for a measurement of the polarised TMD PDF $h_1^{\perp g}$ is unlikely with ATLAS Run II data, it should be enough for determination of the unpolarised TMD PDF f_1^g even with an integrated luminosity of approximately 2.57 fb^{-1} of data with a `2mu4`-type trigger used in this thesis.

Chapter 4

Event Selections

The analysis encompasses two separate measurements of the properties of the J/$\psi + \gamma$ system in pp collisions. The first is of the non-resonant J/$\psi + \gamma$ continuum cross section, as a function of q_{T}^2, for different regions in λ. The measurement of this differential cross section provides information on the properties of the intrinsic transverse momentum distribution of unpolarised gluons inside an unpolarised proton. The second measurement is an attempt to extract the polarised gluon TMD component in an unpolarised proton, through the measurement of the differential cross section with respect to the variable ϕ_{CS}. The separate measurements split the analysis into two streams, each involving different approaches, but they are based on the same event selections and categorisation.

This chapter begins introducing the four samples used in this analysis (one data and three MC), and how they are prepared up to, and including, reconstruction level cuts, detailed in Section 4.1. It then moves onto introducing the variables useful to the analysis, Section 4.2.1, with plots at reconstruction level for each sample. Section 4.2.2 details the common event selection requirements applied to all samples. Section 4.2.3 addresses selections relevant to λ and q_{T}^2 and Section 4.2.4 addresses selections relevant to the angular analysis, and plots of the distributions after event selections. The final section, Section 4.2.5, details selections applicable to the truth variables in the signal MC sample.

4.1 Event Selections

This analysis aims to study the continuum, non-resonant, production of a prompt J/ψ in association with an isolated photon. This section describes the various samples and the main kinematic variables used in the $g + g \rightarrow J/\psi + \gamma$ analysis, that will be later used to extract signal from data through event selection, background suppression, and multivariate analysis techniques.

Section 4.1.1 outlines the 2015 data sample and trigger application, with Section 4.1.2 describing the details of reconstruction level event selections. Section 4.1.3 details the three MC samples utilised, one the signal subprocess, $g + g \rightarrow J/\psi + \gamma$, and two background MC samples describing events containing prompt and non-prompt J/ψ backgrounds. MC samples are generated using `PYTHIA 8.230` [85], which did not contain the $g + g \rightarrow J/\psi + \gamma$ subprocess until this analysis.

4.1.1 Event Selection: Trigger

Data from 2015 at 13 TeV is used, as that year offers the lowest prescales and the lowest possible thresholds on dimuon triggers, with a minimum $p_{\mathrm{T}}(\mu) > 4$ GeV, and relatively low levels of pileup (see Section 8.3). The topology of interest, guided by the theory, is where the transverse momentum q_{T} of the $J/\psi + \gamma$ system is (much) smaller than its invariant mass Q, favouring configurations where the J/ψ and γ are produced back-to-back in the laboratory frame to give the best chance of the transverse momentum of the $J/\psi - \gamma$ system summing to $q_{\mathrm{T}} \sim 0$.

Events are triggered by a pair of oppositely charged muons, originating from the same production vertex and successfully fitted to a common vertex, using the trigger `HLT_2mu4_bJpsimumu_noL2`, active during the data 2015 collection periods. The trigger remained un-prescaled for most of 2015, with prescaling introduced late in the year. Hence, the data from 2015 offers an effective integrated luminosity of 2574 pb^{-1}.

The fit to the dimuon vertex is performed at the HLT stage, which requires candidates with dimuon invariant mass in the range $2.5 \leq m_{\mu\mu} \leq 4.3$ GeV[1] and $\chi^2 \leq 20$. For this particular

[1] $\mu\mu$ refers to $\mu^+\mu^-$

trigger chain, vertexing and mass requirements are applied only at the Event Filter (EF) step, and thus use the muon tracks from full reconstruction, offering improved efficiency compared to some other dimuon trigger chains. Details of the ATLAS muon trigger system during Run 2 can be found in Ref. [87].

4.1.2 Event Selection: Reconstruction

Further event selections occur during the reconstruction stage according to general B-physics J/ψ event selections within ATLAS to capture events of interest within the J/ψ mass window for later analysis. As such, dimuons are required to be in the mass range $2.6 \leq m_{\mu\mu} \leq 3.5$ GeV, with dimuon rapidity $|y| < 2.5$[2]. The muons must have $p_{\mathrm{T}}(\mu^{\pm}) > 4$ GeV, $|\eta| < 2.5$ and be of 'low-p_{T}' or 'tight' quality[3]. Photons must have $p_{\mathrm{T}}(\gamma) > 5$ GeV and $|\eta| < 2.5$. Selected events encompass the entire ATLAS detector acceptance region ($|\eta| < 2.5$).

Photons used in this analysis are unconverted (i.e. have not converted to $\mathrm{e}^{-}\mathrm{e}^{+}$ pairs before reaching the ECAL), thus providing high statistics, and satisfy 'tight' isolation criteria [89]. These selection requirements use both calorimeter-based and track-based isolation criteria, computed within a certain cone of radius ΔR around the photon direction. For 'tight' isolation:

$$E_{\mathrm{T}}^{\mathrm{Iso}}\Big|_{\Delta R<0.4} < 0.022 \times E_{\mathrm{T}} + 2.45 \text{ GeV} \text{ and } p_{\mathrm{T}}^{\mathrm{Iso}}\Big|_{\Delta R<0.2} < 0.05 \times E_{\mathrm{T}}. \tag{4.1}$$

Calorimeter isolation, $E_{\mathrm{T}}^{\mathrm{Iso}}$, is obtained from the sum of the transverse energies of topological clusters in the calorimeters after subtracting on an event-by-event basis the energy deposited by the photon candidate, and the contribution from the underlying event and pileup (see Section 8.3). The track isolation, $p_{\mathrm{T}}^{\mathrm{Iso}}$, is obtained by summing the transverse momenta of all tracks with $p_{\mathrm{T}} > 1$ GeV, and having a distance of closet approach to the beam axis $|z \sin\theta| < 3$ mm and excluding tracks with associated photon conversions.

By considering only 'tight' photons this leads to a significant improvement to the signal-to-background ratio in comparison over 'loose' and 'tight' which were available in

[2] The $\Psi(2S)$ particle has mass 3.69 GeV and therefore excluded from the analysis.
[3] Full definitions of muon quality classification can be found in Ref. [88]

the data sample[4], and is a well-calibrated working point for the later used efficiency scale factor maps to determine how well the signal MC sample is representative of the data sample (see Section 8.2).

4.1.3 Monte Carlo Simulation

MC simulations (at LO) are used to model the background and signal components in data, to understand the data's composition. The main (dominant) backgrounds considered in the data sample are from prompt J/ψ production and non-prompt J/ψ production.

Inclusive prompt J/ψ production, direct from QCD in the hard scatter primary interaction, is simulated generating 5 M events. This is performed in conjunction with `Photos` [90] to improve the simulation of radiative corrections through electromagnetic showers for final state particles, which `PYTHIA` struggles with. At every branching (decay) of an event simulated in `PYTHIA`, `Photos` intervenes with a certain probability to add extra photons and adjust the kinematics of other particles. This package mimics the effect of Bremsstrahlung corrections to decays of particles. Muons have a minimum $p_{\mathrm{T}}(\mu^{\pm}) > 3.5$ GeV. This sample is referred to as the 'pp' sample throughout the remainder of this thesis, and models the main background process.

Inclusive non-prompt J/ψ production, the generation of B-hadrons, is also simulated in conjunction with `Photos`, generating 10 M events. Muons have a minimum $p_{\mathrm{T}}(\mu^{\pm}) > 3.5$ GeV. The b quarks fragment into B hadrons, and one of the two B hadrons is forced to decay into a J/ψ + X (e.g. g $\rightarrow b\bar{b}$, then $\bar{b} \rightarrow B$, and finally $B \rightarrow$ J/ψ). This final state can sometimes contain photons, so occasionally a J/$\psi + \gamma$ final state is created. This sample is referred to as the 'bb' sample throughout this thesis and models a second type of background process.

The signal MC sample is the production of J/$\psi + \gamma$ in a gluon-gluon fusion subprocess, simulated with the aforementioned MC event generator, in conjunction with `Photos`. About 9.4 M truth events were generated. Preliminary studies, contained in Appendix B, show that samples with no generator level minimum p_{T} cuts on the muons and photons left low statistics after realistic event selections. For sizeable event yields in this sample, generator

[4] Full definitions of 'loose' and 'tight' photons can be found in Ref [89].

level cuts were applied on the transverse momenta of the muons (> 3.5 GeV) and the photons (> 4 GeV).

The generated samples are passed through the full `GEANT4` [91] simulation of the ATLAS detector, and are reconstructed with the same software as the data. The bb and pp samples contain MC truth information for the muons from J/ψ decay, but do not contain any hard truth-level photons, although some such photons show up during `Pythia/Photos` hadronisation and reconstruction; a cut is applied on such photons in line with the signal reconstruction. The signal MC sample contains MC truth information on both muons and photons.

A summary of the main features of the three MC samples is shown in Table 4.1 which details the number of events in each sample, the p_{T} cuts applied to the muons and photons, and the luminosity of the samples.

MC Sample Type	Name	Number of Generated Events	$p_{\mathrm{T}}(\mu^{\pm})(>)$ (GeV)	$p_{\mathrm{T}}(\gamma)$ (>) (GeV)	luminosity (fb^{-1})
Signal	Signal	9.4 M Truth 1 M Reconstructed	3.5	4.0	60
Prompt J/ψ	pp	5 M Reconstructed	3.5	-	N/A
Non-prompt J/ψ	bb	10 M Reconstructed	3.5	-	N/A

Table 4.1: Summary of the main features of the three Monte Carlo samples used in the analysis. Each Monte Carlo type is listed with the number of generated events in each sample, the p_{T} cuts, and the luminosity (where available).

4.2 Variable Distributions And Binning

As outlined at the beginning of this chapter, this section introduces the variables considered useful to this analysis, and details selection cuts applied to them.

4.2.1 Reconstructed Variable Distributions

Table 4.2 summarises the details of the main variables used in the analysis. Other variables are introduced where relevant.

Variable	Description
$\cos\theta_{\mathrm{CS}}$	Measured in the Collins-Soper frame
ϕ_{CS}	Measured in the Collins-Soper frame
$\Delta\phi$	Measured in laboratory frame $\Delta\phi = \phi_{\mu\mu} - \phi_{\gamma}$ if $\Delta\phi > \pi \rightarrow \Delta\phi - 2\pi$ if $\Delta\phi < \pi \rightarrow \Delta\phi + 2\pi$
ΔY	Measured in laboratory frame $\Delta Y = Y_{\mu\mu} - \eta_{\gamma}$
$m_{\mu\mu}$	Measured in laboratory frame
$p_{\mathrm{T}}(\mu\mu)$	Measured in laboratory frame
$p_{\mathrm{T}}(\gamma)$	Measured in laboratory frame
λ	Measured in laboratory frame $\lambda = \frac{(p_{\mu\mu}+p_{\gamma})^2}{m^2_{\mathrm{J}/\psi}}$
q^2_{T}	Measured in laboratory frame $q^2_{\mathrm{T}} = \Big(\boldsymbol{p}_{\mathrm{T}}(\mu\mu) + \boldsymbol{p}_{\mathrm{T}}(\gamma)\Big)^2$
$\tau_{\mu\mu}$	Measured in laboratory frame
`HLT_2mu4_bJpsimumu_noL2`	Trigger flag

Table 4.2: Table summarising the main variables in the analysis

Most variables are defined in the laboratory frame, but some are measured in the Collins-Soper (CS) frame, detailed in Appendix A, and Section 3.3.4.

- $\cos\theta_{\mathrm{CS}}$: Cosine of the polar angle of J/ψ production in the subprocess, measured in the Collins-Soper frame.
- ϕ_{CS}: Azimuthal angle of J/ψ production in the subprocess, measured in the Collins-Soper frame.
- $\Delta\phi(\mu\mu, \gamma)$: The difference in ϕ between the produced dimuons and photon, measured in the laboratory frame , and brought to the standard interval $-\pi < \Delta\phi \leq \pi$.
- $\Delta Y(\mu\mu\ , \gamma)$: The difference in rapidity of the produced dimuons and the angle η of the produced photon, measured in the laboratory frame.
- λ: Defined as $\left(\frac{p_{\mu\mu}+p_{\gamma}}{m_{\mathrm{J}/\psi}}\right)^2 \equiv \left(\frac{Q}{m_{\mathrm{J}/\psi}}\right)^2$, the square of the invariant mass of the J/ψ + γ system, Q, divided by the PDG value of the J/ψ mass ($m_{\mathrm{J}/\psi}$= 3.097 GeV) [92]. Division by the $m_{\mathrm{J}/\psi}$ provides a natural scale, and renders λ dimensionless. Measured in the laboratory frame.

- q_{T}^2: Defined as the vector sum squared $(\boldsymbol{p}_{\mathrm{T}}(\mu\mu) + \boldsymbol{p}_{\mathrm{T}}(\gamma))^2$, this is the square of the transverse momentum of the J/$\psi + \gamma$ system. Measured in the laboratory frame.

- $\tau_{\mu\mu}$: The pseudo-proper lifetime of the dimuon system, measured with respect to the primary vertex to the J/ψ direction. Defined as

$$\tau_{\mu\mu} = \frac{L_{xy} m_{\mathrm{J}/\psi}}{c\, p_{\mathrm{T}}} \tag{4.2}$$

  where $m_{\mathrm{J}/\psi}$ is the PDG J/ψ mass, p_{T} is the transverse momentum of the J/ψ candidate dimuon system, c is the speed of light, and L_{xy} is the 'decay length', the distance between the primary pp interaction vertex and the J/$\psi \to \mu^+\mu^-$ decay vertex in the transverse plane. Measured in the laboratory frame.

- `HLT_2mu4_bJpsimumu_noL2`: The flag which is set if this trigger has fired for this event.

- $p_{\mathrm{T}}(\mu\mu)$: The transverse momentum of the dimuon system, measured in the laboratory frame.

- $p_{\mathrm{T}}(\gamma)$: The transverse momentum of the produced photon, measured in the laboratory frame.

Figures 4.1 - 4.10 show distributions for the above aforementioned variables at reconstruction level cuts for each sample.

Figure 4.1 shows the distributions for λ. Each sample has a peak around $\lambda \sim 20$. Below this value, the phase space is dominated by background low p_{T} photons.

Distributions for q_{T}^2 are show in Figure 4.2. The q_{T}^2 peak in signal is around $q_{\mathrm{T}}^2 \sim 0$, whilst the peak in data is around $q_{\mathrm{T}}^2 \sim 30$ GeV^2. The q_{T}^2 peaks in the bb and pp samples are somewhere inbetween the signal and data peaks. One of the aims of the event selections is for the data and signal peaks to coincide at $q_{\mathrm{T}}^2 \sim 0$, once backgrounds have been subtracted from the data sample.

The dimuon mass variable is shown in Figure 4.3 and plotted across the full reconstruction level range, i.e. $2.6 \leq m_{\mu\mu} \leq 3.5$ GeV.

Figure 4.4 compares the dimuon lifetime distributions, and each sample has a peak around $\tau_{\mu\mu} \sim 0$, however the peak is broader in the bb distribution.

Reconstruction level kinematic cuts on muon and photon momenta add angular dependence to Figure 4.5 which is ϕ in the Collins-Soper frame, which would otherwise be flat, see Appendix B for details of this emergence. Some effort in this analysis has gone into finding ways to distinguish this emerging kinematic dependence from possible $\cos(4\phi_{\mathrm{CS}})$ modulation. The peak in data is slightly misaligned with the peaks in the three MC samples, which aims to be addressed through event selections.

The variable $\cos^2\theta_{\mathrm{CS}}$ is shown in Figure 4.6, and all samples peak at $\cos^2\theta_{\mathrm{CS}} = 0$. The bb, pp, and data samples all follow the same shape, slightly peaking towards $\cos^2\theta_{\mathrm{CS}} = 1$.

Interesting features can be seen in the $\Delta\phi$ distributions seen in Figure 4.7. The data, bb, and pp samples each have artificial features around $\Delta\phi \sim 0$, and will disappear after event selections. These are real events with very tiny opening angles and invariant masses which are relics from the creation of the samples.

ΔY is shown in Figure 4.8 which similarly to $\Delta\phi$ contains artificial structures around $\Delta Y \sim 0$. These events will be suppressed following event selections.

The p_{T} of the dimuon system is shown in Figure 4.9, events around 5-8 GeV are very low mass events with small opening angles.

The distributions of the photon p_{T}, can be seen in Figure 4.10, where due to the reconstruction level cut events start at $p_{\mathrm{T}} > 5$ GeV.

It is presently unwise to make conclusions about the data-MC agreement. Although the data is dominated by signal, bb, and pp type events, there are other backgrounds which contribute. These additional backgrounds, and those modelled by the MC background samples, are removed through event selections, a multivariate analysis technique, and background subtraction techniques.

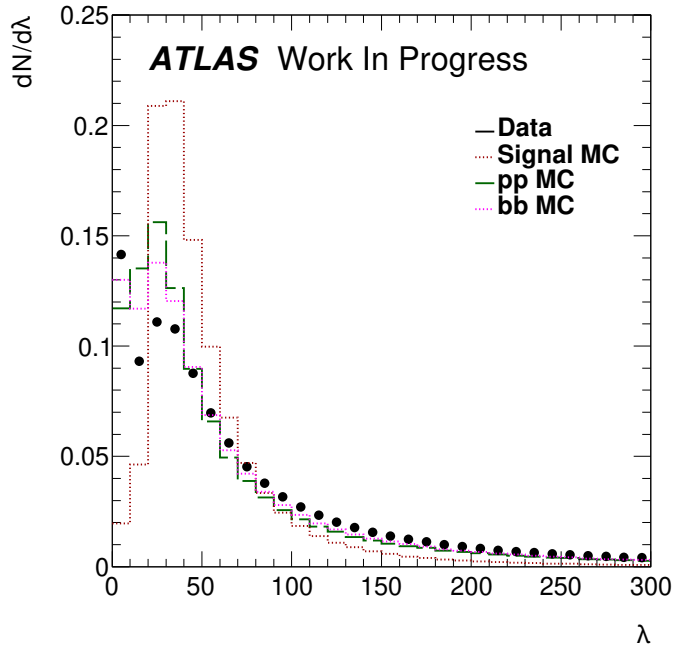

Figure 4.1: Distributions of the variable λ, for data (black dots), signal Monte Carlo (red dotted line), pp Monte Carlo (dashed green line), and bb Monte Carlo (dotted magenta line). Each distribution has been normalised to unit area.

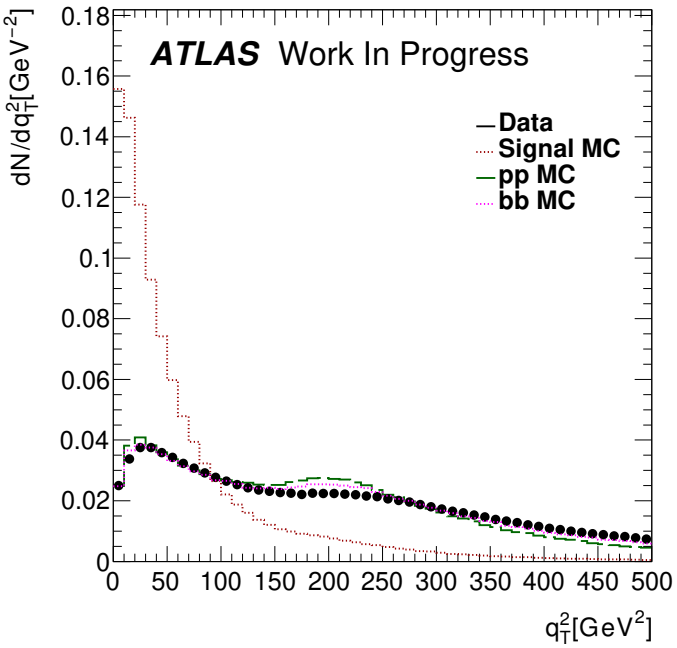

Figure 4.2: Distributions of the variable q_{T}^2, for data (black dots), signal Monte Carlo (red dotted line), pp Monte Carlo (dashed green line), and bb Monte Carlo (dotted magenta line). Each distribution has been normalised to unit area.

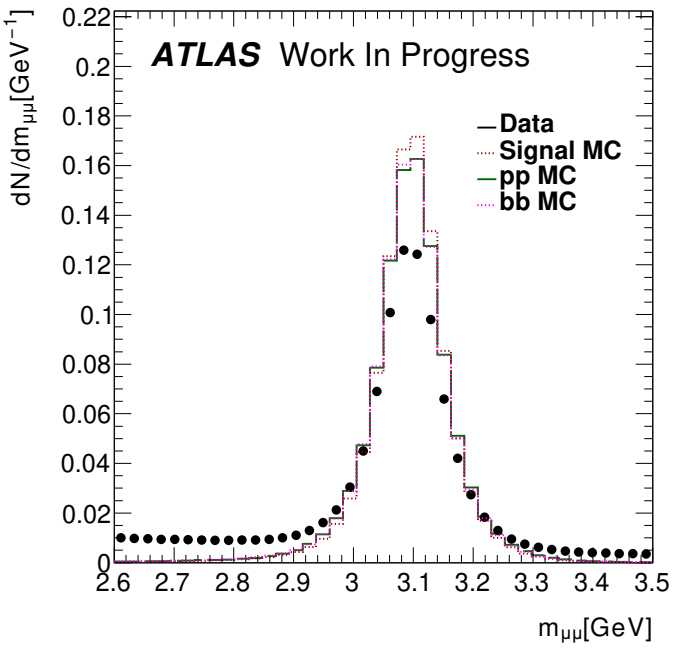

Figure 4.3: Distributions of the dimuon mass($m_{\mu\mu}$), for data (black dots), signal Monte Carlo (red dotted line), pp Monte Carlo (dashed green line), and bb Monte Carlo (dotted magenta line). Each distribution has been normalised to unit area.

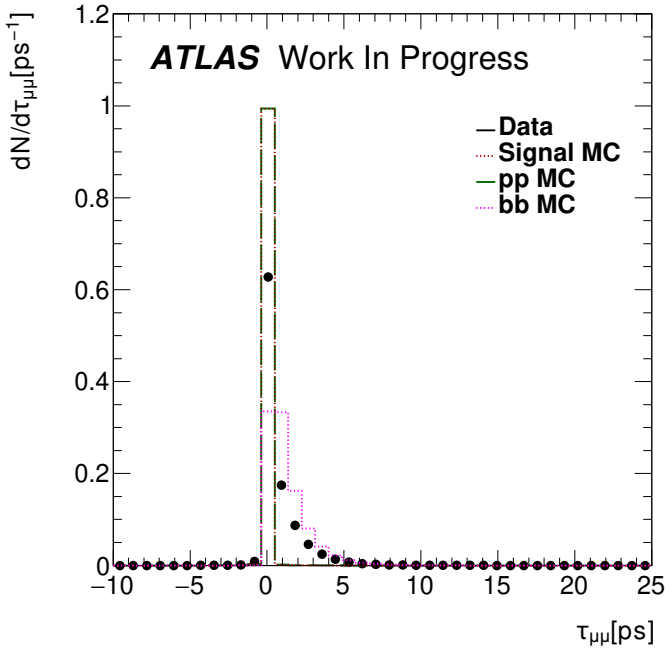

Figure 4.4: Distributions of the dimuon lifetime ($\tau_{\mu\mu}$), for data (black dots), signal Monte Carlo (red dotted line), pp Monte Carlo (dashed green line), and bb Monte Carlo (dotted magenta line). Each distribution has been normalised to unit area.

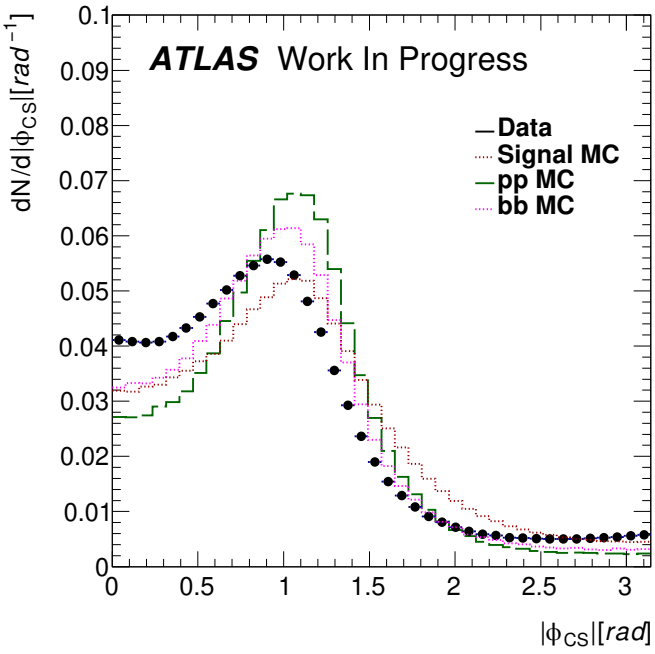

Figure 4.5: Distributions of the variable $|\phi|$ in the Collins-Soper frame, for data (black dots), signal Monte Carlo (red dotted line), pp Monte Carlo (dashed green line), and bb Monte Carlo (dotted magenta line). Each distribution has been normalised to unit area.

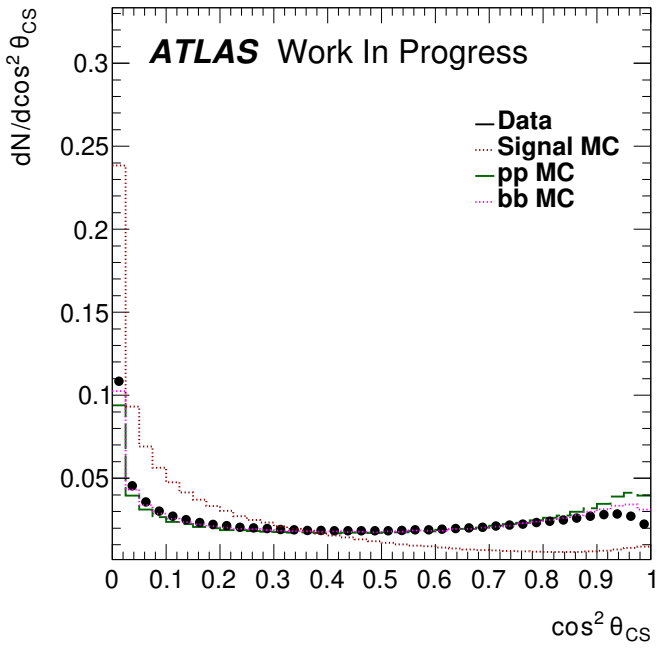

Figure 4.6: Distributions of the variable $\cos\theta$ in the Collins-Soper frame, for data (black dots), signal Monte Carlo (red dotted line), pp Monte Carlo (dashed green line), and bb Monte Carlo (dotted magenta line). Each distribution has been normalised to unit area.

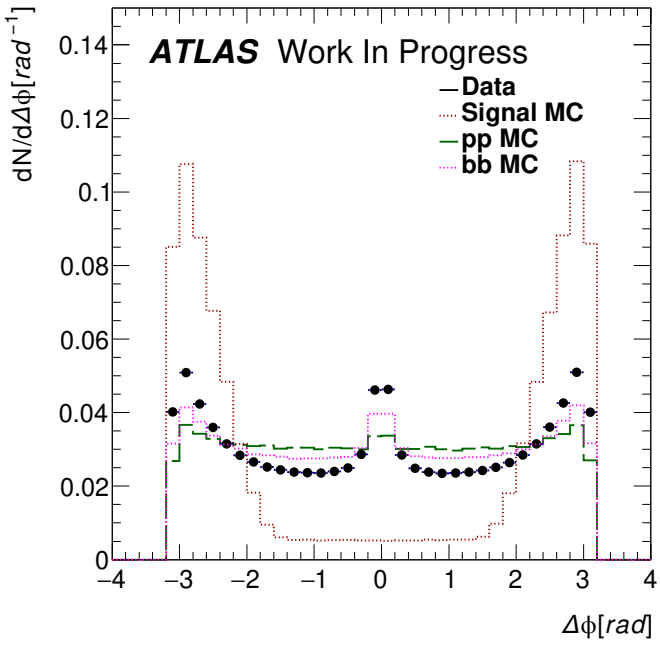

Figure 4.7: Distributions of the variable $\Delta\phi$, for data (black dots), signal Monte Carlo (red dotted line), pp Monte Carlo (dashed green line), and bb Monte Carlo (dotted magenta line). Each distribution has been normalised to unit area.

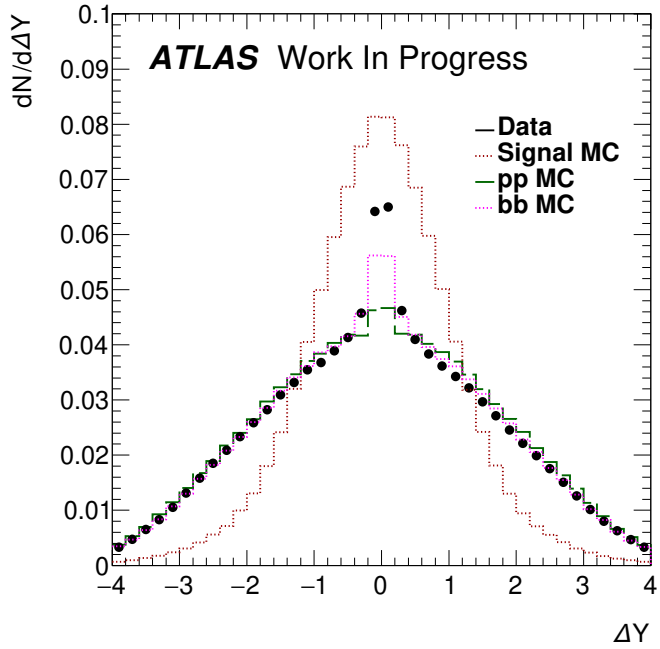

Figure 4.8: Distributions of the variable ΔY, for data (black dots), signal Monte Carlo (red dotted line), pp Monte Carlo (dashed green line), and bb Monte Carlo (dotted magenta line). Each distribution has been normalised to unit area.

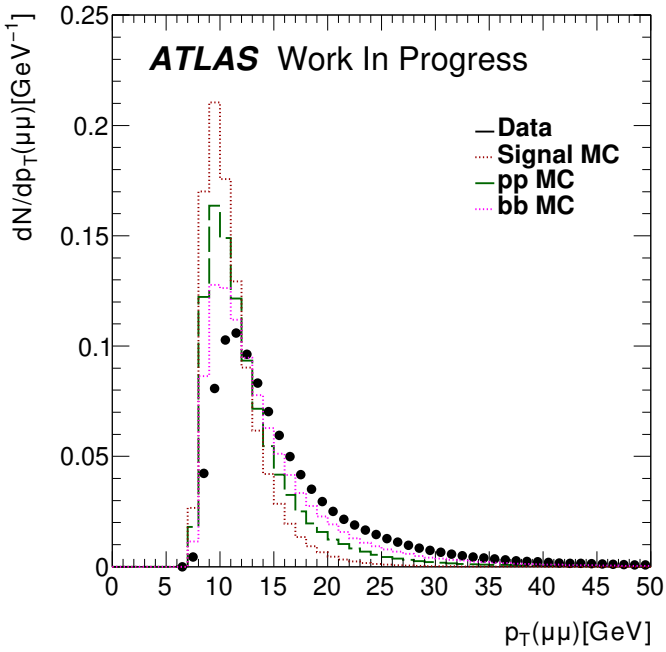

Figure 4.9: Distributions of the variable $p_{\mathrm{T}}(\mu\mu)$, for data (black dots), signal Monte Carlo (red dotted line), pp Monte Carlo (dashed green line), and bb Monte Carlo (dotted magenta line). Each distribution has been normalised to unit area.

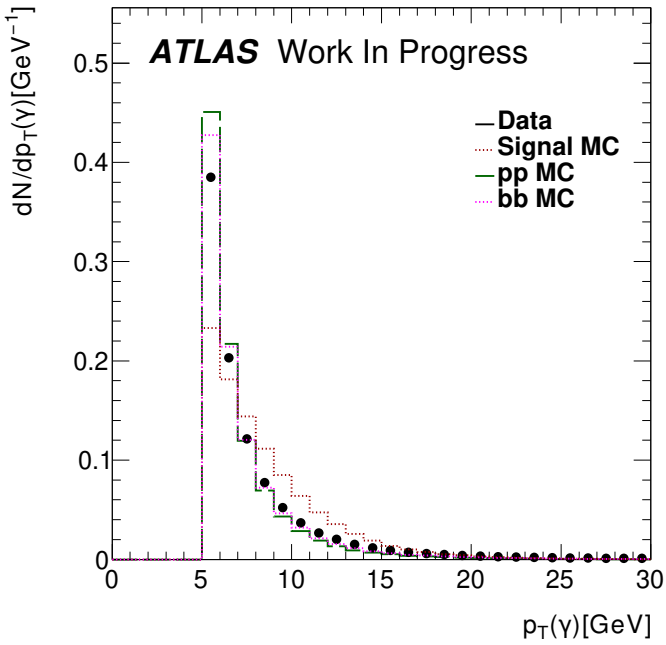

Figure 4.10: Distributions of the variable $p_{\mathrm{T}}(\gamma)$, for data (black dots), signal Monte Carlo (red dotted line), pp Monte Carlo (dashed green line), and bb Monte Carlo (dotted magenta line). Each distribution has been normalised to unit area.

4.2.2 Basic Cuts On Main Reconstructed Variables

With reference to the theory, Section 3.3.5, TMD factorisation requires $Q^2 \gg q_{\mathrm{T}}^2$ and the summation of the transverse momenta of the J/ψ and γ to be as small as possible ($q_{\mathrm{T}} \sim 0$) which is achieved when the J/ψ and γ are produced back-to-back.

If one considers a system with signal reconstruction level kinematic cuts where the J/ψ and γ are produced back-to-back with $p_{\mathrm{T}}(\mathrm{J}/\psi) > 8$ GeV and $p_{\mathrm{T}}(\gamma) > 5$ GeV, then the J/$\psi - \gamma$ system has a large transverse momentum imbalance of approximately 3 GeV, and $Q \sim 13$ GeV. These kinematic cuts are not ideal for the analysis, which leads to applying a tight photon cut ($p_{\mathrm{T}}(\gamma) > 9$ GeV), to give the greatest change the J/$\psi - \gamma$ system has $q_{\mathrm{T}}^2 \sim 0$.

The effect of increasing the $p_{\mathrm{T}}(\gamma)$ cut on a 2-dimensional distribution of events in the λ vs q_T^2 plane is demonstrated in Figure 4.11, where the cut on the minimum $p_{\mathrm{T}}(\gamma)$ is increased from 5 GeV to 9 GeV. Increasing the photon p_{T} removes low λ events faster than low q_{T}^2 events, enabling the analysis to select the desirable events with low transverse momenta and high invariant mass of the J/$\psi + \gamma$ system.

The consequence of increasing the transverse momentum of the photon was found to remove a large number of low p_{T} background photons. Additionally low p_{T} photons are not well calibrated within ATLAS, as there are no photon scale factor maps until $p_{\mathrm{T}}(\gamma) \geq 10$ GeV, so the analysis needs to extrapolate back to 9 GeV. Extrapolating beyond the limits of the map gives reduced confidence, hence extrapolation below 9 GeV will introduce higher uncertainty.

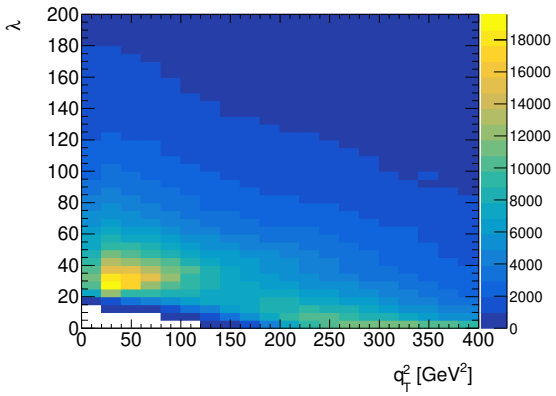

(a) $p_{\mathrm{T}}(\mu^{\pm}) > 4$ GeV, $p_{\mathrm{T}}(\gamma) > 5$ GeV

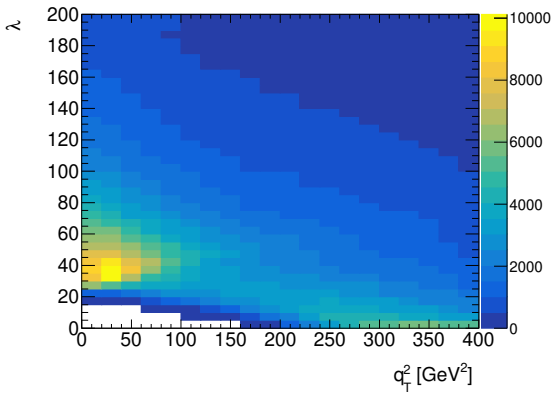

(b) $p_{\mathrm{T}}(\mu^{\pm}) > 4$ GeV, $p_{\mathrm{T}}(\gamma) > 6$ GeV

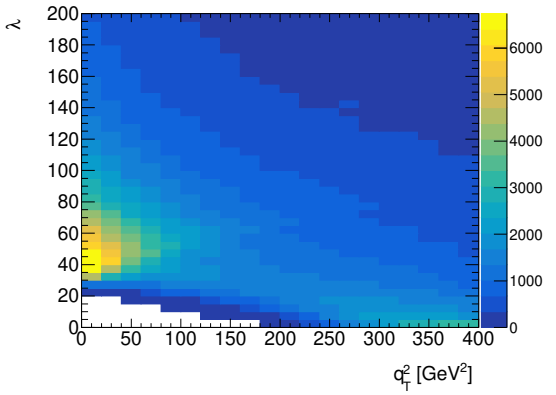

(c) $p_{\mathrm{T}}(\mu^{\pm}) > 4$ GeV, $p_{\mathrm{T}}(\gamma) > 7$ GeV

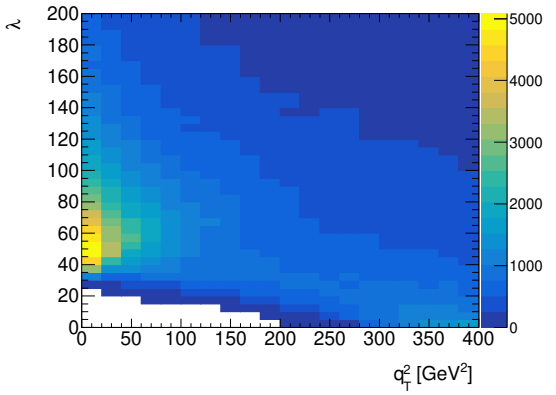

(d) $p_{\mathrm{T}}(\mu^{\pm}) > 4$ GeV, $p_{\mathrm{T}}(\gamma) > 8$ GeV

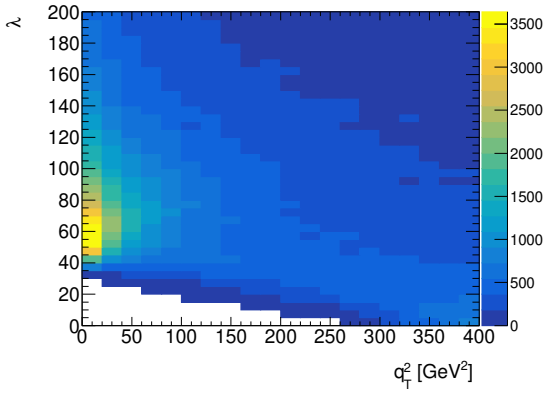

(e) $p_{\mathrm{T}}(\mu^{\pm}) > 4$ GeV, $p_{\mathrm{T}}(\gamma) > 9$ GeV

Figure 4.11: Distributions of λ vs. q_T^2 at varying p_{T} cuts on the photon, increasing from 5 GeV (a) to 9 GeV (e) in steps of 1 GeV. Once the cut on $p_{\mathrm{T}}(\gamma)$ gets close to the cut on $p_{\mathrm{T}}(\mathrm{J}/\psi)$, the interesting area of $q_T^2 \simeq 0$ is no longer suppressed and can be explored.

One of the consequences of this cut ($p_{\mathrm{T}}(\gamma) > 9$ GeV) is that signal events no longer populate the region of low λ, so a cut $\lambda > 15$ can be further applied to eliminate such configurations

in the MC samples and data. Applying this cut to data also removes any intermediate resonance states (e.g g + g $\rightarrow \chi_c \rightarrow$ J/$\psi + \gamma$) due to their mass.

Event selection cuts were applied across the data and MC samples, determined from exploring the distributions of the variables of interest in the analysis, which are summarised in Table 4.3. Events are required to pass the `HLT_2mu4_bJpsimumu_noL2` trigger (Cut 2) which selects oppositely charged muons with $p_{\mathrm{T}}(\mu^{\pm}) > 4$ GeV (see Section 4.1.1 for further details on the trigger). Cut 3 removes background low photon p_{T} events. Cut 4 increases the photon p_{T} cut to 9 GeV to balance the p_{T} of the oppositely flying J/ψ to give a J/$\psi - \gamma$ system with $q_{\mathrm{T}}^2 \sim 0$. Events in the signal distributions (Figures 4.1 and 4.2) were found to populate $0 \leq \lambda < 200$ and $0 \leq q_{\mathrm{T}}^2 < 400$ GeV^2, and so form Cut 5 and Cut 6 respectively. The dimuon mass range was selected to be between 2.7 $\leq m_{\mu\mu} < 3.5$ GeV (Cut 7) as J/ψ signal events populate the $2.9 \leq m_{\mu\mu} < 3.3$ GeV region forming the signal J/ψ peak, but this region does contain some background J/ψs. The regions $2.7 \leq m_{\mu\mu} < 3.1$ GeV and $3.3 \leq m_{\mu\mu} < 3.5$ GeV are known as the 'mass sidebands' containing background J/ψ events. On the assumption that the number of background events under the peak, in comparison to the mass sidebands, is approximately equal, a simple mass sideband subtraction procedure can be later used to remove non-prompt background J/ψs (details of this procedure can be found in Section 5.2). Prompt (signal) J/ψs have a lifetime around $\tau_{\mu\mu} \sim 0$ ps, whilst non-prompt (background) J/ψs have a much longer lifetime, by selecting the lifetime region $-5 \leq \tau_{\mu\mu} < 15$ ps (Cut 8), a long lifetime subtraction procedure can be later used to remove long lifetime J/ψ candidates (this procedure is detailed in Section 5.3). Finally, Cut 9 selects only events which contains 'tight' photons, as described in Section 4.1.2, as scale factor maps are only calibrated for 'tight' photons.

Cut Number	**Cut**	**Additional information**
Cut 1	N(photon) > 0	Some reconstructed events do not contain a photon, these need to be removed from the analysis.
Cut 2	Trigger	Pass `HLT_2mu4_bJpsimumu_noL2` trigger
Cut 3	$\lambda > 15$	No signal MC events in region $\lambda < 15$
Cut 4	449	$p_{\mathrm{T}}(\mu^{\pm}) > 4$ GeV, $p_{\mathrm{T}}(\gamma) > 9$ GeV
Cut 5	$0 \leq \lambda < 200$	$Q \lesssim 44$ GeV
Cut 6	$0 \leq q_{\mathrm{T}}^2 < 400$ GeV^2	$q_T \leq 20$ GeV
Cut 7	$2.7 \leq m_{\mu\mu} < 3.5$ GeV	Dimuon mass range
Cut 8	-5 $\leq \tau_{\mu\mu} < 15$ ps	Dimuon lifetime range
Cut 9	Photon quality	Tight photons only

Table 4.3: Common selection cuts for events applied across all samples (one data and three Monte Carlo).

Some events contain more than one photon candidate, which were ordered in decreasing transverse momentum in the samples. Similarly, the muons were ordered in decreasing transverse momentum, however, after event selections, the average number of dimuon candidates per event was close to 1. The cut flow – number of events in each of the samples after sequential application of the above cuts – is presented in Table 4.4. Each sample is represented by two columns; the number in the first column represents all dimuon-photon combinations, while the second column only counts one combination per event, corresponding to the first ('zeroth') elements in both dimuon and photon arrays (and hence matches the number of surviving events). Comparing the two columns, it is clear that per-event combinatorics is not large to start with, but gets down to about 3% after all nine selection cuts.

Studies have shown that in vast majority of cases the correct photon and dimuon were indeed in the 'zeroth' position in their respective arrays, which helped eliminate any combinatorics by choosing this permutation.

Cut	signal All Cand.	signal 0^{th} Cand.	pp All Cand.	pp 0^{th} Cand.	bb All Cand.	bb 0^{th} Cand.	data All Cand.	data 0^{th} Cand.
1	1027167	935578	501495	463711	588633	539733	3227518	3033090
2	474222	431820	249378	230372	308941	282887	2481458	2338141
3	454572	418663	203536	188220	250009	228977	1986292	1872508
4	151973	149024	27238	26519	36318	35107	362234	352980
5	151973	149024	27238	26519	36318	35107	362234	352980
6	148350	145760	18831	18279	25025	24128	264040	257455
7	148029	145446	18795	18243	24959	24068	251856	245639
8	148028	145445	18795	18243	24954	24064	251803	245589
9	100402	99346	5283	5126	6898	6672	79781	77979

Table 4.4: Numbers of events in various samples after applying sequential event selection requirements. The two columns for each sample compare the number of all dimuon-photon combinations with the case when only the first element in the two arrays were selected.

Note that the numbers in all samples show a dramatic reduction from initial multi-million statistics, especially after the requirement of a photon with transverse momentum above 9 GeV (Cut 4) and the 'tight' photon requirement (Cut 9).

4.2.3 λ And q_{T}^2 Binning

The first part of the analysis, the measurement of the q_{T}^2 dependence of the cross section of J/$\psi + \gamma$ production, is performed in slices of the variable λ. The variable λ, is split into regions (referred to also as slices) with edges $0 - 15 - 25 - 50 - 100 - 200$, originally chosen to contain roughly equal statistics at the stage of '445' cuts. However, after increasing the photon transverse momentum cut to 9 GeV, giving '449' cuts, the first two slices became inaccessible, reducing the number of λ slices to three, with boundaries $25 - 50 - 100 - 200$, which correspond to boundaries in invariant mass Q of $15 - 22 - 31 - 44$ GeV. The variable q_{T}^2 is split into 10 bins with edges $(0 - 4 - 16 - 36 - 64 - 100 - 144 - 196 - 256 - 324 - 400)$ GeV^2, which gives uniform bins in q_{T} $(0 - 2 - 4 - 6 - 8 - 10 - 12 - 14 - 16 - 18 - 20)$ GeV. q_{T}^2 bins in the low GeV^2 regions cannot be much smaller due to potential resolution / bin migration effects explored in Section 8.4.

Each λ slice is labelled $3 - 5$, and each q_{T}^2 bin is labelled $1 - 10$, with label 0 reserved for the full ranges (i.e $0 \leq \lambda \leq 200$ and $0 \leq q_{\mathrm{T}}^2 \leq 400$ GeV^2). Each λ – q_{T}^2 bin is labelled with a combination of two numbers, with the first number referring to the lambda slice, and the second number labelling the q_{T}^2 bin.

4.2.3.1 Photon Matching In The Signal Monte Carlo Sample

Despite selecting the 0^{th} reconstructed photon in the signal MC sample, it was not always matching the true photon from the signal subprocess. To improve the purity of the reconstructed signal MC sample, the matching of the 0^{th} photon with the true correct signal photon was performed, by calculating the angular distance ΔR between them.

The distribution of ΔR after the nine basic selection cuts outlined in Table 4.3 is shown in Figure 4.12.

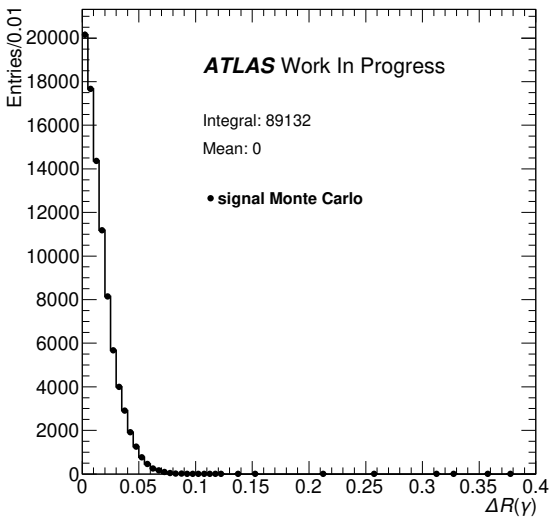

Figure 4.12: A plot of ΔR between truth and reconstructed photons, for slice 00 with kinematical regions $0 \leq \lambda < 200$ and $0 \leq q_{\text{T}}^2 < 400$ GeV^2

A cut at $\Delta R < 0.12$ (dubbed 'Cut 10'), only applied to the signal MC sample, is sufficient to conclude a truth and reconstructed photon is considered matched. The events passing this cut were considered as signal, while the events from the signal sample which did not pass this selection cut were considered to be another type of background (usually a combination of a correct dimuon with an incorrect photon).

The matching criteria divides the samples, after cuts, into two versions for each $\lambda - q_{\text{T}}^2$ slice with the following types of events (see Table 4.5). Two versions are defined in the table, Version 1 where the unmatched signal events have been discarded, and Version 2 where those unmatched events are combined with the pp sample. These two versions will be used at a later stage of the analysis where a TMVA method is used to perform signal

and background separation in the data (see Section 5.1.1). Since the relative weight of the signal and pp samples is not known very well, these two versions are considered to be the two extreme mixes of these two classes of background events. Normally one cannot combine events from different samples as the samples have different normalisations. The unmatched signal events contribute, on average, across the slices an increase of approximately a third to the pp statistics (see for example column 4 versus column 7 of Table 4.6). However, the analysis has concluded that combining samples with different normalisations is not an issue, and has just changed the statistics of the Version 2 pp sample. It is later shown during the likelihood fitting stage (see Chapter 6) that the number of fitted signal events in the data Version 2 slices is within the statistical errors of Version 1 slices, and therefore does not affect the final results.

Version	**Description**
Version 1 (V1)	data pp matched signal
Version 2 (V2)	data pp + unmatched signal matched signal

Table 4.5: The signal matching criteria between the truth and reconstructed photon creates two streams (versions) for the analysis. A version 1 and version 2 exists for each $\lambda - q^2_{\mathrm{T}}$ slice, comprised of the data, pp, and signal events after that slice's event selections. The difference between version 1 and version 2 is that version 2's pp events are combined with the unmatched signal events from the same slice after the signal matching criteria is applied.

Table 4.6 summarises the numbers of events in each $\lambda - q^2_{\mathrm{T}}$ slice for pp, signal and data samples, after all selection cuts detailed in this chapter, including Cut 10. In Table 4.6, slice 00 covers the entire phase space under consideration, $0 \leq \lambda < 200$ and $0 \leq q^2_T < 400$ GeV^2. Slice 30 covers λ slice 3 and the full range of q^2_{T}, i.e. $25 \leq \lambda < 50$ and $0 \leq q^2_T < 400$ GeV^2. Slices 31 - 310 divide slice 30 into the 10 bins in q^2_{T}. The numbers of events in bins 31 to 310 sum up to the number in slice 30. This pattern is repeated across each sample and for λ slices 40, and 50. Note that slices 30 + 40 + 50 $\neq$ 00, as slice 00 also contains slice 20.

Slice	**λ region**	**q_T^2 region** (GeV^2)	**Version 1**			**Version 2**		
			pp	matched signal	data	pp + unmatched signal	matched signal	data
00	$0 \leq \lambda < 200$	$0 \leq q_T^2 < 400$	5127	97472	77979	7001	97472	77979
30	$25 \leq \lambda < 50$	$0 \leq q_T^2 < 400$	1294	19336	13051	1875	19336	13051
31	$25 \leq \lambda < 50$	$0 \leq q_T^2 < 4$	29	2731	578	46	2731	578
32	$25 \leq \lambda < 50$	$4 \leq q_T^2 < 16$	69	4106	936	96	4106	936
33	$25 \leq \lambda < 50$	$16 \leq q_T^2 < 36$	77	3317	937	125	3317	937
34	$25 \leq \lambda < 50$	$36 \leq q_T^2 < 64$	90	3117	1012	138	3117	1012
35	$25 \leq \lambda < 50$	$64 \leq q_T^2 < 100$	116	2428	1112	174	2428	1112
36	$25 \leq \lambda < 50$	$100 \leq q_T^2 < 144$	162	1829	1342	230	1829	1342
37	$25 \leq \lambda < 50$	$144 \leq q_T^2 < 196$	155	1125	1532	230	1125	1532
38	$25 \leq \lambda < 50$	$196 \leq q_T^2 < 256$	188	469	1773	267	469	1773
39	$25 \leq \lambda < 50$	$256 \leq q_T^2 < 324$	192	164	1844	282	164	1844
310	$25 \leq \lambda < 50$	$324 \leq q_T^2 < 400$	216	50	1985	287	50	1985
40	$50 \leq \lambda < 100$	$0 \leq q_T^2 < 400$	2044	56795	33527	2753	56795	33527
41	$50 \leq \lambda < 100$	$0 \leq q_T^2 < 4$	84	6077	1796	124	6077	1796
42	$50 \leq \lambda < 100$	$4 \leq q_T^2 < 16$	173	12676	4352	252	12676	4352
43	$50 \leq \lambda < 100$	$16 \leq q_T^2 < 36$	253	12320	5077	343	12320	5077
44	$50 \leq \lambda < 100$	$36 \leq q_T^2 < 64$	246	9705	4903	316	9705	4903
45	$50 \leq \lambda < 100$	$64 \leq q_T^2 < 100$	250	6784	4124	328	6784	4124
46	$50 \leq \lambda < 100$	$100 \leq q_T^2 < 144$	259	4310	3411	340	4310	3411
47	$50 \leq \lambda < 100$	$144 \leq q_T^2 < 196$	194	2522	2949	280	2522	2949
48	$50 \leq \lambda < 100$	$196 \leq q_T^2 < 256$	186	1406	2428	251	1406	2428
49	$50 \leq \lambda < 100$	$256 \leq q_T^2 < 324$	194	657	2268	256	657	2268
410	$50 \leq \lambda < 100$	$324 \leq q_T^2 < 400$	205	338	2219	263	338	2219
50	$100 \leq \lambda < 200$	$0 \leq q_T^2 < 400$	1478	21269	28908	1921	21269	28908
51	$100 \leq \lambda < 200$	$0 \leq q_T^2 < 4$	60	1515	1130	74	1515	1130
52	$100 \leq \lambda < 200$	$4 \leq q_T^2 < 16$	131	3557	2857	164	3557	2857
53	$100 \leq \lambda < 200$	$16 \leq q_T^2 < 36$	173	3959	3569	218	3959	3569
54	$100 \leq \lambda < 200$	$36 \leq q_T^2 < 64$	150	3612	3802	207	3612	3802
55	$100 \leq \lambda < 200$	$64 \leq q_T^2 < 100$	170	2872	3773	221	2872	3773
56	$100 \leq \lambda < 200$	$100 \leq q_T^2 < 144$	162	2240	3431	206	2240	3431
57	$100 \leq \lambda < 200$	$144 \leq q_T^2 < 196$	160	1521	3042	204	1521	3042
58	$100 \leq \lambda < 200$	$196 \leq q_T^2 < 256$	145	991	2631	194	991	2631
59	$100 \leq \lambda < 200$	$256 \leq q_T^2 < 324$	177	617	2431	225	617	2431
510	$100 \leq \lambda < 200$	$324 \leq q_T^2 < 400$	150	385	2242	208	385	2242

Table 4.6: Table detailing the number of events in each $\lambda - q_T^2$ slice for the pp, signal, and data samples. Version 1 details the data, pp, and signal matched events. Version 2 details the data, pp + unmatched signal events, and signal matched events.

4.2.4 ϕ_{CS} And $\cos\theta_{CS}$ Binning

The cut flow for the second part of the analysis, which consequently is also a measurement of the differential cross section in the angular variable $|\phi_{CS}|$ in slices of $z \equiv \cos\theta_{CS}$ follows

the same pattern to the previous section. The full range of variable $|\phi_{\mathrm{CS}}|$ between 0 and π is split into equal slices of width $\frac{\pi}{8}$. Each slice is labelled 1-8 in sequence, with the full interval assigned the label 0. The cuts listed in Table 4.3 are applied sequentially to each $|\phi_{\mathrm{CS}}|$ slice. Each slice is further split into two regions depending on $z = \cos\theta_{\mathrm{CS}}$: region 'Low' with $z^2 < 0.1$, where the gluon polarisation effects are expected to be enhanced, and the region 'High' with $z^2 \geq 0.1$ where they are suppressed.

Similarly to $\lambda - q_{\mathrm{T}}^2$, signal matching is performed between the truth and reconstructed photon in the signal MC sample, and the events surviving Cut 10 are labelled as 'matched signal', while the events failing that cut are labelled 'unmatched signal', and similarly added to the pp background in 'Version 2'. The tables of event numbers in individual ϕ_{CS} bins/slices are presented in Table 4.7 for Low z^2 slice and in Table 4.8 for High z^2 slice.

Slice	$\|\phi_{\mathrm{CS}}\|$ **region** (rad)	**Version 1**			**Version 2**		
		pp	**matched signal**	**data**	**pp + unmatched signal**	**matched signal**	**data**
0	$0 \leq \|\phi_{\mathrm{CS}}\| < \pi$	1370	51610	25118	1841	51610	25118
1	$0 \leq \|\phi_{\mathrm{CS}}\| < \frac{\pi}{8}$	41	3305	1261	66	3305	1261
2	$\frac{\pi}{8} \leq \|\phi_{\mathrm{CS}}\| < \frac{\pi}{4}$	60	4014	1385	92	4014	1385
3	$\frac{\pi}{4} \leq \|\phi_{\mathrm{CS}}\| < \frac{3\pi}{8}$	113	6033	2095	163	6033	2095
4	$\frac{3\pi}{8} \leq \|\phi_{\mathrm{CS}}\| < \frac{\pi}{2}$	367	10577	4740	541	10577	4740
5	$\frac{\pi}{2} \leq \|\phi_{\mathrm{CS}}\| < \frac{5\pi}{8}$	412	11106	5676	536	11106	5676
6	$\frac{5\pi}{8} \leq \|\phi_{\mathrm{CS}}\| < \frac{3\pi}{4}$	168	7306	3652	203	7306	3652
7	$\frac{3\pi}{4} \leq \|\phi_{\mathrm{CS}}\| < \frac{7\pi}{8}$	112	5180	3122	130	5180	3122
8	$\frac{7\pi}{8} \leq \|\phi_{\mathrm{CS}}\| < \pi$	97	4089	3187	110	4089	3187

Table 4.7: Table of events in the low $\cos^2\theta_{\mathrm{CS}}$ range after event selection cuts, see Table 4.3, and signal matching. The number of events in each slice and sample for Version 1 and Version 2 type events is given.

Slice	$\|\phi_{\mathbf{CS}}\|$ **region** (rad)	**Version 1**			**Version 2**		
		pp	**matched signal**	**data**	**pp + unmatched signal**	**matched signal**	**data**
0	$0 \leq \|\phi_{\mathrm{CS}}\| < \pi$	3757	45862	52861	5160	45862	52861
1	$0 \leq \|\phi_{\mathrm{CS}}\| < \frac{\pi}{8}$	88	2618	1825	142	2618	1825
2	$\frac{\pi}{8} \leq \|\phi_{\mathrm{CS}}\| < \frac{\pi}{4}$	120	3317	2119	171	3317	2119
3	$\frac{\pi}{4} \leq \|\phi_{\mathrm{CS}}\| < \frac{3\pi}{8}$	313	5450	4090	465	5450	4090
4	$\frac{3\pi}{8} \leq \|\phi_{\mathrm{CS}}\| < \frac{\pi}{2}$	1220	9865	12817	1828	9865	12817
5	$\frac{\pi}{2} \leq \|\phi_{\mathrm{CS}}\| < \frac{5\pi}{8}$	1244	10677	15034	1656	10677	15034
6	$\frac{5\pi}{8} \leq \|\phi_{\mathrm{CS}}\| < \frac{3\pi}{4}$	393	6510	7418	473	6510	7418
7	$\frac{3\pi}{4} \leq \|\phi_{\mathrm{CS}}\| < \frac{7\pi}{8}$	193	4144	4967	221	4144	4967
8	$\frac{7\pi}{8} \leq \|\phi_{\mathrm{CS}}\| < \pi$	186	3281	4591	204	3281	4591

Table 4.8: Table of events in the high $\cos^2\theta_{\mathrm{CS}}$ range after event selection cuts, see Table 4.3, and signal matching. The number of events in each slice and sample for Version 1 and Version 2 type events is given.

Following the event selection cuts, including signal photon matching, variable distributions for each of the samples are shown in Figures 4.13 to 4.22. These distributions are for slice 00/0, i.e $0 \leq \lambda < 200$ and $0 \leq q_{\mathrm{T}}^2 < 400$ GeV^2. The event selections are designed to select desirable signal configurations in data, whilst suppressing background events. It is clear from the distributions that the statistics of the bb and pp samples have been heavily reduced in comparison to the signal and data samples.

The peak in the λ distributions (Figure 4.13) is now around $\lambda \sim 60$, whereas at reconstruction level (see Figure 4.1) it was around $\lambda \sim 20$. The kinematical cuts on λ and the photons, has removed background low p_{T} photons.

The peaks in $|\phi_{\mathrm{CS}}|$ (Figure 4.17) are now aligned for all samples. At reconstruction level (see Figure 4.5), the data peaked slightly before the three MC samples.

The artificial peaks at reconstruction level for $\Delta\phi$ (see Figure 4.7) and ΔY (see Figure 4.8) have been removed through the event selection cuts as can be see in Figure 4.19 ($\Delta\phi$) and Figure 4.20 (ΔY).

At this stage of the analysis it is still unwise to make direct comparisons of the data and MC samples, as the main backgrounds (pp and bb) need to be subtracted from the data, as well as other unidentified backgrounds.

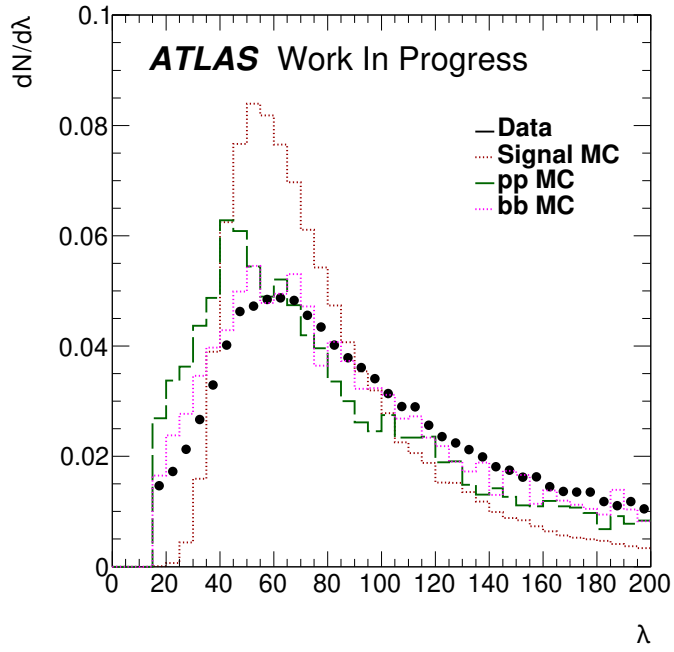

Figure 4.13: Distributions of the variable λ, for data (black dots), signal Monte Carlo (red dotted line), pp Monte Carlo (dashed green line), and bb Monte Carlo (dotted magenta line). Each distribution has been normalised to unit area.

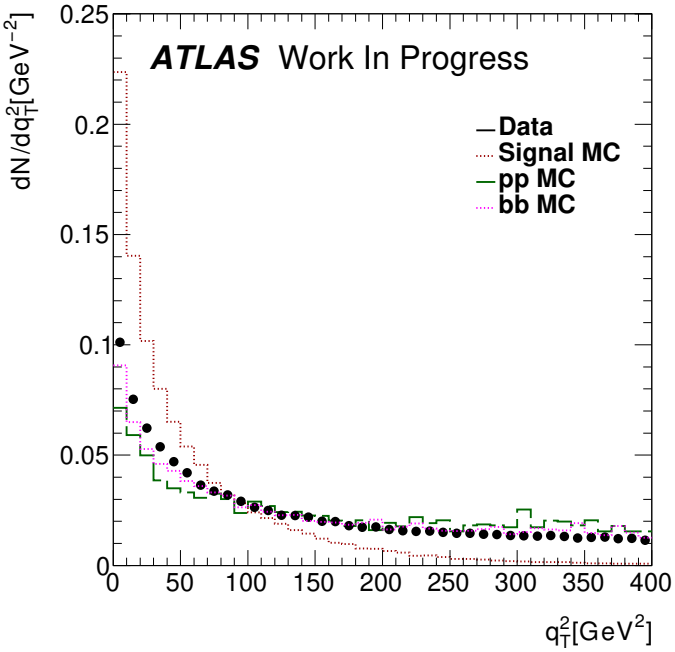

Figure 4.14: Distributions of the variable q_{T}^2, for data (black dots), signal Monte Carlo (red dotted line), pp Monte Carlo (dashed green line), and bb Monte Carlo (dotted magenta line). Each distribution has been normalised to unit area.

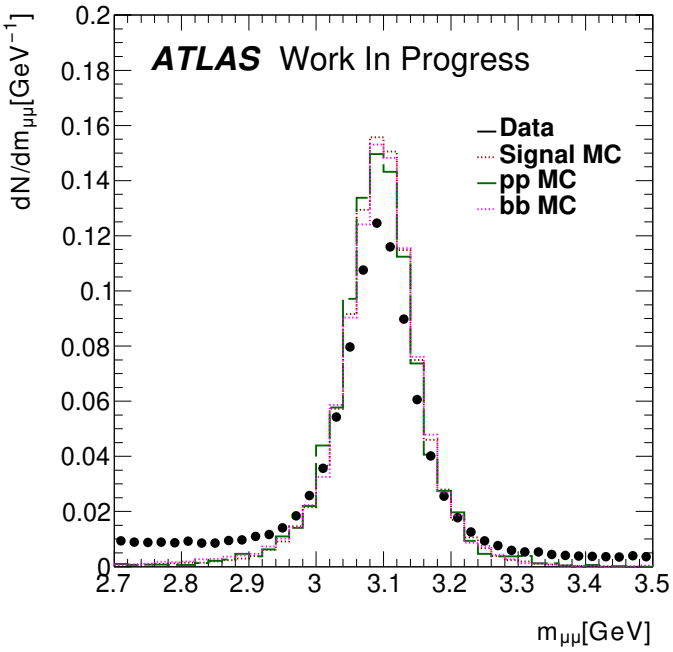

Figure 4.15: Distributions of the dimuon mass ($m_{\mu\mu}$), for data (black dots), signal Monte Carlo (red dotted line), pp Monte Carlo (dashed green line), and bb Monte Carlo (dotted magenta line). Each distribution has been normalised to unit area.

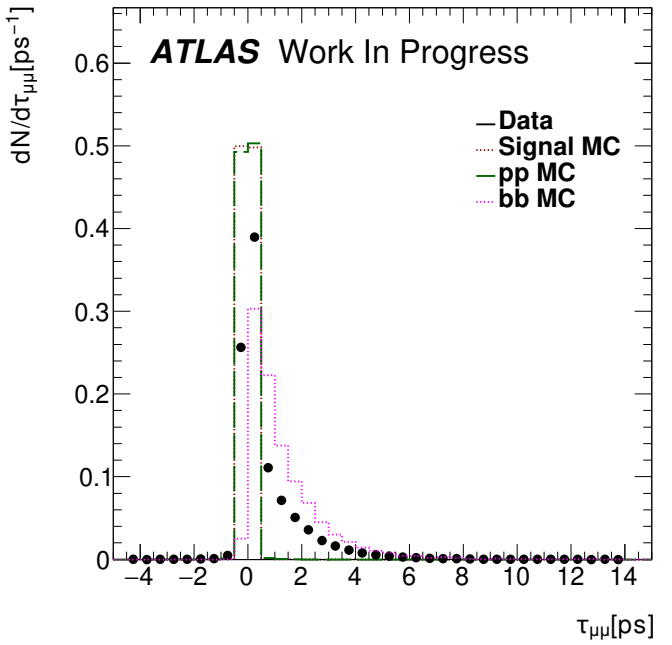

Figure 4.16: Distributions of the dimuon lifetime ($\tau_{\mu\mu}$), for data (black dots), signal Monte Carlo (red dotted line), pp Monte Carlo (dashed green line), and bb Monte Carlo (dotted magenta line). Each distribution has been normalised to unit area.

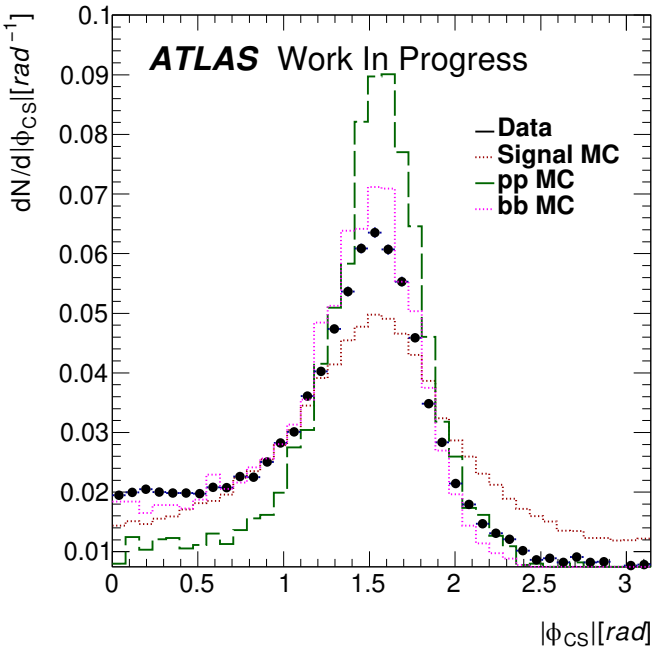

Figure 4.17: Distributions of the variable $|\phi|$ in the Collins-Soper frame, for data (black dots), signal Monte Carlo (red dotted line), pp Monte Carlo (dashed green line), and bb Monte Carlo (dotted magenta line). Each distribution has been normalised to unit area.

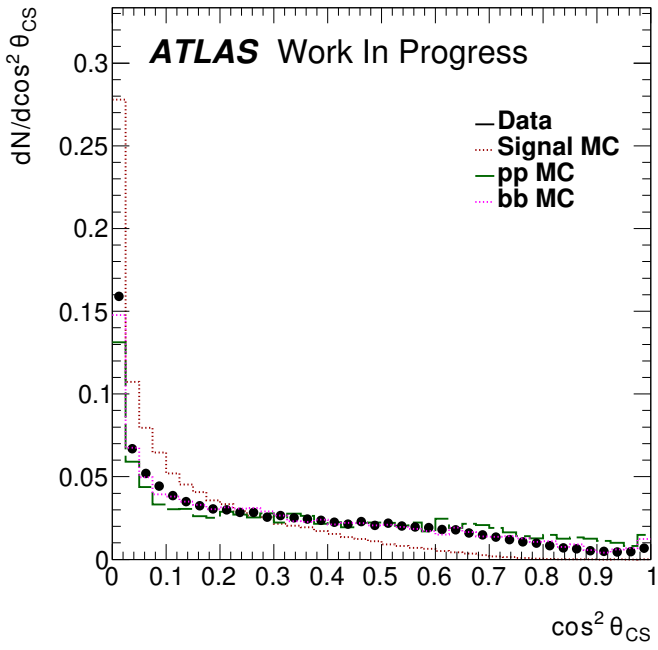

Figure 4.18: Distributions of the variable $\cos\theta$ in the Collins-Soper frame, for data (black dots), signal Monte Carlo (red dotted line), pp Monte Carlo (dashed green line), and bb Monte Carlo (dotted magenta line). Each distribution has been normalised to unit area.

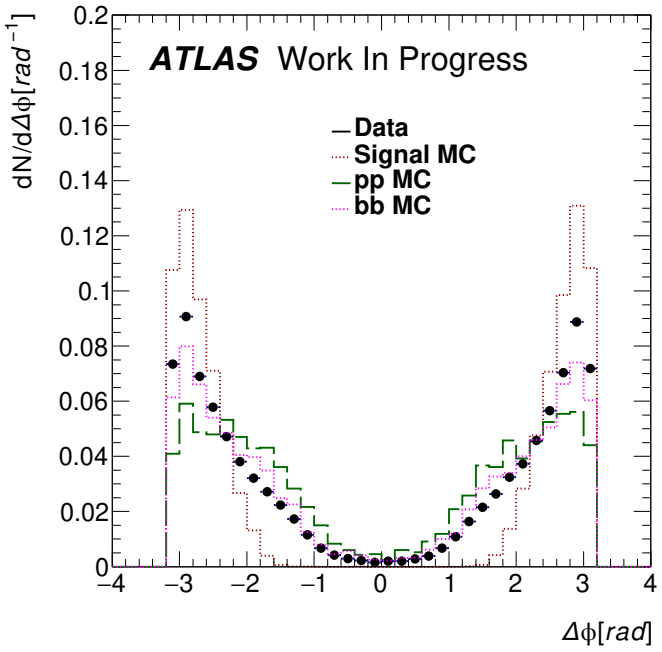

Figure 4.19: Distributions of the variable $\Delta\phi$, for data (black dots), signal Monte Carlo (red dotted line), pp Monte Carlo (dashed green line), and bb Monte Carlo (dotted magenta line). Each distribution has been normalised to unit area.

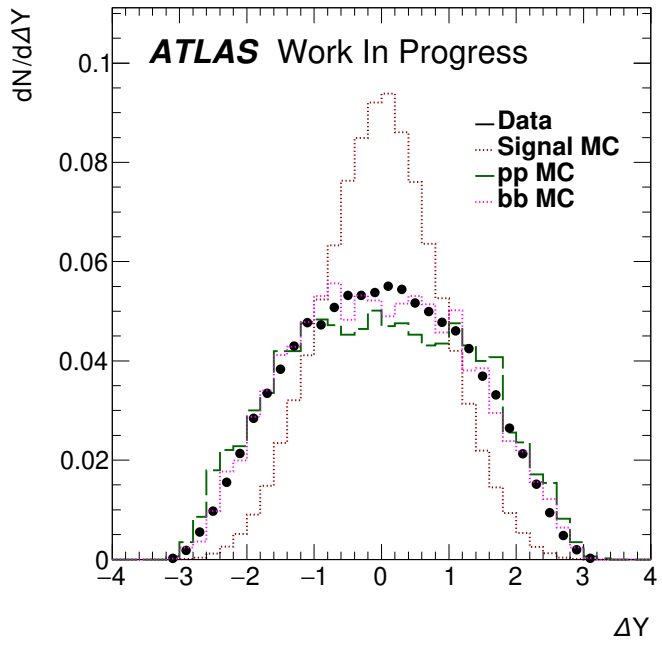

Figure 4.20: Distributions of the variable ΔY, for data (black dots), signal Monte Carlo (red dotted line), pp Monte Carlo (dashed green line), and bb Monte Carlo (dotted magenta line). Each distribution has been normalised to unit area.

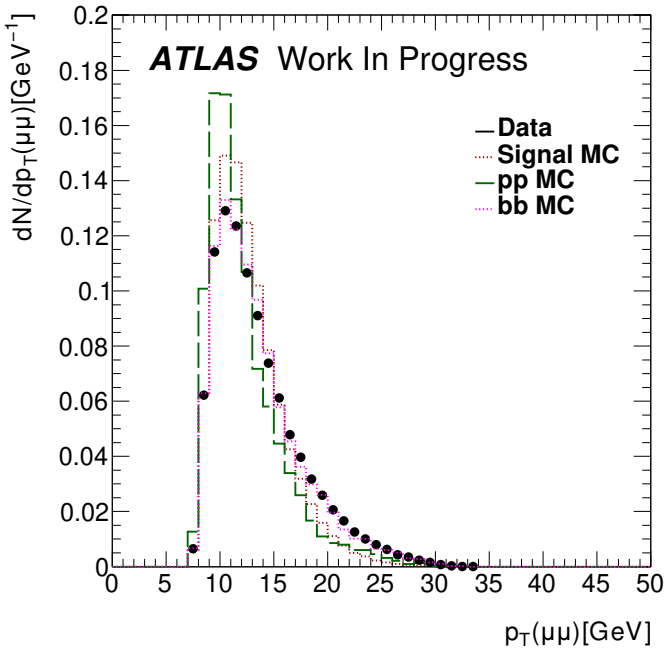

Figure 4.21: Distributions of the variable $p_{\mathrm{T}}(\mu\mu)$, for data (black dots), signal Monte Carlo (red dotted line), pp Monte Carlo (dashed green line), and bb Monte Carlo (dotted magenta line). Each distribution has been normalised to unit area.

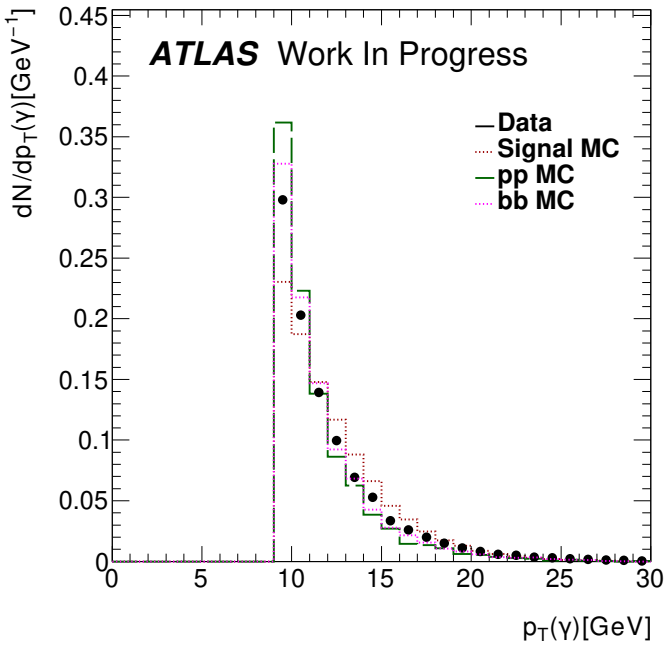

Figure 4.22: Distributions of the variable $p_{\mathrm{T}}(\gamma)$, for data (black dots), signal Monte Carlo (red dotted line), pp Monte Carlo (dashed green line), and bb Monte Carlo (dotted magenta line).

4.2.5 Signal Monte Carlo Truth Variable Selection

At various stages of the analysis, such as efficiency corrections, there is need for distributions of truth-level variables from the signal MC sample. These, however, also need to pass through the series of cuts similar to those listed in Table 4.3.

Cut 1 is replaced by the requirement that there exists a truth-level photon in the event. Cut 2 does not get applied. Cut 3 applied on truth-level variables is essentially obsolete as very few truth events exist in that region of the sample. Cut 4 requires muons from J/ψ decays have their true $p_{\mathrm{T}} > 4$ GeV and photons to have their true $p_{\mathrm{T}} > 9$ GeV. Cuts 5 and 6 are applied to the corresponding truth-level variables for the relevant slice and branch of the analysis. Cuts 7 and 8 are trivial, since the truth-level mass of the J/ψ is always equal to the PDG value and its lifetime is always zero. Cut 9 does not need to be applied.

Table 4.9 shows the numbers of surviving truth events in individual q^2_{T} bins in the three λ slices after all of the above cuts are applied. Similarly, Table 4.10 shows the numbers for ϕ_{CS} bins in the two slices of $\cos^2\theta_{\mathrm{CS}}$.

Bin	Entries	Bin	Entries	Bin	Entries
30	127098	40	254372	50	74991
31	19706	41	29254	51	5803
32	29397	42	59672	52	13372
33	23217	43	56636	53	14454
34	19581	44	42739	54	12609
35	15659	45	29182	55	9952
36	10729	46	18067	56	7428
37	5650	47	10053	57	5003
38	2270	48	5287	58	3166
39	701	49	2407	59	2034
310	188	410	1075	510	1170

Table 4.9: Table of events in each bin of the the $\lambda - q^2_T$ branch of the analysis, after all basic selection cuts applied to the truth-level variables in the signal Monte Carlo sample.

Bin	$z^2 < 0.1$	$z^2 > 0.1$
0	365828	398217
1	26192	25733
2	32037	32343
3	48807	51876
4	79185	89964
5	82855	95060
6	45267	50185
7	28654	29562
8	22831	23494

Table 4.10: Table of events in each ϕ_{CS} bin for low ($z^2 < 0.1$) and high ($z^2 > 0.1$) $\cos^2\theta_{\mathrm{CS}}$ slices, after all basic selection cuts applied to the truth-level variables in the signal Monte Carlo sample.

Chapter 5

Analysis Strategy and Steps

For the aforementioned analysis goals outlined in Chapter 1, various classes of background events need to be subtracted to extract the signal in the selected data events. Two of these backgrounds (bb and pp) are directly addressed, and other unidentified backgrounds are suppressed through event selections (see Chapter 4) and the methods described in this chapter.

The signal subprocess, $g + g \rightarrow \mathrm{J}/\psi + \gamma$, is by definition produced from Single Parton Scattering (SPS) scattering, but there will be events with random combinations of J/ψ and γ produced in separate subprocesses from the same pp collision through Double Parton Scattering (DPS) scattering.

In order to separate SPS and DPS events in data, a multivariate analysis technique is used based on the Boosted Decision Tree (BDT) method. This is described in Section 5.1. This technique is performed separately in each analysis slice for both branches of the analysis (either $\lambda - q_{\mathrm{T}}^2$ or $|\phi_{\mathrm{CS}}|$). This process assigns to each event a score between -1 and 1, where -1 is considered to be an event that is definitely background, and 1 an event which is definitely signal. The analysis selects events with a BDT score > -1.0 and > -0.5. A cut at BDT > -0.5 removes background in each slice.

Then there are two main classes of considered background directly addressed in the analysis which are eliminated in the following order:

1. The dimuon continuum present in the J/ψ mass range. This is suppressed using a sideband subtraction method (see Section 5.2), which suppresses the continuum

background, preserving signal events under the J/ψ peak mass range.

2. Remaining events (under the mass peak) will contain some events originating from non-prompt (B decay) sources. These are suppressed using a long lifetime tail subtraction procedure (see Section 5.3).

After these steps and event selections all non-prompt J/ψ events, and other types of background events are suppressed.

5.1 BDT Analysis

The data sample contains a mixture of SPS signal and DPS background. These two contributions are physically indistinguishable, however separation can be performed statistically, exploiting the expected differences in the properties of the signal and background distributions.

The SPS contribution is expected to follow a back-to-back pattern in $\Delta\phi$, and also have a rather compact distribution in ΔY. On the other hand, the uncorrelated nature of DPS contributions suggests a more uniform distribution in $\Delta\phi$ and a broader ΔY spectrum. The Boosted Decision Tree (BDT) technique [93] method offered by the ROOT TMVA package [94] is employed for the separation of signal and background.

The comparison of these distributions for slice 00/0 ($0 \leq q_{\mathrm{T}}^2 < 400$ GeV^2 and $0 \leq \lambda < 200$) for signal and pp MC samples is given in Figure 5.1.

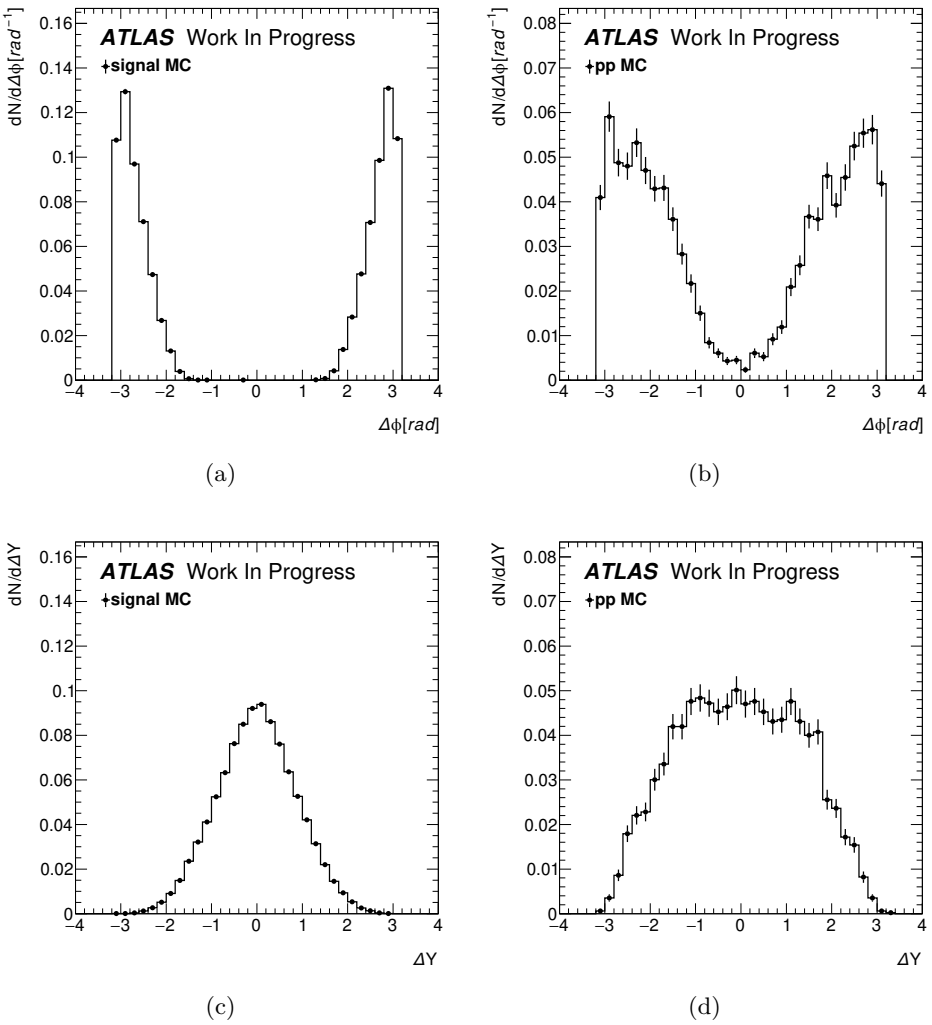

Figure 5.1: Distributions of the two discriminating variables $\Delta\phi$ (top) and ΔY (bottom) for the two MC samples, the signal sample corresponding to the SPS contribution (left) and the pp sample corresponding to the DPS contribution (right). The figures are for slice 00/0 the $\lambda - q_{\mathrm{T}}^2$ region $0 \leq q_{\mathrm{T}}^2 < 400$ GeV^2 and $0 \leq \lambda < 200$.

The acceptance cuts on muon and photon momenta cause significant non-uniformities in $\Delta\phi$ distributions, but the DPS (pp) sample is still clearly different from the SPS (signal) sample. These differences are more visible in 2D distributions of $\Delta\phi$ vs ΔY for slice 00/0 ($0 \leq q_{\mathrm{T}}^2 < 400$ GeV^2 and $0 \leq \lambda < 200$), shown in Figure 5.2.

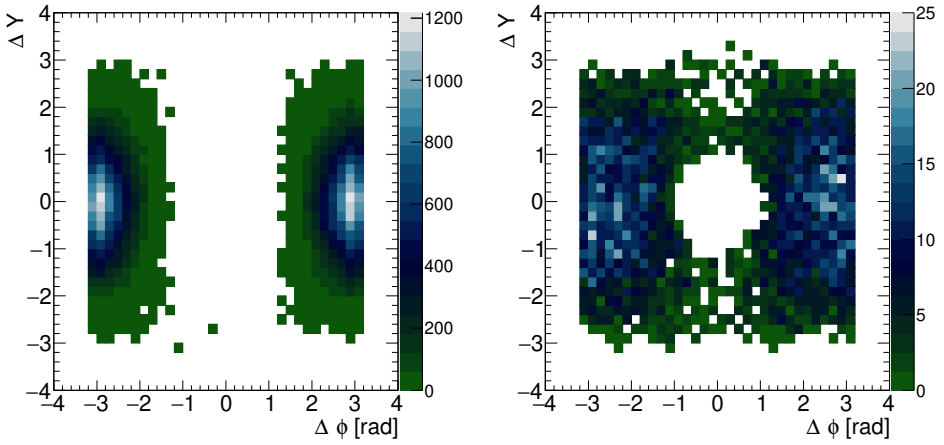

(a) (b)

Figure 5.2: 2D distributions in $\Delta\phi$ vs ΔY for the two MC samples: (a) the signal sample corresponding to the SPS contribution, and (b) the pp sample corresponding to the DPS contribution. The plots include all events surviving the basic selection cuts. The figures are for slice 00/0 the $\lambda - q_{\mathrm{T}}^2$ region $0 \leq q_{\mathrm{T}}^2 < 400$ GeV^2 and $0 \leq \lambda < 200$.

Notation

To aide the reader, each histogram can be identified by a series of labels, which are introduced to easily identify the contents of each histogram. Some of the labelling introduced here will become apparent in the next chapter.

Each histogram can be identified by:

- 1. Sample: either data, signal, pp, or bb.
- 2. The region each slice represents: For $\lambda - q_{\mathrm{T}}^2$ regions, as previously defined, each slice is labelled with two indices from 00 - 510. Regions in $|\phi_{\mathrm{CS}}|$ are identified by a single index 0 - 8.
- 3. The minimum BDT score of events: either BDT > -1.0 or BDT > -0.5, labelled as -1.0 or -0.5 respectively.
- 4. The number of bins in the histogram: If a histogram contains, say, 16 bins this is identified by the label 'B16'.
- 5. The type of events in the histogram either Version 1 or Version2: Version 1 events are labelled 'V1' and Version 2 type events are labelled 'V2'.

- 6. Applicable to $|\phi_{\mathrm{CS}}|$ selections only: The range of $\cos^2\theta$ is either high, or low.

As an example 'data B10 33 -0.5 V1' references data events in the region/slice 33, that has been plotted with 10 bins, and contains version 1 events that have a minimum BDT score $>$ -0.5.

5.1.1 Boosted Decision Tree Training Categories

Discrimination between a signal and a background sample is achieved through a set of discriminating input variables which the MVA trains on, to construct a one-dimensional discriminant, the BDT score. MVAs are trained and evaluated on separate samples to ensure an unbiased result. Training is performed on one half of the events, selected at random, and then applied (tested) on the other half, ensuring orthogonality between the training and testing processes. The final discriminant is built by summing all events, as the physics is expected to be the same in both halves.

In this analysis, the discriminating variables are $\Delta\phi$ and ΔY, and their areas of variation are different and strongly dependent on other kinematic variables, such as λ, q_{T}^2, $\cos\theta_{\mathrm{CS}}$ and ϕ_{CS}. In order to illustrate this fact, Figure 5.3 shows 2D plots of these variables for slices 30, 40, and 50. Although the overall edges of the 2D distributions, determined by the selection cuts and binning, are common for the two samples, the distributions of events in the two samples are quite different, which allows for sufficient level of separation.

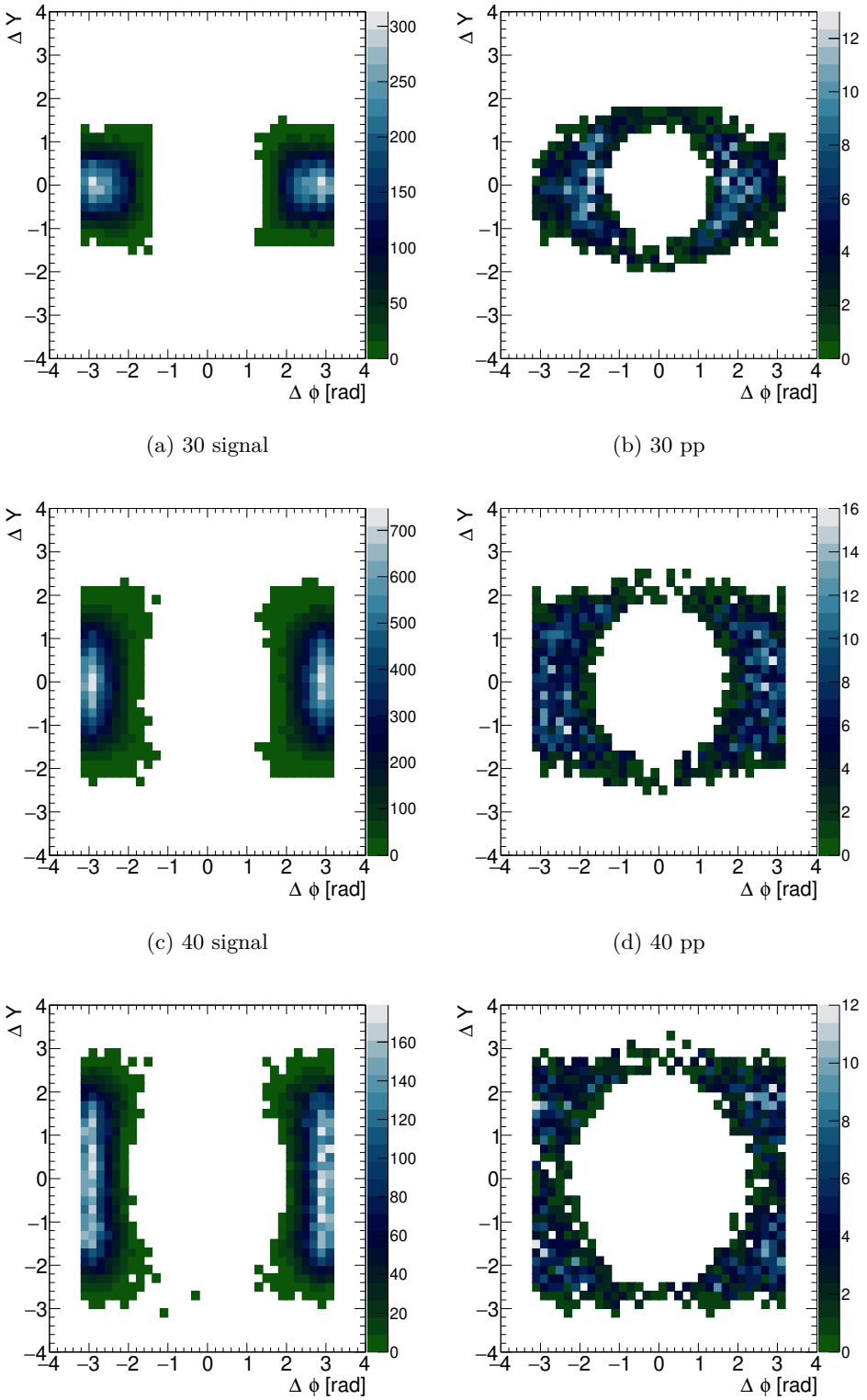

(a) 30 signal

(b) 30 pp

(c) 40 signal

(d) 40 pp

(e) 50 signal

(f) 50 pp

Figure 5.3: 2D distributions in $\Delta\phi$ vs ΔY for the two MC samples: (left) the signal sample corresponding to the SPS contribution, and (right) the pp sample corresponding to the DPS contribution. Top plots correspond to λ slice 30 ($25 \leq \lambda < 50$ and $0 \leq q_{\mathrm{T}}^2 < 400$ GeV^2), middle plots to λ slice 40 ($50 \leq \lambda < 100$ and $0 \leq q_{\mathrm{T}}^2 < 400$ GeV^2), and bottom plots to λ slice 50 ($100 \leq \lambda < 200$ and $0 \leq q_{\mathrm{T}}^2 < 400$ GeV^2).

In order to avoid any biases, the training was performed in individual $\lambda - q_{\mathrm{T}}^2$ bins. The set of hyper-parameters used in the BDT training procedure are listed in Table 5.1. A detailed description of the BDT method and explanation of the hyper-parameters can be reviewed in Ref [94].

BDT Parameter	**Value**
BoostType	AdaBoost
AdaBoostBeta	0.15
Separation Type	Gini Index
NTrees	400
MaxDepth	4
MinNodeSize	5%
NCuts	100
PruneMethod	No Pruning

Table 5.1: Hyper-parameters used in the BDT training

Training was performed separately on each relevant $\lambda - q_{\mathrm{T}}^2$ bin and each version in pp and signal. At the end of the training process, each event is assigned a weight – a BDT score – varying between -1 for pure background to +1 for pure signal.

The Figures 5.4, 5.5 and 5.6 show some results of BDT training and testing for a selection of analysis bins ($\lambda - q_{\mathrm{T}}^2$ bins 38, 44 and 51). In each figure, plots (a) and (b) are the BDT scores for the training and testing phases of the MVA process for Version 1 and Version 2 respectively for a slice. Plots (c) and (d) are 2d plots of ΔY vs. $\Delta\phi$ for the signal sample in a slice for Version 1 and Version 2 respectively. Similarly, plots (e) and (f) are 2d plots of ΔY vs. $\Delta\phi$ for the pp sample. Finally, (g) and (h) are the Received Operating Curve (ROC) distribution for Version 1 and Version 2 respectively in a slice.

The results for other selected slices can be found in Appendix C.

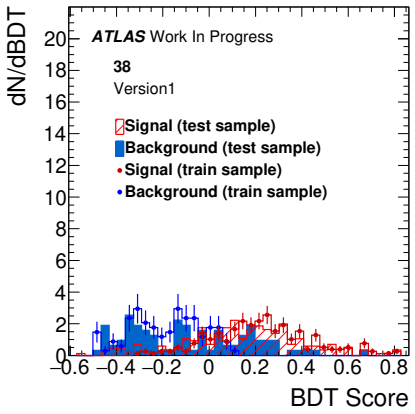

(a) BDT Training 38 V1

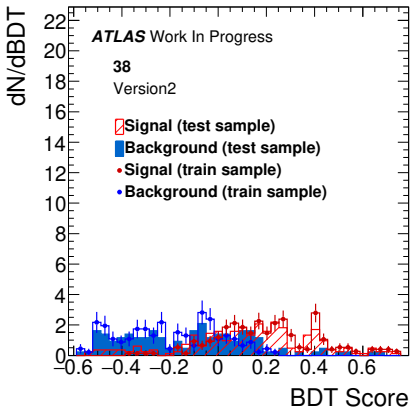

(b) BDT Training 38 V2

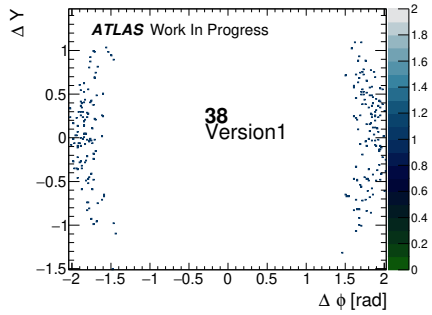

(c) Signal Correlation 38 V1

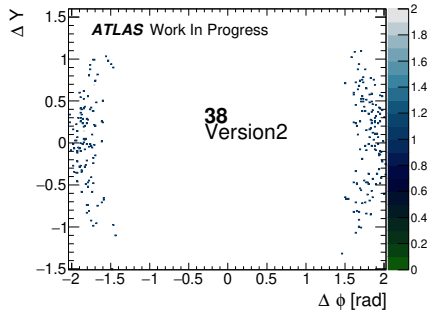

(d) Signal Correlation 38 V2

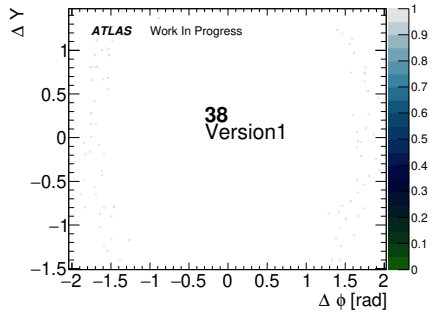

(e) Background Correlation 38 V1

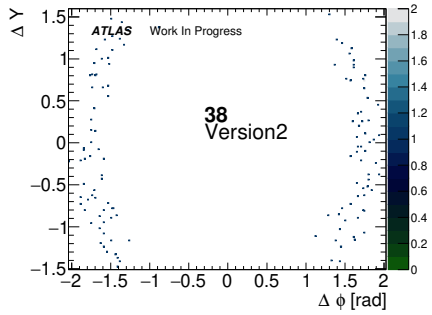

(f) Background Correlation 38 V2

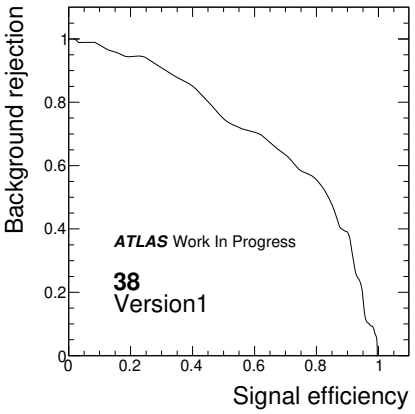

(g) Efficiency 38 V1

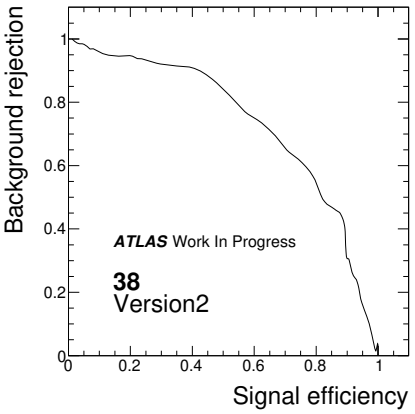

(h) Efficiency 38 V2

Figure 5.4

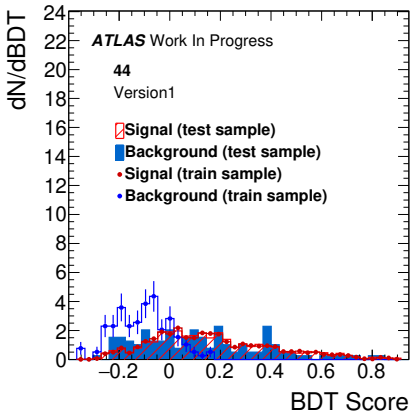

(a) BDT Training 44 V1

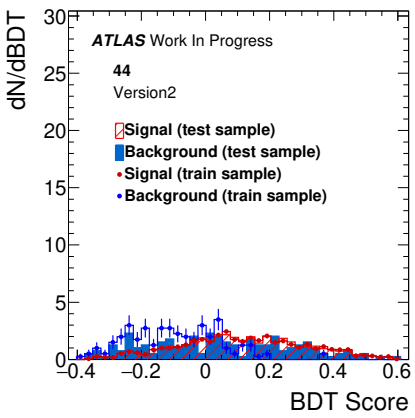

(b) BDT Training 44 V2

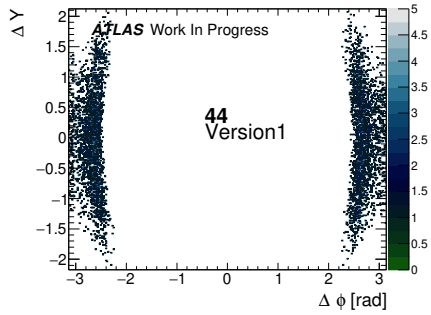

(c) Signal Correlation 44 V1

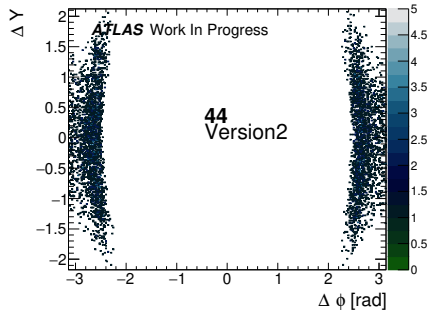

(d) Signal Correlation 44 V2

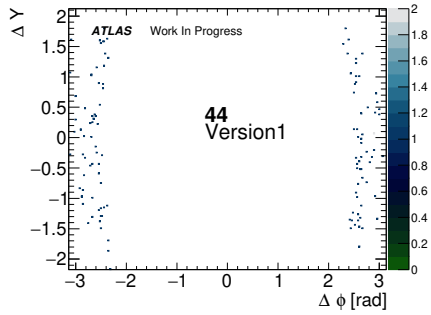

(e) Background Correlation 44 V1

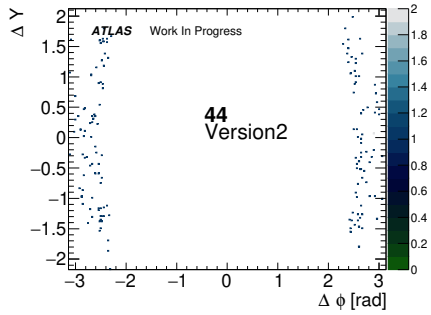

(f) Background Correlation 44 V2

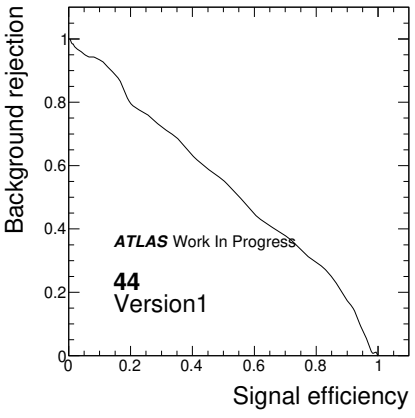

(g) Efficiency 44 V1

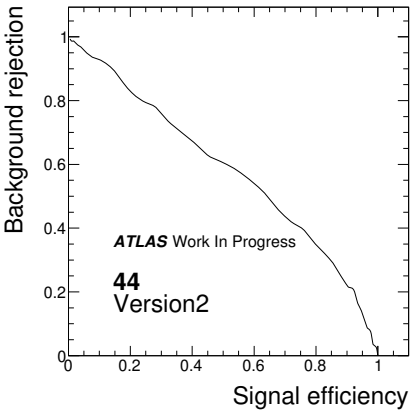

(h) Efficiency 44 V2

Figure 5.5

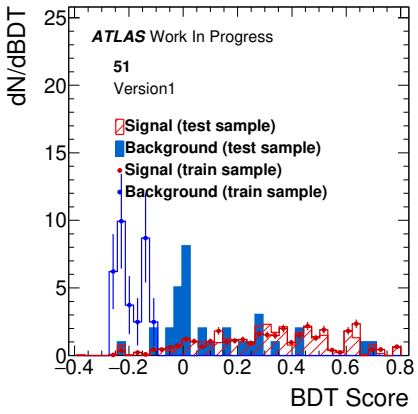

(a) BDT Training 51 V1

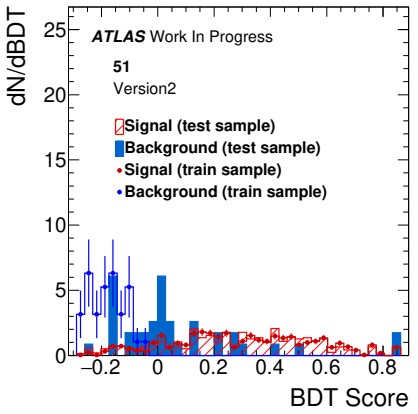

(b) BDT Training 51 V2

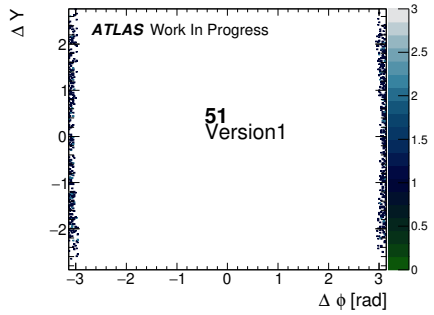

(c) Signal Correlation 51 V1

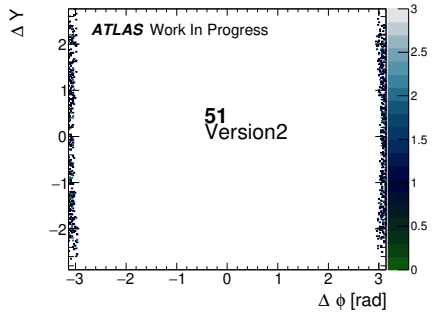

(d) Signal Correlation 51 V2

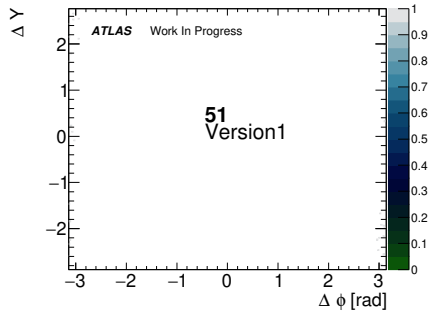

(e) Background Correlation 51 V1

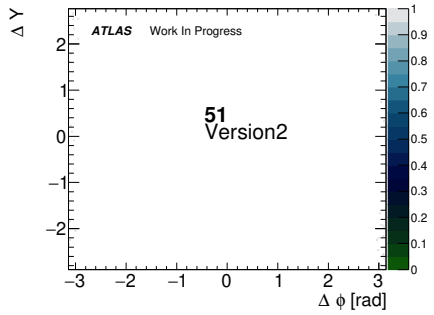

(f) Background Correlation 51 V2

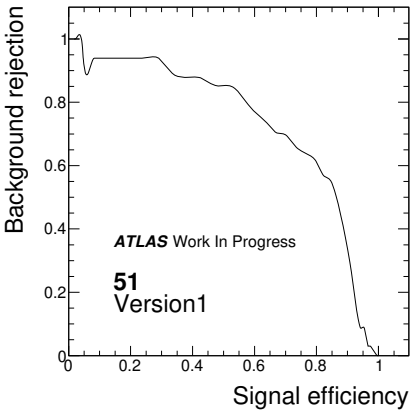

(g) Efficiency 51 V1

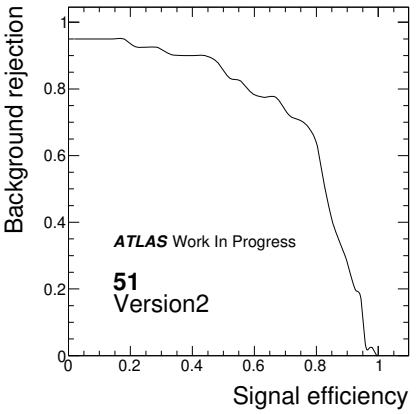

(h) Efficiency 51 V2

Figure 5.6

The analysis suffers from over-training in several $\lambda - q_{\mathrm{T}}^2$ slices. Over-training can be seen in plots (a) and (b) in Figures 5.4, 5.5 and 5.6, where the training and testing BDT scores are different from each other, particularly for the pp sample which has low statistics. Over-training is the inability to differentiate between signal and background events at the testing stage based on the composition of events (and their weightings) during the training stage[1], potentially classifying signal events as background. A BDT generally requires a high number of statistics for both the training and testing phases to be representative of event.

Over-training is seen in $\lambda - q_{\mathrm{T}}^2$ slices which contain a low level of pp statistics, so the BDT has difficulty in differentiating between pp and signal events during the testing phase, potentially classifying signal events as background. Plots (g) and (h) in Figures 5.4, 5.5 and 5.6 show how well the BDT is able to differentiate between signal and background during the testing phases. The higher the curve the better the separation. A higher curve is seen in slices 38 and 51 which contain more signal events.

The results are expected, confirming that various kinematical regions are dominated by signal event configurations with very low pp background. The analysis has used all pp and signal statistics available at time of writing. Although an increase in pp statistics would reduce over-training it would not improve the BDTs ability to separate between signal and background in kinematical regions which are signal dominated.

Results were also achieved for the ϕ_{CS} branch of the analysis. Sample plots, for analysis bins '4 Low' and '4 High' are shown in Figures 5.7 and 5.8, while results for selected other bins are shown in Appendix C.

[1] Over-training can be summarised in the following analogy. Imagine the results of 20 coin flips: 10 heads and 10 tails. The BDT trains on 10 events and tests on 10 events. Suppose the BDT trains on 9 heads and 1 tails, and then tests on 9 tails and 1 heads. During training phase 90% of the events were heads, and so the BDT will assume the majority of events during the testing phase are also heads, which is not true, and will therefore misclassify some of the testing tail events as heads.

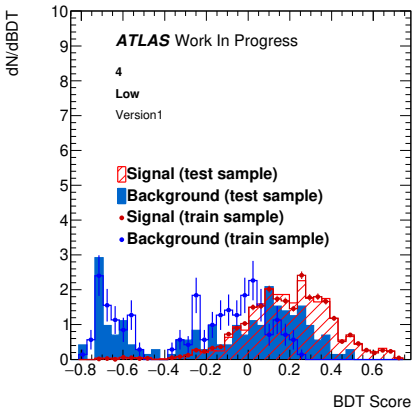

(a) BDT Training 4 V1 Low

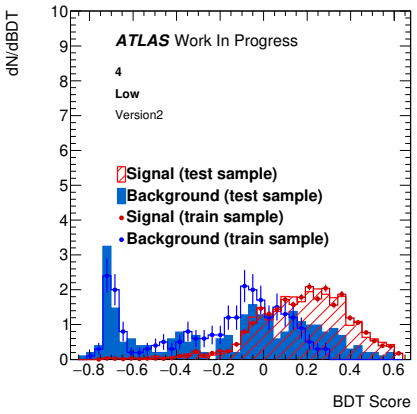

(b) BDT Training 4 V2 Low

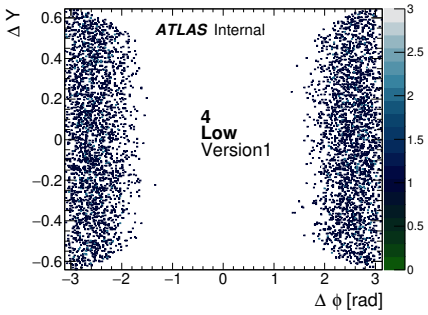

(c) Signal Correlation 4 V1 Low

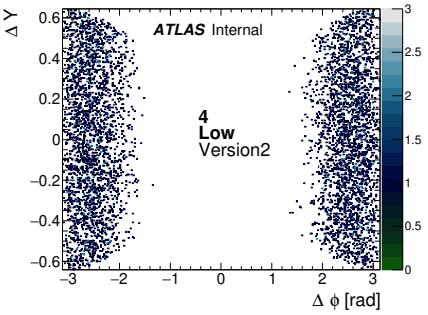

(d) Signal Correlation 4 V2 Low

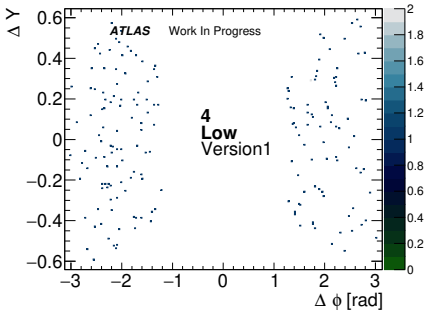

(e) Background Correlation 4 V1 Low

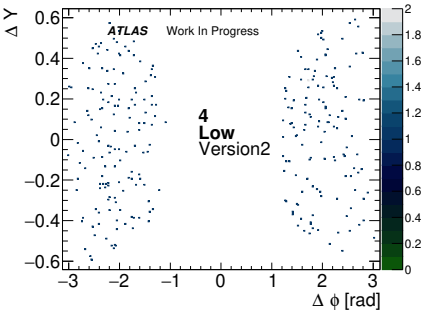

(f) Background Correlation 4 V2 Low

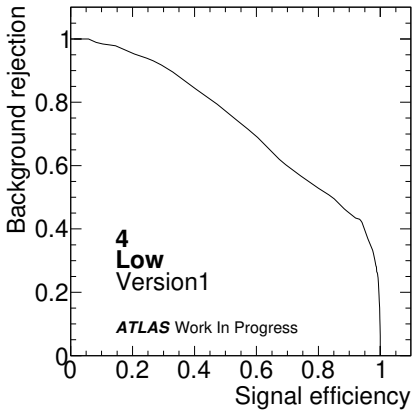

(g) Efficiency 4 V1 Low

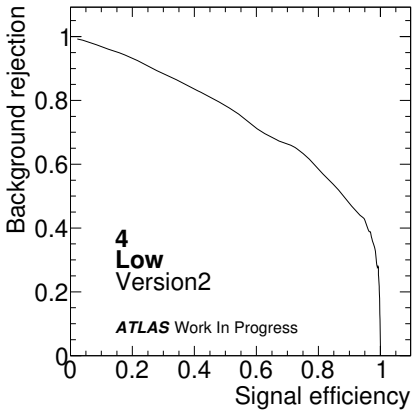

(h) Efficiency 4 V2 Low

Figure 5.7

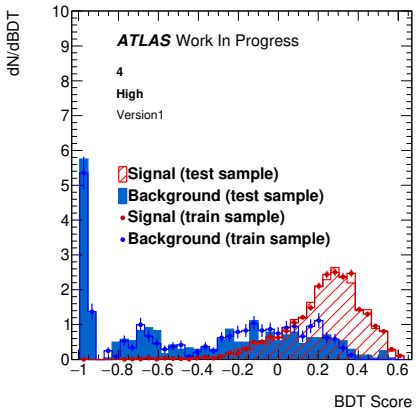

(a) BDT Training 4 V1 High

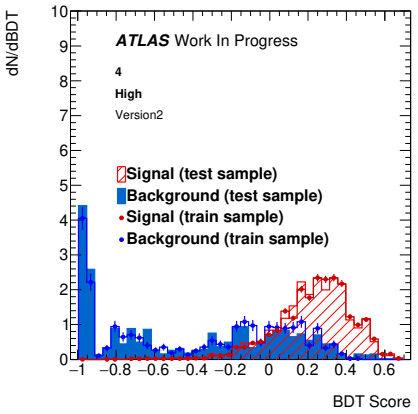

(b) BDT Training 4 V2 High

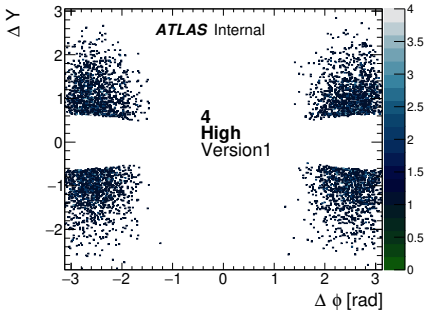

(c) Signal Correlation 4 V1 High

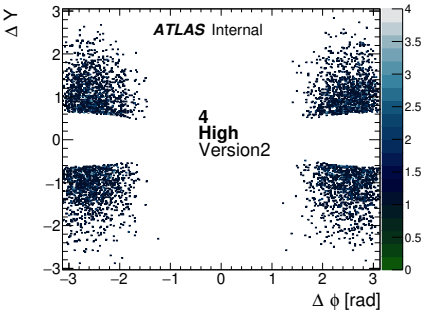

(d) Signal Correlation 4 V2 High

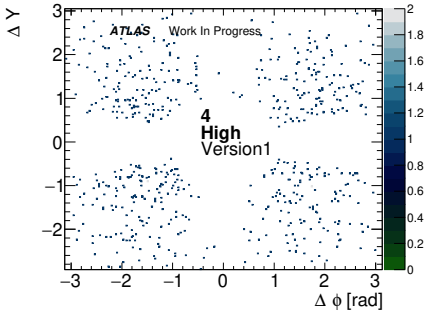

(e) Background Correlation 4 V1 High

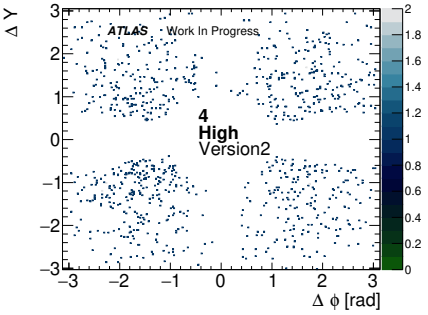

(f) Background Correlation 4 V2 High

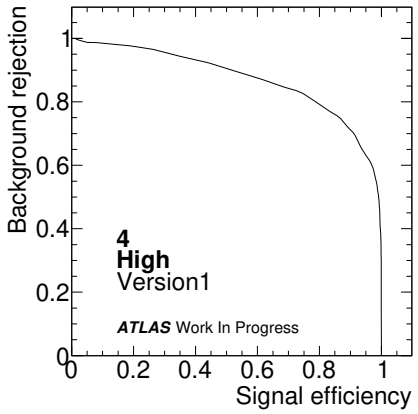

(g) Efficiency 4 V1 High

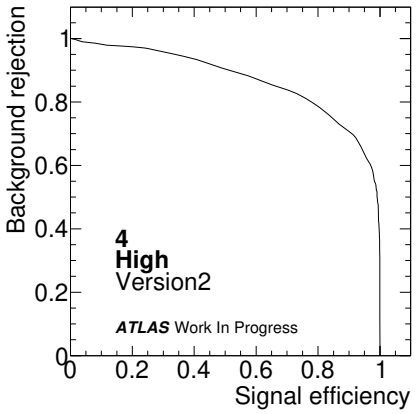

(h) Efficiency 4 V2 High

Figure 5.8

There is much better agreement between the training and testing samples in the $|\phi_{\text{CS}}|$ branch of the analysis (see plots (a) and (b) in Figures 5.7 and 5.8), although there is still some over-training due to low pp statistics.

The BDT is evaluated on the data samples for each branch of the analysis. The BDT weights determined during the training and testing phases are assigned to the data samples. Two BDT score cuts of > -1.0 and > -0.5 are applied to all events across both branches of the analysis.

To conclude this subsection, each $\mu\mu\gamma$ event has a BDT score assigned to it, based on kinematic characteristics, and a BDT score cut applied. The BDT score discriminant is the variable used for the remainder of the analysis. Two background subtraction techniques can now be applied to events.

5.2 Mass Sideband Subtraction

Previous studies of dimuon mass distributions [95–97], indicate that the shape of the background distribution is usually well approximated by an exponential or a linear function. For this analysis, the background is assumed to be linear which leads to a simple background subtraction procedure. As a systematic variation, an exponential background is later considered (see Section 8.1.1).

The dimuon mass distribution for each slice and bin is further divided into into 4 equal mass regions with bin edges $(2.7 - 2.9 - 3.1 - 3.3 - 3.5)$ GeV, with each region labelled 1-4, as illustrated in Figure 5.9 for slice 00/0 ($0 \leq q_{\text{T}}^2 < 400$ GeV^2 and $0 \leq \lambda < 200$) with no BDT score cut applied.

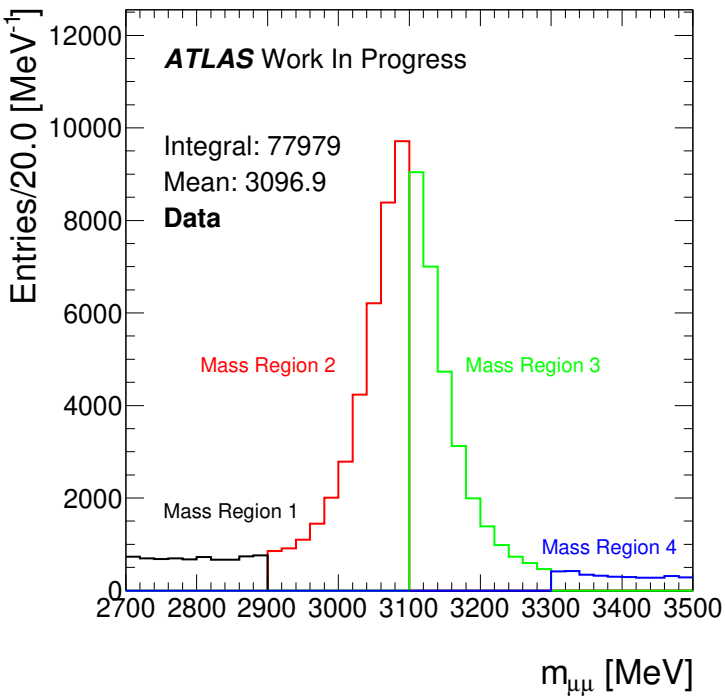

Figure 5.9: Plot of the dimuon mass between 2.7-3.5 GeV, highlighting the 4 mass regions that the BDT is cut into. Region 1: $2.7 \leq m_{\mu\mu} < 2.9$ GeV, region 2: $2.9 \leq m_{\mu\mu} < 3.1$ GeV, region 3: $3.1 \leq m_{\mu\mu} < 3.3$ GeV, and region 4: $3.3 \leq m_{\mu\mu} < 3.5$ GeV. The combination of regions $(2+3) - (1+4)$ is the mass sideband subtraction procedure.

Regions 2 and 3 contain both signal and background, while regions 1 and 4 are assumed to contain only background, as defined in Figure 5.9. Since the background is taken to be linear, the sum over regions 1 and 4 is equal to the background component in regions $2+3$, hence the signal yield is extracted as $(2+3)$ - $(1+4)$. This procedure needs to be performed for any distribution of events in each slice.

5.3 Long Lifetime Subtraction

Previous studies of inclusive J/ψ production [95, 97] have shown that the distributions of J/ψ candidates with respect to the pseudo-proper lifetime $\tau_{\mu\mu}$ have a peak around $\tau_{\mu\mu} = 0$ ps corresponding to prompt production mechanisms and a long (quasi-)exponential tail from non-prompt production from B hadron decays. The fits performed during these inclusive J/ψ production studies had effective lifetime slopes in the region of $1.2 - 1.3$ ps. This corresponds to an effective half-life τ_0 of about 0.86 ps. For slice 00/0 this means that the

number of non-prompt J/ψ candidates with lifetimes above this value is equal to the number of non-prompt candidates with lifetimes below this value. Labelling the region below τ_0 as region 1, and the region above τ_0 as region 2, then the difference $(1-2)$ will contain a good estimate of the number of prompt candidates. This method is applied to all slices in both branches of the analysis, and the bb yield was found to be consistent with zero (within errors) throughout after subtractions. A variation of τ_0 will be used for systematic studies (see Section 8.1.2). This procedure is illustrated in Figure 5.10 where no BDT score cut is applied.

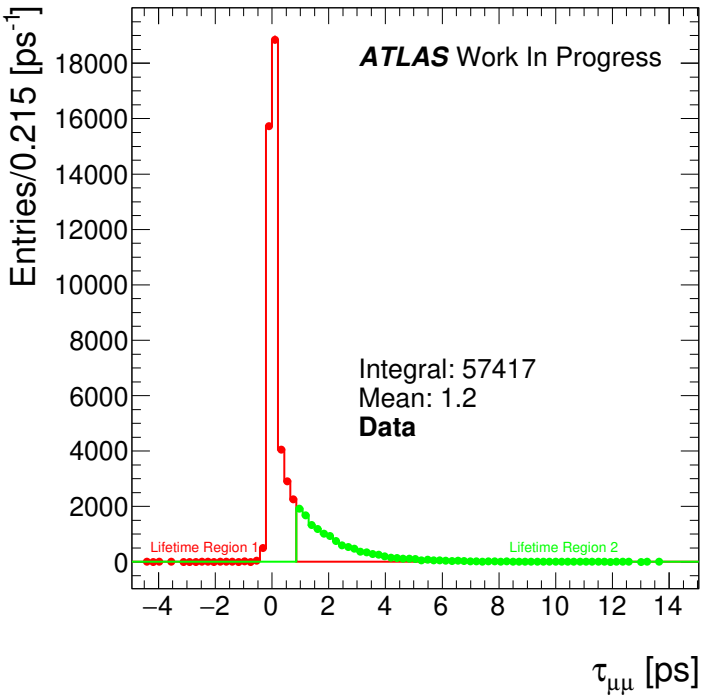

Figure 5.10: Plot of the dimuon lifetimes after mass sideband subtraction, highlighting the 2 lifetime regions. Region 1: -5 $\leq \tau_{\mu\mu} <$ 0.860 ps, and region 2: 0.860 $\leq \tau_{\mu\mu} <$ 15 ps. For a correct choice of the cut, the combination (1) $-$ (2) eliminates the non-prompt component and thus allows to extract the prompt J/ψ signal.

In fact, the mass sideband subtraction and the long lifetime subtraction can be performed simultaneously, by dividing the 2D mass-lifetime plane into 4×2 regions, as illustrated in Figure 5.11 for slice 00/0 ($0 \leq q_{\mathrm{T}}^2 < 400$ GeV^2 and $0 \leq \lambda < 200$) in data. Plot (a) is the 2D mass-lifetime plane, (b) is after mass sideband and long lifetime subtractions. Plot (a) contains 77979 events which is the number of events remaining after Cut 9 in data. Plot (b) contains 31307 events, which is the number of events remaining after mass and

lifetime subtractions in data. In moving from plot (a) to (b) the mass sideband regions $2.7 \leq m_{\mu\mu} < 2.9$ GeV and $3.3 \leq m_{\mu\mu} < 3.5$ GeV have been completely subtracted, leaving events only under the J/ψ peak, mass region $2.9 \leq m_{\mu\mu} < 3.3$ GeV. Long lifetime background events under the J/ψ peak have also been completely subtracted as can be seen in the J/ψ mass peak and lifetime region $0.86 \leq \tau_{\mu\mu} < 15$ ps. The events of interest that remain after mass sideband and long lifetime subtraction are in the region $2.9 \leq m_{\mu\mu} < 3.3$ GeV and $0 \leq \tau_{\mu\mu} < 0.860$ ps.

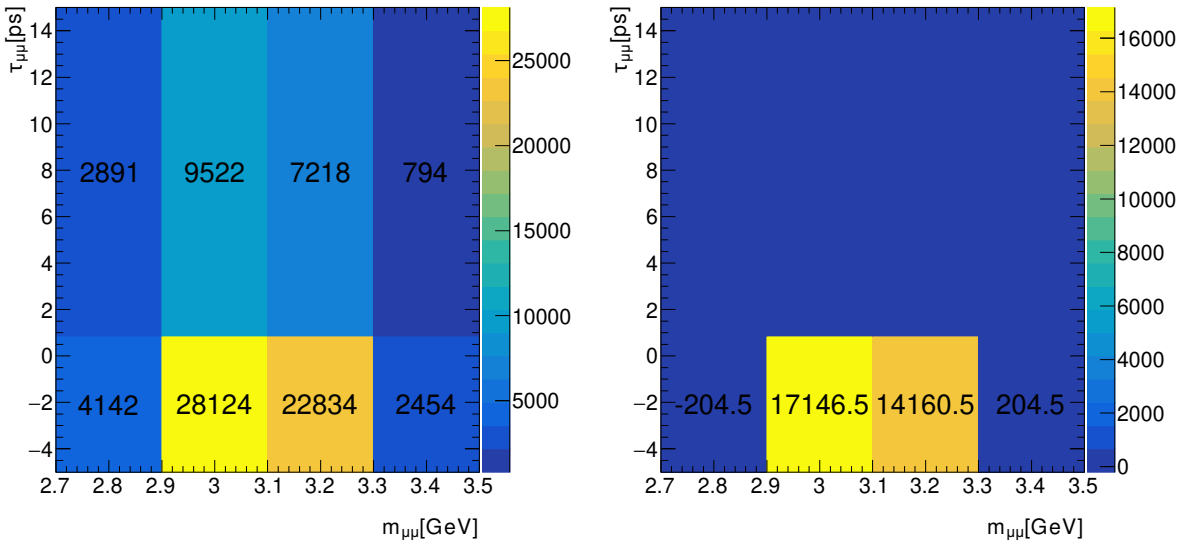

(a) Before subtractions

(b) After subtractions

Figure 5.11: Plots of the 2D mass lifetime plane. Plot (a) is the 2D mass-lifetime plane, and (b) is after mass sideband and long lifetime subtractions for slice 00/0 in data. The number of events is detailed in each bin of the mass-lifetime regions.

The statistical uncertainty on the number of events in each slice after background subtractions is equal to the square root of the total number of events. The continuum background is rather low, and the non-prompt contributions are relatively modest, hence the relative increase in statistical errors is not too large.

In order to fine-tune the lifetime separation cut, and check that the non-prompt contribution is uniformly suppressed for any subset of events, the subtraction procedures were applied to the bb MC sample of non-prompt J/ψ production for slice 00/0 ($0 \leq \lambda < 200$ and $0 \leq q_{\mathrm{T}}^2 < 400$ GeV^2) with no BDT score cut applied. The results are shown in Table 5.2, which indicates the complete suppression of the bb MC sample after the mass sideband

and long-lifetime subtraction procedure. Out of 10M generated events about 24 thousand survived the event selection cuts, out of which only (-100 ± 82) are left after the mass sideband and long-lifetime subtraction procedure. This is repeated for the data, signal, and pp samples, which shows how events are distributed between different mass and lifetime regions.

Cut	**signal**	**pp**	**bb**	**data**
Cut 1: Photon Vector > 0	935578	463711	539733	3033090
Cut 2: HLT_2mu4_bJpsimumu_noL2 Trigger Flag	431820	230372	282887	2338141
Cut 3: $\lambda < 15$	418663	188220	228977	1872508
Cut 4: 449	149024	26519	35107	352980
Cut 5: $0 \leq \lambda < 200$	149024	26519	35107	352980
Cut 6: $0 \leq q_T^2 < 400$ GeV^2	145760	18279	24128	257455
Cut 7: $2.7 \leq m_{\mu\mu} < 3.5$ GeV	145446	18243	24068	245639
Cut 8: $-5 \leq \tau < 15$ ps.	145445	18243	24064	245589
Cut 9: Tight Photons Only	99346	5127	6672	77979
Cut 10: $\Delta R < 0.12$ between signal reconstructed and truth photons	97472	—	—	—
Region 11: $2.7 \leq m_{\mu\mu} < 2.9$ GeV and $-5 \leq \tau_{\mu\mu} < 0.86$ ps	1392	77	77	4142
Region 21: $2.9 \leq m_{\mu\mu} < 3.1$ GeV and $-5 \leq \tau_{\mu\mu} < 0.86$ ps	51249	2761	1699	28124
Region 31: $3.1 \leq m_{\mu\mu} < 3.3$ GeV and $-5 \leq \tau_{\mu\mu} < 0.86$ ps	44300	2245	1512	22834
Region 41: $3.3 \leq m_{\mu\mu} < 3.5$ GeV and $-5 \leq \tau_{\mu\mu} < 0.86$ ps	483	38	22	2454
Region 12: $2.7 \leq m_{\mu\mu} < 2.9$ GeV and $0.86 \leq \tau_{\mu\mu} < 15$ ps	0	0	62	2891
Region 22: $2.9 \leq m_{\mu\mu} < 3.1$ GeV and $0.86 \leq \tau_{\mu\mu} < 15$ ps	14	3	1753	9522
Region 32: $3.1 \leq m_{\mu\mu} < 3.3$ GeV and $0.86 \leq \tau_{\mu\mu} < 15$ ps	32	3	1534	7218
Region 42: $3.3 \leq m_{\mu\mu} < 3.5$ GeV and $0.86 \leq \tau_{\mu\mu} < 15$ ps	2	0	13	794
Region 71: Region 21 + Region 31	95549	5006	3211	50958
Region 81: Region 11 + Region 41	1875	115	99	6596
Region 72: Region 22 + Region 32	46	6	3287	16740
Region 82: Region 12 + Region 42	2	0	75	3685
Region 91: Region 71 - Region 81	93674	4891	3112	44362
Region 92: Region 72 - Region 82	44	6	3212	13055
Region 99: Region 91 - Region 92	93630	4885	-100	31307

Table 5.2: Event selection cut flow for slice 00/0 ($0 \leq \lambda < 200$ and $0 \leq q_{\mathrm{T}}^2 < 400$ GeV^2) of the bb, pp, and signal Monte Carlo samples and data sample.

The 'cut flows' for selected slices can be found in Appendix D which describes the event selections at each step of the analysis.

After these two methods the background dimuon continuum, non-prompt contributions, and other backgrounds, have been subtracted from the samples. The data sample is 'cleaned' up, and now directly comparable to the signal and pp MC samples, a property exploited with the next step of the analysis, the likelihood fitting stage. Plots of the variables after both subtractions are shown in Figures 5.12 - 5.21 (except for Figure 5.15, the dimuon lifetime distribution, which is plotted after the mass sideband subtractions only), for slice 00/0 ($0 \leq \lambda < 200$ and $0 \leq q_{\mathrm{T}}^2 < 400$ GeV^2), with no BDT score cut applied. The

data distributions follow the same shape as the signal distributions, and the data is now a superposition of the signal and pp distributions. As the bb MC sample has been completely subtracted it is not shown.

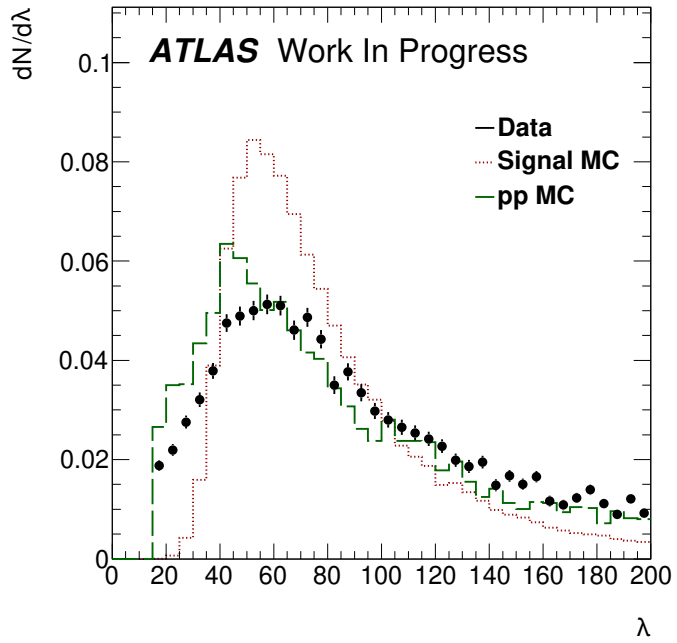

Figure 5.12: Distributions of the variable λ, for data (black dots), signal Monte Carlo (red dotted line), and pp Monte Carlo (dashed green line). Each distribution has been normalised to unit area.

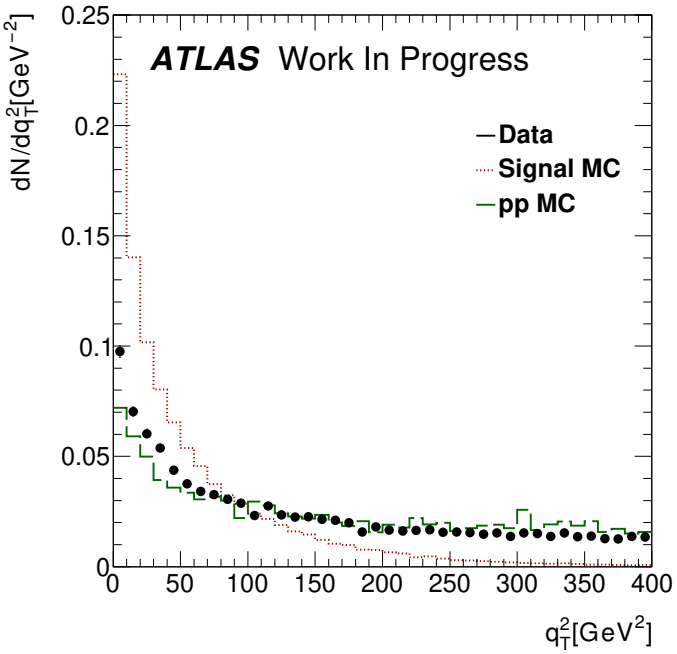

Figure 5.13: Distributions of the variable q_{T}^2, for data (black dots), signal Monte Carlo (red dotted line), and pp Monte Carlo (dashed green line). Each distribution has been normalised to unit area.

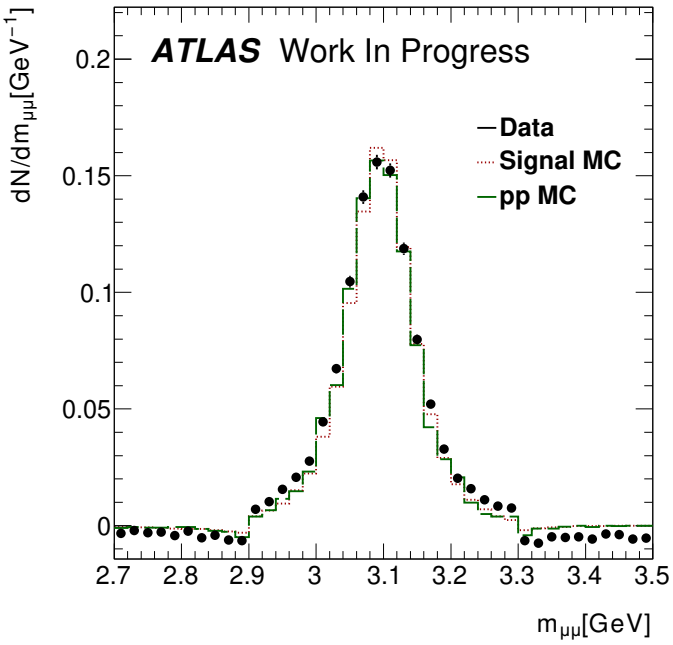

Figure 5.14: Distributions of the dimuon mass ($m_{\mu\mu}$), for data (black dots), signal Monte Carlo (red dotted line), and pp Monte Carlo (dashed green line). Each distribution has been normalised to unit area.

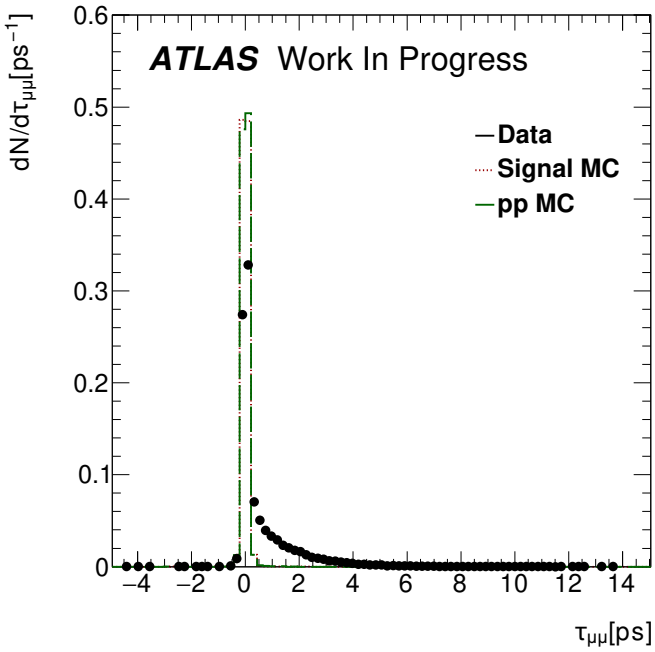

Figure 5.15: Distributions of the dimuon lifetime ($\tau_{\mu\mu}$), after only the mass sideband subractions, for data (black dots), signal Monte Carlo (red dotted line), and pp Monte Carlo (dashed green line). Each distribution has been normalised to unit area.

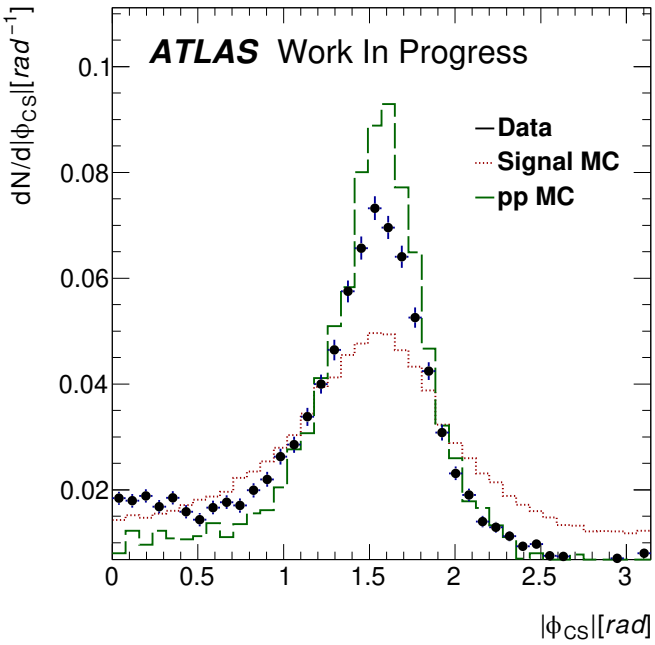

Figure 5.16: Distributions of the variable $|\phi|$ in the Collins-Soper frame, for data (black dots), signal Monte Carlo (red dotted line), and pp Monte Carlo (dashed green line). Each distribution has been normalised to unit area.

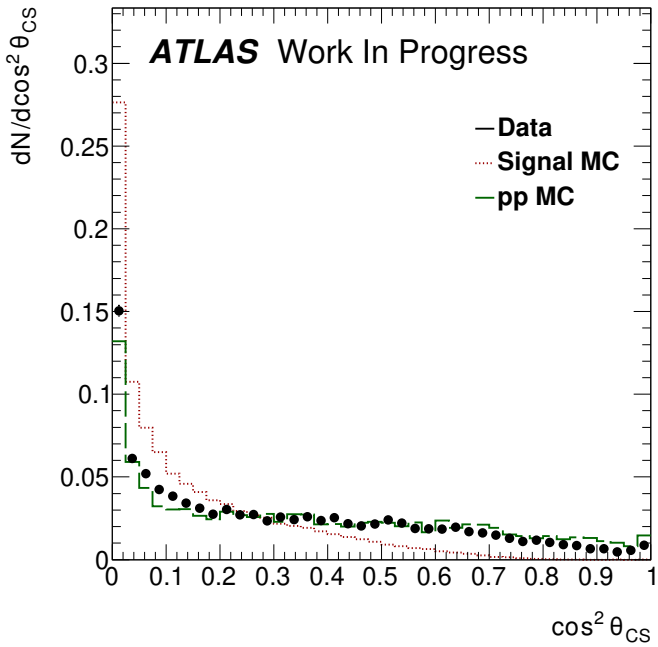

Figure 5.17: Distributions of the variable $\cos\theta$ in the Collins-Soper frame, for data (black dots), signal Monte Carlo (red dotted line), and pp Monte Carlo (dashed green line). Each distribution has been normalised to unit area.

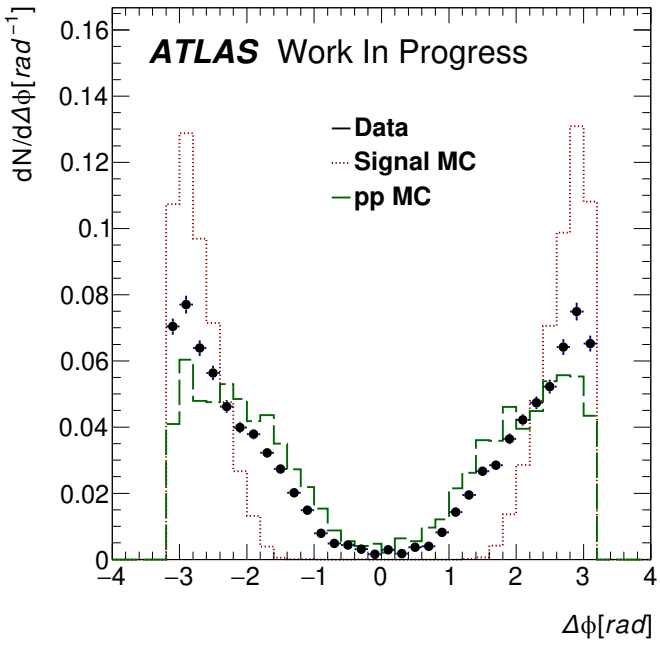

Figure 5.18: Distributions of the variable $\Delta\phi$, for data (black dots), signal Monte Carlo (red dotted line), and pp Monte Carlo (dashed green line). Each distribution has been normalised to unit area.

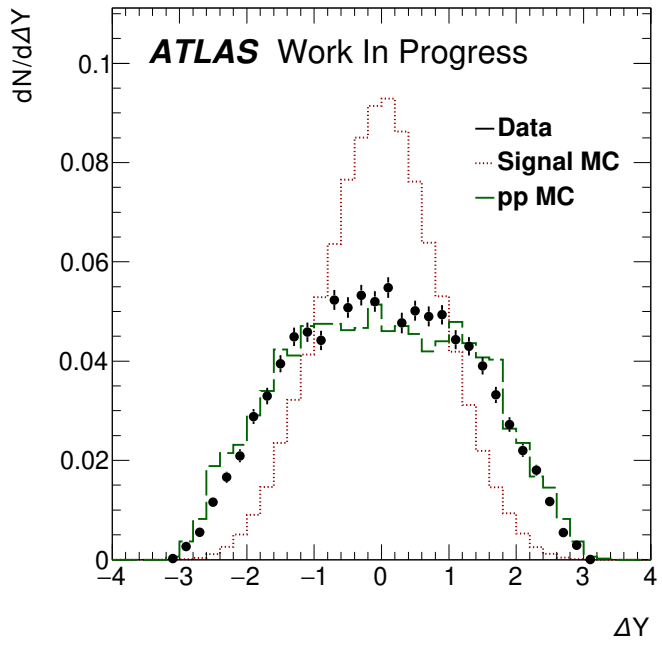

Figure 5.19: Distributions of the variable ΔY, for data (black dots), signal Monte Carlo (red dotted line), and pp Monte Carlo (dashed green line). Each distribution has been normalised to unit area.

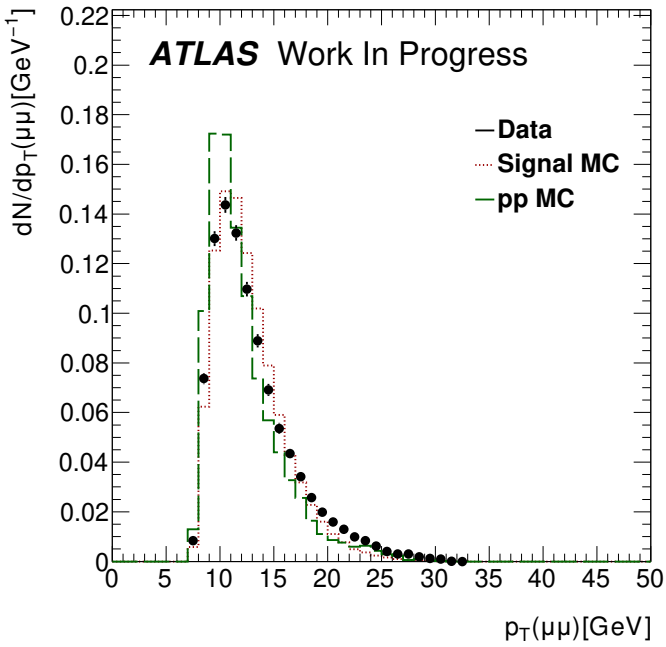

Figure 5.20: Distributions of the variable $p_{\mathrm{T}}(\mu\mu)$, for data (black dots), signal Monte Carlo (red dotted line), and pp Monte Carlo (dashed green line). Each distribution has been normalised to unit area.

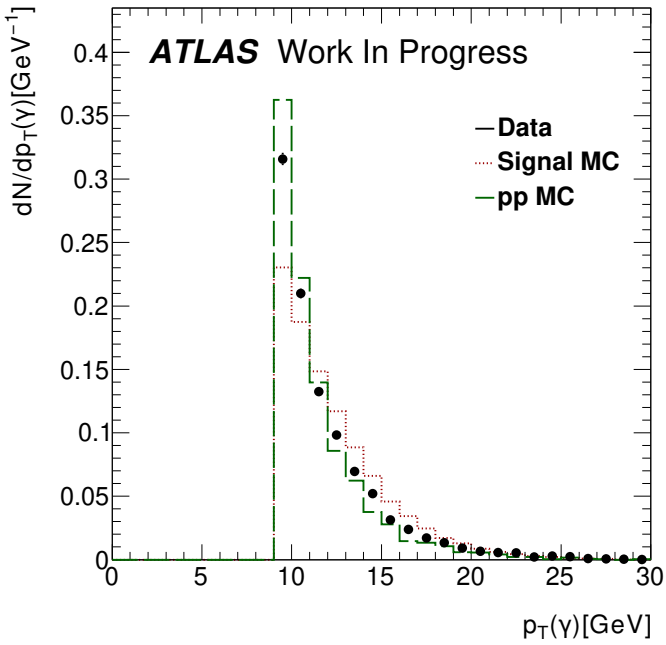

Figure 5.21: Distributions of the variable $p_{\mathrm{T}}(\gamma)$, for data (black dots), signal Monte Carlo (red dotted line), and pp Monte Carlo (dashed green line). Each distribution has been normalised to unit area.

Chapter 6

Likelihood Fits With `HistFactory`

The analysis builds a statistical model called a likelihood fit to infer the signal presence over background in data, through use of the `HistFactory` [98] package within ROOT. `HistFactory` is a package which builds parameterised probability density functions (pdfs) to create a maximum likelihood fit for a set of binned input histograms. The theoretical framework of `HistFactory` can be reviewed in Ref. [98].

In the previous chapter, it was shown how the mass sideband subtraction procedure removes the dimuon continuum background, leaving only events under the J/ψ peak, and how a lifetime subtraction technique removes long lifetime non-prompt J/ψ events. The next type of background mixed with the pp sample, originating from DPS, is also addressed through `HistFactory` fits, is the production of a J/ψ and γ from two uncorrelated scatterings within one pp collision.

Section 6.1 gives an overview of the `HistFactory` formalism relevant to this thesis, and Section 6.2 details how the results from the fitting procedure are sensitive to a number of factors, and how this can be used as a systematic variation.

6.1 HistFactory Formalism

6.1.1 Likelihood Fits With HistFactory

`HistFactory` is a statistical tool that can take systematics into account when performing a binned maximum likelihood fit. The analysis chooses not to utilise this feature and instead

addresses systematics in Chapter 8.

A binned maximum likelihood fit is an method for estimating parameter values of a model. The parameter values are found such that they maximise the likelihood that the process described by the model is representative of the data.

If one considers n independent observable of $x = x_1, x_2, x_3, ..., x_n$, each as a sampling from a probability density function (pdf), $P(x :, \mu, \theta)$, an estimate for parameters μ and θ can be built using the likelihood function, $\mathcal{L}(x)$:

$$\mathcal{L}(x) = -\prod_i P(x_i; \mu, \theta). \tag{6.1}$$

for a bin i in a histogram. `HistFactory` is able to find the global maximum value of the function, by taking the log of the likelihood function, which replaces the product with a sum:

$$\ln(\mathcal{L}) = -\sum_i P(x_i; \mu, \theta). \tag{6.2}$$

`HistFactory` builds parameterised pdfs based on binned histograms, but generally one does not know the form of the pdf as this can only be solved numerically. However, an extended maximum likelihood fit can be used to derive the binned maximum likelihood fit. If one considers data to follow a Poisson probability of obtaining n events in bin i when $S+B$ are expected, where S and B are expected signal and background events respectively, modulated by a pdf then:

$$\mathcal{L}(x_i) = \text{Pois}(n|S+B) \times \prod_i \Big[P(x; \mu, \theta)\Big]. \tag{6.3}$$

$\mathcal{L}(x_i)$ is the extended maximum likelihood function for a bin. Substituting in the definition of a Poisson distribution, $e^{-\alpha}\alpha^n/n!$, where $\alpha = S + B$, then

$$\mathcal{L}(x_i) = \frac{e^{-\alpha}\alpha^n}{n!} \times \prod_i \Big[P(x_i; \mu, \theta)\Big]. \tag{6.4}$$

Taking the natural logarithm of this:

$$\begin{aligned}\ln(\mathcal{L}) &= \ln\Big(\frac{e^{-\alpha}\alpha^{n}}{n!}\Big) \times \ln\Big(\prod_{i}\Big[P(x_i;\mu,\theta)\Big]\Big) \\ &= \ln(e^{-\alpha}) + n\ln(\alpha) - \ln(n!) + \sum_{i}\ln\Big[P(x_i;\mu,\theta)\Big] \\ &= -\alpha + n\ln(\alpha) - \ln(n!) + \sum_{i}\ln\Big[P(x_i;\mu,\theta)\Big].\end{aligned} \tag{6.5}$$

If one supposes the pdf is binned with an expectation of α_j/α in a bin where $\alpha_j = \mu S + \theta B$ then,

$$\begin{aligned}\ln(\mathcal{L}) &= -\alpha + n\ln(\alpha) - \ln(n!) + \sum_{i}\ln(\frac{\alpha_j}{\alpha}) \\ &= -(S+B) + n\ln(S+B) - \ln(n!) + \sum_{i}\left[\frac{\mu S + \theta B}{S+B}\right]\end{aligned} \tag{6.6}$$

which is the extended maximum likelihood fit. As the histograms are binned, it is natural to think of the binned equivalent of the above probability model. An extended maximum likelihood fit with a binned pdf is a binned maximum likelihood fit. Hence the sum must be taken over all bins i of the input histograms, hence

$$\ln(\mathcal{L}) = \sum_{i}\left[-(S_i+B_i) + n_i\ln(S_i+B_i) - \ln(n_i!) + \left[\frac{\mu S_i + \theta B_i}{S_i+B_i}\right]\right] \tag{6.7}$$

is the binned maximum likelihood function used by `HistFactory`.

More practically, `HistFactory` takes the binned (background subtracted) data, pp, and signal MC histograms describing their respective BDT score distributions, for the same slice in either the $\lambda - q_{\mathrm{T}}^2$ or $|\phi_{\mathrm{CS}}|$ branch of the analysis, and scales the shape of the signal and pp distributions to match the shape of the data distribution. A binned maximum likelihood fit is performed to optimise the parameters μ and θ (henceforth called SPP) to scale the signal and pp distributions to give an estimate of the number of fitted signal and background events in data:

$$\mathrm{Fit} = (\mathrm{SignalMC}) \times \mu + (\mathrm{ppBackground}) \times \mathrm{SPP} \tag{6.8}$$

where μ and SPP are the determined fit parameters, and SignalMC and ppBackground are the input histograms for the signal and pp slice respectively.

The fit returns the estimated number of fitted signal events in data, $F_{sig} = \mu \times N_{\mathrm{sig,i}}$, the number of fitted background events in data $F_{pp} = \mathrm{SPP} \times N_{\mathrm{pp,i}}$, the scaling factor for the signal sample, μ, the scaling factor for the background (pp) sample SPP, and the correlation coefficient, ρ, between μ and SPP.

Define

$$\begin{aligned} N_{\mathrm{sig,i}} &= \text{number of signal events in bin i} \\ N_{\mathrm{pp,i}} &= \text{number of pp events in bin i} \\ N_{\mathrm{data,i}} &= \text{number of data events in bin i} \end{aligned} \tag{6.9}$$

Then the fit will optimise the parameters μ and SPP such that the superposition

$$N_{\mathrm{fit},i} = \mu \times N_{\mathrm{sig,i}} + \mathrm{SPP} \times N_{\mathrm{pp,i}} \tag{6.10}$$

in each bin i is as close as possible to the measured value in that bin, $N_{\mathrm{data,i}}$.

Since the binned maximum likelihood fit does not provide a clear measure of the quality of the fit, at the end of the fit two different measures of fit quality were calculated, each based on a different estimate of the fit uncertainty in each bin:

$$\begin{aligned} \chi^2_1 &= \sum_{i=1}^{N} \left(N_{\mathrm{data,i}} - N_{\mathrm{fit,i}}\right)^2 / N^2_{\mathrm{dataErr,i}} \\ \chi^2_2 &= \sum_{i=1}^{N} \left(N_{\mathrm{data,i}} - N_{\mathrm{fit,i}}\right)^2 / (N^2_{\mathrm{dataErr,i}} + N^2_{\mathrm{fitErr,i,v1}}) \end{aligned} \tag{6.11}$$

where the sum is taken over N bins in the histograms. In version χ^2_1, the only uncertainty taken into account is the statistical error of the data. In version χ^2_2 the statistical uncertainties in data, signal and background are added in quadrature.

The formulae used to calculate the uncertainties are given below:

$$\begin{aligned} N^2_{\mathrm{dataErr,i}} &= N_{\mathrm{data,i}} \\ N^2_{\mathrm{fitErr,i,v1}} &= \mu^2 \times N^2_{\mathrm{sigErr,i}} + \mathrm{SPP}^2 \times N^2_{\mathrm{ppErr,i}} \end{aligned} \tag{6.12}$$

where an index Err denotes the error on the indexed variable.

6.2 Variations Of The Fitting Procedure

The fit results are sensitive to a number of factors. This encompasses the choice of background sample (V1 or V2), the number of bins in the BDT distributions, and the range of BDT values used in the fit. To not bias the analysis it was decided to perform fits across 8 variants which encompass different bin choices, the BDT scores applied, and the two background samples. To preserve as much signal as possible, the BDT scores of BDT score > -1 or BDT score > -0.5 are applied. The latter BDT score cut addresses some of the over-training seen at the BDT stage, and removes some background events. The number of bins was chosen to minimise distributions with empty bins which can create technical problems for `HistFactory`. In rare cases, following the background and lifetime subtraction procedure, a data bin contained < 0 events, in which case the bin contents were set to zero.

The 8 variations used in the $\lambda - q^2_{\mathrm{T}}$ branch of the analysis are summarised in Table 6.1, while the variations used in the ϕ_{CS} branch are shown in Table 6.2. The 8 different variants can be used to assess the systematical uncertainty on the `HistFactory` procedure.

Histogram Variant Name	**Number of Bins**	**BDT score cut (>)**	**Version**
B10 -1.0 V1	10	-1.0	V1
B16 -1.0 V1	16	-1.0	V1
B10 -1.0 V2	10	-1.0	V2
B12 -1.0 V2	12	-1.0	V2
B10 -0.5 V1	10	-0.5	V1
B16 -0.5 V1	16	-0.5	V1
B10 -0.5 V2	10	-0.5	V2
B12 -0.5 V2	12	-0.5	V2

Table 6.1: Table outlining the 8 different variants for $\lambda - q^2_{\mathrm{T}}$ slices, dependent on number of bins in the input histograms for `HistFactory`, the minimum BDT score of events, and version.

Histogram Variant Name	**Number of Bins**	**BDT score cut (>)**	**Version**
B12 -1.0 V1	12	-1.0	V1
B14 -1.0 V1	14	-1.0	V1
B14 -1.0 V2	14	-1.0	V2
B20 -1.0 V2	20	-1.0	V2
B12 -0.5 V1	12	-0.5	V1
B14 -0.5 V1	14	-0.5	V1
B14 -0.5 V2	14	-0.5	V2
B20 -0.5 V2	20	-0.5	V2

Table 6.2: Table outlining the 8 different variants for $|\phi_{\mathrm{CS}}|$ slices, dependent on number of bins in the input histograms for `HistFactory`, the minimum BDT score of events, and version.

Some results of individual fits are shown below, with others available in Appendix E and their respective plots are in Appendix F. Table 6.3 shows the results of the 8 fit variations for the $\lambda - q_{\mathrm{T}}^2$ bin 36, with the corresponding histograms shown in Figures 6.1 – 6.2.

Histogram Variant Name	N_{sig}	N_{PP}	N_{Data}	F_{Sig}	F_{PP}	μ	SPP	ρ	χ^2_{v1}/d.o.f	χ^2_{v2}/d.o.f
36 B16 -1.0 V1	1767	148	634	399 ± 34	235 ± 36	0.226 ± 0.019	1.587 ± 0.204	-0.68	1.52	0.18
36 B12 -1.0 V2	1767	216	634	332 ± 33	302 ± 38	0.188 ± 0.018	1.399 ± 0.147	-0.69	0.18	0.02
36 B10 -1.0 V1	1767	148	634	367 ± 33	267 ± 37	0.208 ± 0.018	1.804 ± 0.204	-0.67	1.46	0.24
36 B10 -1.0 V2	1767	216	634	338 ± 33	296 ± 37	0.191 ± 0.018	1.370 ± 0.143	0.68	1.21	0.24
36 B16 -0.5 V1	1767	148	634	399 ± 34	235 ± 36	0.226 ± 0.019	1.587 ± 0.204	-0.68	1.52	0.18
36 B12 -0.5 V2	1767	216	634	332 ± 33	302 ± 38	0.188 ± 0.018	1.399 ± 0.147	-0.69	0.18	0.02
36 B10 -0.5 V1	1767	148	634	367 ± 33	267 ± 37	0.208 ± 0.018	1.804 ± 0.204	-0.67	1.46	0.24

Table 6.3: Table of results for the 8 fit variations for slice 36. The number of signal MC events is given by N_{sig}, and similarly for background MC and data by N_{PP} and N_{Data} respectively. The number of fitted signal events in data is given by F_{Sig}, and similarly the number of fitted background events in data is given by F_{PP}. The scaling of the signal MC events is given by μ and the scaling of the background MC event is given by SPP. The correlation between μ and SPP is given by ρ. The two different χ^2 calculations are given by χ^2_{v1}, and χ^2_{v2}, which are divided by the degrees of freedom (d.o.f).

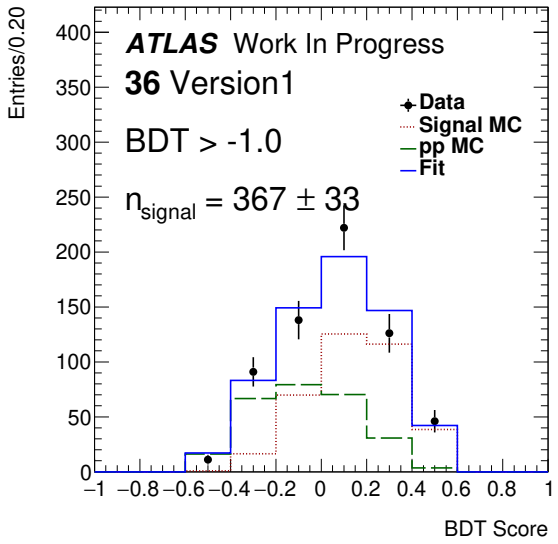

(a) Slice 36 B10 -1.0 V1

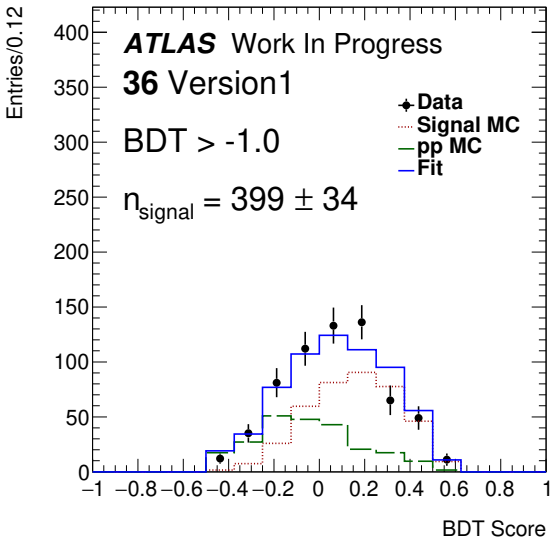

(b) Slice 36 B16 -1.0 V1

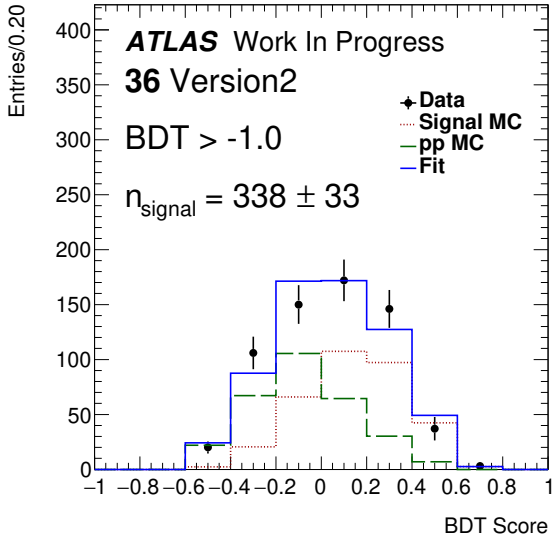

(c) Slice 36 B10 -1.0 V2

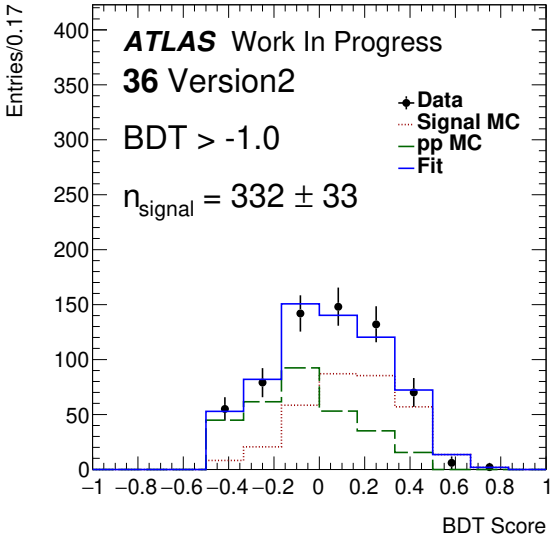

(d) Slice 36 B12 -1.0 V2

Figure 6.1: Plots of the `HistFactory` fits to the data with the pp and signal histograms. Each plot shows the data histogram (black dots), the scaled signal histogram (red dotted line), the scaled pp histogram (green dashed line), and the result of the fit to the data (solid blue line). Every plot shown here is of slice 36 with a BDT scores > -1.0 Figure a) 10 bins and Version 1 type events, b) 16 bins and Version 1 type events, c) 10 bins and Version 2 type events, d) 12 bins and Version 2 type events

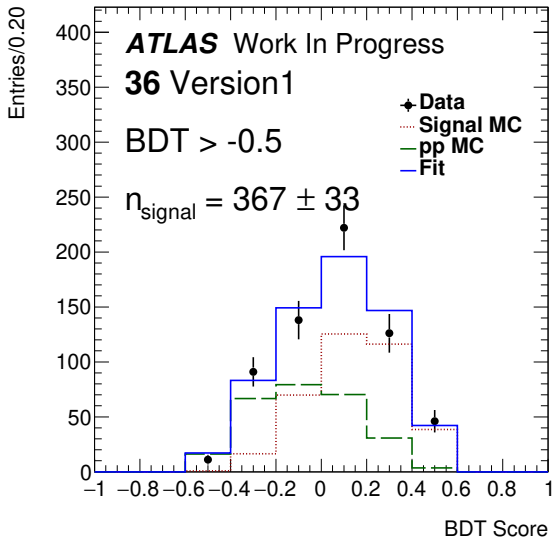

(a) Slice 36 B10 -0.5 V1

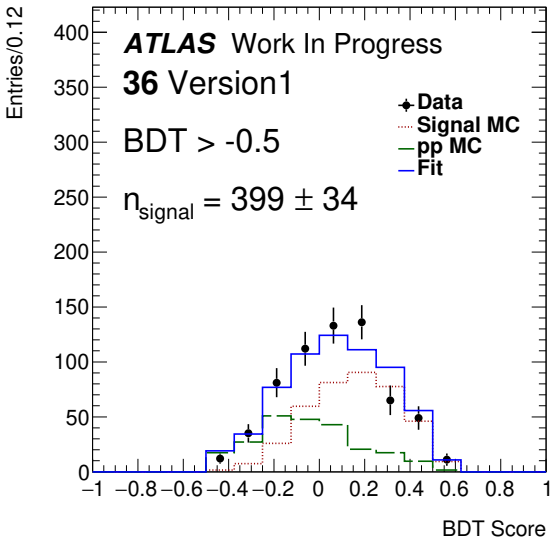

(b) Slice 36 B16 -0.5 V1

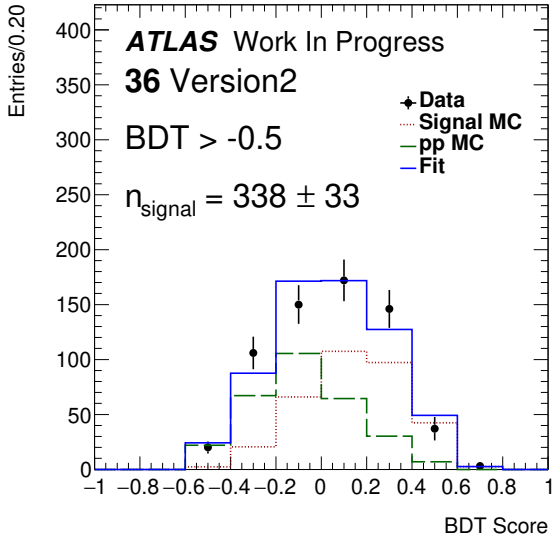

(c) Slice 36 B10 -0.5 V2

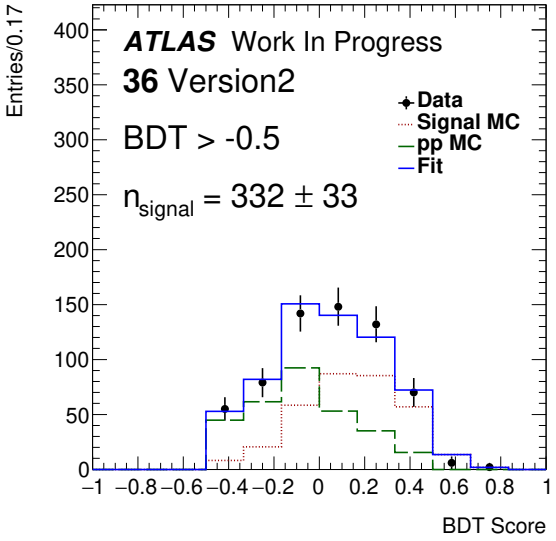

(d) Slice 36 B12 -0.5 V2

Figure 6.2: Plots of the `HistFactory` fits to the data with the pp and signal histograms. Each plot shows the data histogram (black dots), the scaled signal histogram (red dotted line), the scaled pp histogram (green dashed line), and the result of the fit to the data (solid blue line).. Every plot shown here is of slice 36 with a BDT scores > -0.5 Figure a) 10 bins and Version 1 type events, b) 16 bins and Version 1 type events, c) 10 bins and Version 2 type events, d) 12 bins and Version 2 type events

Table 6.4 shows the results of the 8 fit variations for the bin '4 Low' in the ϕ_{CS} branch of the analysis. The corresponding histograms are shown in Figures 6.3 – 6.4.

Histogram Variant Name	N_{sig}	N_{PP}	N_{Data}	F_{Sig}	F_{PP}	μ	SPP	ρ	χ^2_{v1}/d.o.f	χ^2_{v2}/d.o.f
4 B20 Low -1.0 V2	10161	519	2176	721 ± 44	1455 ± 82	0.071 ± 0.004	2.804 ± 0.098	-0.52	3.87	0.77
4 B14 Low -1.0 V1	10161	351	2176	768 ± 43	1408 ± 90	0.076 ± 0.004	4.011 ± 0.141	-0.50	2.91	0.50
4 B14 Low -1.0 V2	10161	519	2176	709 ± 44	1467 ± 82	0.070 ± 0.004	2.826 ± 0.098	-0.52	5.32	1.12
4 B12 Low -1.0 V1	10161	351	2176	783 ± 43	1393 ± 89	0.077 ± 0.004	3.968 ± 0.140	-0.49	3.64	0.69
4 B20 Low -0.5 V2	10092	390	1693	896 ± 51	797 ± 64	0.089 ± 0.005	2.045 ± 0.126	0.66	1.77	0.38
4 B14 Low -0.5 V1	10076	250	1677	909 ± 52	768 ± 69	0.090 ± 0.005	3.073 ± 0.197	-0.67	1.13	0.19
4 B14 Low -0.5 V2	10092	390	1693	882 ± 51	811 ± 64	0.087 ± 0.005	2.079 ± 0.127	0.66	1.92	0.33
4 B12 Low -0.5 V1	10076	250	1677	920 ± 51	757 ± 68	0.091 ± 0.005	3.027 ± 0.195	-0.66	1.44	0.41

Table 6.4: Table of results for the 8 variants for slice 4 Low. The number of signal MC events is given by N_{sig}, and similarly for background MC and data by N_{PP} and N_{Data} respectively. The number of fitted signal events in data is given by F_{Sig}, and similarly the number of fitted background events in data is given by F_{PP}. The scaling of the signal MC events is given by μ and the scaling of the background MC event is given by SPP. The correlation between μ and SPP is given by ρ. The two different χ^2 calculations are given by χ^2_{v1}, and χ^2_{v2}, which are divided by the degrees of freedom (d.o.f).

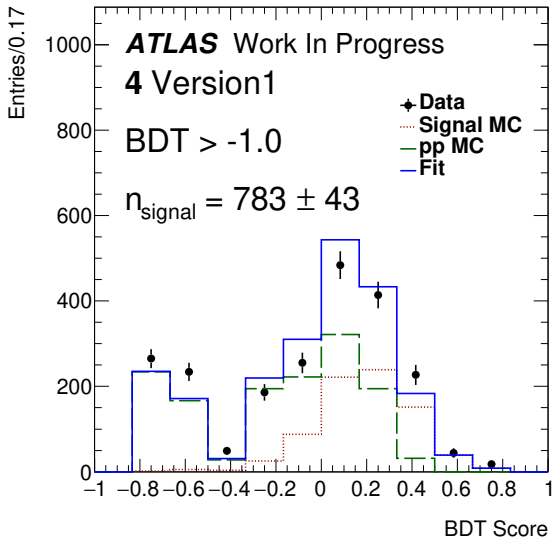

(a) slice 4 B12 -1.0 Low

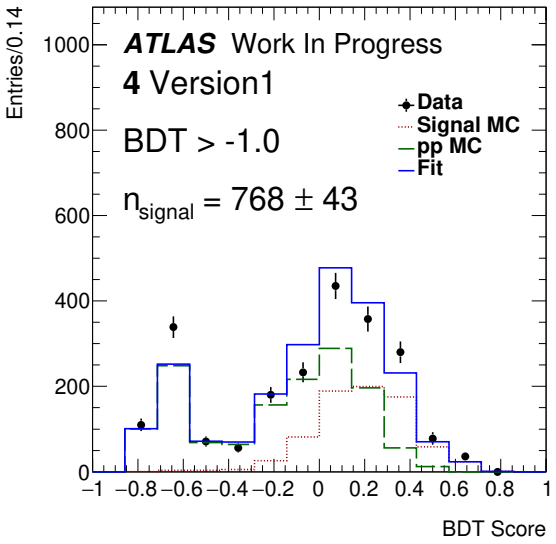

(b) slice 4 B14 -1.0 Low

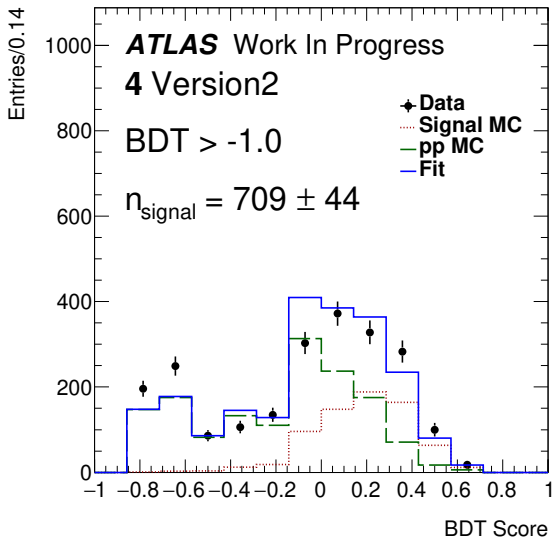

(c) slice 4 B14 -1.0 Low

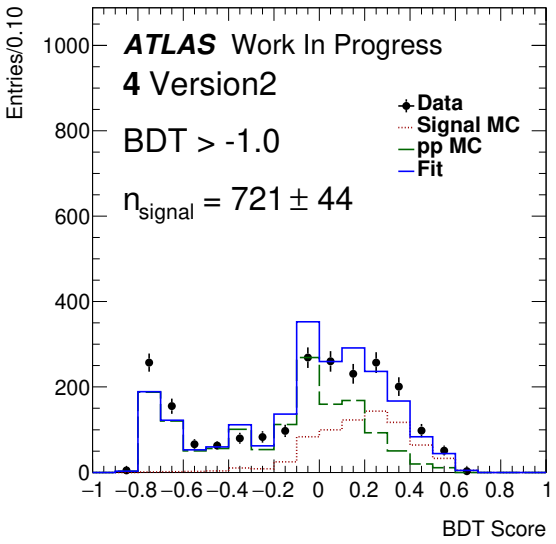

(d) slice 4 B20 -1.0 Low

Figure 6.3: Plots of the `HistFactory` fits to the data with the pp and signal histograms. Each plot shows the data histogram (black dots), the scaled signal histogram (red dotted line), the scaled pp histogram (green dashed line), and the result of the fit to the data (solid blue line). Every plot shown here is of slice 4 across the low range of $\cos^2\theta_{CS}$ with a BDT score > -1.0. Figure a) 12 bins and Version 1 type events, b) 14 bins and Version 1 type events, c) 14 bins and Version 2 type events, and d) 20 bins and Version 2 type events

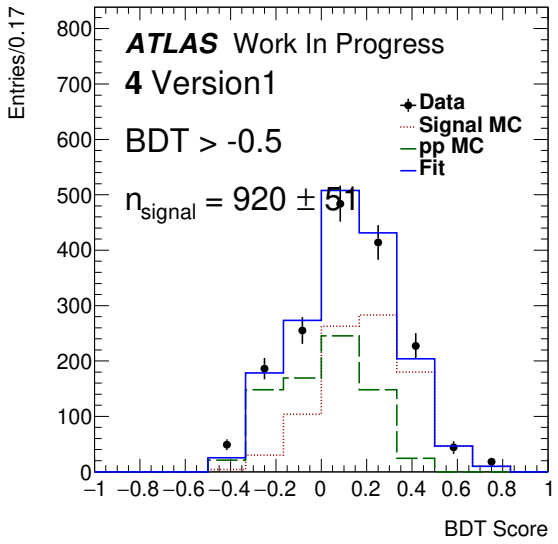

(a) slice 4 B12 -1.0 Low

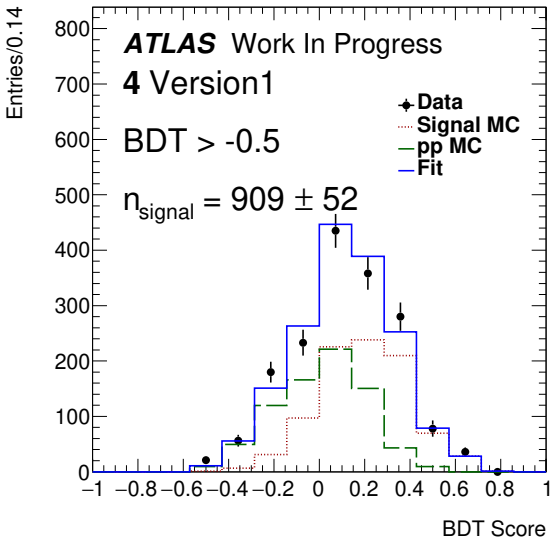

(b) slice 4 B14 -1.0 Low

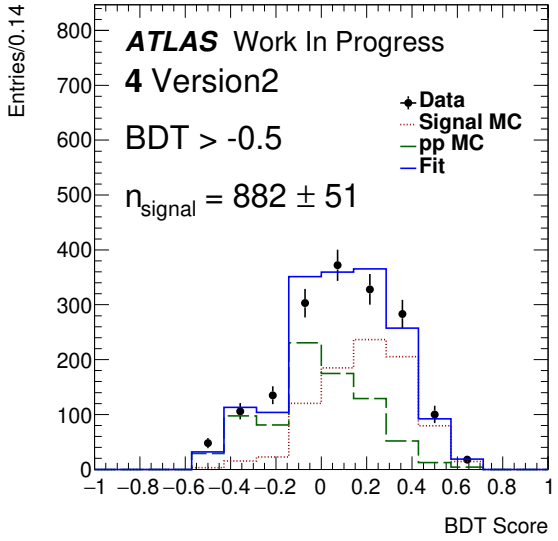

(c) slice 4 B14 -1.0 Low

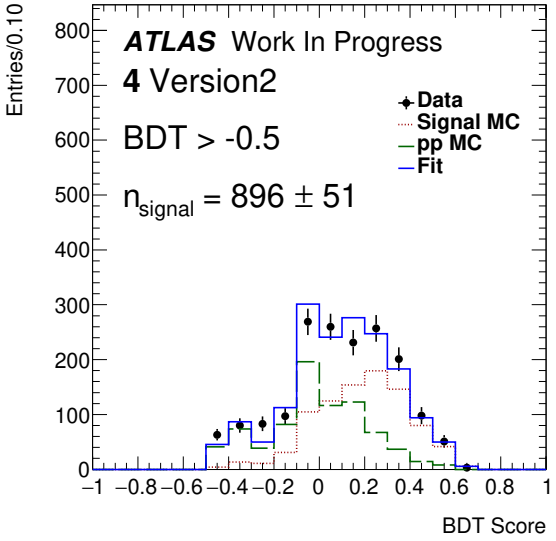

(d) slice 4 B20 -1.0 Low

Figure 6.4: Plots of the `HistFactory` fits to the data with the pp and signal histograms. Each plot shows the data histogram (black dots), the scaled signal histogram (red dotted line), the scaled pp histogram (green dashed line), and the result of the fit to the data (solid blue line). Every plot shown here is of slice 4 across the low range of $\cos^2\theta_{CS}$ with a BDT score > -0.5. Figure a) 12 bins and Version 1 type events, b) 14 bins and Version 1 type events, c) 14 bins and Version 2 type events, and d) 20 bins and Version 2 type events

The reduced χ^2 statistic is given for each of the calculated χ^2 values, seen in Tables 6.3 and 6.4. The reduced χ^2 statistic is the χ^2 divided by the number of degrees of freedom

(d.o.f). d.o.f is the number of bins with content in the fit (blue line) minus the number of fitting parameters (μ and SPP).

Generally a $\chi^2/d.o.f \gg 1$ indicates a poor model fit. A $\chi^2/d.o.f > 1$ indicates that the fit has not fully captured the data. $\chi^2/d.o.f < 1$ indicates that the model is 'over-fitting' the data. A $\chi^2/d.o.f \sim 1$ indicates that the match between observation and data is in accord.

There is no universal definition for calculating χ^2, or the numbers of d.o.f, hence the analysis has two measurements. In Table 6.3, showing results for $\lambda - q_{\mathrm{T}}^2$ region 36 ($25 \leq \lambda < 50$ and $100 \leq q_{\mathrm{T}}^2 < 144$), disregarding the fit produced from the input histograms with 12 bins, $\chi^2_{v1}/d.o.f \gg 1$ and $\chi^2_{v2}/d.o.f \ll 1$ across the 8 variants, which indicate they are not adequate measurements of the fit.

Table 6.4 shows the results of the $|\phi_{\mathrm{CS}}|$ slice 4 low ($\frac{3\pi}{8} \leq |\phi_{\mathrm{CS}}| < \frac{\pi}{2}$). In this slice there are events with BDT>-0.5, so applying a BDT>-0.5 cut affects 4 of the 8 variants. Across the 8 variants $\chi^2_{v1}/d.o.f \gg 1$, which similarly implies this χ^2 is not an adequate measurement of the fit. In the majority of cases χ^2_{v2} is not around 1, so the fit is not in agreement with the data, which is apparent in Figures 6.3 and 6.4.

Chapter 7

Cross Section Determination

The signal yields, F_{sig}, determined in each analysis variant and bin, are used to determine the measured cross section. The yield is divided by the appropriate bin width and by the effective integrated luminosity L, associated with the trigger. The resulting uncorrected cross section is then divided by the selection efficiency, $\epsilon_{\rm sel}$, to give efficiency-corrected distributions.

$$B(J/\psi \to \mu^+\mu^-)\frac{d\sigma_{\rm eff}(pp \to J/\psi + \gamma + X)}{dq_{\rm T}^2} = \frac{N_{\rm sig}}{L \cdot \epsilon_{\rm sel} \cdot \Delta q_{\rm T}^2} \quad (7.1)$$

$$B(J/\psi \to \mu^+\mu^-)\frac{d\sigma_{\rm eff}(pp \to J/\psi + \gamma + X)}{d|\phi_{\rm CS}|} = \frac{N_{\rm sig}}{L \cdot \epsilon_{\rm sel} \cdot (\pi/8)} \quad (7.2)$$

In the $\lambda - q_{\rm T}^2$ branch of the analysis, the analysis bins in $q_{\rm T}^2$ are of variable size, as shown in Table 7.1.

Bin	1	2	3	4	5	6	7	8	9	10
Lower edge, GeV^2	0	4	16	36	64	100	144	196	256	324
Upper edge, GeV^2	4	16	36	64	100	144	196	256	324	400
Bin width $\Delta q_{\rm T}^2$, GeV^2	4	12	20	28	36	44	52	60	68	76

Table 7.1: bin edges and bin widths for the $\lambda - q_{\rm T}^2$ branch of the analysis.

For the $\phi_{\rm CS}$ branch, the full range of $|\phi_{\rm CS}|$ between 0 and π is divided into 8 equally sized bins, each of width $\pi/8$. As for the integrated luminosity L, it was determined by the

standard ATLAS tools to be 2575 pb^{-1} for the trigger, and after the Good Run's List (GRL) application, for data collected in 2015. When the LHC is in operation, data taking is split into luminosity blocks called 'runs'. Sometimes during a run there can be an issue, so the data collected is considered 'bad'. Application of the GRL to a data sample, allows those bad runs to be removed so are not used for later analysis.

7.0.1 Efficiency Determination

Efficiencies were obtained from the signal MC sample, based on truth level distributions, described in Section 4.2.5, and the reconstruction-level distributions, described in Sections 4.2.3 and 4.2.4, determined for each analysis slice. Reconstruction selections followed the same procedure as data, including photon matching, see Section 4.2.3.1, and mass-sideband and long-lifetime-subtraction steps (see Sections 5.2 and 5.3 respectively). The latter steps were for completeness, affecting a small number of events as the signal MC sample contains low dimuon continuum background and non-prompt J/ψs.

The correction factors based on the efficiency defined above are thus designed to correct to the level of the 'fiducial' cross section, where no attempt is made to correct for (truth-level) acceptance cuts on muons and photons:

$$p_T(\mu) > 4\text{GeV}, \qquad |\eta(\mu)| < 2.5 \tag{7.3}$$

$$p_T(\gamma) > 9\text{GeV}, \qquad |\eta(\gamma)| < 2.5 \tag{7.4}$$

The measurement of the fiducial cross section allows to avoid uncertainties related to the spin alignment of the produced J/ψ meson, as well as the complexities of dealing with low energy photon tails. However, this will, regrettably, add a layer of complexity for any attempt to compare the measurement to the theoretical calculations.

The efficiency was determined as the ratio of reconstructed and truth distributions; these are shown in Figures 7.1 – 7.3 for the q_{T}^2 distributions in the three λ slices (with full range in q_{T}^2).

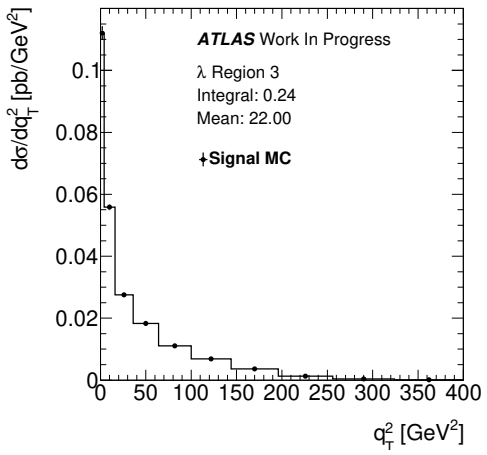

(a) λ slice 30, Reco level

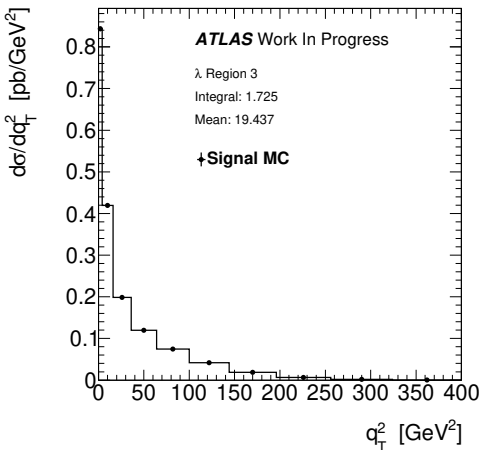

(b) λ slice 30, Truth level

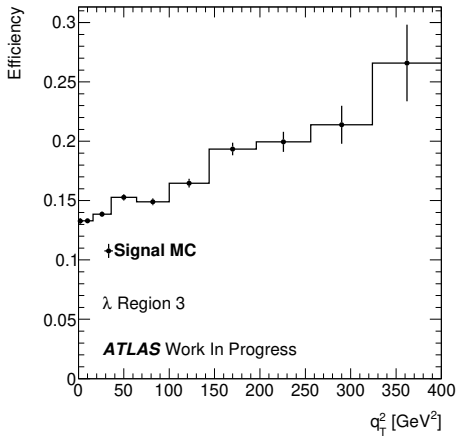

(c) λ slice 30, Efficiency

Figure 7.1: Differential cross sections for $\lambda - q_{\mathrm{T}}^2$ slice 30 ($25 \leq \lambda < 50$ and $0 \leq q_{\mathrm{T}}^2 < 400$ GeV^2), calculated at the reconstruction level (a) and the truth level (b), followed by their ratio (c) which is used as the efficiency of the selection process.

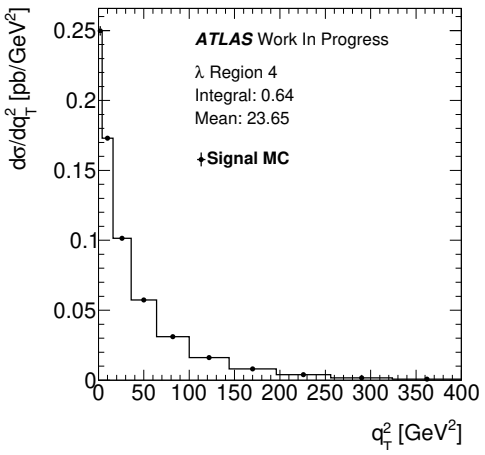

(a) λ slice 40, Reco level

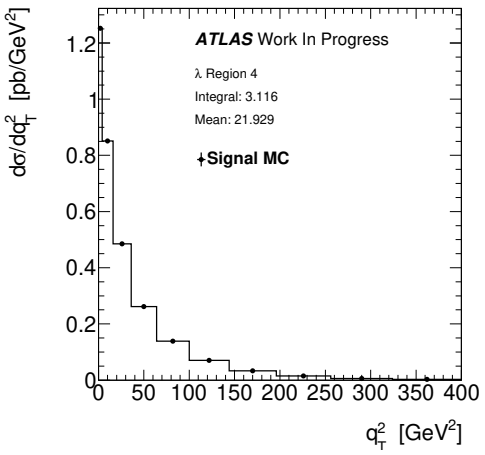

(b) λ slice 40, Truth level

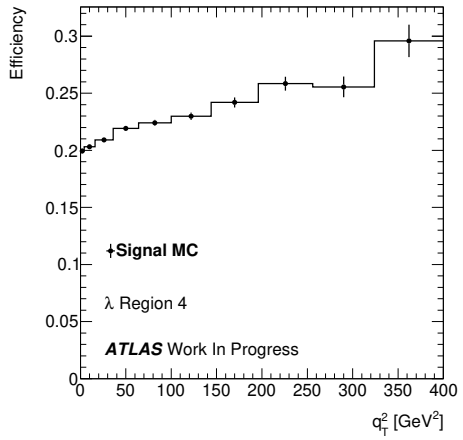

(c) λ slice 40, Efficiency

Figure 7.2: Differential cross sections for $\lambda - q_{\mathrm{T}}^2$ slice 40 ($50 \leq \lambda < 100$ and $0 \leq q_{\mathrm{T}}^2 < 400$ GeV^2), calculated at the reconstruction level (a) and the truth level (b), followed by their ratio (c) which is used as the efficiency of the selection process.

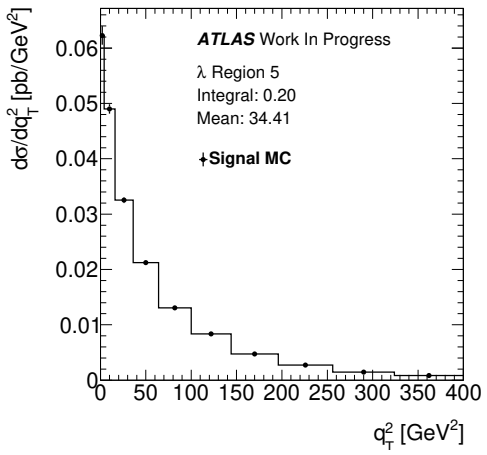

(a) λ slice 50, Reco level

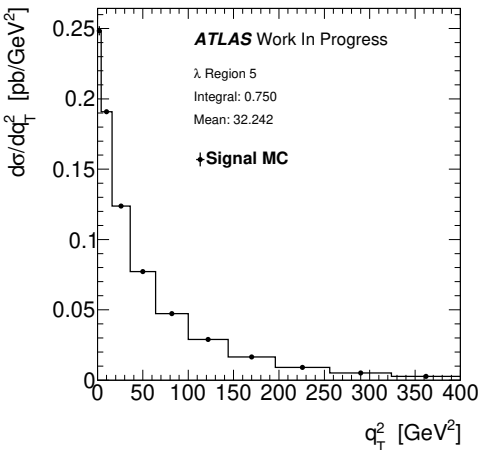

(b) λ slice 50, Truth level

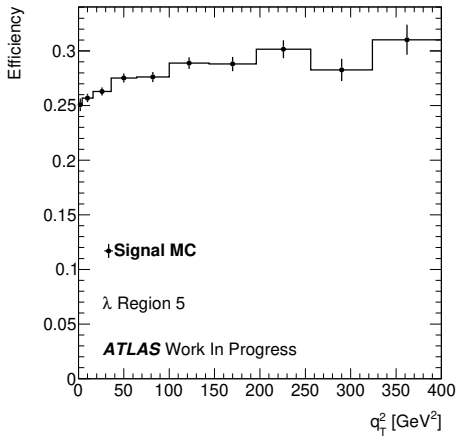

(c) λ slice 50, Efficiency

Figure 7.3: Differential cross sections for $\lambda - q_{\mathrm{T}}^2$ slice 50 ($100 \leq \lambda < 200$ and $0 \leq q_{\mathrm{T}}^2 < 400$ GeV^2), calculated at the reconstruction level (a) and the truth level (b), followed by their ratio (c) which is used as the efficiency of the selection process.

It can be seen that the efficiency varies quite smoothly from about 13% at low q_{T}^2 and low λ to about 30% at high q_{T}^2 and high λ.

A very similar procedure was adopted for efficiency determination in $|\phi_{\mathrm{CS}}|$ branch of the analysis. The corresponding plots are shown in Figures 7.4 and 7.5 for the Low and High $\cos^2\theta_{\mathrm{CS}}$ slices, respectively.

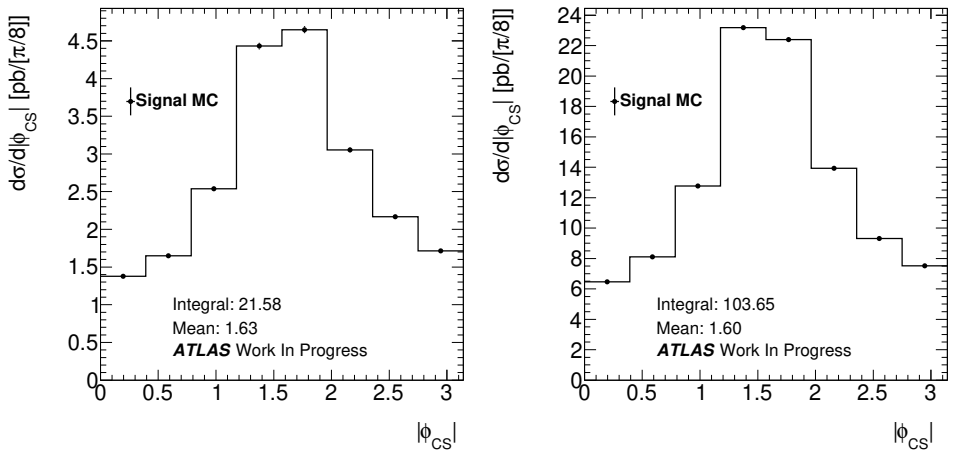

(a) $\cos^2\theta_{\mathrm{CS}}$ Low, Reco level

(b) $\cos^2\theta_{\mathrm{CS}}$ Low, Truth level

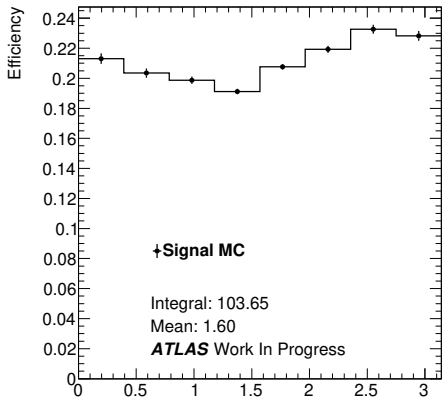

(c) $\cos^2\theta_{\mathrm{CS}}$ Low, Efficiency

Figure 7.4: Differential cross sections for the Low $\cos^2\theta_{\mathrm{CS}}$ slice, calculated at the reconstruction level (a) and the truth level (b), followed by their ratio (c) which is used as the efficiency of our selection process.

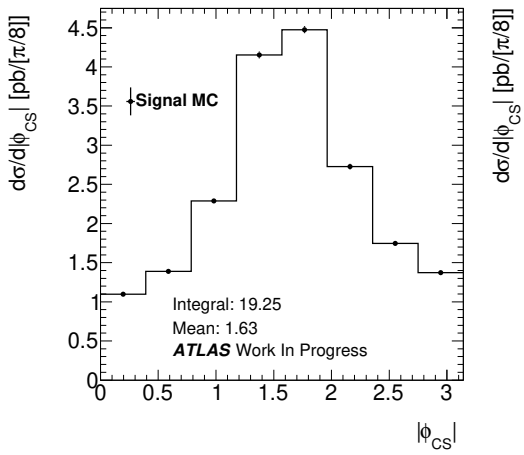

(a) $\cos^2\theta_{\mathrm{CS}}$ High, Reco level

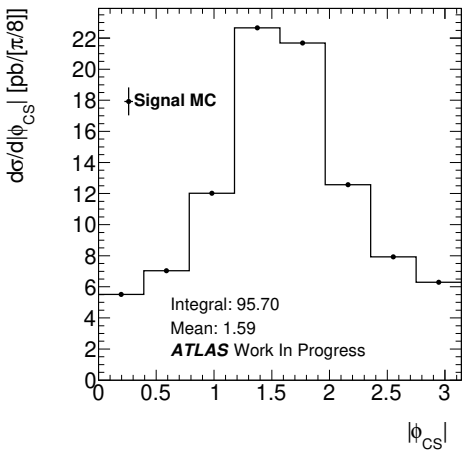

(b) $\cos^2\theta_{\mathrm{CS}}$ High, Truth level

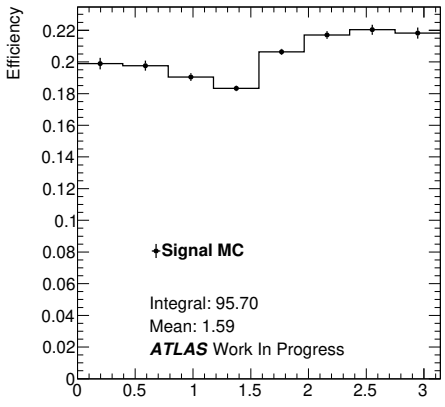

(c) $\cos^2\theta_{\mathrm{CS}}$ High, Efficiency

Figure 7.5: Differential cross sections for the High $\cos^2\theta_{\mathrm{CS}}$ slice, calculated at the reconstruction level (a) and the truth level (b), followed by their ratio (c) which is used as the efficiency of the selection process.

The efficiency is fairly uniform, with no dramatic angular dependence in the Collins-Soper frame. In both $\cos^2\theta_{\mathrm{CS}}$ slices, the efficiency distributions are similar, implying the absence of any strong efficiency corrections to the Low-to-High ratio in $|\phi_{\mathrm{CS}}|$.

This simplified approach to efficiency determination is sufficient due to the low level of statistics available. Several corrections are incorporated during systematic studies, such as scale factor corrections related to the trigger, and muon and photon reconstruction efficiency determinations, which appear to be modest. The details are presented in Chapter 8, which covers the various systematic studies which were performed as part of this analysis.

The error bars on the efficiency plots are due to MC statistics. These will also be taken into account at the stage of systematic studies.

7.0.2 Differential Cross Sections

The results of the calculations using Eqn. 7.1 for the slice 30 ($25 \leq \lambda < 50$ and $0 \leq q^2_{\mathrm{T}} < 400$ GeV^2) of the $\lambda - q^2_{\mathrm{T}}$ branch of the analysis are shown in Table 7.2. Tables 7.3 and 7.4 show the same for λ slices 40 ($50 \leq \lambda < 100$ and $0 \leq q^2_{\mathrm{T}} < 400$ GeV^2) and 50 ($100 \leq \lambda < 200$ and $0 \leq q^2_{\mathrm{T}} < 400$ GeV^2), respectively. Each table is built from taking the differential distributions across the 8 variants and dividing by the appropriate efficiency distribution. The results for each bin in $\lambda - q^2_{\mathrm{T}}$ or $|\phi_{\mathrm{CS}}|$ are given, where each row represents the kinematical region for that bin. The final column in each table details the average (Avg) signal yield across the 8 variants for that bin. The maximum statistical error (max.stat) is the largest statistical error amongst the 8 variants. The BDT systematic error (BDT.syst) is assessed to be the average of the difference between the largest and smallest signal yields amongst the 8 variants.

Bin	q^2_{T} region (GeV^2)	B10 -1.0 V1 (pb/GeV^2)	B16 -1.0 V1 (pb/GeV^2)	B10 -1.0 V2 (pb/GeV^2)	B12 -1.0 V2 (pb/GeV^2)	B10 -0.5 V1 (pb/GeV^2)	B16 -0.5 V1 (pb/GeV^2)	B10 -0.5 V2 (pb/GeV^2)	B12 -0.5 V2 (pb/GeV^2)	Avg±max.stat±BDT.syst (pb/GeV^2)
1	$0 \leq q^2_{\mathrm{T}} < 4$	0.1666 ± 0.0126	0.1732 ± 0.0125	0.1757 ± 0.0138	0.1769 ± 0.0123	0.1666 ± 0.0126	0.1732 ± 0.0125	0.1757 ± 0.0138	0.1769 ± 0.0123	0.1731 ± 0.0138 ± 0.0051
2	$4 \leq q^2_{\mathrm{T}} < 16$	0.1060 ± 0.0056	0.1060 ± 0.0056	0.1041 ± 0.0067	0.1021 ± 0.0065	0.1060 ± 0.0056	0.1060 ± 0.0056	0.1041 ± 0.0067	0.1021 ± 0.0065	0.1046 ± 0.0067 ± 0.0020
3	$16 \leq q^2_{\mathrm{T}} < 36$	0.0529 ± 0.0030	0.0530 ± 0.0030	0.0454 ± 0.0041	0.0466 ± 0.0040	0.0529 ± 0.0030	0.0530 ± 0.0030	0.0454 ± 0.0041	0.0466 ± 0.0040	0.0495 ± 0.0041 ± 0.0038
4	$36 \leq q^2_{\mathrm{T}} < 64$	0.0341 ± 0.0025	0.0339 ± 0.0025	0.0332 ± 0.0026	0.0334 ± 0.0025	0.0341 ± 0.0025	0.0339 ± 0.0025	0.0332 ± 0.0026	0.0334 ± 0.0025	0.0336 ± 0.0026 ± 0.0004
5	$64 \leq q^2_{\mathrm{T}} < 100$	0.0322 ± 0.0022	0.0328 ± 0.0022	0.0317 ± 0.0023	0.0314 ± 0.0023	0.0322 ± 0.0022	0.0328 ± 0.0022	0.0317 ± 0.0023	0.0314 ± 0.0023	0.0320 ± 0.0023 ± 0.0007
6	$100 \leq q^2_{\mathrm{T}} < 144$	0.0197 ± 0.0018	0.0214 ± 0.0019	0.0181 ± 0.0018	0.0178 ± 0.0018	0.0197 ± 0.0018	0.0214 ± 0.0019	0.0181 ± 0.0018	0.0178 ± 0.0018	0.0192 ± 0.0019 ± 0.0018
7	$144 \leq q^2_{\mathrm{T}} < 196$	0.0163 ± 0.0014	0.0161 ± 0.0014	0.0139 ± 0.0014	0.0140 ± 0.0014	0.0163 ± 0.0014	0.0161 ± 0.0014	0.0135 ± 0.0014	0.0136 ± 0.0014	0.0150 ± 0.0014 ± 0.0014
8	$196 \leq q^2_{\mathrm{T}} < 256$	0.0072 ± 0.0009	0.0075 ± 0.0009	0.0072 ± 0.0009	0.0078 ± 0.0009	0.0073 ± 0.0009	0.0075 ± 0.0009	0.0072 ± 0.0009	0.0078 ± 0.0009	0.0074 ± 0.0009 ± 0.0003
9	$256 \leq q^2_{\mathrm{T}} < 324$	0.0021 ± 0.0005	0.0022 ± 0.0004	0.0023 ± 0.0005	0.0029 ± 0.0005	0.0021 ± 0.0005	0.0021 ± 0.0005	0.0018 ± 0.0004	0.0025 ± 0.0005	0.0023 ± 0.0005 ± 0.0005
10	$324 \leq q^2_{\mathrm{T}} < 400$	0.0014 ± 0.0004	0.0016 ± 0.0004	0.0010 ± 0.0003	0.0014 ± 0.0004	0.0014 ± 0.0004	0.0015 ± 0.0004	0.0009 ± 0.0003	0.0014 ± 0.0004	0.0013 ± 0.0004 ± 0.0003

Table 7.2: Table of results for the calculation of the average, statistical and systematic errors across the 8 BDT variations, for the efficiency-corrected q^2_{T}-differential cross section in $\lambda - q^2_{\mathrm{T}}$ slice 30 ($25 \leq \lambda < 50$ and $0 \leq q^2_{\mathrm{T}} < 400$ GeV^2).

Bin	q_T^2 region (GeV^2)	B10 -1.0 V1 (pb/GeV^2)	B16 -1.0 V1 (pb/GeV^2)	B10 -1.0 V2 (pb/GeV^2)	B12 -1.0 V2 (pb/GeV^2)	B10 -0.5 V1 (pb/GeV^2)	B16 -0.5 V1 (pb/GeV^2)	B10 -0.5 V2 (pb/GeV^2)	B12 -0.5 V2 (pb/GeV^2)	Avg±max.stat±BDT.syst (pb/GeV^2)
1	$0 \leq q_T^2 < 4$	0.2403 ± 0.0181	0.2429 ± 0.0178	0.2647 ± 0.0182	0.2699 ± 0.0180	0.2403 ± 0.0181	0.2429 ± 0.0178	0.2647 ± 0.0182	0.2699 ± 0.0180	0.2545 ± 0.0182 ± 0.0148
2	$4 \leq q_T^2 < 16$	0.2110 ± 0.0095	0.2086 ± 0.0092	0.1722 ± 0.0096	0.1775 ± 0.0096	0.2110 ± 0.0095	0.2086 ± 0.0092	0.1722 ± 0.0096	0.1775 ± 0.0096	0.1923 ± 0.0096 ± 0.0194
3	$16 \leq q_T^2 < 36$	0.1473 ± 0.0075	0.1421 ± 0.0073	0.1329 ± 0.0075	0.1311 ± 0.0074	0.1473 ± 0.0075	0.1421 ± 0.0073	0.1329 ± 0.0075	0.1311 ± 0.0074	0.1384 ± 0.0075 ± 0.0081
4	$36 \leq q_T^2 < 64$	0.0725 ± 0.0044	0.0759 ± 0.0043	0.0708 ± 0.0046	0.0727 ± 0.0045	0.0725 ± 0.0044	0.0759 ± 0.0043	0.0708 ± 0.0046	0.0727 ± 0.0045	0.0730 ± 0.0046 ± 0.0025
5	$64 \leq q_T^2 < 100$	0.0430 ± 0.0026	0.0453 ± 0.0026	0.0430 ± 0.0027	0.0435 ± 0.0027	0.0430 ± 0.0026	0.0453 ± 0.0026	0.0430 ± 0.0027	0.0435 ± 0.0027	0.0437 ± 0.0027 ± 0.0012
6	$100 \leq q_T^2 < 144$	0.0285 ± 0.0019	0.0293 ± 0.0019	0.0280 ± 0.0019	0.0266 ± 0.0019	0.0285 ± 0.0019	0.0293 ± 0.0019	0.0278 ± 0.0019	0.0264 ± 0.0019	0.0281 ± 0.0019 ± 0.0015
7	$144 \leq q_T^2 < 196$	0.0173 ± 0.0012	0.0181 ± 0.0012	0.0169 ± 0.0012	0.0164 ± 0.0012	0.0173 ± 0.0012	0.0181 ± 0.0012	0.0177 ± 0.0012	0.0172 ± 0.0012	0.0174 ± 0.0012 ± 0.0008
8	$196 \leq q_T^2 < 256$	0.0097 ± 0.0008	0.0100 ± 0.0008	0.0096 ± 0.0008	0.0098 ± 0.0008	0.0099 ± 0.0008	0.0102 ± 0.0008	0.0095 ± 0.0008	0.0097 ± 0.0008	0.0098 ± 0.0008 ± 0.0004
9	$256 \leq q_T^2 < 324$	0.0057 ± 0.0006	0.0059 ± 0.0006	0.0066 ± 0.0006	0.0065 ± 0.0006	0.0053 ± 0.0006	0.0057 ± 0.0006	0.0064 ± 0.0006	0.0063 ± 0.0006	0.0060 ± 0.0006 ± 0.0006
10	$324 \leq q_T^2 < 400$	0.0033 ± 0.0004	0.0033 ± 0.0004	0.0036 ± 0.0004	0.0036 ± 0.0004	0.0031 ± 0.0004	0.0032 ± 0.0004	0.0032 ± 0.0005	0.0033 ± 0.0004	0.0033 ± 0.0005 ± 0.0002

Table 7.3: Table of results for the calculation of the average, statistical and systematic errors across the 8 BDT variations, for the efficiency-corrected q_T^2-differential cross section in $\lambda - q_T^2$ slice 40 ($50 \leq \lambda < 100$ and $0 \leq q_T^2 < 400$ GeV^2).

Bin	q_T^2 region (GeV^2)	B10 -1.0 V1 (pb/GeV^2)	B16 -1.0 V1 (pb/GeV^2)	B10 -1.0 V2 (pb/GeV^2)	B12 -1.0 V2 (pb/GeV^2)	B10 -0.5 V1 (pb/GeV^2)	B16 -0.5 V1 (pb/GeV^2)	B10 -0.5 V2 (pb/GeV^2)	B12 -0.5 V2 (pb/GeV^2)	Avg±max.stat±BDT.syst (pb/GeV^2)
1	$0 \leq q_T^2 < 4$	0.0909 ± 0.0087	0.1131 ± 0.0093	0.1054 ± 0.0091	0.1091 ± 0.0091	0.0909 ± 0.0087	0.1131 ± 0.0093	0.1054 ± 0.0091	0.1091 ± 0.0091	0.1046 ± 0.0093 ± 0.0111
2	$4 \leq q_T^2 < 16$	0.0585 ± 0.0046	0.0619 ± 0.0045	0.0640 ± 0.0046	0.0626 ± 0.0045	0.0585 ± 0.0046	0.0619 ± 0.0045	0.0640 ± 0.0046	0.0626 ± 0.0045	0.0618 ± 0.0046 ± 0.0027
3	$16 \leq q_T^2 < 36$	0.0513 ± 0.0030	0.0524 ± 0.0030	0.0473 ± 0.0029	0.0485 ± 0.0029	0.0513 ± 0.0030	0.0524 ± 0.0030	0.0473 ± 0.0029	0.0485 ± 0.0029	0.0499 ± 0.0030 ± 0.0025
4	$36 \leq q_T^2 < 64$	0.0409 ± 0.0021	0.0416 ± 0.0021	0.0402 ± 0.0022	0.0393 ± 0.0021	0.0409 ± 0.0021	0.0416 ± 0.0021	0.0402 ± 0.0022	0.0393 ± 0.0021	0.0405 ± 0.0022 ± 0.0011
5	$64 \leq q_T^2 < 100$	0.0280 ± 0.0018	0.0297 ± 0.0018	0.0269 ± 0.0017	0.0270 ± 0.0017	0.0280 ± 0.0018	0.0297 ± 0.0018	0.0269 ± 0.0017	0.0270 ± 0.0017	0.0279 ± 0.0018 ± 0.0014
6	$100 \leq q_T^2 < 144$	0.0168 ± 0.0012	0.0159 ± 0.0011	0.0143 ± 0.0011	0.0140 ± 0.0011	0.0168 ± 0.0012	0.0159 ± 0.0011	0.0143 ± 0.0011	0.0140 ± 0.0011	0.0152 ± 0.0012 ± 0.0014
7	$144 \leq q_T^2 < 196$	0.0139 ± 0.0009	0.0137 ± 0.0009	0.0123 ± 0.0009	0.0124 ± 0.0009	0.0139 ± 0.0009	0.0137 ± 0.0009	0.0123 ± 0.0009	0.0124 ± 0.0009	0.0131 ± 0.0009 ± 0.0008
8	$196 \leq q_T^2 < 256$	0.0104 ± 0.0007	0.0106 ± 0.0007	0.0111 ± 0.0007	0.0112 ± 0.0007	0.0102 ± 0.0007	0.0104 ± 0.0007	0.0108 ± 0.0007	0.0109 ± 0.0007	0.0107 ± 0.0007 ± 0.0005
9	$256 \leq q_T^2 < 324$	0.0080 ± 0.0006	0.0080 ± 0.0006	0.0077 ± 0.0006	0.0077 ± 0.0006	0.0078 ± 0.0006	0.0078 ± 0.0006	0.0072 ± 0.0006	0.0073 ± 0.0006	0.0077 ± 0.0006 ± 0.0004
10	$324 \leq q_T^2 < 400$	0.0041 ± 0.0004	0.0044 ± 0.0005	0.0042 ± 0.0004	0.0042 ± 0.0004	0.0041 ± 0.0005	0.0045 ± 0.0005	0.0040 ± 0.0005	0.0040 ± 0.0005	0.0042 ± 0.0005 ± 0.0002

Table 7.4: Table of results for the calculation of the average, statistical and systematic errors across the 8 BDT variations, for the efficiency-corrected q_T^2-differential cross section in $\lambda - q_T^2$ slice 50 ($100 \leq \lambda < 200$ and $0 \leq q_T^2 < 400$ GeV^2).

Matching results for the ϕ_{CS}-differential cross sections in Low $\cos^2\theta_{CS}$ and High $\cos^2\theta_{CS}$ slices, calculated using Eqn. 7.2, are shown in Tables 7.5 and 7.6.

Bin	$\lvert\phi_{CS}\rvert$ bin (rad)	B14 -1.0 V1 (pb/rad)	B12 -1.0 V1 (pb/rad)	B14 -1.0 V2 (pb/rad)	B20 -1.0 V2 (pb/rad)	B14 -0.5 V1 (pb/rad)	B12 -0.5 V1 (pb/rad)	B14 -0.5 V2 (pb/rad)	B20 -0.8 V2 (pb/rad)	Avg±max.stat±BDT.syst (pb/rad)
1	$0 \leq \lvert\phi_{CS}\rvert < \frac{\pi}{8}$	1.8381 ± 0.1101	1.8174 ± 0.1122	1.7253 ± 0.1183	1.7546 ± 0.1134	1.8381 ± 0.1101	1.8174 ± 0.1122	1.7253 ± 0.1183	1.7546 ± 0.1134	1.7839 ± 0.1183 ± 0.0564
2	$\frac{\pi}{8} \leq \lvert\phi_{CS}\rvert < \frac{\pi}{4}$	2.3480 ± 0.1187	2.3383 ± 0.1184	2.2822 ± 0.1422	2.3042 ± 0.1174	2.3480 ± 0.1187	2.3383 ± 0.1184	2.2822 ± 0.1422	2.3042 ± 0.1174	2.3182 ± 0.1422 ± 0.0329
3	$\frac{\pi}{4} \leq \lvert\phi_{CS}\rvert < \frac{3\pi}{8}$	3.2696 ± 0.1756	3.2553 ± 0.1764	2.8327 ± 0.1817	2.9156 ± 0.1801	3.2696 ± 0.1756	3.2553 ± 0.1764	2.8573 ± 0.1835	2.9416 ± 0.1820	3.0746 ± 0.1835 ± 0.2184
4	$\frac{3\pi}{8} \leq \lvert\phi_{CS}\rvert < \frac{\pi}{2}$	3.9704 ± 0.2266	4.0504 ± 0.2260	3.6684 ± 0.2281	3.7280 ± 0.2282	4.7407 ± 0.2726	4.7995 ± 0.2709	4.5947 ± 0.2690	4.6643 ± 0.2692	4.2771 ± 0.2726 ± 0.5656
5	$\frac{\pi}{2} \leq \lvert\phi_{CS}\rvert < \frac{5\pi}{8}$	3.4794 ± 0.2222	3.4277 ± 0.2224	3.3014 ± 0.2168	3.3384 ± 0.2147	4.1027 ± 0.2456	4.0505 ± 0.2470	3.8423 ± 0.2450	3.8608 ± 0.2412	3.6754 ± 0.2470 ± 0.4006
6	$\frac{5\pi}{8} \leq \lvert\phi_{CS}\rvert < \frac{3\pi}{4}$	4.2976 ± 0.2158	4.1734 ± 0.2108	4.0071 ± 0.2229	4.0786 ± 0.2232	4.2976 ± 0.2158	4.1734 ± 0.2108	4.0071 ± 0.2229	4.0786 ± 0.2232	4.1392 ± 0.2232 ± 0.1452
7	$\frac{3\pi}{4} \leq \lvert\phi_{CS}\rvert < \frac{7\pi}{8}$	2.8935 ± 0.1597	2.9424 ± 0.1588	2.3065 ± 0.1688	2.3647 ± 0.1718	2.8935 ± 0.1597	2.9424 ± 0.1588	2.3065 ± 0.1688	2.3647 ± 0.1718	2.6268 ± 0.1718 ± 0.3179
8	$\frac{7\pi}{8} \leq \lvert\phi_{CS}\rvert < \pi$	3.9848 ± 0.1967	4.0642 ± 0.1983	3.9836 ± 0.2030	4.0913 ± 0.2027	3.9848 ± 0.1967	4.0642 ± 0.1983	3.9836 ± 0.2030	4.0913 ± 0.2027	4.0310 ± 0.2030 ± 0.0538

Table 7.5: Table of results for the calculation of the average, statistical and systematic errors across the 8 BDT variations, for the efficiency-corrected ϕ_{CS}-differential cross section Low $\cos^2\theta_{CS}$ slice.

Bin	$\lvert\phi_{CS}\rvert$ bin (rad)	B14 -1.0 V1 (pb/rad)	B12 -1.0 V1 (pb/rad)	B14 -1.0 V2 (pb/rad)	B20 -1.0 V2 (pb/rad)	B14 -0.5 V1 (pb/rad)	B12 -0.5 V1 (pb/rad)	B14 -0.5 V2 (pb/rad)	B20 -0.8 V2 (pb/rad)	Avg±max.stat±BDT.syst (pb/rad)
1	$0 \leq \lvert\phi_{CS}\rvert < \frac{\pi}{8}$	2.4346 ± 0.1458	2.3749 ± 0.1460	2.3919 ± 0.1484	2.4499 ± 0.1498	2.4864 ± 0.1480	2.4262 ± 0.1488	2.4643 ± 0.1537	2.5316 ± 0.1556	2.4450 ± 0.1556 ± 0.0784
2	$\frac{\pi}{8} \leq \lvert\phi_{CS}\rvert < \frac{\pi}{4}$	2.0293 ± 0.1775	1.9124 ± 0.1779	2.1480 ± 0.1704	2.1074 ± 0.1699	2.0293 ± 0.1775	1.9124 ± 0.1779	2.2313 ± 0.1750	2.1842 ± 0.1737	2.0693 ± 0.1779 ± 0.1594
3	$\frac{\pi}{4} \leq \lvert\phi_{CS}\rvert < \frac{3\pi}{8}$	3.4801 ± 0.2090	3.4290 ± 0.2113	3.1540 ± 0.2151	3.0807 ± 0.2139	3.3793 ± 0.2157	3.3104 ± 0.2186	3.0213 ± 0.2296	2.9285 ± 0.2274	3.2229 ± 0.2296 ± 0.2758
4	$\frac{3\pi}{8} \leq \lvert\phi_{CS}\rvert < \frac{\pi}{2}$	5.5366 ± 0.2903	5.4677 ± 0.2889	5.0245 ± 0.2923	5.1251 ± 0.2907	5.2640 ± 0.3173	5.1789 ± 0.3149	4.1893 ± 0.3181	4.3693 ± 0.3147	5.0194 ± 0.3181 ± 0.6737
5	$\frac{\pi}{2} \leq \lvert\phi_{CS}\rvert < \frac{5\pi}{8}$	5.7923 ± 0.2969	5.3986 ± 0.2991	5.2730 ± 0.3016	5.4491 ± 0.2977	5.2304 ± 0.3246	4.6175 ± 0.3303	4.5288 ± 0.3375	4.8246 ± 0.3293	5.1393 ± 0.3375 ± 0.6318
6	$\frac{5\pi}{8} \leq \lvert\phi_{CS}\rvert < \frac{3\pi}{4}$	4.4474 ± 0.2458	4.1026 ± 0.2491	4.3410 ± 0.2457	4.3213 ± 0.2493	4.8734 ± 0.2620	4.5131 ± 0.2640	4.7421 ± 0.2630	4.7347 ± 0.2664	4.5094 ± 0.2664 ± 0.3854
7	$\frac{3\pi}{4} \leq \lvert\phi_{CS}\rvert < \frac{7\pi}{8}$	4.0088 ± 0.2255	4.0522 ± 0.2271	3.6494 ± 0.2269	3.7825 ± 0.2265	4.0088 ± 0.2255	4.0522 ± 0.2271	3.6562 ± 0.2271	3.7825 ± 0.2265	3.8741 ± 0.2271 ± 0.2014
8	$\frac{7\pi}{8} \leq \lvert\phi_{CS}\rvert < \pi$	4.0099 ± 0.2690	3.8144 ± 0.2769	3.9115 ± 0.2708	4.0574 ± 0.2655	4.0099 ± 0.2690	3.8144 ± 0.2769	3.9115 ± 0.2708	4.0574 ± 0.2655	3.9483 ± 0.2769 ± 0.1215

Table 7.6: Table of results for the calculation of the average, statistical and systematic errors across the 8 BDT variations, for the efficiency-corrected ϕ_{CS}-differential cross section High $\cos^2\theta_{CS}$ slice.

Figures 7.6, 7.7 and 7.8 show the efficiency-corrected differential cross sections in the three λ slices as a function of q_{T}^2, illustrating the results summarised in Tables 7.2 – 7.4. Efficiency-corrected differential cross section distributions in ϕ_{CS} for the two slices of $\cos^2\theta_{\mathrm{CS}}$ are presented in Figures 7.9 and 7.10, based on results in Tables 7.5 and 7.6.

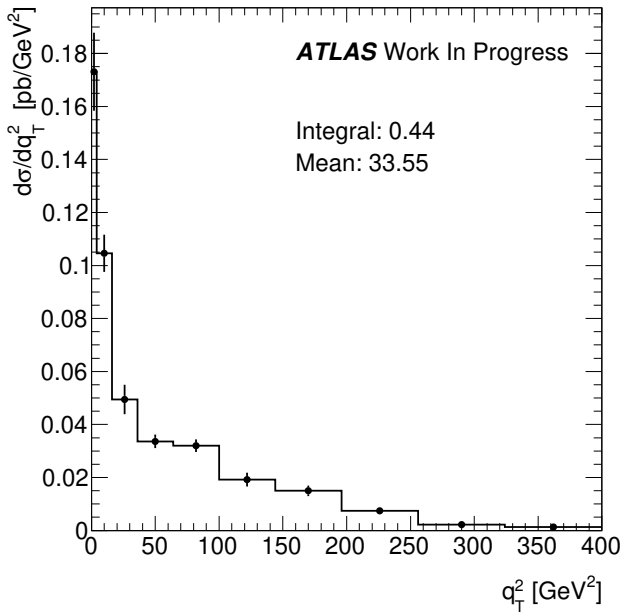

Figure 7.6: Efficiency-corrected differential cross section with respect to q_{T}^2 for $\lambda - q_{\mathrm{T}}^2$ slice 30 ($25 \leq \lambda < 50$ and $0 \leq q_{\mathrm{T}}^2 < 400$ GeV^2). Statistical and BDT-systematic errors are added in quadrature.

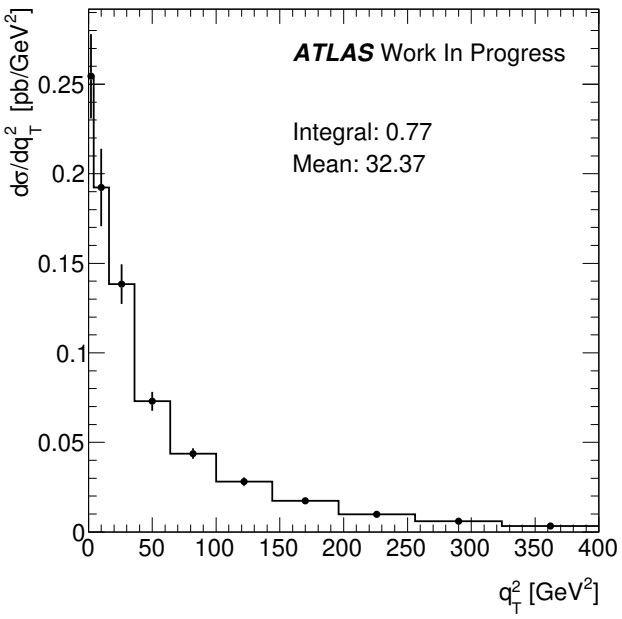

Figure 7.7: Efficiency-corrected differential cross section with respect to q_{T}^2 for $\lambda - q_{\mathrm{T}}^2$ slice 40 ($50 \leq \lambda < 100$ and $0 \leq q_{\mathrm{T}}^2 < 400$ GeV^2). Statistical and BDT-systematic errors are added in quadrature.

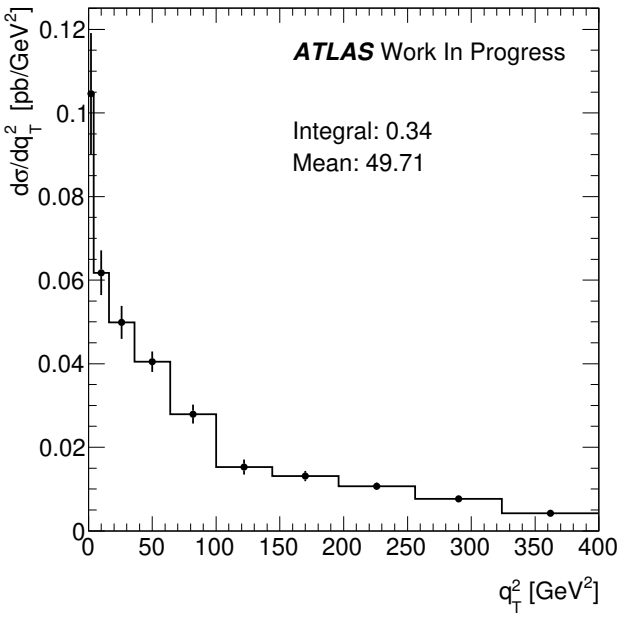

Figure 7.8: Efficiency-corrected differential cross section with respect to q_{T}^2 for $\lambda - q_{\mathrm{T}}^2$ slice 50 ($100 \leq \lambda < 200$ and $0 \leq q_{\mathrm{T}}^2 < 400$ GeV^2). Statistical and BDT-systematic errors are added in quadrature.

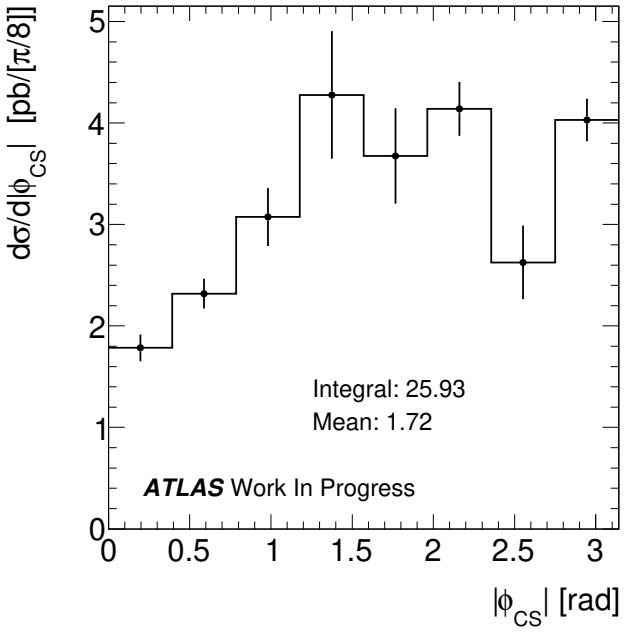

Figure 7.9: Efficiency-corrected differential cross section with respect to $|\phi_{\mathrm{CS}}|$ for $\cos^2\theta_{\mathrm{CS}}$ slice Low. Statistical and BDT-systematic errors are added in quadrature.

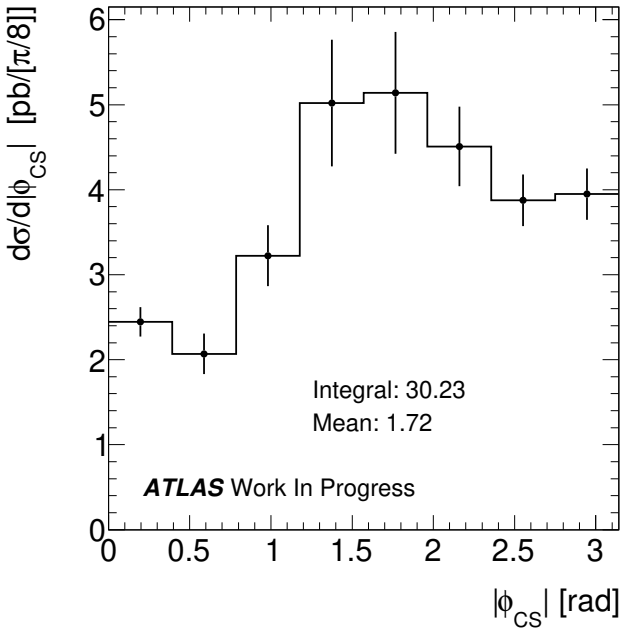

Figure 7.10: Efficiency-corrected differential cross section with respect to $|\phi_{\mathrm{CS}}|$ for $\cos^2\theta_{\mathrm{CS}}$ slice High. Statistical and BDT-systematic errors are added in quadrature.

Chapter 8

Systematics

In the LHC era, systematic uncertainties can dominate more than statistical uncertainties, contributing a significant proportion to the overall uncertainty of a measurement. Statistical uncertainties are a result of stochastic fluctuations arising from a measurement based on differing observations, and the statistical uncertainty is a measure of this range of variation.

Systematic uncertainties arise from the experimental apparatus (LHC and ATLAS detector), assumptions made during the analysis (such as the event selection window of variables), or the model used to make inferences based on data. Unlike statistical variations, where variations between measurements are uncorrelated, systematic variations are, generally, correlated from one measurement to the next. There is little formal guidance in the literature on how to define systematic uncertainties, and current practices are based on informal convention and tradition [99]. It is typical within ATLAS to assess systematics related to the LHC apparatus and ATLAS detector (pileup and resolution), and ones specific to an analysis (event selections and techniques/methods). For the analysis several sources of systematic uncertainties, including correction factors, are considered and applied where necessary. Systematic uncertainties incorporate variations to the measured values, such as mass sideband subtraction boundaries.

One major source of systematic uncertainties arises from the BDT procedure, to extract signal from background, which has already been taken into account (as per Section 6.2 and Chapter 7), and is shown in the column 'BDT syst.' of Tables 8.1 – 8.5.

8.1 Event Selection Systematics

8.1.1 Mass Sideband Subtraction Systematics

The analysis uses four mass intervals for the mass sideband subtraction procedure, outlined in Section 5.2, with bin boundaries $2.7 - 2.9 - 3.1 - 3.5$ GeV. At reconstruction level, the J/ψ mass range is $2.6 \leq m_{\mu\mu} \leq 3.5$ GeV which limits how the bin intervals can be adjusted to assess the statistical fluctuations whilst keeping the bin widths of equal size. Towards 2.6 GeV the mass distribution becomes smeared due to the trigger which would interfere with the model if the lower mass sideband is extended towards this reconstruction level cut. The bin widths are already at the upper limit of the mass range possible, hence each mass region can only be reduced. One systematic variation was to reduce each interval's bin width from 200 MeV to 180 MeV, whilst keeping the 3.1 GeV bin edge fixed, thus changing the interval boundaries to $2.74 - 2.92 - 3.1 - 3.28 - 3.46$ GeV. The entire analysis chain was repeated with these new bin intervals. The difference in the resulting differential cross section in each analysis bin was assigned as the respective uncertainty. The results are shown as the '$m_{\mu\mu}$ syst' column in Tables 8.1 – 8.5.

Another uncertainty, was the assumption that the mass continuum background is linear, which was implicitly applied. However, the mass continuum background could also be modelled exponentially which causes the background contribution to fall whilst increasing the signal contribution. Employing an exponential function, tests indicated that the number of background events decreases by a factor to $0.93 - 0.97$ of the linear background modelling results. This corresponds to $\sim$ %1 change in number of signal events. These results are shown under 'bkg Model' in Tables 8.1 – 8.5.

8.1.2 Long Lifetime Subtraction Systematics

The long lifetime subtraction procedure, detailed in Section 5.3, effectively removes the contribution from background non-prompt J/ψ production. However, there is a residual contribution from this process in various different bins. The effective half life $\tau_0 = 0.86$ ps was determined from fitting studies of inclusive J/ψ production of currently ongoing (at time of writing) analyses. This corresponds to an effective lifetime range of 1.24 ± 0.7 ps, which

conservatively covers all bins of the J/ψ production range. Two small cut off variations are introduced, $\tau_1 = 0.91$ ps and $\tau_2 = 0.81$ ps, and the full analysis chain is repeated. The bb yield was found to be consistent with 0 within errors after subtractions, but not always exactly 0. Studies have shown that there was some residual non-prompt J/ψ contribution which varied from one analysis bin to another. It was found that the value of the cutoff, corresponding to complete subtraction of the bb sample, across all slices and bins, was within the τ range τ_1 and τ_2.

The average deviation from the central value in each analysis bin was assigned as the corresponding systematic uncertainty, and is presented in the appropriate column of Tables 8.1 – 8.5, as either 'τ_1 syst', or 'τ_2 syst'.

Bin	q^2_{T} Region (GeV^2)	$d\sigma/dq^2_{\mathrm{T}}$ (pb/GeV^2)	Stat. (pb/GeV^2)	BDT syst. (pb/GeV^2)	$m_{\mu\mu}$ syst. (pb/GeV^2)	bkg Model (pb/GeV^2)	τ_1 syst. (pb/GeV^2)	τ_2 syst. (pb/GeV^2)
1	$0 \leq q^2_{\mathrm{T}} < 4$	0.1731	0.0138	0.0051	0.0054	0.0017	0.0047	0.0030
2	$4 \leq q^2_{\mathrm{T}} < 16$	0.1046	0.0067	0.0020	0.0020	0.0010	0.0016	0.0026
3	$16 \leq q^2_{\mathrm{T}} < 36$	0.0495	0.0041	0.0038	0.0012	0.0005	0.0021	0.0006
4	$36 \leq q^2_{\mathrm{T}} < 64$	0.0336	0.0026	0.0004	0.0007	0.0003	0.0020	0.0011
5	$64 \leq q^2_{\mathrm{T}} < 100$	0.0320	0.0023	0.0007	0.0023	0.0003	0.0009	0.0001
6	$100 \leq q^2_{\mathrm{T}} < 144$	0.0192	0.0019	0.0018	0.0009	0.0002	0.0001	0.0012
7	$144 \leq q^2_{\mathrm{T}} < 196$	0.0150	0.0014	0.0014	0.0001	0.0001	0.0008	0.0010
8	$196 \leq q^2_{\mathrm{T}} < 256$	0.0074	0.0009	0.0003	0.0003	0.0001	0.0003	0.0005
9	$256 \leq q^2_{\mathrm{T}} < 324$	0.0023	0.0005	0.0005	0.0002	0.0000	0.0001	0.0000
10	$324 \leq q^2_{\mathrm{T}} < 400$	0.0013	0.0004	0.0003	0.0000	0.0000	0.0002	0.0001

Table 8.1: Table of event selection systematic results for λ region 30 ($25 \leq \lambda < 50$ and $0 \leq q^2_{\mathrm{T}} < 400$ GeV^2).

Bin	q^2_{T} Region (GeV^2)	$d\sigma/dq^2_{\mathrm{T}}$ (pb/GeV^2)	Stat. (pb/GeV^2)	BDT syst. (pb/GeV^2)	$m_{\mu\mu}$ syst. (pb/GeV^2)	bkg Model (pb/GeV^2)	τ_1 syst. (pb/GeV^2)	τ_2 syst. (pb/GeV^2)
1	$0 \leq q^2_{\mathrm{T}} < 4$	0.2545	0.0182	0.0148	0.0069	0.0025	0.0092	0.0056
2	$4 \leq q^2_{\mathrm{T}} < 16$	0.1923	0.0096	0.0194	0.0004	0.0019	0.0107	0.0049
3	$16 \leq q^2_{\mathrm{T}} < 36$	0.1384	0.0075	0.0081	0.0028	0.0014	0.0036	0.0053
4	$36 \leq q^2_{\mathrm{T}} < 64$	0.0730	0.0046	0.0025	0.0011	0.0007	0.0045	0.0016
5	$64 \leq q^2_{\mathrm{T}} < 100$	0.0437	0.0027	0.0012	0.0009	0.0004	0.0025	0.0023
6	$100 \leq q^2_{\mathrm{T}} < 144$	0.0281	0.0019	0.0015	0.0016	0.0003	0.0018	0.0013
7	$144 \leq q^2_{\mathrm{T}} < 196$	0.0174	0.0012	0.0008	0.0008	0.0002	0.0008	0.0005
8	$196 \leq q^2_{\mathrm{T}} < 256$	0.0098	0.0008	0.0004	0.0001	0.0001	0.0003	0.0005
9	$256 \leq q^2_{\mathrm{T}} < 324$	0.0060	0.0006	0.0006	0.0001	0.0001	0.0006	0.0005
10	$324 \leq q^2_{\mathrm{T}} < 400$	0.0033	0.0005	0.0002	0.0001	0.0000	0.0001	0.0001

Table 8.2: Table of event selection systematic results for λ region 40 ($50 \leq \lambda < 100$ and $0 \leq q^2_{\mathrm{T}} < 400$ GeV^2).

Bin	q_T^2 Region (GeV^2)	$d\sigma/dq_T^2$ (pb/GeV^2)	Stat. (pb/GeV^2)	BDT syst. (pb/GeV^2)	$m_{\mu\mu}$ syst. (pb/GeV^2)	bkg Model (pb/GeV^2)	τ_1 syst. (pb/GeV^2)	τ_2 syst. (pb/GeV^2)
1	$0 \leq q_T^2 < 4$	0.1046	0.0093	0.0111	0.0028	0.0010	0.0023	0.0037
2	$4 \leq q_T^2 < 16$	0.0618	0.0046	0.0027	0.0051	0.0006	0.0016	0.0056
3	$16 \leq q_T^2 < 36$	0.0499	0.0030	0.0025	0.0003	0.0005	0.0023	0.0031
4	$36 \leq q_T^2 < 64$	0.0405	0.0022	0.0011	0.0000	0.0004	0.0028	0.0024
5	$64 \leq q_T^2 < 100$	0.0279	0.0018	0.0014	0.0013	0.0003	0.0013	0.0015
6	$100 \leq q_T^2 < 144$	0.0152	0.0012	0.0014	0.0008	0.0002	0.0011	0.0005
7	$144 \leq q_T^2 < 196$	0.0131	0.0009	0.0008	0.0001	0.0001	0.0009	0.0009
8	$196 \leq q_T^2 < 256$	0.0107	0.0007	0.0005	0.0003	0.0001	0.0002	0.0005
9	$256 \leq q_T^2 < 324$	0.0077	0.0006	0.0004	0.0001	0.0001	0.0003	0.0003
10	$324 \leq q_T^2 < 400$	0.0042	0.0005	0.0002	0.0003	0.0000	0.0002	0.0003

Table 8.3: Table of event selection systematic results for λ region 50 ($100 \leq \lambda < 200$ and $0 \leq q_T^2 < 400$ GeV^2).

Bin	$\lvert\phi_{CS}\rvert$ Region (rad)	$d\sigma/d\lvert\phi_{CS}\rvert$ (pb/rad)	Stat. (pb/rad)	BDT syst. (pb/rad)	$m_{\mu\mu}$ syst. (pb/rad)	bkg Model (pb/rad)	τ_1 syst. (pb/rad)	τ_2 syst. (pb/rad)
1	$0 \leq \lvert\phi_{CS}\rvert < \frac{\pi}{8}$	1.7839	0.1183	0.0564	0.0183	0.0178	0.0008	0.0008
2	$\frac{\pi}{8} \leq \lvert\phi_{CS}\rvert < \frac{\pi}{4}$	2.3182	0.1422	0.0329	0.0298	0.0232	0.0434	0.0434
3	$\frac{\pi}{4} \leq \lvert\phi_{CS}\rvert < \frac{3\pi}{8}$	3.0746	0.1835	0.2184	0.0418	0.0307	0.0458	0.0458
4	$\frac{3\pi}{8} \leq \lvert\phi_{CS}\rvert < \frac{\pi}{2}$	4.2771	0.2726	0.5656	0.0423	0.0428	0.0601	0.0601
5	$\frac{\pi}{2} \leq \lvert\phi_{CS}\rvert < \frac{5\pi}{8}$	3.6754	0.2470	0.4006	0.0459	0.0368	0.0638	0.0638
6	$\frac{5\pi}{8} \leq \lvert\phi_{CS}\rvert < \frac{3\pi}{4}$	4.1392	0.2232	0.1452	0.0551	0.0414	0.3561	0.3561
7	$\frac{3\pi}{4} \leq \lvert\phi_{CS}\rvert < \frac{7\pi}{8}$	2.6268	0.1718	0.3179	0.0321	0.0263	0.1355	0.1355
8	$\frac{7\pi}{8} \leq \lvert\phi_{CS}\rvert < \pi$	4.0310	0.2030	0.0538	0.0487	0.0403	0.1843	0.1843

Table 8.4: Table of event selection systematic results for $|\phi_{CS}|$ low region.

Bin	$\lvert\phi_{CS}\rvert$ Region (rad)	$d\sigma/d\lvert\phi_{CS}\rvert$ (pb/rad)	Stat. (pb/rad)	BDT syst. (pb/rad)	$m_{\mu\mu}$ syst. (pb/rad)	bkg Model (pb/rad)	τ_1 syst. (pb/rad)	τ_2 syst. (pb/rad)
1	$0 \leq \lvert\phi_{CS}\rvert < \frac{\pi}{8}$	2.4450	0.1556	0.0784	0.0355	0.0244	0.0728	0.0728
2	$\frac{\pi}{8} \leq \lvert\phi_{CS}\rvert < \frac{\pi}{4}$	2.0693	0.1779	0.1594	0.0203	0.0207	0.1197	0.1197
3	$\frac{\pi}{4} \leq \lvert\phi_{CS}\rvert < \frac{3\pi}{8}$	3.2229	0.2296	0.2758	0.0359	0.0322	0.1117	0.1117
4	$\frac{3\pi}{8} \leq \lvert\phi_{CS}\rvert < \frac{\pi}{2}$	5.0194	0.3181	0.6737	0.0655	0.0502	0.2019	0.2019
5	$\frac{\pi}{2} \leq \lvert\phi_{CS}\rvert < \frac{5\pi}{8}$	5.1393	0.3375	0.6318	0.0448	0.0514	0.2568	0.2568
6	$\frac{5\pi}{8} \leq \lvert\phi_{CS}\rvert < \frac{3\pi}{4}$	4.5094	0.2664	0.3854	0.0542	0.0451	0.0936	0.0936
7	$\frac{3\pi}{4} \leq \lvert\phi_{CS}\rvert < \frac{7\pi}{8}$	3.8741	0.2271	0.2014	0.0332	0.0387	0.1744	0.1744
8	$\frac{7\pi}{8} \leq \lvert\phi_{CS}\rvert < \pi$	3.9483	0.2769	0.1215	0.0585	0.0395	0.3050	0.3050

Table 8.5: Table of event selection systematic results for $|\phi_{CS}|$ high region.

8.2 Efficiency Correction Systematics

The efficiencies determined were obtained from the signal MC, which has its own statistical uncertainty due to the amount of MC statistics in each bin. The relative statistical uncertainty in each analysis bin is shown in the 'Stat.' column of Tables 8.6 – 8.10.

The fidelity of the Monte Carlo simulation was assessed based on the 'scale factors' for trigger, muon reconstruction, and photon reconstruction, provided by the corresponding

performance groups within ATLAS. In particular, the distributions for the trigger scale factors were built for each analysis bin, with means and root mean square (r.m.s.) values presented in the appropriate columns of Tables 8.6 – 8.10. The values of the scale factors in each bin were approximately the same, around 0.9, indicating that the trigger efficiency in the data was actually slightly lower than in the signal MC, so the appropriate correction will be applied to the measured cross section determined in Chapter 7, with the associated relative uncertainty calculated as r.m.s/mean, as shown in Tables 8.6 – 8.10.

The scale factors corresponding to muon reconstruction were investigated in detail for the J/ψ cross section analysis. They were found to be small, well below the level of 1%.

The EGamma group provided scale factor maps associated with photon reconstruction and their uncertainties. Photon scale factor maps are applied to the signal MC to match the measured efficiency in data, based on the transverse momentum and η of the photon [100]. The mean efficiency ratio $\epsilon^{\text{data}}/\epsilon^{\text{sig}}$ is calculated in each analysis bin, where ϵ^{data} is the efficiency in data and ϵ^{sig} is the efficiency predicted by the signal MC [101]. The associated mean efficiencies were found to be around (97 ± 2) %, with values for individual bins shown in the appropriate columns of Tables 8.6 – 8.10.

The last column in Tables 8.6 – 8.10 show the quadratic sum of all efficiency-related systematic errors.

Bin	q_{T}^2 Region (GeV^2)	$d\sigma/dq_{\text{T}}^2$ (pb/GeV^2)	Stat. (pb/GeV^2)	Trigger scale factor mean (pb/GeV^2)	Trigger scale factor rms (pb/GeV^2)	Photon scale factor mean (pb/GeV^2)	Photon scale factor rms (pb/GeV^2)	Trigger $\frac{\text{rms}}{\text{mean}}$ %	Photon $\frac{\text{rms}}{\text{mean}}$ %	Muon Reco Scale Factor %	Signal MC. Stat. Err %	Quad. Sum %
1	$0 \leq q_{\text{T}}^2 < 4$	0.1731	0.0138	0.9024	0.0591	0.9734	0.0233	6.55	2.40	<1	1.85	7.29
2	$4 \leq q_{\text{T}}^2 < 16$	0.1046	0.0067	0.9050	0.0594	0.9738	0.0236	6.56	2.42	<1	1.52	7.23
3	$16 \leq q_{\text{T}}^2 < 36$	0.0495	0.0041	0.9039	0.0595	0.9737	0.0235	6.58	2.41	<1	1.66	7.28
4	$36 \leq q_{\text{T}}^2 < 64$	0.0336	0.0026	0.9008	0.0577	0.9735	0.0234	6.41	2.41	<1	1.71	7.13
5	$64 \leq q_{\text{T}}^2 < 100$	0.0320	0.0023	0.8963	0.0573	0.9724	0.0230	6.39	2.37	<1	1.94	7.15
6	$100 \leq q_{\text{T}}^2 < 144$	0.0192	0.0019	0.8910	0.0563	0.9729	0.0233	6.32	2.39	<1	2.20	7.18
7	$144 \leq q_{\text{T}}^2 < 196$	0.0150	0.0014	0.8864	0.0531	0.9729	0.0232	5.99	2.38	<1	2.75	7.07
8	$196 \leq q_{\text{T}}^2 < 256$	0.0074	0.0009	0.8832	0.0512	0.9738	0.0232	5.80	2.38	<1	4.26	7.64
9	$256 \leq q_{\text{T}}^2 < 324$	0.0023	0.0005	0.8776	0.0457	0.9703	0.0209	5.21	2.16	<1	7.48	9.42
10	$324 \leq q_{\text{T}}^2 < 400$	0.0013	0.0004	0.8798	0.0468	0.9667	0.0198	5.32	2.05	<1	12.12	13.43

Table 8.6: Table of efficiency correction systematic results for λ region 30 ($25 \leq \lambda < 50$ and $0 \leq q_{\text{T}}^2 < 400$ GeV^2).

Bin	q_T^2 Region (GeV^2)	$d\sigma/dq_T^2$ (pb/GeV^2)	Stat. (pb/GeV^2)	Trigger scale factor mean (pb/GeV^2)	Trigger scale factor rms (pb/GeV^2)	Photon scale factor mean (pb/GeV^2)	Photon scale factor rms (pb/GeV^2)	Trigger $\frac{\text{rms}}{\text{mean}}$ %	Photon $\frac{\text{rms}}{\text{mean}}$ %	Muon Reco Scale Factor %	Signal MC. Stat. Err %	Quad. Sum %
1	$0 \le q_T^2 < 4$	0.2545	0.0182	0.8840	0.0502	0.9720	0.0230	5.68	2.36	<1	1.19	6.35
2	$4 \le q_T^2 < 16$	0.1923	0.0096	0.8826	0.0489	0.9727	0.0230	5.54	2.37	<1	0.82	6.16
3	$16 \le q_T^2 < 36$	0.1384	0.0075	0.8805	0.0489	0.9729	0.0228	5.55	2.34	<1	0.83	6.16
4	$36 \le q_T^2 < 64$	0.0730	0.0046	0.8785	0.0489	0.9733	0.0225	5.57	2.31	<1	0.92	6.18
5	$64 \le q_T^2 < 100$	0.0437	0.0027	0.8766	0.0481	0.9740	0.0223	5.49	2.29	<1	1.10	6.13
6	$100 \le q_T^2 < 144$	0.0281	0.0019	0.8748	0.0468	0.9739	0.0217	5.35	2.23	<1	1.38	6.04
7	$144 \le q_T^2 < 196$	0.0174	0.0012	0.8716	0.0450	0.9741	0.0217	5.17	2.23	<1	1.79	5.99
8	$196 \le q_T^2 < 256$	0.0098	0.0008	0.8712	0.0443	0.9760	0.0213	5.08	2.18	<1	2.35	6.09
9	$256 \le q_T^2 < 324$	0.0060	0.0006	0.8692	0.0431	0.9760	0.0203	4.96	2.08	<1	3.56	6.53
10	$324 \le q_T^2 < 400$	0.0033	0.0005	0.8663	0.0388	0.9753	0.0198	4.48	2.03	<1	4.79	6.94

Table 8.7: Table of efficiency correction systematic results for λ region 40 ($50 \le \lambda < 100$ and $0 \le q_T^2 < 400$ GeV^2).

Bin	q_T^2 Region (GeV^2)	$d\sigma/dq_T^2$ (pb/GeV^2)	Stat. (pb/GeV^2)	Trigger scale factor mean (pb/GeV^2)	Trigger scale factor rms (pb/GeV^2)	Photon scale factor mean (pb/GeV^2)	Photon scale factor rms (pb/GeV^2)	Trigger $\frac{\text{rms}}{\text{mean}}$ %	Photon $\frac{\text{rms}}{\text{mean}}$ %	Muon Reco Scale Factor %	Signal MC. Stat. Err %	Quad. Sum %
1	$0 \le q_T^2 < 4$	0.1046	0.0093	0.8702	0.0440	0.9782	0.0213	5.05	2.18	<1	2.30	6.05
2	$4 \le q_T^2 < 16$	0.0618	0.0046	0.8715	0.0431	0.9767	0.0207	4.95	2.12	<1	1.49	5.67
3	$16 \le q_T^2 < 36$	0.0499	0.0030	0.8674	0.0418	0.9774	0.0205	4.82	2.10	<1	1.41	5.54
4	$36 \le q_T^2 < 64$	0.0405	0.0022	0.8679	0.0417	0.9782	0.0202	4.81	2.06	<1	1.46	5.53
5	$64 \le q_T^2 < 100$	0.0279	0.0018	0.8673	0.0402	0.9777	0.0196	4.63	2.01	<1	1.65	5.40
6	$100 \le q_T^2 < 144$	0.0152	0.0012	0.8674	0.0388	0.9789	0.0193	4.47	1.98	<1	1.84	5.32
7	$144 \le q_T^2 < 196$	0.0131	0.0009	0.8677	0.0372	0.9793	0.0191	4.29	1.95	<1	2.26	5.32
8	$196 \le q_T^2 < 256$	0.0107	0.0007	0.8674	0.0377	0.9798	0.0190	4.34	1.93	<1	2.73	5.57
9	$256 \le q_T^2 < 324$	0.0077	0.0006	0.8687	0.0370	0.9811	0.0181	4.26	1.84	<1	3.61	5.96
10	$324 \le q_T^2 < 400$	0.0042	0.0005	0.8686	0.0353	0.9808	0.0178	4.06	1.81	<1	4.43	6.36

Table 8.8: Table of efficiency correction systematic results for λ region 50 ($100 \le \lambda < 200$ and $0 \le q_T^2 < 400$ GeV^2).

Bin	$\lvert\phi_{CS}\rvert$ Region (rad)	$d\sigma/d\lvert\phi_{CS}\rvert$ (pb/rad)	Stat. (pb/rad)	Trigger scale factor mean (pb/rad)	Trigger scale factor rms (pb/rad)	Photon scale factor mean (pb/rad)	Photon scale factor rms (pb/rad)	Trigger $\frac{\text{rms}}{\text{mean}}$ %	Photon $\frac{\text{rms}}{\text{mean}}$ %	Muon Reco Scale Factor %	Signal MC. Stat. Err %	Quad. Sum %
1	$0 \le \lvert\phi_{CS}\rvert < \frac{\pi}{8}$	1.7839	0.1183	0.8936	0.0561	0.9776	0.0195	6.27	2.00	<1	1.61	6.85
2	$\frac{\pi}{8} \le \lvert\phi_{CS}\rvert < \frac{\pi}{4}$	2.3182	0.1422	0.8923	0.0552	0.9782	0.0197	6.18	2.01	<1	1.48	6.74
3	$\frac{\pi}{4} \le \lvert\phi_{CS}\rvert < \frac{3\pi}{8}$	3.0746	0.1835	0.8925	0.0569	0.9766	0.0207	6.37	2.12	<1	1.19	6.89
4	$\frac{3\pi}{8} \le \lvert\phi_{CS}\rvert < \frac{\pi}{2}$	4.2771	0.2726	0.8884	0.0542	0.9737	0.0220	6.10	2.26	<1	0.91	6.64
5	$\frac{\pi}{2} \le \lvert\phi_{CS}\rvert < \frac{5\pi}{8}$	3.6754	0.2470	0.8763	0.0467	0.9718	0.0223	5.33	2.30	<1	0.88	5.96
6	$\frac{5\pi}{8} \le \lvert\phi_{CS}\rvert < \frac{3\pi}{4}$	4.1392	0.2232	0.8685	0.0409	0.9710	0.0222	4.71	2.29	<1	1.07	5.44
7	$\frac{3\pi}{4} \le \lvert\phi_{CS}\rvert < \frac{7\pi}{8}$	2.6268	0.1718	0.8670	0.0395	0.9710	0.0223	4.56	2.29	<1	1.26	5.35
8	$\frac{7\pi}{8} \le \lvert\phi_{CS}\rvert < \pi$	4.0310	0.2030	0.8661	0.0379	0.9708	0.0222	4.38	2.29	<1	1.42	5.24

Table 8.9: Table of efficiency correction systematic results for $|\phi_{CS}|$ low region.

Bin	$\|\phi_{\mathrm{CS}}\|$ Region (rad)	$d\sigma/d\|\phi_{\mathrm{CS}}\|$ (pb/rad)	Stat. (pb/rad)	Trigger scale factor mean (pb/rad)	Trigger scale factor rms (pb/rad)	Photon scale factor mean (pb/rad)	Photon scale factor rms (pb/rad)	Trigger $\frac{\text{rms}}{\text{mean}}$ %	Photon $\frac{\text{rms}}{\text{mean}}$ %	Muon Reco Scale Factor %	Signal MC. Stat. Err %	Quad. Sum %
1	$0 \leq \|\phi_{\mathrm{CS}}\| < \frac{\pi}{8}$	2.4450	0.1556	0.8953	0.0556	0.9781	0.0203	6.21	2.08	<1	1.81	6.87
2	$\frac{\pi}{8} \leq \|\phi_{\mathrm{CS}}\| < \frac{\pi}{4}$	2.0693	0.1779	0.8957	0.0562	0.9772	0.0205	6.28	2.10	<1	1.61	6.89
3	$\frac{\pi}{4} \leq \|\phi_{\mathrm{CS}}\| < \frac{3\pi}{8}$	3.2229	0.2296	0.8931	0.0549	0.9768	0.0214	6.15	2.19	<1	1.26	6.73
4	$\frac{3\pi}{8} \leq \|\phi_{\mathrm{CS}}\| < \frac{\pi}{2}$	5.0194	0.3181	0.8915	0.0551	0.9752	0.0228	6.18	2.33	<1	0.94	6.74
5	$\frac{\pi}{2} \leq \|\phi_{\mathrm{CS}}\| < \frac{5\pi}{8}$	5.1393	0.3375	0.8771	0.0468	0.9745	0.0234	5.33	2.40	<1	0.89	6.00
6	$\frac{5\pi}{8} \leq \|\phi_{\mathrm{CS}}\| < \frac{3\pi}{4}$	4.5094	0.2664	0.8695	0.0412	0.9746	0.0236	4.73	2.42	<1	1.14	5.53
7	$\frac{3\pi}{4} \leq \|\phi_{\mathrm{CS}}\| < \frac{7\pi}{8}$	3.8741	0.2271	0.8666	0.0389	0.9748	0.0236	4.49	2.42	<1	1.41	5.39
8	$\frac{7\pi}{8} \leq \|\phi_{\mathrm{CS}}\| < \pi$	3.9483	0.2769	0.8670	0.0389	0.9744	0.0236	4.49	2.42	<1	1.60	5.44

Table 8.10: Table of efficiency correction systematic results for $|\phi_{CS}|$ high region.

8.3 Pileup Dependence

The primary purpose of the LHC is to explore physics at high energies, at the TeV scale. To maximise the collision rate, the number of protons per beam can be increased, or by improving beam optics by focalising the beams at interaction points. The net effect of either or both increases the collision rate so that several *pp* collisions occur during one bunch crossing. The effect of simultaneous collisions, resulting in multiple primary vertices, μ, is called pileup.

The calorimeter sits approximately 1 m from the collision point, at the level of particle interactions it does not have good resolution with respect to primary vertices. The analysis seeks events with a J/ψ and γ originating from the same vertex, but there are currently no tools to distinguish whether a γ came from the same vertex or a different one. Hopefully the analysis chain removes the majority of 'bad' candidate photons, leaving only good candidates including the signal γ. The analysis then selects the highest $p_{\mathrm{T}}(\gamma)$ in an event, as background events contain low p_{T} photons. However, this does not mean the γ came from the same vertex as the J/ψ, but it is very likely. Creating a J/ψ in a collision is rare, and creating a hard isolated γ with $p_{\mathrm{T}} > 9$ GeV is also rare. The occurrence of both in the same bunch crossing is not frequent so pileup should be low.

It is expected that pileup effects should not be too dramatic for 2015 data as $\mu \sim 13$. Events with two muons originating from different vertices is suppressed by the dimuon quality fit requirement, therefore unlikely to fall under the J/ψ signal peak. Sources of pileup could include events where the dimuon comes from one primary vertex and the photon from another. Like the pp background, they are not expected to have any angular correlations.

The convenience of this means that if these types of events exist they will mimic the pp background and will have been separated from the signal-like events during the TMVA stage of the analysis.

In order to ensure there is little, if any, pileup dependence present, several studies were conducted.

8.3.1 Study Of Pileup Effects With Data

The distribution of the average number of interactions per bunch crossing, μ, for the data sample after event selections is shown in Figure 8.1. The distribution is fairly narrow as the average number of interactions per bunch crossing was low compared to later years of dating taking during Run II, with $\mu \sim 50$. Pileup effects in data were studied by dividing the data into low and high pileup regions, separated at $\mu = 12.7$, with each region containing approximately equal number of events.

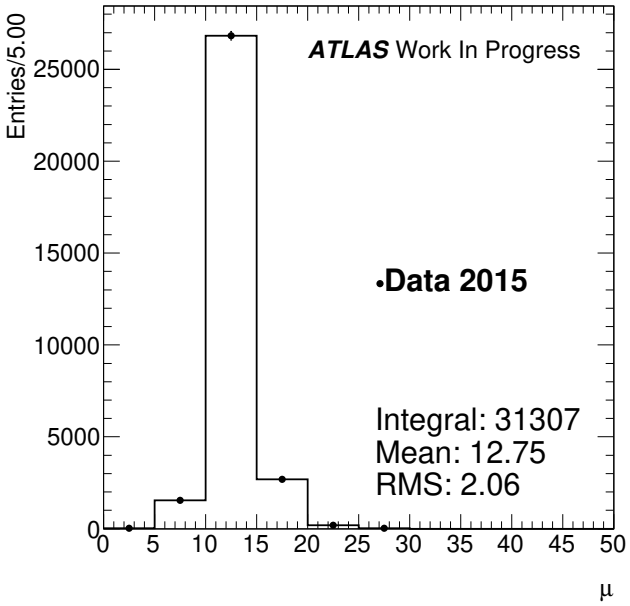

Figure 8.1: Average number of primary interactions per bunch crossing for selected data events.

The ratio of the low and high pileup regions as a function of q_{T}^2 are plotted for λ slices 00/0,

30, 40, and 50. The distributions are fitted with a straight line of the form:

$$F(q_{\mathrm{T}}^2) = p_0 \times (1 + p_1 x) \tag{8.1}$$

where p_1 is the parameter of interest, describing the gradient of the slope. These distributions are shown in Figure 8.2.

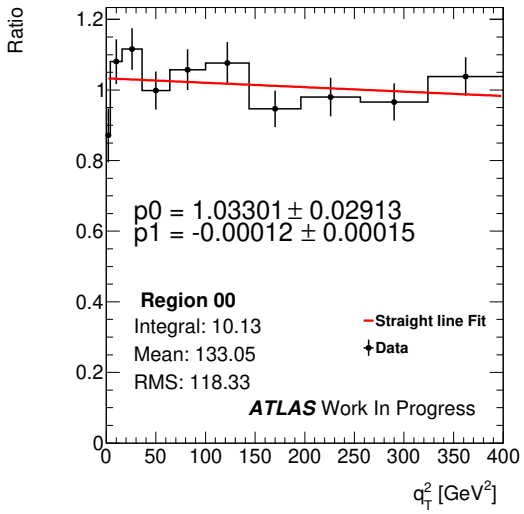

(a) λ region 00: $0 \leq \lambda \leq 200$

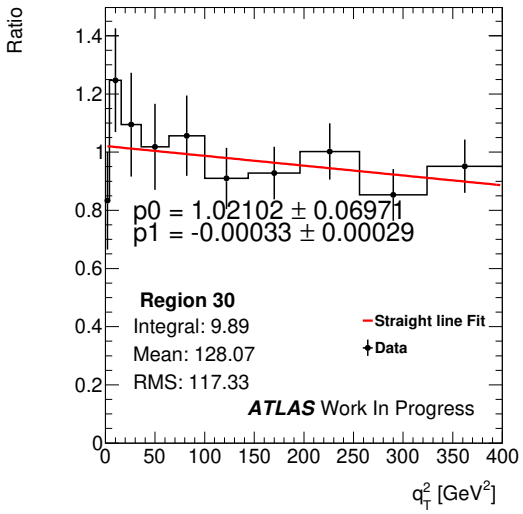

(b) λ region 30: $25 \leq \lambda \leq 50$

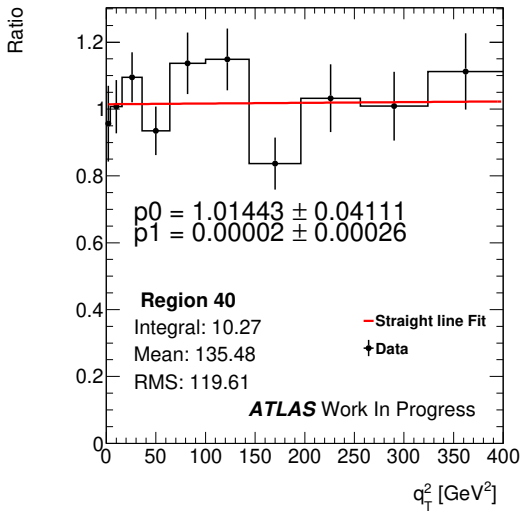

(c) λ region 40: $50 \leq \lambda \leq 100$

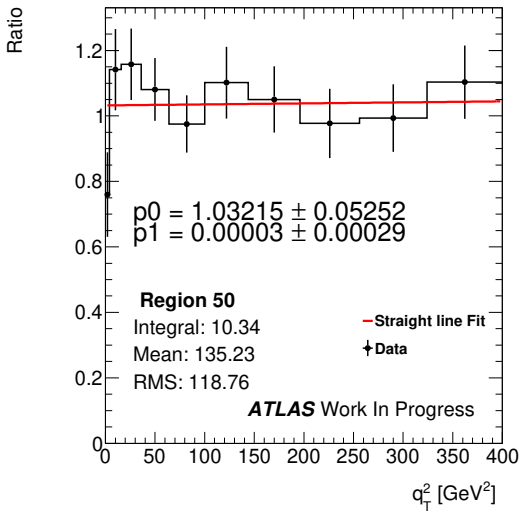

(d) λ region 50: $100 \leq \lambda \leq 200$

Figure 8.2: Ratio of low/high pile up regions as a function of q_{T}^2 for slice 00(0) in (a), slice 30 in (b), slice 40 in (c), and Slice 50 in (d).

All fits are consistent with a horizontal line (the gradient of the slope, given by p_1 is ~ 0 across the slices), confirming that the q_{T}^2 distributions are the same for low and high pileup events, and there is no significant enhancement at high $\lambda - q_{\mathrm{T}}^2$ slices.

8.3.2 Signal Monte Carlo Pileup Effects

The signal MC sample contains a large amount of pileup, as it was produced with data-taking 2016 conditions. The distribution of the average number of interactions per bunch crossing after selection cuts is shown in Figure 8.3.

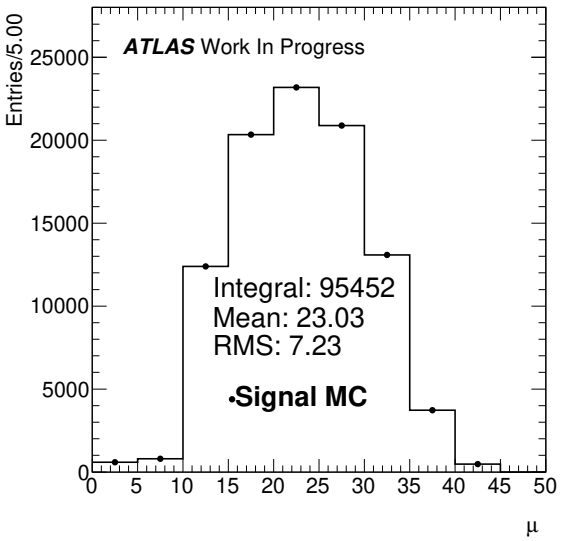

Figure 8.3: Average number of primary interactions per bunch crossing in the signal Monte Carlo sample.

In order to compare pileup dependence, pileup distributions were obtained for different λ regions, and divided by the pileup distribution for slice 00/0. If the pileup is different in different λ regions, the ratio will show this as a non-trivial (non-constant) dependence. The distributions for $\lambda - q_{\mathrm{T}}^2$ slices 30, 40, 50 and 33 are shown in Figure 8.4, fitted to a straight line of the form:

$$F(\mu) = p_0 \times (1 + p_1 x) \tag{8.2}$$

where p_1 is the parameter of interest, describing the gradient of the slope.

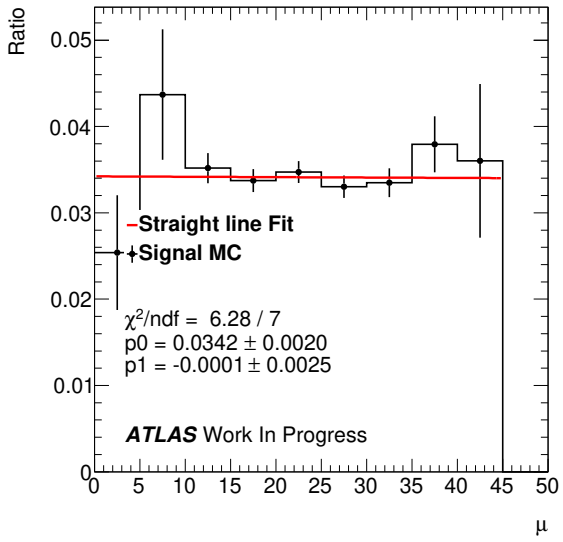

(a) Pileup distribution ratio 33/00

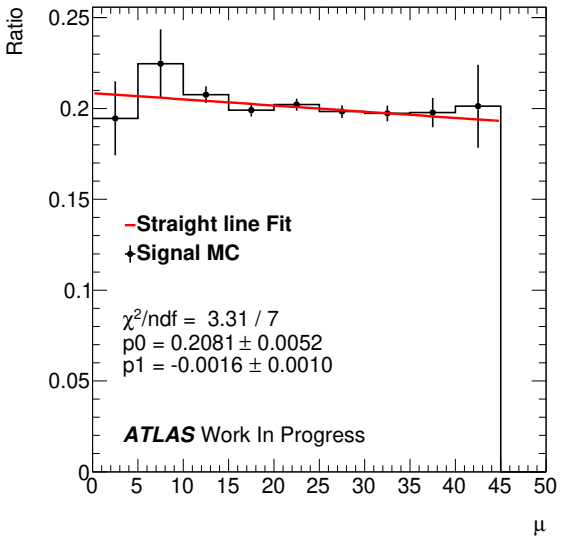

(b) Pileup distribution ratio 30/00

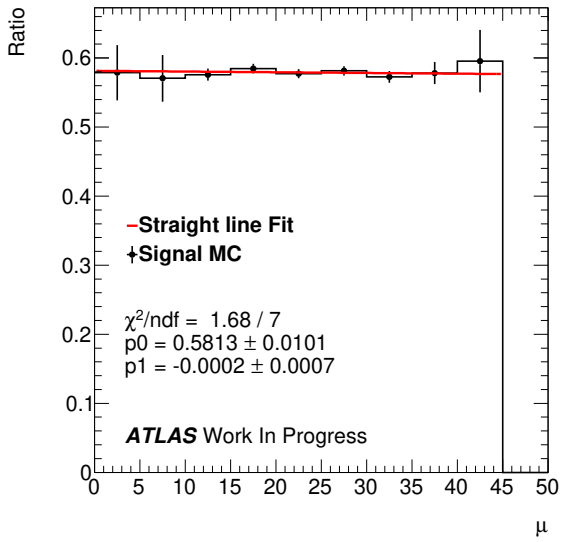

(c) Pileup distribution ratio 40/00

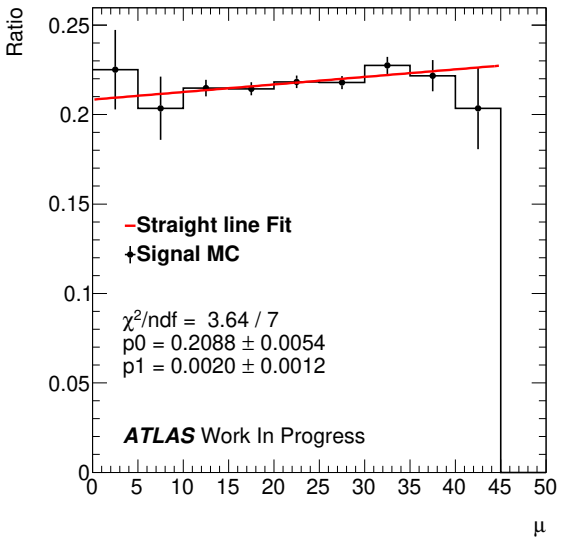

(d) Pileup distribution ratio 50/00

Figure 8.4: Ratios of pileup distributions for different q_{T}^2 and λ slices. The red line describes a straight-line fit, with parameters shown in the legend.

In the Figure 8.4, and indeed across all $\lambda - q_{\mathrm{T}}^2$ slices, p_1 was found to be consistent with 0, which suggests no pileup dependence.

Further investigation into signal MC pileup conditions for different λ regions involved splitting the signal MC events into 2 regions: 1) low pileup ($\mu < 15$) and 2) high pileup ($15 < \mu < 18$), as shown in Figure 8.5. In Figure 8.3, the average number of interactions

per collision is $\mu \sim 22$ for the signal MC sample, whereas in data $\mu \sim 13$ (see Figure 8.1). The signal MC sample is from 2016 when there were more interactions per collision due to different LHC operating conditions compared to 2015 which is the year data for the analysis was collected. As the majority of data events are in the third bin, $10 \leq \mu \leq 15$, the high pile up region in signal is limited to $\mu = 18$ to be representative of the data.

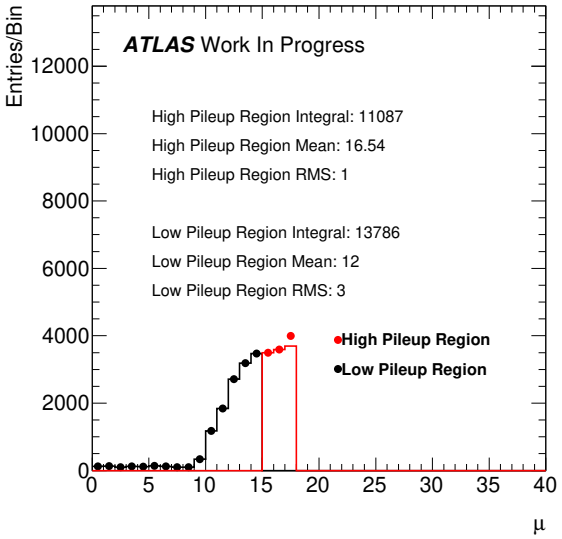

Figure 8.5: Average number of primary interactions for the two subsets of events discussed in the text.

The ratio of the low and high pileup regions was plotted as a function of q_{T}^2, and are shown for slices 00, 30, 40 and 50, in Figures 8.6 and 8.7. The ratios have been fitted with the following straight line fit function:

$$F(q_{\mathrm{T}}^2) = p_0 \times (1 + p_1 x) \tag{8.3}$$

where p_1 is the parameter of interest, describing the gradient of the slope.

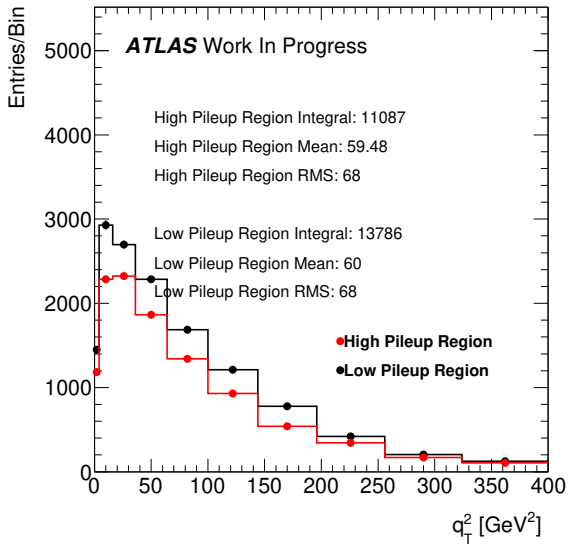

(a) λ region 0: $0 \leq \lambda \leq 200$

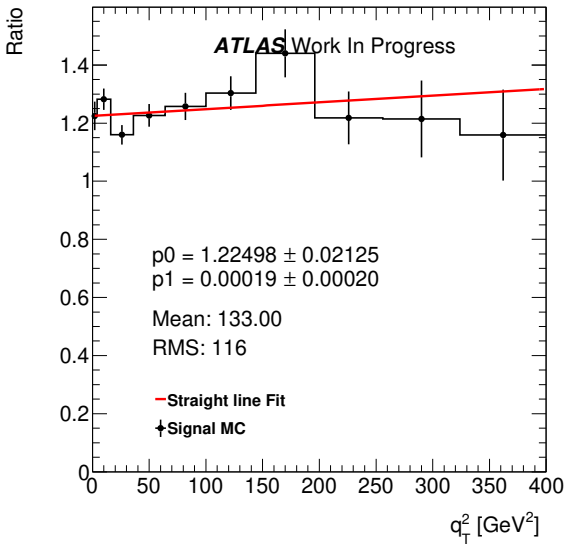

(b) λ region 0: $0 \leq \lambda \leq 200$

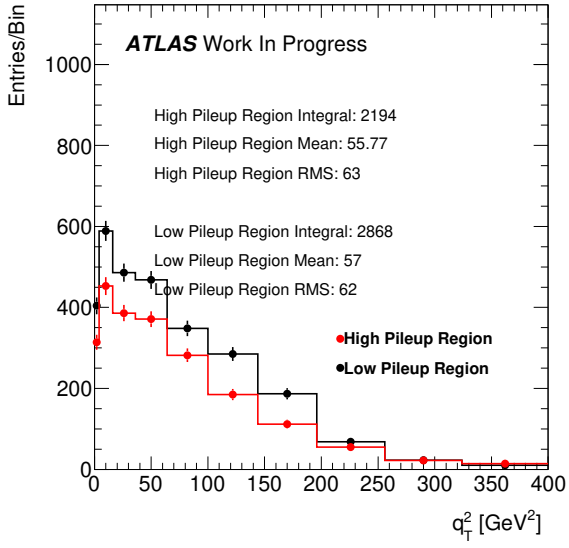

(c) λ region 3: $25 \leq \lambda \leq 50$

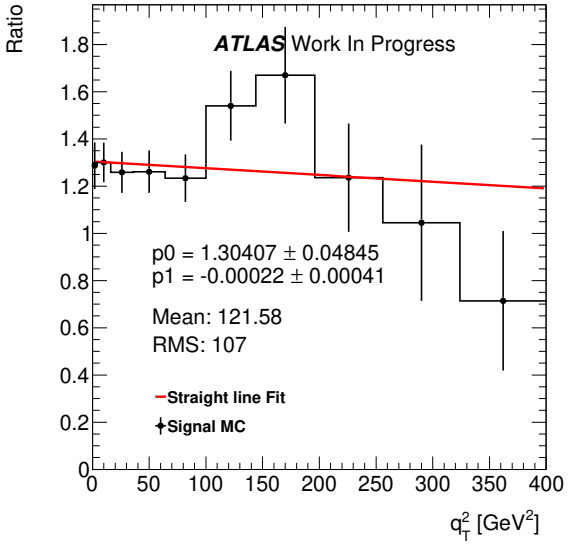

(d) λ region 3: $25 \leq \lambda \leq 50$

Figure 8.6: Plots of the low and high pile up regions and their ratios for slice 00, figures a) and b), and slice 30 figures c) and d) respectively

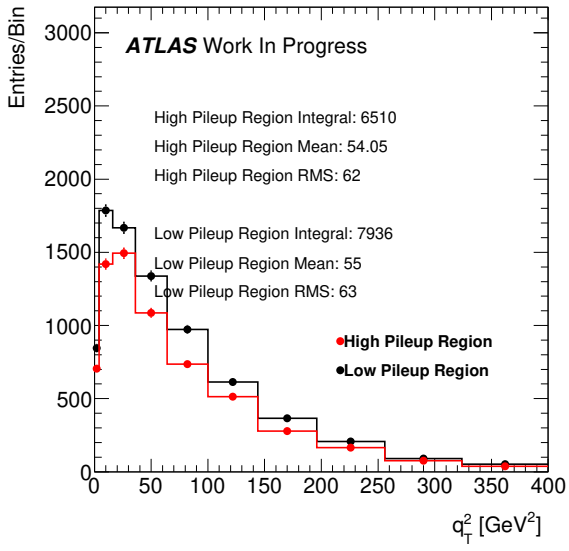

(a) λ region 4: $50 \leq \lambda \leq 100$

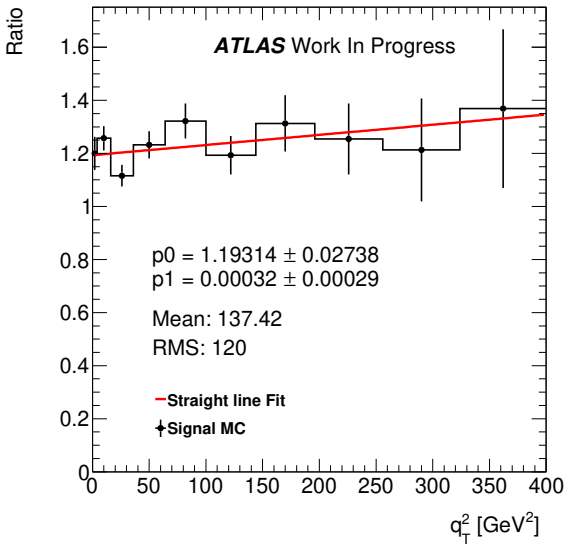

(b) λ region 4: $50 \leq \lambda \leq 100$

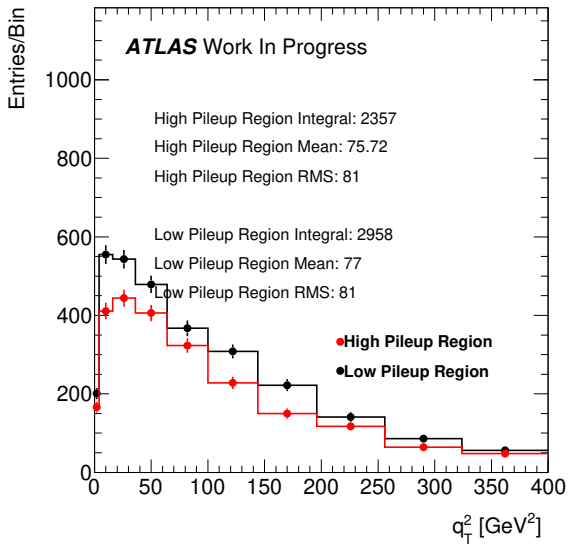

(c) λ region 5: $100 \leq \lambda \leq 200$

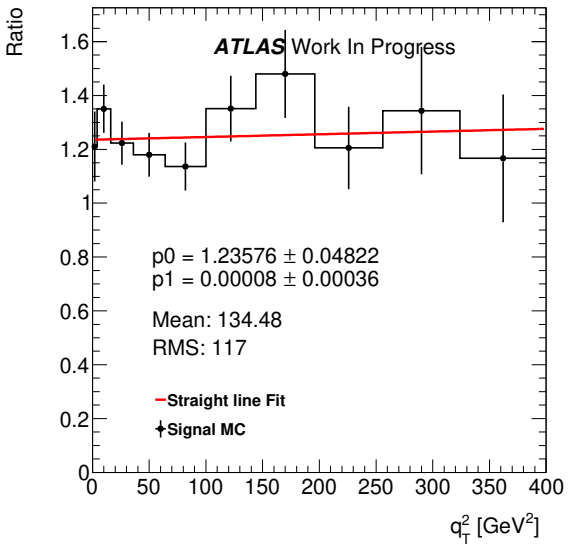

(d) λ region 5: $100 \leq \lambda \leq 200$

Figure 8.7: Plots of the low and high pile up regions and their ratios for slice 40, figures a) and b), and slice 50 figures c) and d) respectively

The conclusion of these studies of pileup dependence is that for the data and signal MC data-sets, at this level of statistics, there was found to be no q_{T}^2 dependence on pileup. Hence there is no pileup related bias to the analysis, so no correction or associated systematic uncertainty was assigned.

8.4 Resolution And Bin Migration Study

To ensure that the measured q^2_{T} distributions are an accurate representation, studies are required to determine any possible effects of the measurement resolution in q^2_{T}, and possible migration effects between neighbouring bins.

Thankfully, as the overall efficiency is determined from the comparison of signal MC truth to signal MC reconstructed, then if the resolution is deemed reasonably good, then bin migration effects will be corrected at the efficiency correction stage.

The significance of bin migration may be investigated by studying the resolution of q^2_{T} measurements in each q^2_{T} analysis bin. The resulting plots show the resolution in q^2_{T} by comparing the number of true q^2_{T} events (y-axis) versus the number of reconstructed q^2_{T} events (x-axis) for the signal MC sample. The plots are shown in Figure 8.8 for each of the three λ slices. The number of events on the off diagonals is very small compared to the number of events on the diagonals, with detailed event statistics shown in Tables 8.11, 8.12, and 8.13 for λ slices 30, 40, and 50 respectively. As such the number of events crossing the bin boundaries is not large and will have already been taken into account by the efficiency correction process.

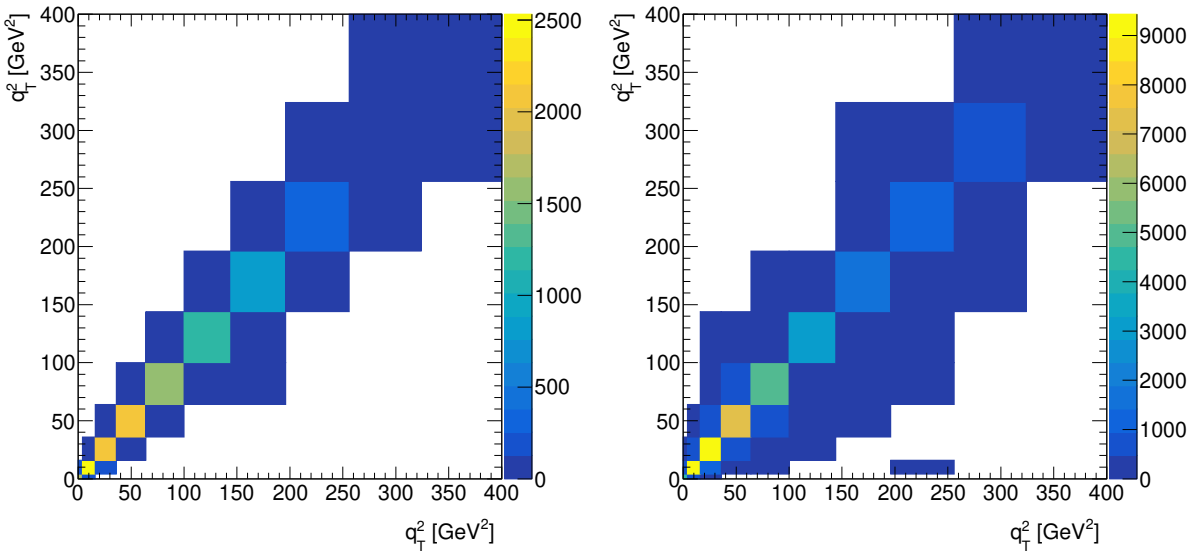

(a) λ region 30: $25 \leq \lambda \leq 50$

(b) λ region 40: $50 \leq \lambda \leq 100$

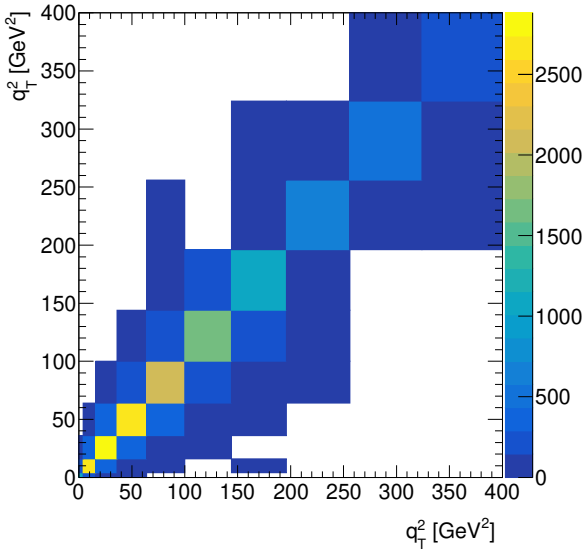

(c) λ region 50: $100 \leq \lambda \leq 200$

Figure 8.8: The 2D plots illustrating the resolution in q_{T}^2 for (a) λ region 30 ($25 \leq \lambda < 50$), (b) λ region 40 ($50 \leq \lambda < 100$), and (c) λ region 50 ($100 \leq \lambda < 200$), for the full range in q_{T}^2 ($0 \leq q_{\mathrm{T}}^2 < 400$ GeV^2). True values of q_{T}^2 are shown on the y-axis, while the reconstructed values are shown on the x-axis.

$324 \leq q_{\mathrm{T}}^2 < 400$	0	0	0	0	0	0	0	0	2	32
$256 \leq q_{\mathrm{T}}^2 < 324$	0	0	0	0	0	0	0	13	108	8
$196 \leq q_{\mathrm{T}}^2 < 256$	0	0	0	0	0	0	52	336	27	0
$144 \leq q_{\mathrm{T}}^2 < 196$	0	0	0	0	0	74	785	59	0	0
$100 \leq q_{\mathrm{T}}^2 < 144$	0	0	0	0	104	1255	96	0	0	0
$64 \leq q_{\mathrm{T}}^2 < 100$	0	0	0	105	1633	122	0	0	0	0
$36 \leq q_{\mathrm{T}}^2 < 64$	0	0	84	2074	107	0	0	0	0	0
$16 \leq q_{\mathrm{T}}^2 < 36$	0	95	2089	118	0	0	0	0	0	0
$4 \leq q_{\mathrm{T}}^2 < 16$	147	2531	155	0	0	0	0	0	0	0
$0 \leq q_{\mathrm{T}}^2 < 4$	1716	185	0	0	0	0	0	0	0	0
True ↑ Reconstructed → q_{T}^2 Region (GeV^2)	$0 \leq q_{\mathrm{T}}^2 < 4$	$4 \leq q_{\mathrm{T}}^2 < 16$	$16 \leq q_{\mathrm{T}}^2 < 36$	$36 \leq q_{\mathrm{T}}^2 < 64$	$64 \leq q_{\mathrm{T}}^2 < 100$	$100 \leq q_{\mathrm{T}}^2 < 144$	$144 \leq q_{\mathrm{T}}^2 < 196$	$196 \leq q_{\mathrm{T}}^2 < 256$	$256 \leq q_{\mathrm{T}}^2 < 324$	$324 \leq q_{\mathrm{T}}^2 < 400$

Table 8.11: A numerical description of the resolution for λ region 30 ($25 \leq \lambda < 50$) in each q_{T}^2 bin. True values of q_{T}^2 are shown on the y-'axis', while the reconstructed values are shown on the x-'axis'. Each cell shows the number of events after truth and reconstructed cuts in each $\lambda - q_{\mathrm{T}}^2$ region.

$324 \leq q_{\mathrm{T}}^2 < 400$	0	0	0	0	0	0	0	0	32	235
$256 \leq q_{\mathrm{T}}^2 < 324$	0	0	0	0	0	0	3	65	476	54
$196 \leq q_{\mathrm{T}}^2 < 256$	0	0	0	0	0	0	120	1055	83	0
$144 \leq q_{\mathrm{T}}^2 < 196$	0	0	0	0	2	214	1827	138	1	0
$100 \leq q_{\mathrm{T}}^2 < 144$	0	0	1	6	341	3240	271	4	0	0
$64 \leq q_{\mathrm{T}}^2 < 100$	0	0	8	500	4975	370	6	1	0	0
$36 \leq q_{\mathrm{T}}^2 < 64$	0	12	706	7245	611	2	1	0	0	0
$16 \leq q_{\mathrm{T}}^2 < 36$	5	868	9192	761	15	1	0	0	0	0
$4 \leq q_{\mathrm{T}}^2 < 16$	781	9431	953	16	1	0	0	1	0	0
$0 \leq q_{\mathrm{T}}^2 < 4$	4553	811	11	0	0	0	0	0	0	0
True ↑ Reconstructed → q_{T}^2 Region (GeV^2)	$0 \leq q_{\mathrm{T}}^2 < 4$	$4 \leq q_{\mathrm{T}}^2 < 16$	$16 \leq q_{\mathrm{T}}^2 < 36$	$36 \leq q_{\mathrm{T}}^2 < 64$	$64 \leq q_{\mathrm{T}}^2 < 100$	$100 \leq q_{\mathrm{T}}^2 < 144$	$144 \leq q_{\mathrm{T}}^2 < 196$	$196 \leq q_{\mathrm{T}}^2 < 256$	$256 \leq q_{\mathrm{T}}^2 < 324$	$324 \leq q_{\mathrm{T}}^2 < 400$

Table 8.12: A numerical description of the resolution for λ region 40 ($50 \leq \lambda < 100$) in each q_{T}^2 bin. True values of q_{T}^2 are shown on the y-'axis', while the reconstructed values are shown on the x-'axis'. Each cell shows the number of events after truth and reconstructed cuts in each $\lambda - q_{\mathrm{T}}^2$ region.

$324 \leq q_{\mathrm{T}}^2 < 400$	0	0	0	0	0	0	0	0	48	262
$256 \leq q_{\mathrm{T}}^2 < 324$	0	0	0	0	0	0	2	66	445	42
$196 \leq q_{\mathrm{T}}^2 < 256$	0	0	0	0	1	0	116	712	66	2
$144 \leq q_{\mathrm{T}}^2 < 196$	0	0	0	0	5	146	1104	135	0	0
$100 \leq q_{\mathrm{T}}^2 < 144$	0	0	0	9	212	1641	178	3	0	0
$64 \leq q_{\mathrm{T}}^2 < 100$	0	0	6	278	2088	234	5	1	0	0
$36 \leq q_{\mathrm{T}}^2 < 64$	0	10	325	2624	289	5	2	0	0	0
$16 \leq q_{\mathrm{T}}^2 < 36$	4	297	2882	305	6	2	0	0	0	0
$4 \leq q_{\mathrm{T}}^2 < 16$	216	2659	347	10	1	0	1	0	0	0
$0 \leq q_{\mathrm{T}}^2 < 4$	1143	249	5	1	0	0	0	0	0	0
True ↑ Reconstructed → q_{T}^2 Region (GeV^2)	$0 \leq q_{\mathrm{T}}^2 < 4$	$4 \leq q_{\mathrm{T}}^2 < 16$	$16 \leq q_{\mathrm{T}}^2 < 36$	$36 \leq q_{\mathrm{T}}^2 < 64$	$64 \leq q_{\mathrm{T}}^2 < 100$	$100 \leq q_{\mathrm{T}}^2 < 144$	$144 \leq q_{\mathrm{T}}^2 < 196$	$196 \leq q_{\mathrm{T}}^2 < 256$	$256 \leq q_{\mathrm{T}}^2 < 324$	$324 \leq q_{\mathrm{T}}^2 < 400$

Table 8.13: A numerical description of the resolution for λ region 50 ($100 \leq \lambda < 200$) in each q_{T}^2 bin. True values of q_{T}^2 are shown on the y-'axis', while the reconstructed values are shown on the x-'axis'. Each cell shows the number of events after truth and reconstructed cuts in each $\lambda - q_{\mathrm{T}}^2$ region.

Chapter 9

Results

9.0.1 Differential Distributions In q_T^2

The summary of (relative) errors collected from the systematic studies, for the differential cross sections with respect to q_T^2 in the three λ slices, is given in Tables 9.1 – 9.3.

The third column in the tables the relative statistical error, and the fourth column is the relative BDT systematic error for a bin. The fifth and sixth columns are the relative mass and lifetime (tau) systematics for a bin. The relative tau systematic is the relative average of the τ_1 and τ_2 systematics added in quadrature, as seen column 6 in the tables. Column seven is the relative efficiency systematic which is taken from the last column in Tables 8.6 – 8.10. The total relative systematic error and total relative error are given in columns eight and nine.

Bin	q^2_{T} Region (GeV^2)	Rel. Stat. Error %	Rel. BDT Syst. %	Rel. Mass Syst. %	Rel. Tau Syst. %	Rel. eff-cy Syst. %	Total rel. Syst %	Total rel. error %
1	$0 \leq q^2_{\mathrm{T}} < 4$	7.9	3.0	3.3	2.2	7.3	8.8	11.9
2	$4 \leq q^2_{\mathrm{T}} < 16$	6.4	1.9	2.2	2.0	7.2	8.0	10.3
3	$16 \leq q^2_{\mathrm{T}} < 36$	8.2	7.6	2.6	2.7	7.3	11.2	13.9
4	$36 \leq q^2_{\mathrm{T}} < 64$	7.6	1.3	2.2	4.6	7.1	8.9	11.7
5	$64 \leq q^2_{\mathrm{T}} < 100$	7.3	2.1	7.4	1.7	7.2	10.6	12.9
6	$100 \leq q^2_{\mathrm{T}} < 144$	9.8	9.4	4.6	3.3	7.2	13.1	16.4
7	$144 \leq q^2_{\mathrm{T}} < 196$	9.3	9.3	1.2	5.8	7.1	13.1	16.1
8	$196 \leq q^2_{\mathrm{T}} < 256$	12.5	4.5	4.5	5.0	7.6	11.1	16.7
9	$256 \leq q^2_{\mathrm{T}} < 324$	22.2	24.0	9.8	3.5	9.4	27.8	35.6
10	$324 \leq q^2_{\mathrm{T}} < 400$	28.6	23.5	2.8	9.5	13.4	28.9	40.7

Table 9.1: Relative error summary table for λ slice 30: $25 \leq \lambda < 50$ region.

Bin	q^2_{T} Region (GeV^2)	Rel. Stat. Error %	Rel. BDT Syst. %	Rel. Mass Syst. %	Rel. Tau Syst. %	Rel. eff-cy Syst. %	Total rel. Syst %	Total rel. error %
1	$0 \leq q^2_{\mathrm{T}} < 4$	7.2	5.8	2.9	2.9	6.3	9.5	11.9
2	$4 \leq q^2_{\mathrm{T}} < 16$	5.0	10.1	1.0	4.0	6.2	12.5	13.5
3	$16 \leq q^2_{\mathrm{T}} < 36$	5.4	5.8	2.2	3.2	6.2	9.3	10.8
4	$36 \leq q^2_{\mathrm{T}} < 64$	6.3	3.5	1.8	4.2	6.2	8.4	10.5
5	$64 \leq q^2_{\mathrm{T}} < 100$	6.3	2.6	2.3	5.6	6.1	9.0	11.0
6	$100 \leq q^2_{\mathrm{T}} < 144$	6.9	5.2	5.6	5.5	6.0	11.2	13.2
7	$144 \leq q^2_{\mathrm{T}} < 196$	7.2	4.8	4.8	3.8	6.0	9.8	12.2
8	$196 \leq q^2_{\mathrm{T}} < 256$	8.6	3.6	1.7	4.2	6.1	8.4	12.0
9	$256 \leq q^2_{\mathrm{T}} < 324$	10.7	10.6	2.2	9.1	6.5	15.6	18.9
10	$324 \leq q^2_{\mathrm{T}} < 400$	13.6	7.2	1.9	3.8	6.9	10.9	17.4

Table 9.2: Relative error summary table for λ slice 40: $50 \leq \lambda < 100$ region.

Bin	q_T^2 Region (GeV^2)	Rel. Stat. Error %	Rel. BDT Syst. %	Rel. Mass Syst. %	Rel. Tau Syst. %	Rel. eff-cy Syst. %	Total rel. Syst %	Total rel. error %
1	$0 \leq q_T^2 < 4$	8.9	10.6	2.9	2.9	6.0	12.9	15.6
2	$4 \leq q_T^2 < 16$	7.5	4.4	8.3	5.8	5.7	12.4	14.5
3	$16 \leq q_T^2 < 36$	6.1	5.1	1.2	5.4	5.5	9.4	11.2
4	$36 \leq q_T^2 < 64$	5.4	2.8	1.0	6.5	5.5	9.0	10.5
5	$64 \leq q_T^2 < 100$	6.4	5.0	4.6	5.0	5.4	10.0	11.9
6	$100 \leq q_T^2 < 144$	7.6	9.1	5.6	5.2	5.3	13.0	15.1
7	$144 \leq q_T^2 < 196$	6.9	6.1	1.3	6.8	5.3	10.7	12.7
8	$196 \leq q_T^2 < 256$	7.0	4.6	2.5	3.4	5.6	8.4	10.9
9	$256 \leq q_T^2 < 324$	8.3	5.4	1.6	3.4	6.0	8.8	12.2
10	$324 \leq q_T^2 < 400$	11.4	5.4	6.9	6.0	6.4	12.3	16.8

Table 9.3: Relative error summary table for λ slice 50: $100 \leq \lambda < 200$ region.

The final sets of corrections and uncertainties, were applied to the cross sections determined in Chapter 7. The differential cross sections with respect to the transverse momentum squared of the dimuon-photon system, q_T^2, are shown below in the form of tables Tables 9.4, 9.5 and 9.6 covering the λ slices 30, 40 and 50, respectively. The latter three columns in each table detail the statistical error, the total systematic error, and the total error respectively.

Bin	q_T^2 Region (GeV^2)	$d\sigma/dq_T^2$ (pb/GeV^2)	Stat. Error (pb/GeV^2)	Syst. Error (pb/GeV^2)	Total error (pb/GeV^2)
1	$0 \leq q_T^2 < 4$	0.1971	0.0157	0.0174	0.0234
2	$4 \leq q_T^2 < 16$	0.1187	0.0076	0.0095	0.0122
3	$16 \leq q_T^2 < 36$	0.0562	0.0046	0.0063	0.0078
4	$36 \leq q_T^2 < 64$	0.0384	0.0029	0.0034	0.0045
5	$64 \leq q_T^2 < 100$	0.0367	0.0027	0.0039	0.0047
6	$100 \leq q_T^2 < 144$	0.0222	0.0022	0.0029	0.0036
7	$144 \leq q_T^2 < 196$	0.0174	0.0016	0.0023	0.0028
8	$196 \leq q_T^2 < 256$	0.0087	0.0011	0.0010	0.0015
9	$256 \leq q_T^2 < 324$	0.0026	0.0006	0.0007	0.0009
10	$324 \leq q_T^2 < 400$	0.0016	0.0004	0.0005	0.0006

Table 9.4: Fully corrected differential cross section results in q_T^2 bins for λ slice 30: $25 \leq \lambda < 50$ region.

Bin	q_{T}^2 Region (GeV^2)	$d\sigma/dq_{\mathrm{T}}^2$ ($\mathrm{pb/GeV}^2$)	Stat. Error ($\mathrm{pb/GeV}^2$)	Syst. Error ($\mathrm{pb/GeV}^2$)	Total error ($\mathrm{pb/GeV}^2$)
1	$0 \leq q_{\mathrm{T}}^2 < 4$	0.2962	0.0212	0.0282	0.0353
2	$4 \leq q_{\mathrm{T}}^2 < 16$	0.2240	0.0112	0.0281	0.0302
3	$16 \leq q_{\mathrm{T}}^2 < 36$	0.1615	0.0088	0.0151	0.0175
4	$36 \leq q_{\mathrm{T}}^2 < 64$	0.0853	0.0054	0.0072	0.0090
5	$64 \leq q_{\mathrm{T}}^2 < 100$	0.0512	0.0032	0.0046	0.0056
6	$100 \leq q_{\mathrm{T}}^2 < 144$	0.0329	0.0023	0.0037	0.0043
7	$144 \leq q_{\mathrm{T}}^2 < 196$	0.0205	0.0015	0.0020	0.0025
8	$196 \leq q_{\mathrm{T}}^2 < 256$	0.0115	0.0010	0.0010	0.0014
9	$256 \leq q_{\mathrm{T}}^2 < 324$	0.0071	0.0008	0.0011	0.0013
10	$324 \leq q_{\mathrm{T}}^2 < 400$	0.0039	0.0005	0.0004	0.0007

Table 9.5: Fully corrected differential cross section results in q_{T}^2 bins for λ slice 40: $50 \leq \lambda < 100$ region.

Bin	q_{T}^2 Region (GeV^2)	$d\sigma/dq_{\mathrm{T}}^2$ ($\mathrm{pb/GeV}^2$)	Stat. Error ($\mathrm{pb/GeV}^2$)	Syst. Error ($\mathrm{pb/GeV}^2$)	Total error ($\mathrm{pb/GeV}^2$)
1	$0 \leq q_{\mathrm{T}}^2 < 4$	0.1229	0.0109	0.0158	0.0192
2	$4 \leq q_{\mathrm{T}}^2 < 16$	0.0726	0.0054	0.0090	0.0105
3	$16 \leq q_{\mathrm{T}}^2 < 36$	0.0588	0.0036	0.0055	0.0066
4	$36 \leq q_{\mathrm{T}}^2 < 64$	0.0477	0.0026	0.0043	0.0050
5	$64 \leq q_{\mathrm{T}}^2 < 100$	0.0329	0.0021	0.0033	0.0039
6	$100 \leq q_{\mathrm{T}}^2 < 144$	0.0180	0.0014	0.0023	0.0027
7	$144 \leq q_{\mathrm{T}}^2 < 196$	0.0154	0.0011	0.0016	0.0020
8	$196 \leq q_{\mathrm{T}}^2 < 256$	0.0126	0.0009	0.0011	0.0014
9	$256 \leq q_{\mathrm{T}}^2 < 324$	0.0090	0.0008	0.0008	0.0011
10	$324 \leq q_{\mathrm{T}}^2 < 400$	0.0049	0.0006	0.0006	0.0008

Table 9.6: Fully corrected differential cross section results in q_{T}^2 bins for λ slice 50: $100 \leq \lambda < 200$ region.

The distributions for the differential cross sections are shown in Figures 9.1(a), 9.2(a) and 9.3(a). With reference to Section 3.3.7, it is shown that a measurement of the differential cross section (see Eqn. 3.3.7) as a function of q_{T}^2 is a measurement of the convolution $\mathcal{C}[f_1^g f_1^g]$ where the convolution definition is Eqn. 3.9, with the choice of f_1^g given by Eqn. 3.10. The Gaussian definition for f_1^g is dependent on the average k_{T} of a gluon, which motivates fitting the distributions with an exponential:

$$F(q_T^2) = p_0 \cdot \exp\left(-\frac{q_T^2}{2p_1^2}\right) + p_2 \cdot \exp\left(-\frac{q_T^2}{2p_3^2}\right) \tag{9.1}$$

Following the theoretical considerations which can be reviewed in Section 3.3.7, the smallest of the two parameters, p_3, is characterising the width of the intrinsic transverse momentum of the gluon distribution, while the larger one, p_1, describes the behaviour of the high-q_{T} tail, likely due to hard(er) gluon emission at some stage of the reaction.

In order to highlight the Gaussian nature of the distributions in terms of q_{T} (as opposed to q_{T}^2, where the distribution is exponential), the distributions were re-binned with q_{T} bins on the x-axis. These are shown in Figures 9.1(b), 9.2(b) and 9.3(b) for the three λ slices. As mentioned before, the binning in q_{T}^2 was chosen such that in q_{T} the bins have equal widths of 2 GeV.

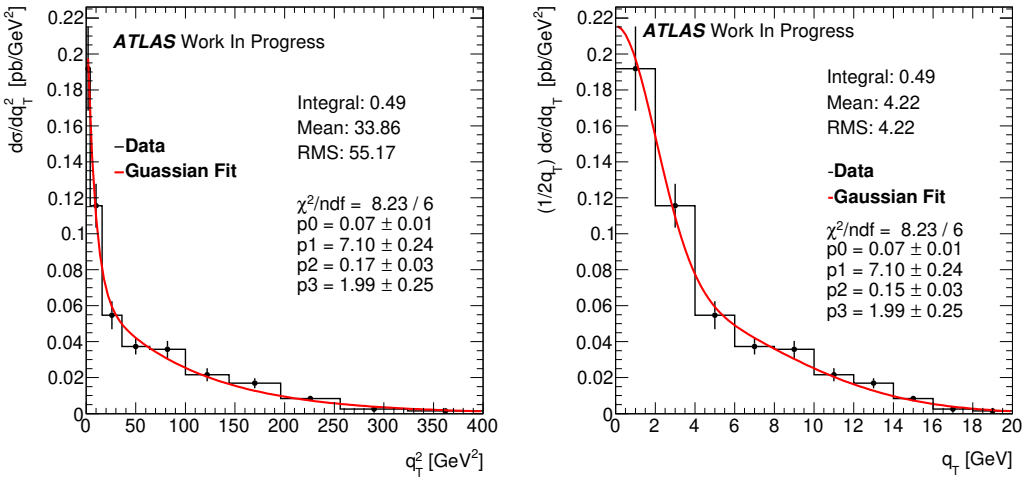

Figure 9.1: Differential cross sections presented as a function of (a) q_{T}^2 and as a function of (b) q_{T}, for λ slice 30: $25 \leq \lambda < 50$.

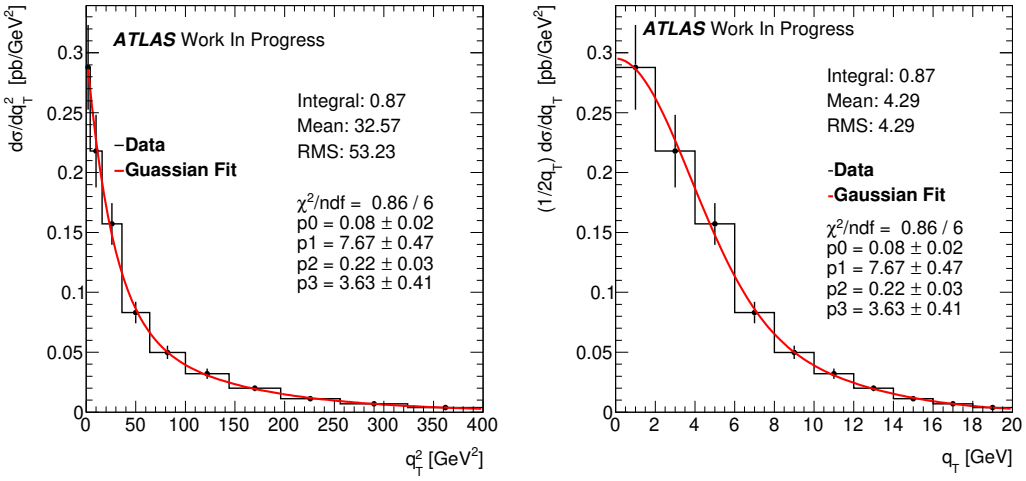

Figure 9.2: Differential cross sections presented as a function of (a) q_{T}^2 and as a function of (b) q_{T}, for λ slice 40: $50 \leq \lambda < 100$.

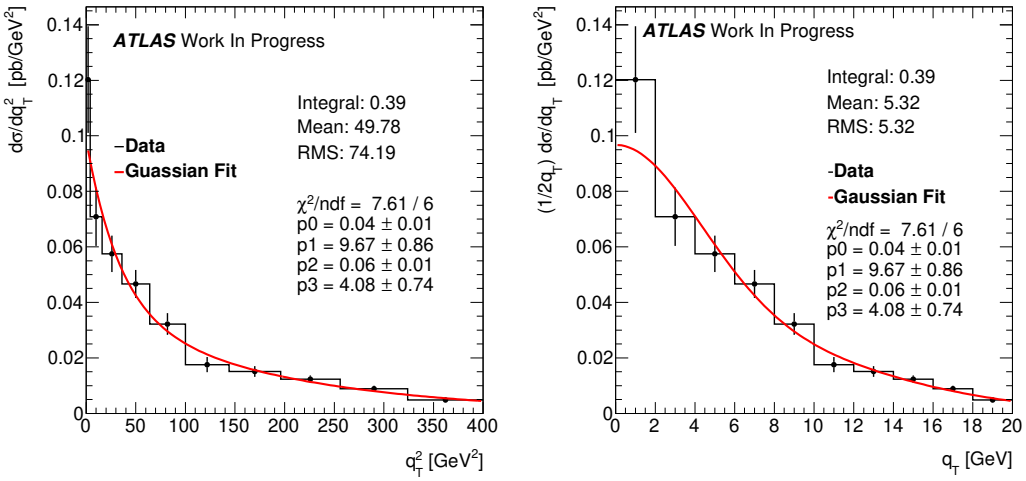

Figure 9.3: Differential cross sections presented as a function of(a) q_{T}^2 and as a function of (b) q_{T}, for λ slice 50: $100 \leq \lambda < 200$.

To summarise, the average k_{T} of a gluon has been measured in three different λ regions as a function of q_{T}, which the results compiled in Table 9.7. As the invariant mass of the J/$\psi - \gamma$ system is increased, so does the mean intrinsic k_{T} of a gluon, which is reflected in the p_3 parameter, shown in Table 9.8. These results are in agreement with those found in a truth study presented in Section 3.3.7, which says that the mean intrinsic k_{T} should increase with increasing Q. In the results presented in Table 9.7, it can be seen that with

increasing invariant mass, the average k_{T} of a gluon increases its width faster than the term describing the tail which is given by the parameter p_1.

λ Slice	Invariant Mass Range Q GeV	p_0	p_1	p_2	p_3
3	$15 \leq Q < 22$	0.07 ± 0.01	7.10 ± 0.24	0.15 ± 0.03	1.99 ± 0.25
4	$22 \leq Q < 31$	0.08 ± 0.02	7.67 ± 0.47	0.22 ± 0.03	3.63 ± 0.41
5	$31 \leq Q < 44$	0.04 ± 0.01	9.67 ± 0.86	0.06 ± 0.01	4.08 ± 0.74

Table 9.7: Table of fit results for q_{T} for each of the fitting parameters. The parameters of interest are p_1 and p_3. p_1 describes the behaviour of the high q_{T} tail, and p_3 characterises the width of the intrinsic mean transverse momentum of a gluon.

Q (GeV)	$\sqrt{\langle k_{\mathrm{T}}^2 \rangle}$ (GeV)
$15 \leq Q < 22$	1.99 ± 0.25
$22 \leq Q < 31$	3.63 ± 0.41
$31 \leq Q < 44$	4.08 ± 0.74

Table 9.8: Table of results for the intrinsic mean gluon transverse momentum, $\sqrt{\langle k_{\mathrm{T}}^2 \langle}$, measured at three different invariant mass ranges, Q, of the J/$\psi + \gamma$ system.

9.0.2 Angular Analysis In The Collins-Soper Frame

Numerical results for the relative errors in bins of Collins-Soper angular variable ϕ_{CS} are shown in Tables 9.9 and 9.10 for Low and High z^2 slices respectively. The fully corrected numerical results for the respective cross sections are shown in Tables 9.11 and 9.12 and are shown in Figure 9.4.

Bin	$\lvert\phi_{\mathrm{CS}}\rvert$ Region (rad)	Rel. Stat. Error %	Rel. BDT Syst. %	Rel. Mass Syst. %	Rel. Tau Syst. %	Rel. eff-cy Syst. %	Total rel. Syst %	Total rel. error %
1	$0 \leq \lvert\phi_{\mathrm{CS}}\rvert < \frac{\pi}{8}$	6.6	3.2	1.4	0.4	6.8	8.0	10.4
2	$\frac{\pi}{8} \leq \lvert\phi_{\mathrm{CS}}\rvert < \frac{\pi}{4}$	6.1	1.4	1.6	1.9	6.7	8.1	10.1
3	$\frac{\pi}{4} \leq \lvert\phi_{\mathrm{CS}}\rvert < \frac{3\pi}{8}$	6.0	7.1	1.7	1.5	6.9	11.3	12.8
4	$\frac{3\pi}{8} \leq \lvert\phi_{\mathrm{CS}}\rvert < \frac{\pi}{2}$	6.4	13.2	1.4	1.4	6.6	16.0	17.3
5	$\frac{\pi}{2} \leq \lvert\phi_{\mathrm{CS}}\rvert < \frac{5\pi}{8}$	6.7	10.9	1.6	1.7	6.0	13.9	15.4
6	$\frac{5\pi}{8} \leq \lvert\phi_{\mathrm{CS}}\rvert < \frac{3\pi}{4}$	5.4	3.5	1.7	8.6	5.4	12.8	13.9
7	$\frac{3\pi}{4} \leq \lvert\phi_{\mathrm{CS}}\rvert < \frac{7\pi}{8}$	6.5	12.1	1.6	5.2	5.3	14.8	16.2
8	$\frac{7\pi}{8} \leq \lvert\phi_{\mathrm{CS}}\rvert < \pi$	5.0	1.3	1.6	4.6	5.2	9.5	10.7

Table 9.9: Relative error summary table for $|\phi_{CS}|$ low.

Bin	$\lvert\phi_{\mathrm{CS}}\rvert$ Region (rad)	Rel. Stat. Error %	Rel. BDT Syst. %	Rel. Mass Syst. %	Rel. Tau Syst. %	Rel. eff-cy Syst. %	Total rel. Syst %	Total rel. error %
1	$0 \leq \lvert\phi_{\mathrm{CS}}\rvert < \frac{\pi}{8}$	6.4	3.2	1.8	3.0	6.9	9.2	11.2
2	$\frac{\pi}{8} \leq \lvert\phi_{\mathrm{CS}}\rvert < \frac{\pi}{4}$	8.6	7.7	1.4	5.8	6.9	12.2	14.9
3	$\frac{\pi}{4} \leq \lvert\phi_{\mathrm{CS}}\rvert < \frac{3\pi}{8}$	7.1	8.6	1.5	3.5	6.7	12.4	14.3
4	$\frac{3\pi}{8} \leq \lvert\phi_{\mathrm{CS}}\rvert < \frac{\pi}{2}$	6.3	13.4	1.6	4.0	6.7	17.6	18.7
5	$\frac{\pi}{2} \leq \lvert\phi_{\mathrm{CS}}\rvert < \frac{5\pi}{8}$	6.6	12.3	1.3	5.0	6.0	16.1	17.4
6	$\frac{5\pi}{8} \leq \lvert\phi_{\mathrm{CS}}\rvert < \frac{3\pi}{4}$	5.9	8.5	1.6	2.1	5.5	12.6	13.9
7	$\frac{3\pi}{4} \leq \lvert\phi_{\mathrm{CS}}\rvert < \frac{7\pi}{8}$	5.9	5.2	1.3	4.5	5.4	10.1	11.7
8	$\frac{7\pi}{8} \leq \lvert\phi_{\mathrm{CS}}\rvert < \pi$	7.0	3.1	1.8	7.7	5.4	12.2	14.1

Table 9.10: Relative error summary table for $|\phi_{CS}|$ high.

Bin	$\lvert\phi_{\mathrm{CS}}\rvert$ Region (rad)	$d\sigma/d\lvert\phi_{\mathrm{CS}}\rvert$ (pb/rad)	Stat. Error (pb/rad)	Syst. Error (pb/rad)	Total error (pb/rad)
1	$0 \leq \lvert\phi_{\mathrm{CS}}\rvert < \frac{\pi}{8}$	2.04	0.14	0.16	0.21
2	$\frac{\pi}{8} \leq \lvert\phi_{\mathrm{CS}}\rvert < \frac{\pi}{4}$	2.66	0.16	0.21	0.27
3	$\frac{\pi}{4} \leq \lvert\phi_{\mathrm{CS}}\rvert < \frac{3\pi}{8}$	3.53	0.21	0.40	0.45
4	$\frac{3\pi}{8} \leq \lvert\phi_{\mathrm{CS}}\rvert < \frac{\pi}{2}$	4.94	0.32	0.79	0.85
5	$\frac{\pi}{2} \leq \lvert\phi_{\mathrm{CS}}\rvert < \frac{5\pi}{8}$	4.32	0.29	0.60	0.66
6	$\frac{5\pi}{8} \leq \lvert\phi_{\mathrm{CS}}\rvert < \frac{3\pi}{4}$	4.91	0.26	0.63	0.68
7	$\frac{3\pi}{4} \leq \lvert\phi_{\mathrm{CS}}\rvert < \frac{7\pi}{8}$	3.12	0.20	0.46	0.50
8	$\frac{7\pi}{8} \leq \lvert\phi_{\mathrm{CS}}\rvert < \pi$	4.79	0.24	0.46	0.52

Table 9.11: Fully corrected differential cross section results in $|\phi_{CS}|$ bins for low z^2.

Bin	$\lvert\phi_{\mathrm{CS}}\rvert$ Region (rad)	$d\sigma/d\lvert\phi_{\mathrm{CS}}\rvert$ (pb/rad)	Stat. Error (pb/rad)	Syst. Error (pb/rad)	Total error (pb/rad)
1	$0 \leq \lvert\phi_{\mathrm{CS}}\rvert < \frac{\pi}{8}$	2.79	0.18	0.26	0.31
2	$\frac{\pi}{8} \leq \lvert\phi_{\mathrm{CS}}\rvert < \frac{\pi}{4}$	2.36	0.20	0.29	0.35
3	$\frac{\pi}{4} \leq \lvert\phi_{\mathrm{CS}}\rvert < \frac{3\pi}{8}$	3.69	0.26	0.46	0.53
4	$\frac{3\pi}{8} \leq \lvert\phi_{\mathrm{CS}}\rvert < \frac{\pi}{2}$	5.77	0.37	1.02	1.08
5	$\frac{\pi}{2} \leq \lvert\phi_{\mathrm{CS}}\rvert < \frac{5\pi}{8}$	6.01	0.39	0.97	1.04
6	$\frac{5\pi}{8} \leq \lvert\phi_{\mathrm{CS}}\rvert < \frac{3\pi}{4}$	5.32	0.31	0.67	0.74
7	$\frac{3\pi}{4} \leq \lvert\phi_{\mathrm{CS}}\rvert < \frac{7\pi}{8}$	4.59	0.27	0.46	0.54
8	$\frac{7\pi}{8} \leq \lvert\phi_{\mathrm{CS}}\rvert < \pi$	4.67	0.33	0.57	0.66

Table 9.12: Fully corrected differential cross section results in $|\phi_{CS}|$ bins for high z^2.

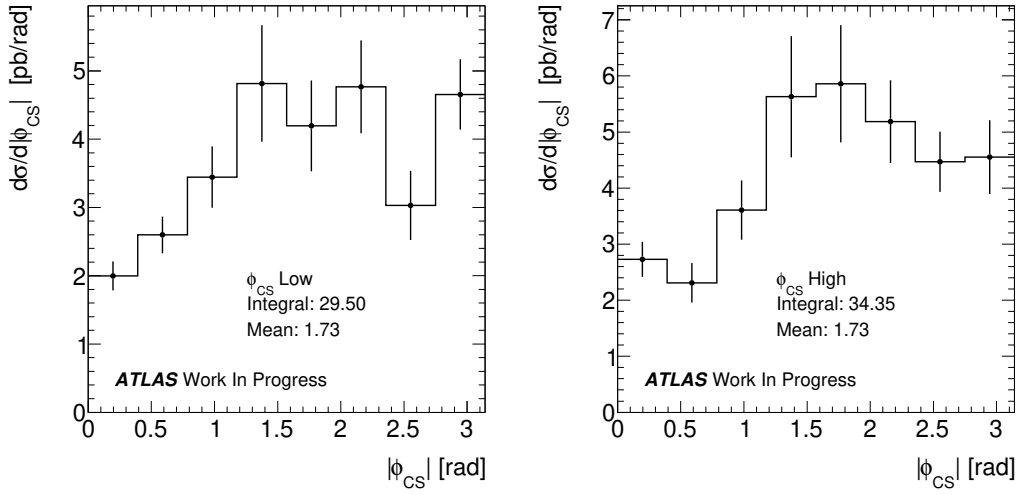

Figure 9.4: Differential cross sections as functions of $|\phi_{CS}|$, for (a) $\cos^2\theta_{CS} < 0.1$ and (b) $\cos^2\theta_{CS} > 0.1$.

The ratio of the two distributions is presented in Figure 9.5. The figure also shows the results of a fit to a Fourier series truncated after the $4\phi_{\mathrm{CS}}$ term:

$$\frac{d\sigma(z^2 < 0.1)}{d\sigma(z^2 > 0.1)} = p_0 \cdot (1 + p_1 \cos\phi_{CS} + p_2 \cos 2\phi_{CS} + p_3 \cos 3\phi_{CS} + p_4 \cos 4\phi_{CS})\,. \qquad (9.2)$$

Terms of $\mathcal{O}(\cos(5\phi_{CS}))$ are negligible, and the basis functions (cosines) are orthogonal, hence their coefficients are independent. Removing odd terms in the series should not change the values of the even term's coefficients. Keeping odd terms gives confidence to the results as they should not be large.

The interesting parameter here is the coefficient p_4 in front of the $\cos(4\phi_{CS})$ term seen in Eqn. 3.3.7, which, according to the theory, should indicate the relative size of the polarised gluon TMD $h_1^{\perp g}$ with respect to the unpolarised gluon TMD f_1^g. The fit resulted in the value

$$p_4 = -0.050 \pm 0.104(\text{stat.}) \pm 0.015(\text{syst.}) \tag{9.3}$$

Although this result for p_4 is zero within errors, it is a first measurement of its kind! The analysis has measured the coefficient of the $\cos(4\phi_{\text{CS}})$ term in Eqn. 3.3.7, relative to the ϕ_{CS} independent term. This term was not expected to be large, and in the theoretical models described in Section 3.3.6, the amplitude of the term is predicted to be between $1 - 5$ %, so one cannot exclude a zero result, however it is apparent that the analysis under current LHC conditions is not sensitive enough to make a measurement.

In order to check the sensitivity of the parameter p_4 towards the variation of the low-high separating cut on $z^2 \equiv \cos^2\theta_{CS}$, the cut was varied from its nominal value of 0.1 to 0.095 and then separately to 0.105, and the analysis was repeated. This serves as the systematic uncertainty in the value of p_4. The corresponding changes in the values of p_4 were within 0.02 of the central number, as shown by the second uncertainty in Eqn. 9.3.

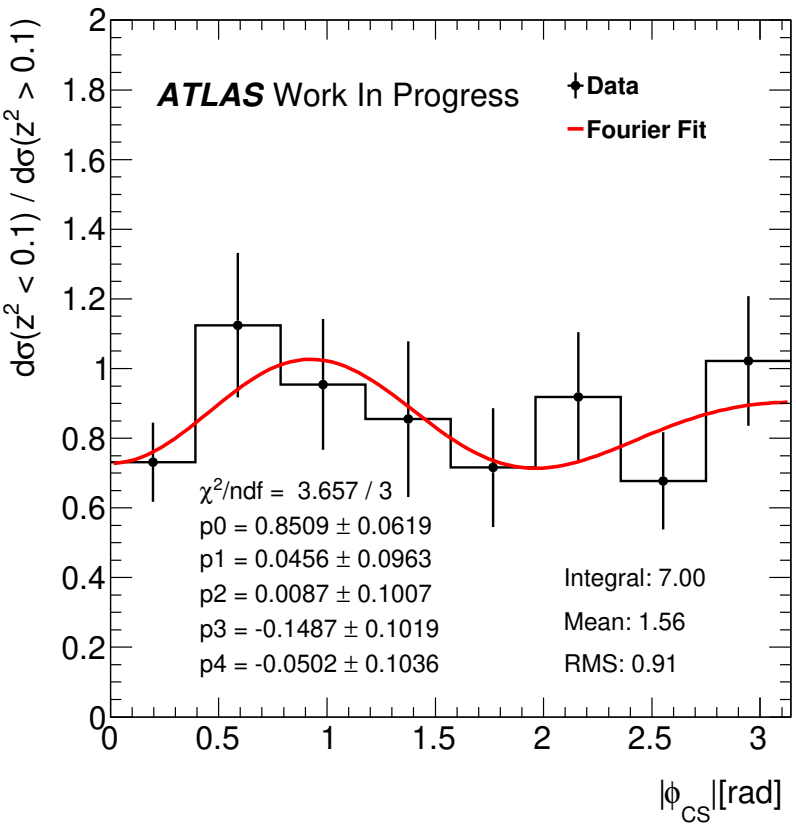

Figure 9.5: The Low/High ratio of the two distributions in $|\phi_{CS}|$, fitted to a truncated Fourier series.

Chapter 10

Conclusions

To conclude this thesis, the process of inclusive associated production of a J/ψ meson and a γ in a gluon fusion process was used to perform two first measurements in the area of transverse-momentum-dependent (TMD) distributions, whilst simultaneously making a measurement of the continuum J/$\psi + \gamma$ cross section.. The measurements have been performed on data collected by the ATLAS experiment at a C.o.M energy of 13 TeV in 2015, and uses events triggered by a dimuon trigger with a threshold $p_{\mathrm{T}}(\mu^{\pm}) > 4$ GeV, corresponding to an effective luminosity of 2574 pb^{-1}.

The first measurement concerns the TMD function f_1^g which describes the distribution of unpolarised gluons inside an unpolarised proton. Assuming a Gaussian shape of the TMD distribution $f_1^g(k_{\mathrm{T}}^2)$ with dependence on the intrinsic transverse momentum of a gluon, k_{T}, a measurement of the mean transverse momentum was performed at three different invariant mass ranges, Q, of the J/$\psi - \gamma$ system as a function of the transverse momentum q_{T} of said system. For the lowest invariant mass range considered, $15 \leq Q < 22$ GeV it was found that $\sqrt{\langle k_{\mathrm{T}}^2 \rangle} = 1.99 \pm 0.25$ GeV. In the second mass range considered $22 \leq Q < 31$ GeV, it was measured that $\sqrt{\langle k_{\mathrm{T}}^2 \rangle} = 3.63 \pm 0.41$ GeV. Finally, for the last mass range $31 \leq Q < 44$ GeV it was found that $\sqrt{\langle k_{\mathrm{T}}^2 \rangle} = 4.08 \pm 0.74$ GeV. The mean transverse momentum, k_{T}, increases for increasing invariant mass range Q, which is in agreement with results from a truth study performed in Section 3.3.7.

The second measurement was an attempt to measure the contribution of the TMD function $h_1^{\perp g}(k_{\mathrm{T}}^2)$ which describes the distribution of linearly polarised gluons inside an unpolarised

proton. This was performed through a measurement of the differential cross section of the J/$\psi - \gamma$ system as a function of ϕ in the Collins-Soper frame, ϕ_{CS}. Interacting polarised gluons are expected to lead to angular distributions modulated by a $\cos(4\phi_{\mathrm{CS}})$ term, which the analysis sought to measure. No statistically significant modulation was observed, with the coefficient of the $\cos(4\phi_{\mathrm{CS}})$ term measured to be -0.050 ± 0.104 (stat.) ± 0.015 (syst.). This result is consistent with zero, which is to be expected based on conclusions drawn from a truth study in Section 3.3.6.

A future analysis using the full Run II statistics will have to use a dimuon trigger with higher thresholds, but could nevertheless produce a similar set of measurements for a broader range of invariant masses with a higher statistical precision.

Appendices

Appendix A

Collins-Soper Frame

The analysis has a $2 \rightarrow 2$ signal subprocess, $\mathrm{g} + \mathrm{g} \rightarrow \mathrm{J}/\psi + \gamma$, where an isolated photon is produced back to back with a J/ψ. The Collins-Soper (CS) frame is an ideal frame of reference to conduct angular distribution measurements, that attributes physical meaning to the spatial orientation of final state particles.

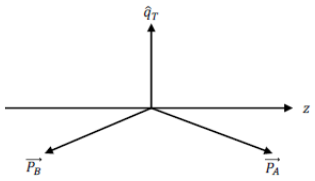

Figure A.1: Collins-Soper frame. $\underline{\mathrm{P}}_A$ is the initial momentum of the first colliding parton and $\underline{\mathrm{P}}_B$ is that of the second colliding parton. THe z-axis bisects the angle formed between the momentum of $\underline{\mathrm{P}})_A$ is the inverse momentum of the second parton -$\underline{\mathrm{P}}_B$. $\hat{q}_\mathrm{T}$ is the transverse unit vector normal to the plane spanned by the two incoming parton momenta, and the y-axis is the vector normal to that plane. x-axis is chosen to complete the right handed co-ordinate system [73].

In the CS frame, the z-axis bisects the angle between the direction of the intial momentum of the first colliding parton, $\bar{P}_A$, and the inverse momentum of the second colliding parton, $\bar{P}_B$, in the J/ψ rest frame. The y-axis is defined as the vector normal to the plane spanned by the two incoming parton momenta, and the x-axis is defined so as to complete a right handed Cartesian co-ordinate system. The variable θ_{CS} is defined as the angle between the momentum vector of one of the final state particles and the z-axis. The azimuthal angle ϕ_{CS}, is measured relative to a transverse unit vector $\hat{q}_\mathrm{T}$, normal to the plane spanned by the initial momenta of the colliding gluons. Angular distributions in the CS frame can be measured from the momentum components of final state particles in the laboratory frame.

$\cos\theta_{CS}$ is given by

$$\cos\theta_{CS} = \frac{2}{Q\sqrt{Q^2 + p_\mathrm{T}^2(\mathrm{J}/\psi + \gamma)x}}(P_1^+ P_2^- - P_1^- P_2^+) \tag{A.1}$$

with

$$P_i^{\pm} = \frac{1}{\sqrt{2}}(E_i \pm p_{z,i})$$

E_i an $p_{z,i}$ are the energy and longitudinal momentum of the J/ψ ($i = 1$) and the photon ($i = 2$) respectively. The invariant mass of the J/$\psi + \gamma$ system is given by Q, and the longitudinal momentum of this system is $p_z(\mathrm{J}/\psi + \gamma)$. ϕ_{CS} is given by

$$\phi_{CS} = \tan^{-1}\left[\frac{\sqrt{Q^2 + p_{\mathrm{T}}^2(\mathrm{J}/\psi + \gamma)}}{Q}\frac{\bar{\Delta}_{\mathrm{T}} \cdot R_{\mathrm{T}}}{\bar{\Delta}_{\mathrm{T}} \cdot p_{\mathrm{T}}}\right] \tag{A.2}$$

where $\Delta^j = p_{z,q}^j - p_{z,2}^j$, $\hat{p}_{\mathrm{T}}$, is a transverse unit vector in the direction of $p_{\mathrm{T}}(\mathrm{J}/\psi + \gamma)$, and $\hat{R}_{\mathrm{T}}$ is a transverse vector in the direction $\underline{\mathrm{P}}_A \times \underline{\mathrm{Q}}$.

Appendix B

Angular Dependencies

The introduction of kinematical generator level cuts on the muons and photons adds visible structures to the variable $|\phi_{CS}|$, which is evident in B.1. In (a) no generator level cuts have been applied, i.e $p_{\mathrm{T}}(\mu) = p_{\mathrm{T}}(\gamma) = 0$, and the distribution is essentially flat. This is to be expected in the absence of polarised gluons. Introducing kinematical cuts, even at $p_{\mathrm{T}}(\mu) = p_{\mathrm{T}}(\gamma) = 2$ GeV introduces structure to the variable $|\phi_{CS}|$, as can be seen in (b).

The analysis was guided to select $p_{\mathrm{T}}(\mu) > 4$ GeV and $p_{\mathrm{T}}(\gamma) > 9$ GeV which is more severe, leaving low numbers of events.

Any $|\phi_{CS}|$ modulation due to polarisation effects is likely to be very small, which is impeeded by the kinematical bias. The effect of the kinematic dependence is reduced by measuring the ratio of low to high $\cos^2\theta_{CS}$ slices.

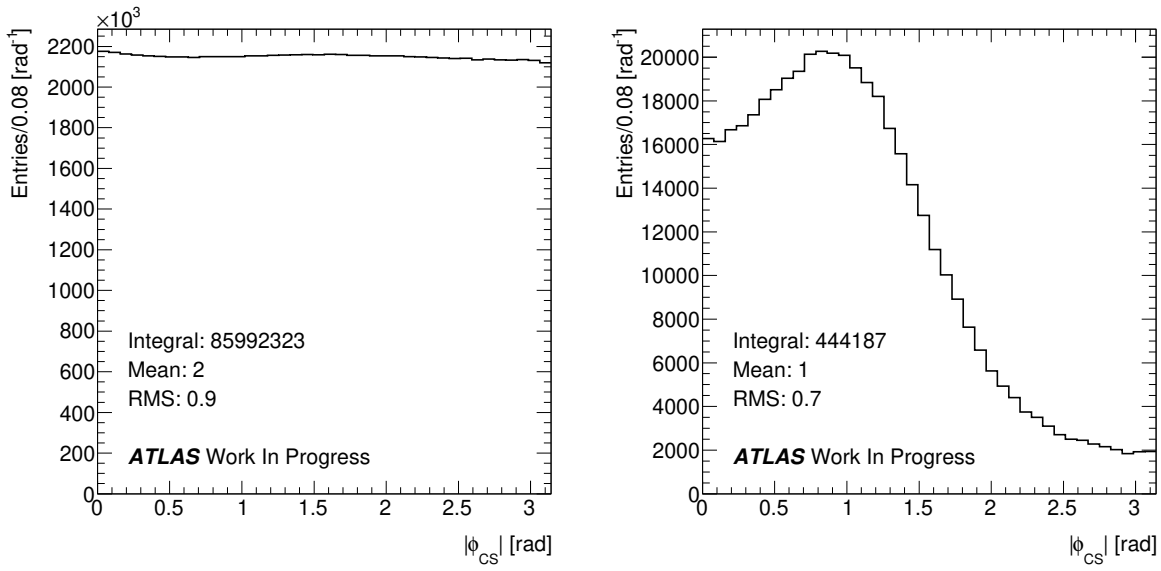

(a) (b)

Figure B.1: Figure (a) A sample Monte Carlo sample with about 86 million generated truth events with no generator level kinematic cuts, plotted as a function of the variable $|\phi_{CS}|$. Figure (b) The same sample with kinematic selection cuts $p_{\mathrm{T}}(\mu) > 2$ GeV and $p_{\mathrm{T}}(\gamma) > 2$ GeV applied. Note the dramatic reduction of the number of events, down to about 500 thousand, and rather severe ϕ_{CS} dependence of the distribution.

Appendix C

BDT Training And Performance

This appendix contains plots of the BDT score (training and testing), the signal correlation between ΔY and $\Delta\phi$, and similarly for the background correlation, and the efficiency of the BDT trainings for the pp and signal samples in each $\lambda - q_{\mathrm{T}}^2$ and $|\phi_{CS}|$ slices.

C.1 Plots Of The BDT Training, Testing And Performance For $\lambda - q_T^2$ Regions

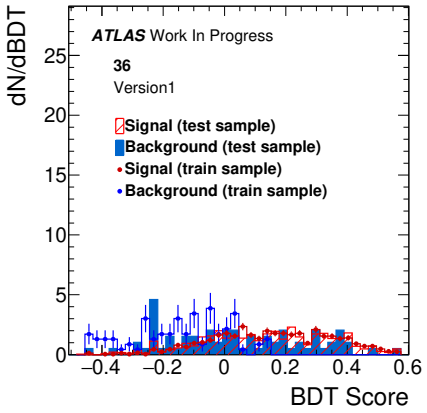

(a) BDT Scores 36 V1

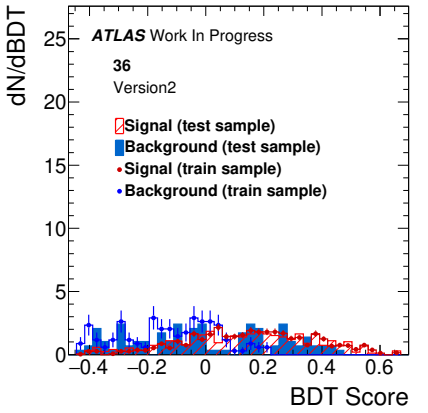

(b) BDT Scores 36 V2

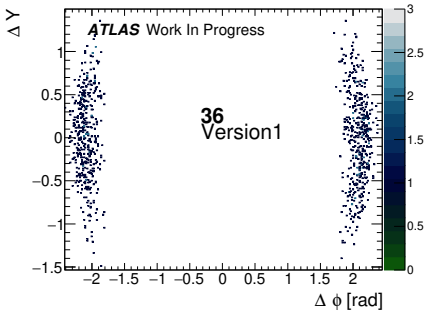

(c) Signal Correlation 36 V1

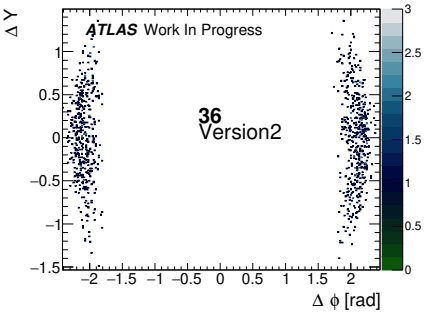

(d) Signal Correlation 36 V2

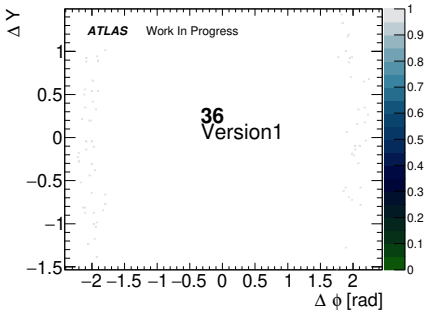

(e) Background Correlation 36 V1

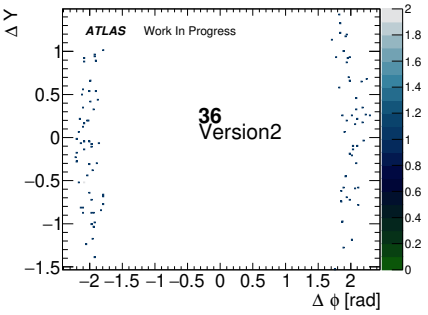

(f) Background Correlation 36 V2

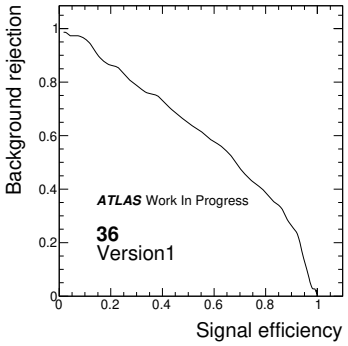

(g) Efficiency 36 V1

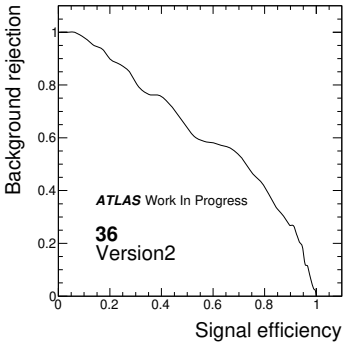

(h) Efficiency 36 V2

Figure C.1

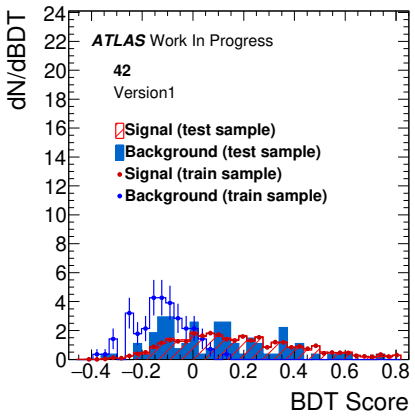

(a) BDT Scores 42 V1

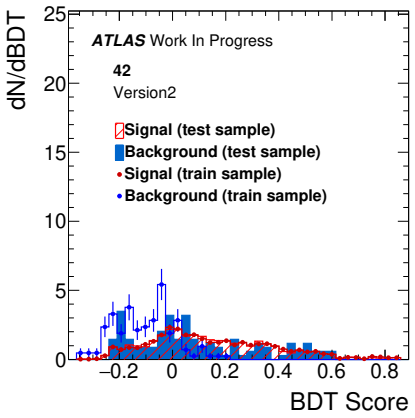

(b) BDT Scores 42 V2

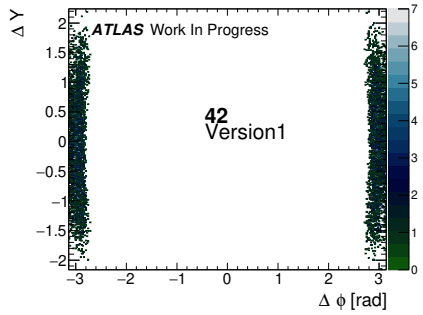

(c) Signal Correlation 42 V1

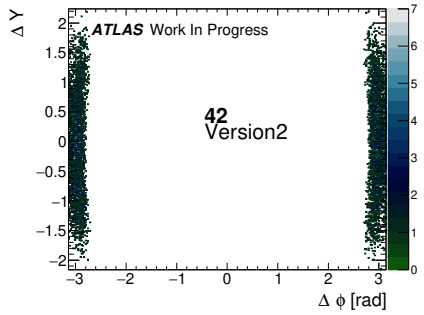

(d) Signal Correlation 42 V2

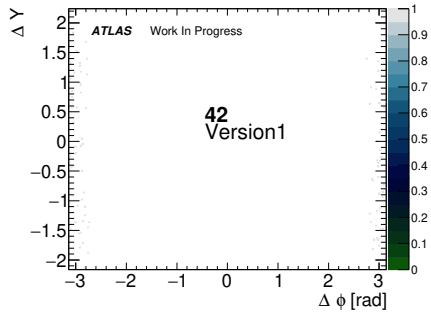

(e) Background Correlation 42 V1

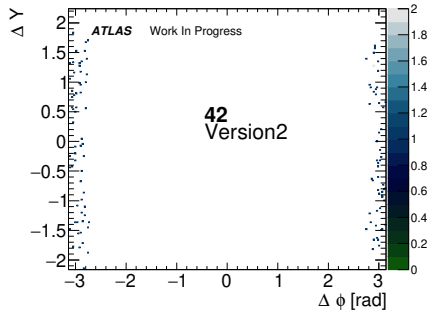

(f) Background Correlation 42 V2

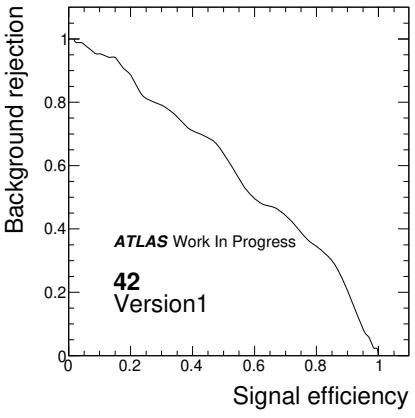

(g) Efficiency 42 V1

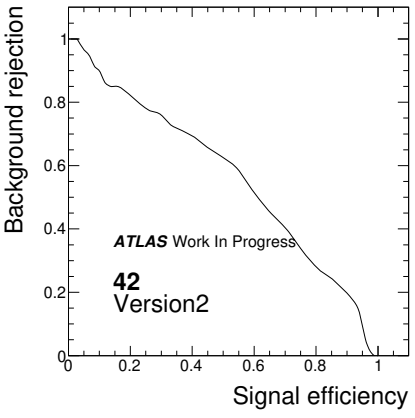

(h) Efficiency 42 V2

Figure C.2

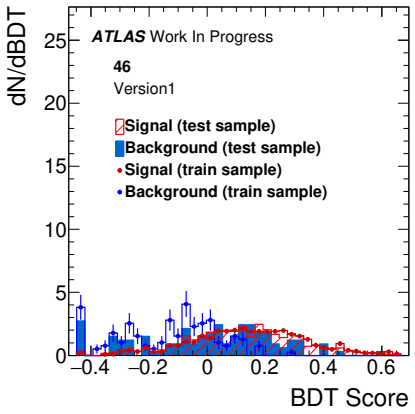

(a) BDT Scores 46 V1

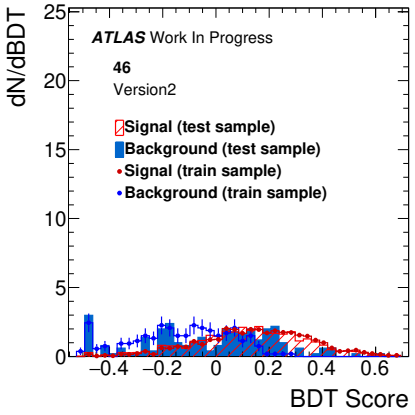

(b) BDT Scores 46 V2

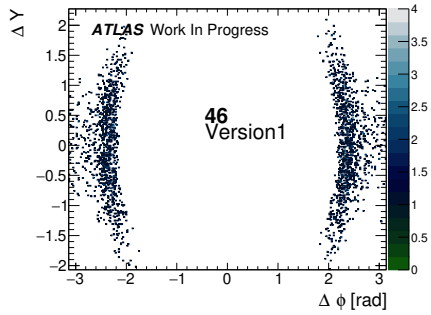

(c) Signal Correlation 46 V1

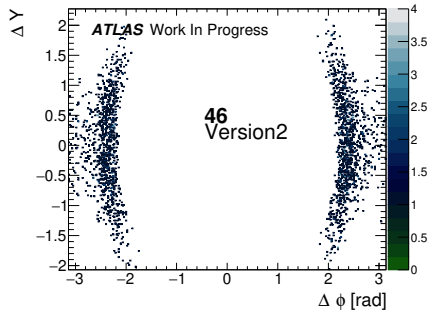

(d) Signal Correlation 46 V2

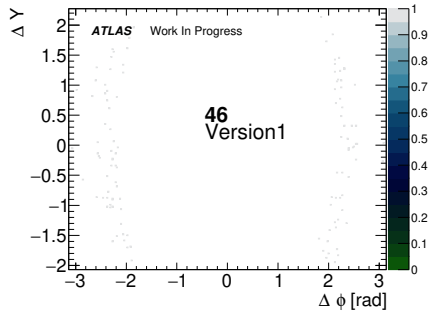

(e) Background Correlation 46 V1

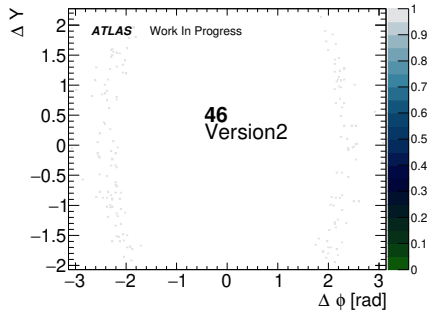

(f) Background Correlation 46 V2

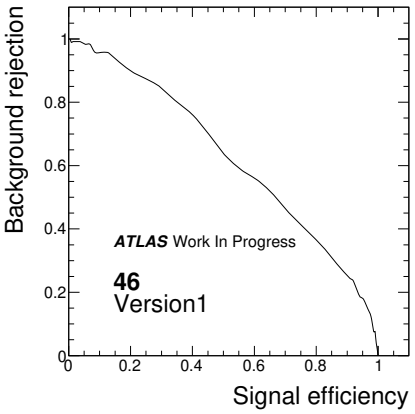

(g) Efficiency 46 V1

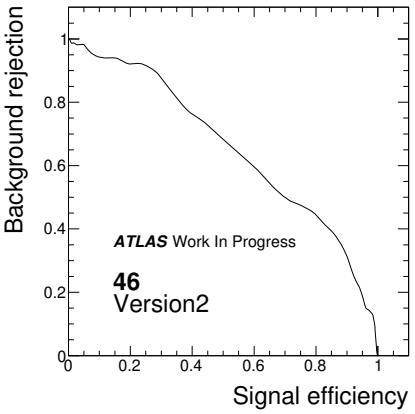

(h) Efficiency 46 V2

Figure C.3

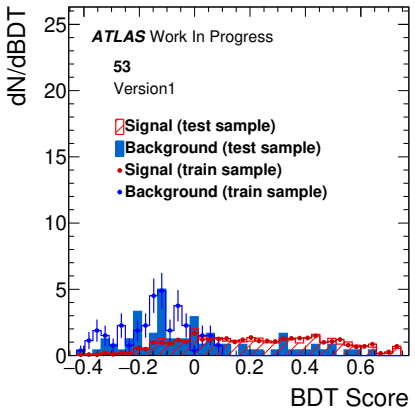

(a) BDT Scores 53 V1

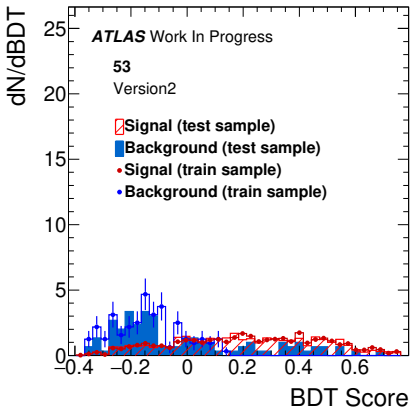

(b) BDT Scores 53 V2

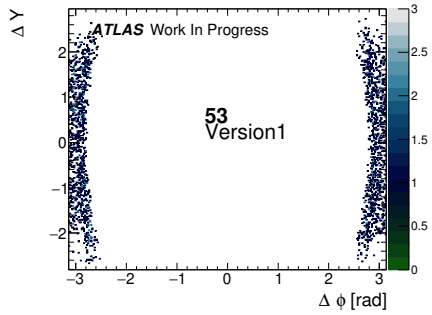

(c) Signal Correlation 53 V1

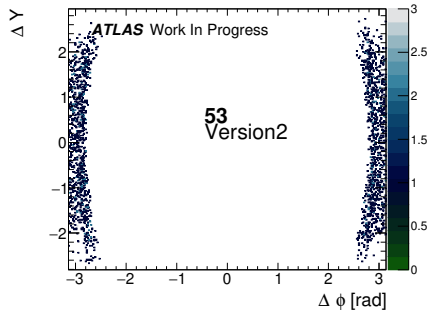

(d) Signal Correlation 53 V2

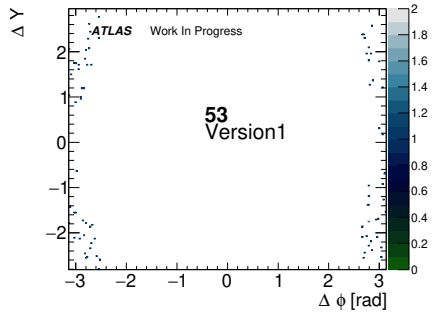

(e) Background Correlation 53 V1

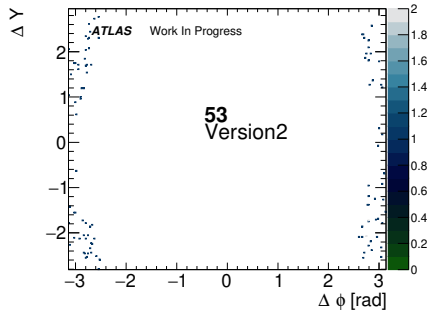

(f) Background Correlation 53 V2

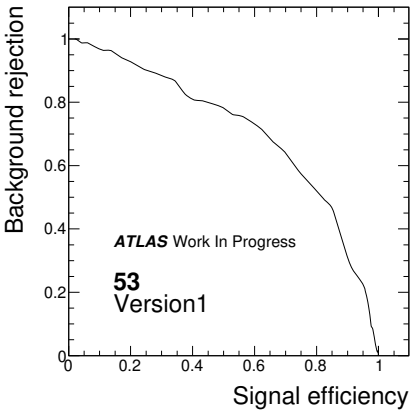

(g) Efficiency 53 V1

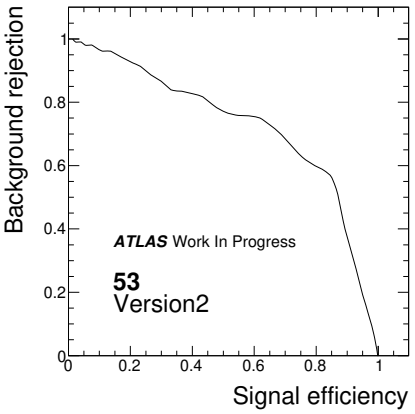

(h) Efficiency 53 V2

Figure C.4

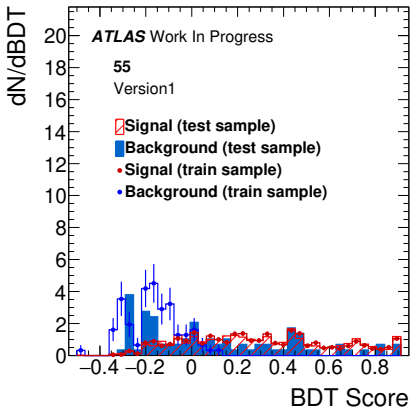

(a) BDT Scores 55 V1

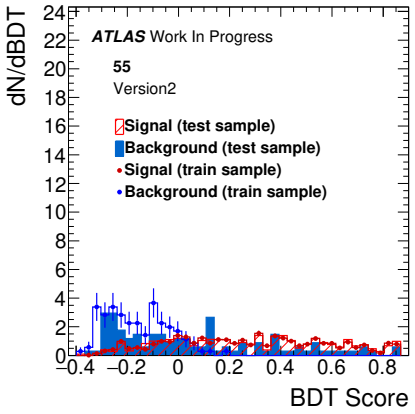

(b) BDT Scores 55 V2

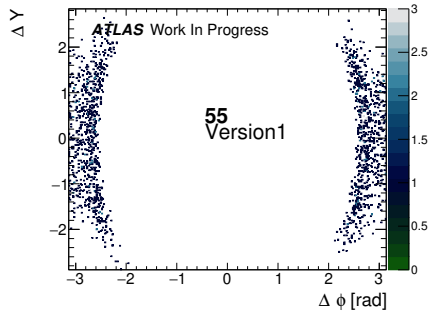

(c) Signal Correlation 55 V1

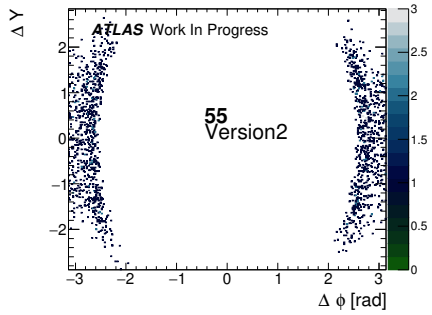

(d) Signal Correlation 55 V2

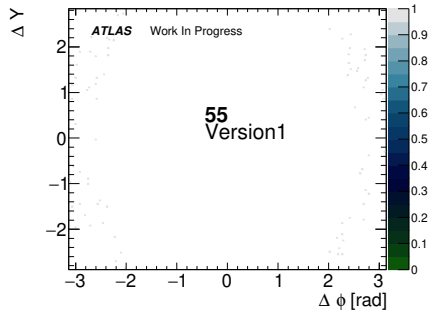

(e) Background Correlation 55 V1

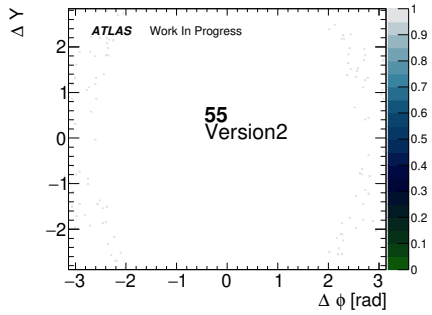

(f) Background Correlation 55 V2

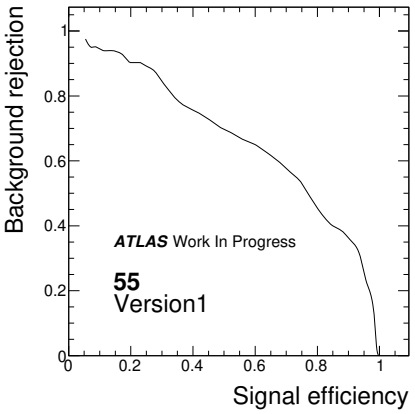

(g) Efficiency 55 V1

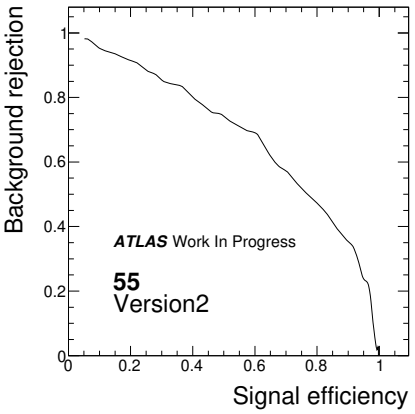

(h) Efficiency 55 V2

Figure C.5

C.2 Plots Of The BDT Training, Testing And Performance For $|\phi_{CS}|$ Regions

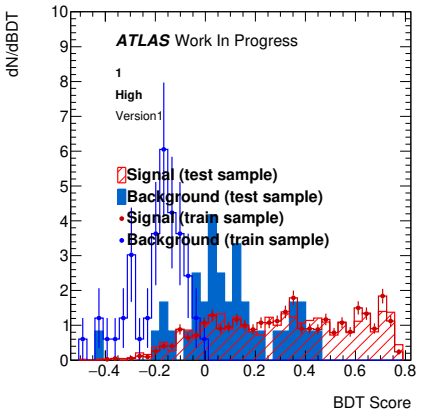

(a) BDT Scores 1 V1 High

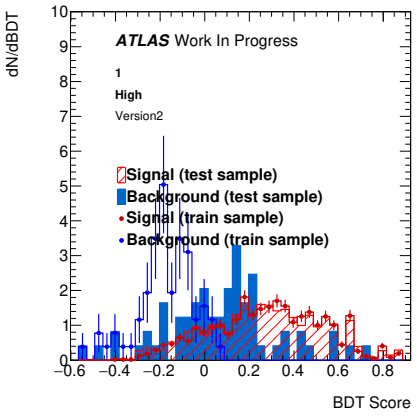

(b) BDT Scores 1 V2 High

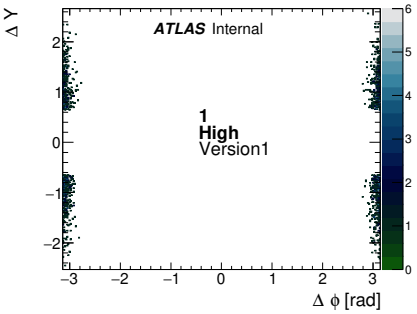

(c) Signal Correlation 1 V1 High

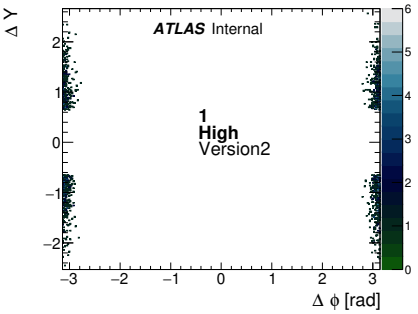

(d) Signal Correlation 1 V2 High

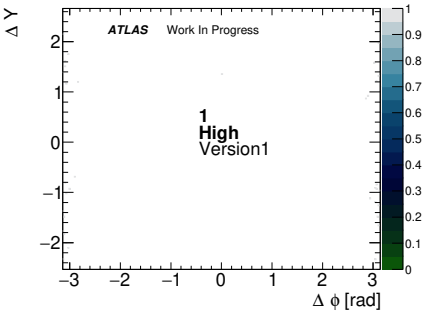

(e) Background Correlation 1 V1 High

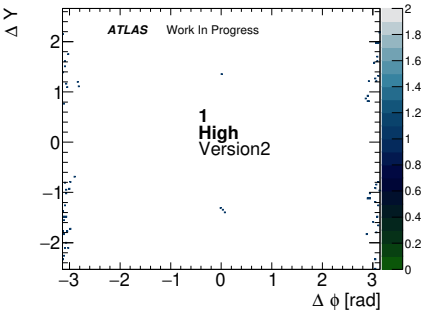

(f) Background Correlation 1 V2 High

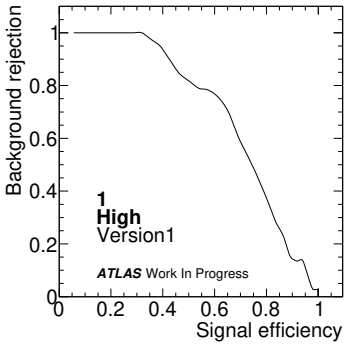

(g) Efficiency 1 V1 High

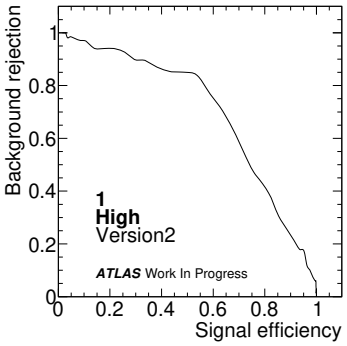

(h) Efficiency 1 V2 High

Figure C.6

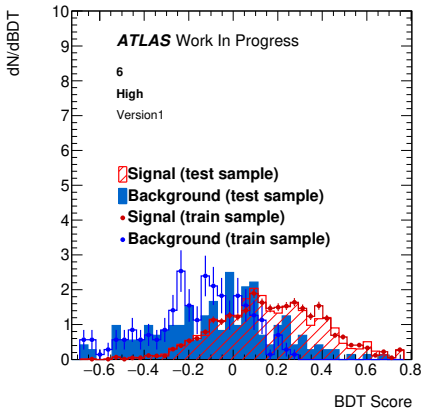

(a) BDT Scores 6 V1 High

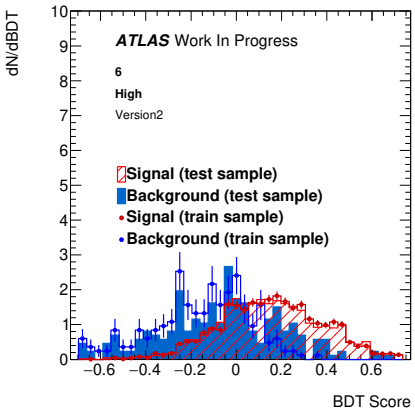

(b) BDT Scores 6 V2 High

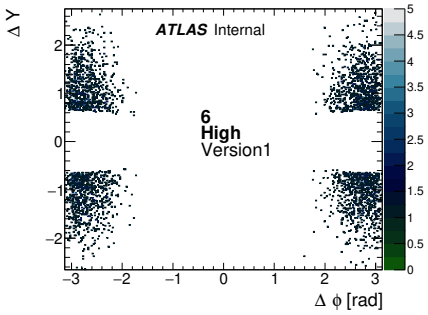

(c) Signal Correlation 6 V1 High

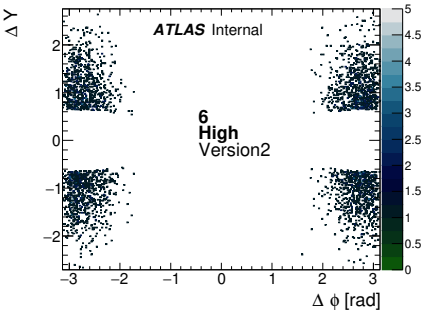

(d) Signal Correlation 6 V2 High

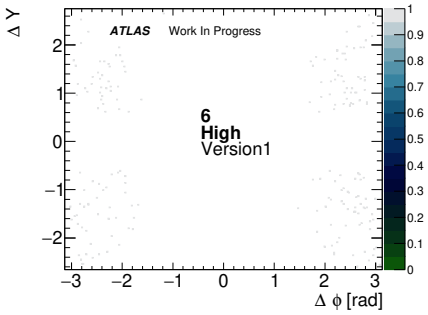

(e) Background Correlation 6 V1 High

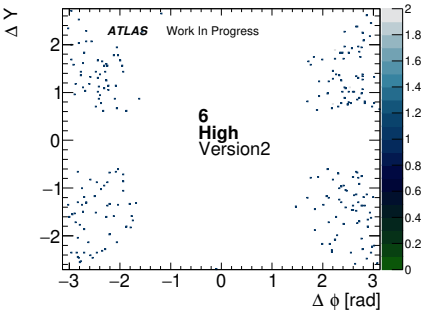

(f) Background Correlation 6 V2 High

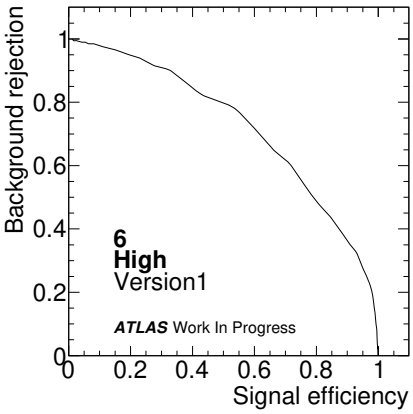

(g) Efficiency 6 V1 High

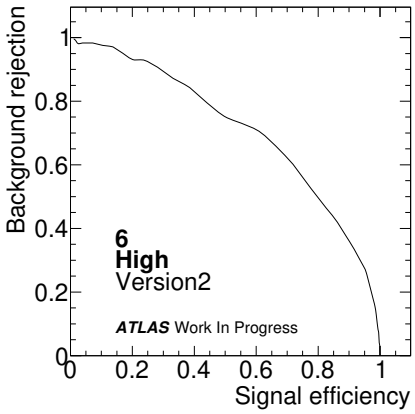

(h) Efficiency 6 V2 High

Figure C.7

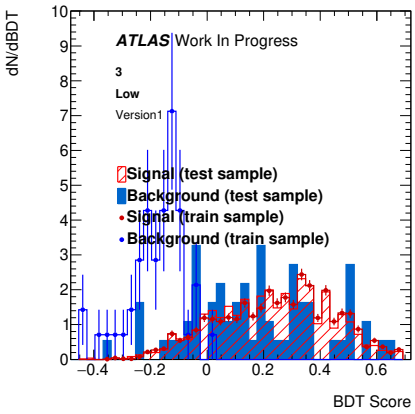

(a) BDT Scores 3 V1 Low

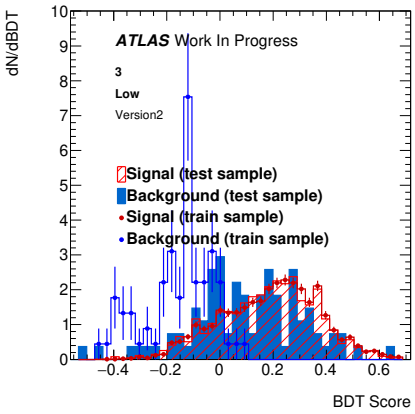

(b) BDT Scores 3 V2 Low

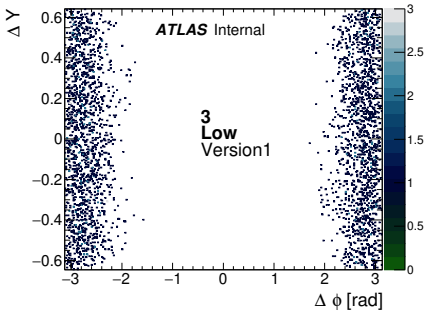

(c) Signal Correlation 3 V1 Low

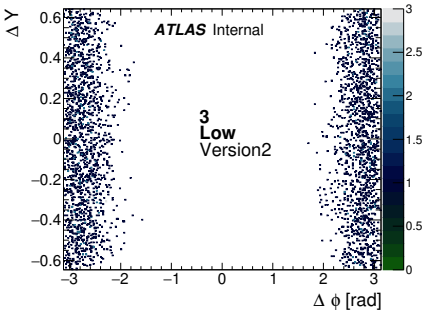

(d) Signal Correlation 3 V2 Low

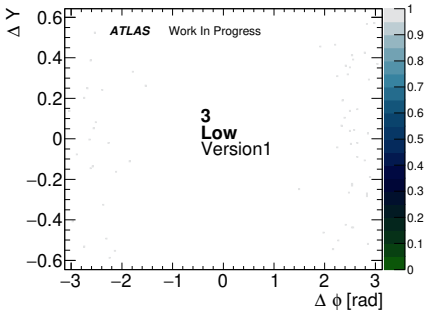

(e) Background Correlation 3 V1 Low

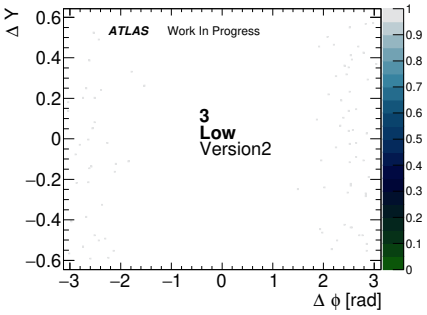

(f) Background Correlation 3 V2 Low

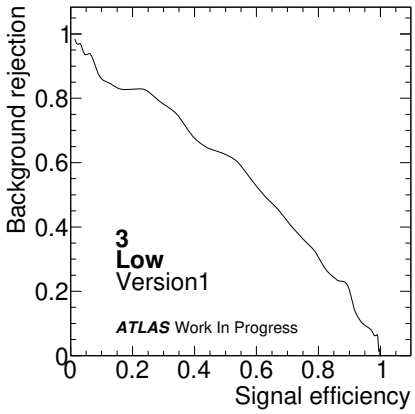

(g) Efficiency 3 V1 Low

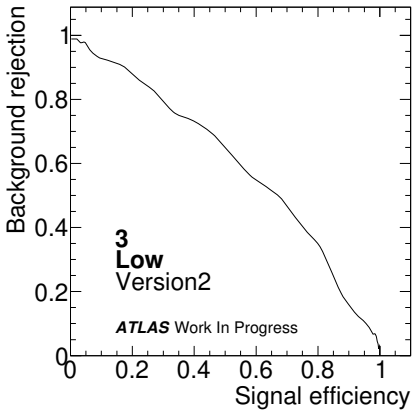

(h) Efficiency 3 V2 Low

Figure C.8

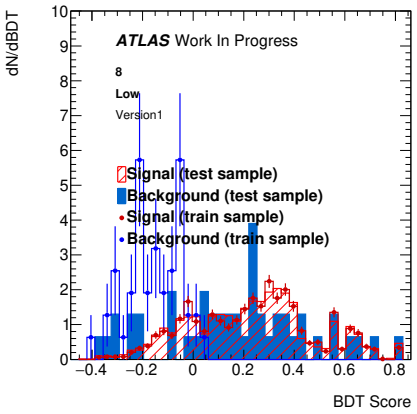

(a) BDT Scores 8 V1 Low

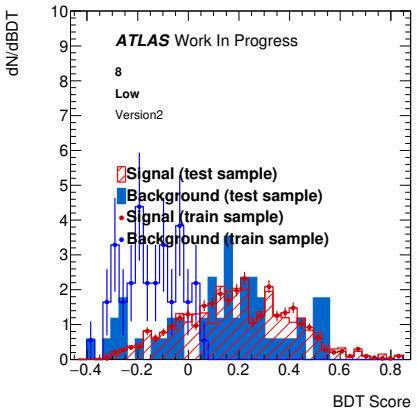

(b) BDT Scores 8 V2 Low

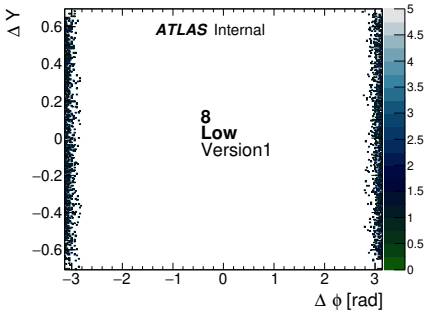

(c) Signal Correlation 8 V1 Low

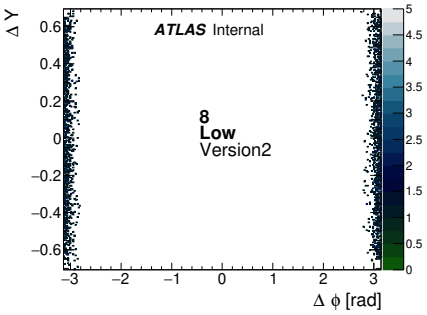

(d) Signal Correlation 8 V2 Low

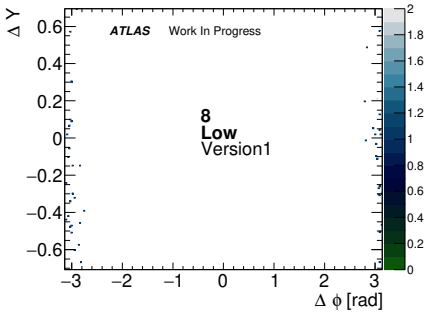

(e) Background Correlation 8 V1 Low

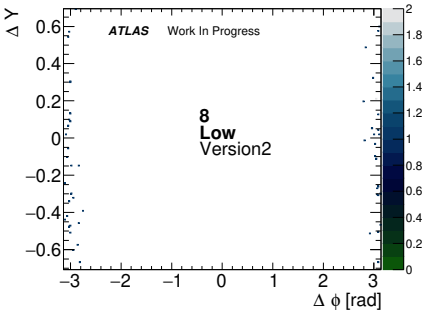

(f) Background Correlation 8 V2 Low

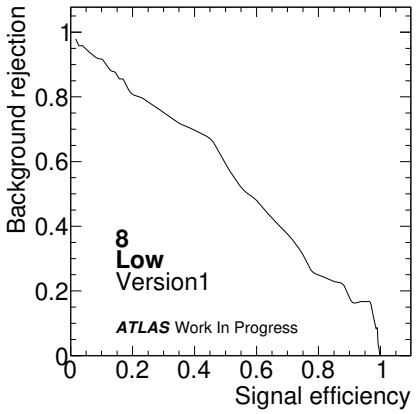

(g) Efficiency 8 V1 Low

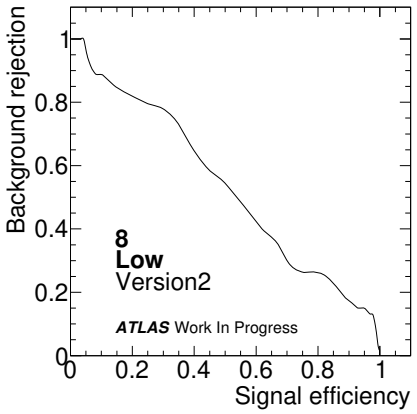

(h) Efficiency 8 V2 Low

Figure C.9

Appendix D

Cut Flows

D.1 Cut Flows For $\lambda - q_{\mathrm{T}}^2$ Regions

Cut	**signal**	**pp**	**bb**	**data**
Cut 1: Photon Vec > 0	935578	463711	539733	3033090
Cut 2: HLT_2mu4_bJpsimumu_noL2 Trigger	431820	230372	282887	2338141
Cut 3: $\lambda < 15$	418663	188220	228977	1872508
Cut 4: 449	149024	26519	35107	352980
Cut 5: $25 \leq \lambda < 50$	31962	6816	7629	65904
Cut 6: $100 \leq q_T^2 < 144$ GeV^2	2965	501	466	4362
Cut 7: $2.7 \leq m_{\mu\mu} < 3.5$ GeV	2960	499	464	4192
Cut 8: $-5 \leq \tau < 15$ ps.	2960	499	464	4189
Cut 9: Tight Photons Only	1897	162	112	1342
Cut 10: $\Delta R < 0.12$ between signal reconstructed and truth photons	1829	—	—	—
Region 11: $2.7 \leq m_{\mu\mu} < 2.9$ GeV and $-5 \leq \tau_{\mu\mu} < 0.86$ ps	27	5	0	69
Region 21: $2.9 \leq m_{\mu\mu} < 3.1$ GeV and $-5 \leq \tau_{\mu\mu} < 0.86$ ps	947	87	27	538
Region 31: $3.1 \leq m_{\mu\mu} < 3.3$ GeV and $-5 \leq \tau_{\mu\mu} < 0.86$ ps	851	68	29	397
Region 41: $3.3 \leq m_{\mu\mu} < 3.5$ GeV and $-5 \leq \tau_{\mu\mu} < 0.86$ ps	4	1	0	33
Region 12: $2.7 \leq m_{\mu\mu} < 2.9$ GeV and $0.86 \leq \tau_{\mu\mu} < 15$ ps	0	0	0	39
Region 22: $2.9 \leq m_{\mu\mu} < 3.1$ GeV and $0.86 \leq \tau_{\mu\mu} < 15$ ps	0	1	34	160
Region 32: $3.1 \leq m_{\mu\mu} < 3.3$ GeV and $0.86 \leq \tau_{\mu\mu} < 15$ ps	0	0	22	92
Region 42: $3.3 \leq m_{\mu\mu} < 3.5$ GeV and $0.86 \leq \tau_{\mu\mu} < 15$ ps	0	0	0	14
Region 71: Region 21 + Region 31	1798	155	56	935
Region 81: Region 11 + Region 41	31	6	0	102
Region 72: Region 22 + Region 32	0	1	56	252
Region 82: Region 12 + Region 42	0	0	0	53
Region 91: Region 71 - Region 81	1767	149	56	833
Region 92: Region 72 - Region 82	0	1	56	199
Region 99: Region 91 - Region 92	1767	148	0	634

Table D.1: Event selection cut flow for region 36

Cut	**signal**	**pp**	**bb**	**data**
Cut 1: Photon Vec > 0	935578	463711	539733	3033090
Cut 2: HLT_2mu4_bJpsimumu_noL2 Trigger	431820	230372	282887	2338141
Cut 3: $\lambda < 15$	418663	188220	228977	1872508
Cut 4: 449	149024	26519	35107	352980
Cut 5: $25 \leq \lambda < 50$	31962	6816	7629	65904
Cut 6: $196 \leq q_T^2 < 256$ GeV^2	983	677	680	5620
Cut 7: $2.7 \leq m_{\mu\mu} < 3.5$ GeV	982	677	679	5408
Cut 8: $-5 \leq \tau < 15$ ps.	982	677	679	5406
Cut 9: Tight Photons Only	548	188	190	1773
Cut 10: $\Delta R < 0.12$ between signal reconstructed and truth photons	469	—	—	—
Region 11: $2.7 \leq m_{\mu\mu} < 2.9$ GeV and $-5 \leq \tau_{\mu\mu} < 0.86$ ps	6	3	4	74
Region 21: $2.9 \leq m_{\mu\mu} < 3.1$ GeV and $-5 \leq \tau_{\mu\mu} < 0.86$ ps	243	92	47	690
Region 31: $3.1 \leq m_{\mu\mu} < 3.3$ GeV and $-5 \leq \tau_{\mu\mu} < 0.86$ ps	218	92	36	565
Region 41: $3.3 \leq m_{\mu\mu} < 3.5$ GeV and $-5 \leq \tau_{\mu\mu} < 0.86$ ps	2	1	0	47
Region 12: $2.7 \leq m_{\mu\mu} < 2.9$ GeV and $0.86 \leq \tau_{\mu\mu} < 15$ ps	0	0	0	60
Region 22: $2.9 \leq m_{\mu\mu} < 3.1$ GeV and $0.86 \leq \tau_{\mu\mu} < 15$ ps	0	0	60	192
Region 32: $3.1 \leq m_{\mu\mu} < 3.3$ GeV and $0.86 \leq \tau_{\mu\mu} < 15$ ps	0	0	43	138
Region 42: $3.3 \leq m_{\mu\mu} < 3.5$ GeV and $0.86 \leq \tau_{\mu\mu} < 15$ ps	0	0	0	7
Region 71: Region 21 + Region 31	461	184	83	1255
Region 81: Region 11 + Region 41	8	4	4	121
Region 72: Region 22 + Region 32	0	0	103	330
Region 82: Region 12 + Region 42	0	0	0	67
Region 91: Region 71 - Region 81	453	180	79	1134
Region 92: Region 72 - Region 82	0	0	103	263
Region 99: Region 91 - Region 92	453	180	-24	871

Table D.2: Event selection cut flow for region 38

Cut	**signal**	**pp**	**bb**	**data**
Cut 1: Photon Vec > 0	935578	463711	539733	3033090
Cut 2: HLT_2mu4_bJpsimumu_noL2 Trigger	431820	230372	282887	2338141
Cut 3: $\lambda < 15$	418663	188220	228977	1872508
Cut 4: 449	149024	26519	35107	352980
Cut 5: $50 \leq \lambda < 100$	84493	10017	13604	137249
Cut 6: $4 \leq q_T^2 < 16$ GeV^2	18517	703	1210	14344
Cut 7: $2.7 \leq m_{\mu\mu} < 3.5$ GeV	18488	700	1204	13595
Cut 8: -5 $\leq \tau <$ 15 ps.	18488	700	1203	13591
Cut 9: Tight Photons Only	12755	173	348	4352
Cut 10: $\Delta R < 0.12$ between signal reconstructed and truth photons	12676	—	—	—
Region 11: $2.7 \leq m_{\mu\mu} < 2.9$ GeV and -5 $\leq \tau_{\mu\mu} <$ 0.86 ps	214	2	4	237
Region 21: $2.9 \leq m_{\mu\mu} < 3.1$ GeV and -5 $\leq \tau_{\mu\mu} <$ 0.86 ps	6664	93	95	1592
Region 31: $3.1 \leq m_{\mu\mu} < 3.3$ GeV and -5 $\leq \tau_{\mu\mu} <$ 0.86 ps	5735	78	75	1213
Region 41: $3.3 \leq m_{\mu\mu} < 3.5$ GeV and -5 $\leq \tau_{\mu\mu} <$ 0.86 ps	58	0	2	156
Region 12: $2.7 \leq m_{\mu\mu} < 2.9$ GeV and 0.86 $\leq \tau_{\mu\mu} <$ 15 ps	0	0	4	158
Region 22: $2.9 \leq m_{\mu\mu} < 3.1$ GeV and 0.86 $\leq \tau_{\mu\mu} <$ 15 ps	0	0	89	566
Region 32: $3.1 \leq m_{\mu\mu} < 3.3$ GeV and 0.86 $\leq \tau_{\mu\mu} <$ 15 ps	4	0	78	385
Region 42: $3.3 \leq m_{\mu\mu} < 3.5$ GeV and 0.86 $\leq \tau_{\mu\mu} <$ 15 ps	1	0	1	45
Region 71: Region 21 + Region 31	12399	171	170	2805
Region 81: Region 11 + Region 41	272	2	6	393
Region 72: Region 22 + Region 32	4	0	167	951
Region 82: Region 12 + Region 42	1	0	5	203
Region 91: Region 71 - Region 81	12127	169	164	2412
Region 92: Region 72 - Region 82	3	0	162	748
Region 99: Region 91 - Region 92	12124	169	2	1664

Table D.3: Event selection cut flow for region 42

Cut	**signal**	**pp**	**bb**	**data**
Cut 1: Photon Vec > 0	935578	463711	539733	3033090
Cut 2: HLT_2mu4_bJpsimumu_noL2 Trigger	431820	230372	282887	2338141
Cut 3: $\lambda < 15$	418663	188220	228977	1872508
Cut 4: 449	149024	26519	35107	352980
Cut 5: $50 \leq \lambda < 100$	84493	10017	13604	137249
Cut 6: $36 \leq q_T^2 < 64$ GeV^2	14170	910	1439	15746
Cut 7: $2.7 \leq m_{\mu\mu} < 3.5$ GeV	14146	909	1436	15027
Cut 8: $-5 \leq \tau < 15$ ps.	14146	909	1436	15024
Cut 9: Tight Photons Only	9775	246	414	4903
Cut 10: $\Delta R < 0.12$ between signal reconstructed and truth photons	9705	—	—	—
Region 11: $2.7 \leq m_{\mu\mu} < 2.9$ GeV and $-5 \leq \tau_{\mu\mu} < 0.86$ ps	116	1	3	300
Region 21: $2.9 \leq m_{\mu\mu} < 3.1$ GeV and $-5 \leq \tau_{\mu\mu} < 0.86$ ps	5072	136	96	1736
Region 31: $3.1 \leq m_{\mu\mu} < 3.3$ GeV and $-5 \leq \tau_{\mu\mu} < 0.86$ ps	4464	107	87	1376
Region 41: $3.3 \leq m_{\mu\mu} < 3.5$ GeV and $-5 \leq \tau_{\mu\mu} < 0.86$ ps	51	1	1	157
Region 12: $2.7 \leq m_{\mu\mu} < 2.9$ GeV and $0.86 \leq \tau_{\mu\mu} < 15$ ps	0	0	5	190
Region 22: $2.9 \leq m_{\mu\mu} < 3.1$ GeV and $0.86 \leq \tau_{\mu\mu} < 15$ ps	0	0	112	619
Region 32: $3.1 \leq m_{\mu\mu} < 3.3$ GeV and $0.86 \leq \tau_{\mu\mu} < 15$ ps	2	1	107	469
Region 42: $3.3 \leq m_{\mu\mu} < 3.5$ GeV and $0.86 \leq \tau_{\mu\mu} < 15$ ps	0	0	3	56
Region 71: Region 21 + Region 31	9536	243	183	3112
Region 81: Region 11 + Region 41	167	2	4	457
Region 72: Region 22 + Region 32	2	1	219	1088
Region 82: Region 12 + Region 42	0	0	8	246
Region 91: Region 71 - Region 81	9369	241	179	2655
Region 92: Region 72 - Region 82	2	1	211	842
Region 99: Region 91 - Region 92	9367	240	-32	1813

Table D.4: Event selection cut flow for region 44

Cut	**signal**	**pp**	**bb**	**data**
Cut 1: Photon Vec > 0	935578	463711	539733	3033090
Cut 2: HLT_2mu4_bJpsimumu_noL2 Trigger	431820	230372	282887	2338141
Cut 3: $\lambda < 15$	418663	188220	228977	1872508
Cut 4: 449	149024	26519	35107	352980
Cut 5: $50 \leq \lambda < 100$	84493	10017	13604	137249
Cut 6: $100 \leq q_T^2 < 144$ GeV^2	6473	881	1140	11127
Cut 7: $2.7 \leq m_{\mu\mu} < 3.5$ GeV	6460	879	1139	10654
Cut 8: $-5 \leq \tau < 15$ ps.	6460	879	1139	10652
Cut 9: Tight Photons Only	4391	259	301	3411
Cut 10: $\Delta R < 0.12$ between signal reconstructed and truth photons	4310	—	—	—
Region 11: $2.7 \leq m_{\mu\mu} < 2.9$ GeV and $-5 \leq \tau_{\mu\mu} < 0.86$ ps	61	2	3	139
Region 21: $2.9 \leq m_{\mu\mu} < 3.1$ GeV and $-5 \leq \tau_{\mu\mu} < 0.86$ ps	2231	141	78	1256
Region 31: $3.1 \leq m_{\mu\mu} < 3.3$ GeV and $-5 \leq \tau_{\mu\mu} < 0.86$ ps	2001	113	70	1016
Region 41: $3.3 \leq m_{\mu\mu} < 3.5$ GeV and $-5 \leq \tau_{\mu\mu} < 0.86$ ps	15	3	0	99
Region 12: $2.7 \leq m_{\mu\mu} < 2.9$ GeV and $0.86 \leq \tau_{\mu\mu} < 15$ ps	0	0	3	133
Region 22: $2.9 \leq m_{\mu\mu} < 3.1$ GeV and $0.86 \leq \tau_{\mu\mu} < 15$ ps	2	0	72	425
Region 32: $3.1 \leq m_{\mu\mu} < 3.3$ GeV and $0.86 \leq \tau_{\mu\mu} < 15$ ps	0	0	74	312
Region 42: $3.3 \leq m_{\mu\mu} < 3.5$ GeV and $0.86 \leq \tau_{\mu\mu} < 15$ ps	0	0	1	31
Region 71: Region 21 + Region 31	4232	254	148	2272
Region 81: Region 11 + Region 41	76	5	3	238
Region 72: Region 22 + Region 32	2	0	146	737
Region 82: Region 12 + Region 42	0	0	4	164
Region 91: Region 71 - Region 81	4156	249	145	2034
Region 92: Region 72 - Region 82	2	0	142	573
Region 99: Region 91 - Region 92	4154	249	3	1461

Table D.5: Event selection cut flow for region 46

Cut	**signal**	**pp**	**bb**	**data**
Cut 1: Photon Vec > 0	935578	463711	539733	3033090
Cut 2: HLT_2mu4_bJpsimumu_noL2 Trigger	431820	230372	282887	2338141
Cut 3: $\lambda < 15$	418663	188220	228977	1872508
Cut 4: 449	149024	26519	35107	352980
Cut 5: $100 \leq \lambda < 200$	31531	7378	11285	127452
Cut 6: $0 \leq q_T^2 < 4$ GeV^2	2120	188	265	3736
Cut 7: $2.7 \leq m_{\mu\mu} < 3.5$ GeV	2114	187	265	3527
Cut 8: $-5 \leq \tau < 15$ ps.	2114	187	265	3526
Cut 9: Tight Photons Only	1529	60	75	1130
Cut 10: $\Delta R < 0.12$ between signal reconstructed and truth photons	1515	—	—	—
Region 11: $2.7 \leq m_{\mu\mu} < 2.9$ GeV and $-5 \leq \tau_{\mu\mu} < 0.86$ ps	22	2	4	64
Region 21: $2.9 \leq m_{\mu\mu} < 3.1$ GeV and $-5 \leq \tau_{\mu\mu} < 0.86$ ps	801	35	19	379
Region 31: $3.1 \leq m_{\mu\mu} < 3.3$ GeV and $-5 \leq \tau_{\mu\mu} < 0.86$ ps	684	23	17	335
Region 41: $3.3 \leq m_{\mu\mu} < 3.5$ GeV and $-5 \leq \tau_{\mu\mu} < 0.86$ ps	6	0	0	49
Region 12: $2.7 \leq m_{\mu\mu} < 2.9$ GeV and $0.86 \leq \tau_{\mu\mu} < 15$ ps	0	0	1	41
Region 22: $2.9 \leq m_{\mu\mu} < 3.1$ GeV and $0.86 \leq \tau_{\mu\mu} < 15$ ps	1	0	17	125
Region 32: $3.1 \leq m_{\mu\mu} < 3.3$ GeV and $0.86 \leq \tau_{\mu\mu} < 15$ ps	1	0	17	122
Region 42: $3.3 \leq m_{\mu\mu} < 3.5$ GeV and $0.86 \leq \tau_{\mu\mu} < 15$ ps	0	0	0	15
Region 71: Region 21 + Region 31	1485	58	36	714
Region 81: Region 11 + Region 41	28	2	4	113
Region 72: Region 22 + Region 32	2	0	34	247
Region 82: Region 12 + Region 42	0	0	1	56
Region 91: Region 71 - Region 81	1457	56	32	601
Region 92: Region 72 - Region 82	2	0	33	191
Region 99: Region 91 - Region 92	1455	56	-1	410

Table D.6: Event selection cut flow for region 51

Cut	**signal**	**pp**	**bb**	**data**
Cut 1: Photon Vec > 0	935578	463711	539733	3033090
Cut 2: HLT_2mu4_bJpsimumu_noL2 Trigger	431820	230372	282887	2338141
Cut 3: $\lambda < 15$	418663	188220	228977	1872508
Cut 4: 449	149024	26519	35107	352980
Cut 5: $100 \leq \lambda < 200$	31531	7378	11285	127452
Cut 6: $16 \leq q_T^2 < 36$ GeV^2	5505	583	919	12420
Cut 7: $2.7 \leq m_{\mu\mu} < 3.5$ GeV	5493	582	916	11781
Cut 8: -5 $\leq \tau <$ 15 ps.	5493	582	916	11775
Cut 9: Tight Photons Only	4004	173	247	3569
Cut 10: $\Delta R < 0.12$ between signal reconstructed and truth photons	3959	—	—	—
Region 11: $2.7 \leq m_{\mu\mu} < 2.9$ GeV and -5 $\leq \tau_{\mu\mu} <$ 0.86 ps	51	4	2	202
Region 21: $2.9 \leq m_{\mu\mu} < 3.1$ GeV and -5 $\leq \tau_{\mu\mu} <$ 0.86 ps	2076	108	63	1260
Region 31: $3.1 \leq m_{\mu\mu} < 3.3$ GeV and -5 $\leq \tau_{\mu\mu} <$ 0.86 ps	1804	61	69	990
Region 41: $3.3 \leq m_{\mu\mu} < 3.5$ GeV and -5 $\leq \tau_{\mu\mu} <$ 0.86 ps	27	0	2	129
Region 12: $2.7 \leq m_{\mu\mu} < 2.9$ GeV and 0.86 $\leq \tau_{\mu\mu} <$ 15 ps	0	0	3	138
Region 22: $2.9 \leq m_{\mu\mu} < 3.1$ GeV and 0.86 $\leq \tau_{\mu\mu} <$ 15 ps	0	0	51	479
Region 32: $3.1 \leq m_{\mu\mu} < 3.3$ GeV and 0.86 $\leq \tau_{\mu\mu} <$ 15 ps	1	0	57	338
Region 42: $3.3 \leq m_{\mu\mu} < 3.5$ GeV and 0.86 $\leq \tau_{\mu\mu} <$ 15 ps	0	0	0	33
Region 71: Region 21 + Region 31	3880	169	132	2250
Region 81: Region 11 + Region 41	78	4	4	331
Region 72: Region 22 + Region 32	1	0	108	817
Region 82: Region 12 + Region 42	0	0	3	171
Region 91: Region 71 - Region 81	3802	165	128	1919
Region 92: Region 72 - Region 82	1	0	105	646
Region 99: Region 91 - Region 92	3801	165	23	1273

Table D.7: Event selection cut flow for region 53

Cut	**signal**	**pp**	**bb**	**data**
Cut 1: Photon Vec > 0	935578	463711	539733	3033090
Cut 2: HLT_2mu4_bJpsimumu_noL2 Trigger	431820	230372	282887	2338141
Cut 3: $\lambda < 15$	418663	188220	228977	1872508
Cut 4: 449	149024	26519	35107	352980
Cut 5: $100 \leq \lambda < 200$	31531	7378	11285	127452
Cut 6: $64 \leq q_T^2 < 100$ GeV^2	4065	584	1007	12675
Cut 7: $2.7 \leq m_{\mu\mu} < 3.5$ GeV	4051	584	1003	12047
Cut 8: -5 $\leq \tau <$ 15 ps.	4051	584	1003	12044
Cut 9: Tight Photons Only	2923	170	284	3773
Cut 10: $\Delta R < 0.12$ between signal reconstructed and truth photons	2872	—	—	—
Region 11: $2.7 \leq m_{\mu\mu} < 2.9$ GeV and -5 $\leq \tau_{\mu\mu} <$ 0.86 ps	43	8	5	219
Region 21: $2.9 \leq m_{\mu\mu} < 3.1$ GeV and -5 $\leq \tau_{\mu\mu} <$ 0.86 ps	1504	83	57	1251
Region 31: $3.1 \leq m_{\mu\mu} < 3.3$ GeV and -5 $\leq \tau_{\mu\mu} <$ 0.86 ps	1306	74	70	1094
Region 41: $3.3 \leq m_{\mu\mu} < 3.5$ GeV and -5 $\leq \tau_{\mu\mu} <$ 0.86 ps	16	5	3	114
Region 12: $2.7 \leq m_{\mu\mu} < 2.9$ GeV and 0.86 $\leq \tau_{\mu\mu} <$ 15 ps	0	0	1	174
Region 22: $2.9 \leq m_{\mu\mu} < 3.1$ GeV and 0.86 $\leq \tau_{\mu\mu} <$ 15 ps	1	0	74	516
Region 32: $3.1 \leq m_{\mu\mu} < 3.3$ GeV and 0.86 $\leq \tau_{\mu\mu} <$ 15 ps	2	0	74	353
Region 42: $3.3 \leq m_{\mu\mu} < 3.5$ GeV and 0.86 $\leq \tau_{\mu\mu} <$ 15 ps	0	0	0	52
Region 71: Region 21 + Region 31	2810	157	127	2345
Region 81: Region 11 + Region 41	59	13	8	333
Region 72: Region 22 + Region 32	3	0	148	869
Region 82: Region 12 + Region 42	0	0	1	226
Region 91: Region 71 - Region 81	2751	144	119	2012
Region 92: Region 72 - Region 82	3	0	147	643
Region 99: Region 91 - Region 92	2748	144	-28	1369

Table D.8: Event Selection cut flow for region 55

D.2 Cut Flows For $|\phi_{CS}|$ Regions

Cut	**signal**	**pp**	**bb**	**data**
Cut 1: Photon Vec > 0	958488	505874	595897	3485326
Cut 2: HLT_2mu4_bJpsimumu_noL2 Trigger	444489	254178	316703	2657060
Cut 3: $\lambda < 15$	431332	212026	262793	2191427
Cut 4: 449	157864	34096	47754	503369
z^2 Cut: $0.1 \leq \cos^2\theta_{CS} < 1.0$	157864	34096	47754	503369
Cut 5: $0 \leq \lambda < 200$	149024	26519	35107	352980
Cut 6: $0 \leq q_T^2 < 400$ GeV^2	145760	18279	24128	257455
ϕ_{CS} Cut: $0 \leq \lvert\phi_{CS}\rvert < \frac{\pi}{8}$	10971	1042	2133	26938
Cut 7: $2.7 \leq m_{\mu\mu} < 3.5$ GeV	10951	1040	2130	25632
Cut 8: $-5 \leq \tau < 15$ ps.	10951	1040	2130	25630
Cut 9: Tight Photons	7401	283	594	7778
Cut 10: $\Delta R < 0.12$ between signal reconstructed and truth photons	7370	—	—	—
Region 11: $2.7 \leq m_{\mu\mu} < 2.9$ GeV and $-5 \leq \tau_{\mu\mu} < 0.86$ ps	83	6	11	375
Region 21: $2.9 \leq m_{\mu\mu} < 3.1$ GeV and $-5 \leq \tau_{\mu\mu} < 0.86$ ps	3768	145	140	2660
Region 31: $3.1 \leq m_{\mu\mu} < 3.3$ GeV and $-5 \leq \tau_{\mu\mu} < 0.86$ ps	3461	126	145	2217
Region 41: $3.3 \leq m_{\mu\mu} < 3.5$ GeV and $-5 \leq \tau_{\mu\mu} < 0.86$ ps	58	5	2	190
Region 12: $2.7 \leq m_{\mu\mu} < 2.9$ GeV and $0.86 \leq \tau_{\mu\mu} < 15$ ps	0	0	6	323
Region 22: $2.9 \leq m_{\mu\mu} < 3.1$ GeV and $0.86 \leq \tau_{\mu\mu} < 15$ ps	0	0	140	1041
Region 32: $3.1 \leq m_{\mu\mu} < 3.3$ GeV and $0.86 \leq \tau_{\mu\mu} < 15$ ps	0	1	149	866
Region 42: $3.3 \leq m_{\mu\mu} < 3.5$ GeV and $0.86 \leq \tau_{\mu\mu} < 15$ ps	0	0	1	106
Region 71: Region 21 + Region 31	7229	271	285	4877
Region 81: Region 11 + Region 41	141	11	13	565
Region 72: Region 22 + Region 32	0	1	289	1907
Region 82: Region 12 + Region 42	0	0	7	429
Region 91: Region 71 - Region 81	7088	260	272	4312
Region 92: Region 72 - Region 82	0	1	282	1478
Region 99: Region 91 - Region 92	7088	259	-10	2834

Table D.9: Event selection cut flow for region 1 High

Cut	**signal**	**pp**	**bb**	**data**
Cut 1: Photon Vec > 0	958488	505874	595897	3485326
Cut 2: HLT_2mu4_bJpsimumu_noL2 Trigger	444489	254178	316703	2657060
Cut 3: $\lambda < 15$	431332	212026	262793	2191427
Cut 4: 449	157864	34096	47754	503369
z^2 Cut: $0.1 \leq \cos^2\theta_{CS} < 1.0$	157864	34096	47754	503369
Cut 5: $0 \leq \lambda < 200$	149024	26519	35107	352980
Cut 6: $0 \leq q_T^2 < 400$ GeV^2	145760	18279	24128	257455
ϕ_{CS} Cut: $\frac{3}{8}\pi \leq \lvert\phi_{CS}\rvert < \frac{1}{2}\pi$	33610	5940	7240	67727
Cut 7: $2.7 \leq m_{\mu\mu} < 3.5$ GeV	33543	5935	7223	64741
Cut 8: -5 $\leq \tau <$ 15 ps.	33543	5935	7221	64728
Cut 9: Tight Photons	22319	1656	1992	20710
Cut 10: $\Delta R < 0.12$ between signal reconstructed and truth photons	21783	—	—	—
Region 11: $2.7 \leq m_{\mu\mu} < 2.9$ GeV and -5 $\leq \tau_{\mu\mu} <$ 0.86 ps	311	28	18	1018
Region 21: $2.9 \leq m_{\mu\mu} < 3.1$ GeV and -5 $\leq \tau_{\mu\mu} <$ 0.86 ps	11230	887	511	7576
Region 31: $3.1 \leq m_{\mu\mu} < 3.3$ GeV and -5 $\leq \tau_{\mu\mu} <$ 0.86 ps	10122	722	472	6263
Region 41: $3.3 \leq m_{\mu\mu} < 3.5$ GeV and -5 $\leq \tau_{\mu\mu} <$ 0.86 ps	114	17	7	595
Region 12: $2.7 \leq m_{\mu\mu} < 2.9$ GeV and 0.86 $\leq \tau_{\mu\mu} <$ 15 ps	0	0	19	744
Region 22: $2.9 \leq m_{\mu\mu} < 3.1$ GeV and 0.86 $\leq \tau_{\mu\mu} <$ 15 ps	4	1	521	2495
Region 32: $3.1 \leq m_{\mu\mu} < 3.3$ GeV and 0.86 $\leq \tau_{\mu\mu} <$ 15 ps	2	1	436	1822
Region 42: $3.3 \leq m_{\mu\mu} < 3.5$ GeV and 0.86 $\leq \tau_{\mu\mu} <$ 15 ps	0	0	8	197
Region 71: Region 21 + Region 31	21352	1609	983	13839
Region 81: Region 11 + Region 41	425	45	25	1613
Region 72: Region 22 + Region 32	6	2	957	4317
Region 82: Region 12 + Region 42	0	0	27	941
Region 91: Region 71 - Region 81	20927	1564	958	12226
Region 92: Region 72 - Region 82	6	2	930	3376
Region 99: Region 91 - Region 92	20921	1562	28	8850

Table D.10: Event selection cut flow for region 4 High

Cut	**signal**	**pp**	**bb**	**data**
Cut 1: Photon Vec > 0	958488	505874	595897	3485326
Cut 2: HLT_2mu4_bJpsimumu_noL2 Trigger	444489	254178	316703	2657060
Cut 3: $\lambda < 15$	431332	212026	262793	2191427
Cut 4: 449	157864	34096	47754	503369
z^2 Cut: $0.1 \leq \cos^2\theta_{CS} < 1.0$	157864	34096	47754	503369
Cut 5: $0 \leq \lambda < 200$	149024	26519	35107	352980
Cut 6: $0 \leq q_T^2 < 400$ GeV^2	145760	18279	24128	257455
ϕ_{CS} Cut: $\frac{5}{8}\pi \leq \lvert\phi_{CS}\rvert < \frac{3}{4}\pi$	16537	1448	1641	19995
Cut 7: $2.7 \leq m_{\mu\mu} < 3.5$ GeV	16495	1445	1637	19050
Cut 8: $-5 \leq \tau < 15$ ps.	16494	1445	1637	19041
Cut 9: Tight Photons	11685	426	428	6185
Cut 10: $\Delta R < 0.12$ between signal reconstructed and truth photons	11483	—	—	—
Region 11: $2.7 \leq m_{\mu\mu} < 2.9$ GeV and $-5 \leq \tau_{\mu\mu} < 0.86$ ps	161	4	2	395
Region 21: $2.9 \leq m_{\mu\mu} < 3.1$ GeV and $-5 \leq \tau_{\mu\mu} < 0.86$ ps	6143	252	102	2303
Region 31: $3.1 \leq m_{\mu\mu} < 3.3$ GeV and $-5 \leq \tau_{\mu\mu} < 0.86$ ps	5133	168	98	1764
Region 41: $3.3 \leq m_{\mu\mu} < 3.5$ GeV and $-5 \leq \tau_{\mu\mu} < 0.86$ ps	40	1	2	248
Region 12: $2.7 \leq m_{\mu\mu} < 2.9$ GeV and $0.86 \leq \tau_{\mu\mu} < 15$ ps	0	0	3	219
Region 22: $2.9 \leq m_{\mu\mu} < 3.1$ GeV and $0.86 \leq \tau_{\mu\mu} < 15$ ps	1	1	100	709
Region 32: $3.1 \leq m_{\mu\mu} < 3.3$ GeV and $0.86 \leq \tau_{\mu\mu} < 15$ ps	5	0	121	483
Region 42: $3.3 \leq m_{\mu\mu} < 3.5$ GeV and $0.86 \leq \tau_{\mu\mu} < 15$ ps	0	0	0	64
Region 71: Region 21 + Region 31	11276	420	200	4067
Region 81: Region 11 + Region 41	201	5	4	643
Region 72: Region 22 + Region 32	6	1	221	1192
Region 82: Region 12 + Region 42	0	0	3	283
Region 91: Region 71 - Region 81	11075	415	196	3424
Region 92: Region 72 - Region 82	6	1	218	909
Region 99: Region 91 - Region 92	11069	414	-22	2515

Table D.11: Event selection cut flow for region 6 High

Cut	**signal**	**pp**	**bb**	**data**
Cut 1: Photon Vec > 0	958488	505874	595897	3485326
Cut 2: HLT_2mu4_bJpsimumu_noL2 Trigger	444489	254178	316703	2657060
Cut 3: $\lambda < 15$	431332	212026	262793	2191427
Cut 4: 449	157864	34096	47754	503369
z^2 Cut: $0 \leq \cos^2\theta_{CS} < 0.1$	157864	34096	47754	503369
Cut 5: $0 \leq \lambda < 200$	149024	26519	35107	352980
Cut 6: $0 \leq q_T^2 < 400$ GeV^2	145760	18279	24128	257455
ϕ_{CS} Cut: $\frac{\pi}{4} \leq \lvert\phi_{CS}\rvert < \frac{3}{8}\pi$	20591	2037	3486	36807
Cut 7: $2.7 \leq m_{\mu\mu} < 3.5$ GeV	20551	2034	3481	35117
Cut 8: -5 $\leq \tau <$ 15 ps.	20551	2034	3481	35114
Cut 9: Tight Photons	13987	564	968	11116
Cut 10: $\Delta R < 0.12$ between signal reconstructed and truth photons	13872	—	—	—
Region 11: $2.7 \leq m_{\mu\mu} < 2.9$ GeV and -5 $\leq \tau_{\mu\mu} <$ 0.86 ps	188	5	14	581
Region 21: $2.9 \leq m_{\mu\mu} < 3.1$ GeV and -5 $\leq \tau_{\mu\mu} <$ 0.86 ps	7128	288	230	3829
Region 31: $3.1 \leq m_{\mu\mu} < 3.3$ GeV and -5 $\leq \tau_{\mu\mu} <$ 0.86 ps	6458	265	217	3195
Region 41: $3.3 \leq m_{\mu\mu} < 3.5$ GeV and -5 $\leq \tau_{\mu\mu} <$ 0.86 ps	92	6	5	334
Region 12: $2.7 \leq m_{\mu\mu} < 2.9$ GeV and 0.86 $\leq \tau_{\mu\mu} <$ 15 ps	0	0	9	463
Region 22: $2.9 \leq m_{\mu\mu} < 3.1$ GeV and 0.86 $\leq \tau_{\mu\mu} <$ 15 ps	1	0	261	1411
Region 32: $3.1 \leq m_{\mu\mu} < 3.3$ GeV and 0.86 $\leq \tau_{\mu\mu} <$ 15 ps	3	0	231	1182
Region 42: $3.3 \leq m_{\mu\mu} < 3.5$ GeV and 0.86 $\leq \tau_{\mu\mu} <$ 15 ps	2	0	1	121
Region 71: Region 21 + Region 31	13586	553	447	7024
Region 81: Region 11 + Region 41	280	11	19	915
Region 72: Region 22 + Region 32	4	0	492	2593
Region 82: Region 12 + Region 42	2	0	10	584
Region 91: Region 71 - Region 81	13306	542	428	6109
Region 92: Region 72 - Region 82	2	0	482	2009
Region 99: Region 91 - Region 92	13304	542	-54	4100

Table D.12: Event selection cut flow for region 3 low

Cut	**signal**	**pp**	**bb**	**data**
Cut 1: Photon Vec > 0	958488	505874	595897	3485326
Cut 2: HLT_2mu4_bJpsimumu_noL2 Trigger	444489	254178	316703	2657060
Cut 3: $\lambda < 15$	431332	212026	262793	2191427
Cut 4: 449	157864	34096	47754	503369
z^2 Cut: $0 \leq \cos^2\theta_{CS} < 0.1$	157864	34096	47754	503369
Cut 5: $0 \leq \lambda < 200$	149024	26519	35107	352980
Cut 6: $0 \leq q_T^2 < 400$ GeV^2	145760	18279	24128	257455
ϕ_{CS} Cut: $\frac{3}{8}\pi \leq \lvert\phi_{CS}\rvert < \frac{1}{2}\pi$	33610	5940	7240	67727
Cut 7: $2.7 \leq m_{\mu\mu} < 3.5$ GeV	33543	5935	7223	64741
Cut 8: -5 $\leq \tau <$ 15 ps.	33543	5935	7221	64728
Cut 9: Tight Photons	22319	1656	1992	20710
Cut 10: $\Delta R < 0.12$ between signal reconstructed and truth photons	21783	—	—	—
Region 11: $2.7 \leq m_{\mu\mu} < 2.9$ GeV and -5 $\leq \tau_{\mu\mu} <$ 0.86 ps	311	28	18	1018
Region 21: $2.9 \leq m_{\mu\mu} < 3.1$ GeV and -5 $\leq \tau_{\mu\mu} <$ 0.86 ps	11230	887	511	7576
Region 31: $3.1 \leq m_{\mu\mu} < 3.3$ GeV and -5 $\leq \tau_{\mu\mu} <$ 0.86 ps	10122	722	472	6263
Region 41: $3.3 \leq m_{\mu\mu} < 3.5$ GeV and -5 $\leq \tau_{\mu\mu} <$ 0.86 ps	114	17	7	595
Region 12: $2.7 \leq m_{\mu\mu} < 2.9$ GeV and 0.86 $\leq \tau_{\mu\mu} <$ 15 ps	0	0	19	744
Region 22: $2.9 \leq m_{\mu\mu} < 3.1$ GeV and 0.86 $\leq \tau_{\mu\mu} <$ 15 ps	4	1	521	2495
Region 32: $3.1 \leq m_{\mu\mu} < 3.3$ GeV and 0.86 $\leq \tau_{\mu\mu} <$ 15 ps	2	1	436	1822
Region 42: $3.3 \leq m_{\mu\mu} < 3.5$ GeV and 0.86 $\leq \tau_{\mu\mu} <$ 15 ps	0	0	8	197
Region 71: Region 21 + Region 31	21352	1609	983	13839
Region 81: Region 11 + Region 41	425	45	25	1613
Region 72: Region 22 + Region 32	6	2	957	4317
Region 82: Region 12 + Region 42	0	0	27	941
Region 91: Region 71 - Region 81	20927	1564	958	12226
Region 92: Region 72 - Region 82	6	2	930	3376
Region 99: Region 91 - Region 92	20921	1562	28	8850

Table D.13: Event selection cut flow for region 4 low

Cut	**signal**	**pp**	**bb**	**data**
Cut 1: Photon Vec > 0	958488	505874	595897	3485326
Cut 2: HLT_2mu4_bJpsimumu_noL2 Trigger	444489	254178	316703	2657060
Cut 3: $\lambda < 15$	431332	212026	262793	2191427
Cut 4: 449	157864	34096	47754	503369
z^2 Cut: $0 \leq \cos^2\theta_{CS} < 0.1$	157864	34096	47754	503369
Cut 5: $0 \leq \lambda < 200$	149024	26519	35107	352980
Cut 6: $0 \leq q_T^2 < 400$ GeV^2	145760	18279	24128	257455
ϕ_{CS} Cut: $\frac{7}{8}\pi \leq \lvert\phi_{CS}\rvert < \pi$	8326	462	687	10665
Cut 7: $2.7 \leq m_{\mu\mu} < 3.5$ GeV	8304	461	683	10011
Cut 8: $-5 \leq \tau < 15$ ps.	8304	461	683	10006
Cut 9: Tight Photons	6002	129	180	3086
Cut 10: $\Delta R < 0.12$ between signal reconstructed and truth photons	5923	—	—	—
Region 11: $2.7 \leq m_{\mu\mu} < 2.9$ GeV and $-5 \leq \tau_{\mu\mu} < 0.86$ ps	98	4	2	225
Region 21: $2.9 \leq m_{\mu\mu} < 3.1$ GeV and $-5 \leq \tau_{\mu\mu} < 0.86$ ps	3292	79	50	1059
Region 31: $3.1 \leq m_{\mu\mu} < 3.3$ GeV and $-5 \leq \tau_{\mu\mu} < 0.86$ ps	2505	46	37	849
Region 41: $3.3 \leq m_{\mu\mu} < 3.5$ GeV and $-5 \leq \tau_{\mu\mu} < 0.86$ ps	24	0	3	145
Region 12: $2.7 \leq m_{\mu\mu} < 2.9$ GeV and $0.86 \leq \tau_{\mu\mu} < 15$ ps	0	0	0	138
Region 22: $2.9 \leq m_{\mu\mu} < 3.1$ GeV and $0.86 \leq \tau_{\mu\mu} < 15$ ps	1	0	46	364
Region 32: $3.1 \leq m_{\mu\mu} < 3.3$ GeV and $0.86 \leq \tau_{\mu\mu} < 15$ ps	3	0	42	275
Region 42: $3.3 \leq m_{\mu\mu} < 3.5$ GeV and $0.86 \leq \tau_{\mu\mu} < 15$ ps	0	0	0	31
Region 71: Region 21 + Region 31	5797	125	87	1908
Region 81: Region 11 + Region 41	122	4	5	370
Region 72: Region 22 + Region 32	4	0	88	639
Region 82: Region 12 + Region 42	0	0	0	169
Region 91: Region 71 - Region 81	5675	121	82	1538
Region 92: Region 72 - Region 82	4	0	88	470
Region 99: Region 91 - Region 92	5671	121	-6	1068

Table D.14: Event selection cut flow for region 8 low

Appendix E

HistFactory Fit Results Tables

E.1 HistFactory Results For $\lambda - q_T^2$ Regions

Histogram Variant Name	N_{sig}	N_{PP}	N_{Data}	F_{Sig}	F_{PP}	μ	SPP	ρ	χ^2_{v1}/d.o.f	χ^2_{v2}/d.o.f
38 B16 -1.0 V1	453	180	871	231 ± 26	640 ± 57	0.509 ± 0.053	3.558 ± 0.175	-0.46	1.39	0.44
38 B12 -1.0 V2	453	259	869	242 ± 26	627 ± 50	0.533 ± 0.052	2.423 ± 0.118	-0.43	3.74	1.63
38 B10 -1.0 V1	453	180	873	222 ± 27	651 ± 58	0.491 ± 0.055	3.614 ± 0.179	-0.49	1.23	0.38
38 B10 -1.0 V2	453	259	871	221 ± 25	650 ± 51	0.488 ± 0.051	2.510 ± 0.120	-0.44	2.04	0.89
38 B16 -0.5 V1	452	179	860	231 ± 26	629 ± 56	0.512 ± 0.053	3.513 ± 0.175	-0.46	1.52	0.49
38 B12 -0.5 V2	450	240	821	240 ± 26	581 ± 48	0.533 ± 0.052	2.421 ± 0.125	-0.45	4.37	1.86
38 B10 -0.5 V1	452	179	860	226 ± 27	634 ± 57	0.499 ± 0.055	3.544 ± 0.179	-0.49	1.29	0.42
38 B10 -0.5 V2	450	240	821	220 ± 25	601 ± 49	0.490 ± 0.052	2.502 ± 0.127	-0.45	2.57	1.10

Table E.1: Table of results for the 8 variants for λ slice 38

Histogram Variant Name	N_{sig}	N_{PP}	N_{Data}	F_{Sig}	F_{PP}	μ	SPP	ρ	χ^2_{v1}/d.o.f	χ^2_{v2}/d.o.f
42 B16 -1.0 V1	12124	169	1664	1310 ± 57	354 ± 53	0.108 ± 0.005	2.096 ± 0.272	0.69	0.47	0.00
42 B12 -1.0 V2	12124	244	1664	1114 ± 60	550 ± 64	0.092 ± 0.005	2.253 ± 0.220	0.74	0.21	0.04
42 B10 -1.0 V1	12124	169	1664	1324 ± 59	340 ± 55	0.109 ± 0.005	2.009 ± 0.286	0.72	0.88	0.01
42 B10 -1.0 V2	12124	244	1664	1081 ± 60	584 ± 66	0.089 ± 0.005	2.392 ± 0.223	0.74	0.15	0.00
42 B16 -0.5 V1	12124	169	1664	1310 ± 57	354 ± 53	0.108 ± 0.005	2.096 ± 0.272	0.69	0.47	0.00
42 B12 -0.5 V2	12124	244	1664	1114 ± 60	550 ± 64	0.092 ± 0.005	2.253 ± 0.220	0.74	0.21	0.04
42 B10 -0.5 V1	12124	169	1664	1324 ± 59	340 ± 55	0.109 ± 0.005	2.009 ± 0.286	0.72	0.88	0.01
42 B10 -0.5 V2	12124	244	1664	1081 ± 60	584 ± 66	0.089 ± 0.005	2.392 ± 0.223	0.74	0.15	0.00

Table E.2: Table of results for the 8 variants for λ slice 42

Histogram Variant Name	N_{sig}	N_{PP}	N_{Data}	F_{Sig}	F_{PP}	μ	SPP	ρ	χ^2_{v1}/d.o.f	χ^2_{v2}/d.o.f
44 B16 -1.0 V1	9367	240	1813	1200 ± 66	613 ± 72	0.128 ± 0.007	2.556 ± 0.252	-0.77	2.95	0.07
44 B12 -1.0 V2	9367	306	1813	1148 ± 70	665 ± 76	0.123 ± 0.007	2.173 ± 0.215	-0.80	0.59	0.05
44 B10 -1.0 V1	9367	240	1813	1145 ± 69	668 ± 77	0.122 ± 0.007	2.784 ± 0.267	-0.79	0.77	0.01
44 B10 -1.0 V2	9367	306	1814	1119 ± 72	695 ± 78	0.119 ± 0.008	2.271 ± 0.221	-0.81	0.22	0.00
44 B16 -0.5 V1	9367	240	1813	1200 ± 66	613 ± 72	0.128 ± 0.007	2.556 ± 0.252	-0.77	2.95	0.07
44 B12 -0.5 V2	9367	306	1813	1148 ± 70	665 ± 76	0.123 ± 0.007	2.173 ± 0.215	-0.80	0.59	0.05
44 B10 -0.5 V1	9367	240	1813	1145 ± 69	668 ± 77	0.122 ± 0.007	2.784 ± 0.267	-0.79	0.77	0.01
44 B10 -0.5 V2	9367	306	1814	1119 ± 72	695 ± 78	0.119 ± 0.008	2.271 ± 0.221	-0.81	0.22	0.00

Table E.3: Table of results for the 8 variants for λ slice 44

Histogram Variant Name	N_{sig}	N_{PP}	N_{Data}	F_{Sig}	F_{PP}	μ	SPP	ρ	χ^2_{v1}/d.o.f	χ^2_{v2}/d.o.f
46 B16 -1.0 V1	4154	249	1461	762 ± 50	699 ± 65	0.184 ± 0.012	2.806 ± 0.191	-0.68	0.92	0.15
46 B12 -1.0 V2	4154	328	1461	694 ± 48	768 ± 64	0.167 ± 0.011	2.340 ± 0.145	-0.67	0.59	0.17
46 B10 -1.0 V1	4154	249	1461	743 ± 49	718 ± 66	0.179 ± 0.011	2.882 ± 0.190	-0.68	1.34	0.22
46 B10 -1.0 V2	4154	328	1461	730 ± 49	731 ± 62	0.176 ± 0.011	2.229 ± 0.145	-0.68	0.54	0.05
46 B16 -0.5 V1	4154	249	1461	762 ± 50	699 ± 65	0.184 ± 0.012	2.806 ± 0.191	-0.68	0.92	0.15
46 B12 -0.5 V2	4153	326	1460	686 ± 48	774 ± 64	0.165 ± 0.011	2.374 ± 0.146	-0.67	0.68	0.18
46 B10 -0.5 V1	4154	249	1461	743 ± 49	718 ± 66	0.179 ± 0.011	2.882 ± 0.190	-0.68	1.34	0.22
46 B10 -0.5 V2	4153	326	1460	724 ± 49	736 ± 63	0.174 ± 0.011	2.259 ± 0.146	-0.68	0.58	0.06

Table E.4: Table of results for the 8 variants for λ slice 46

Histogram Variant Name	N_{sig}	N_{PP}	N_{Data}	F_{Sig}	F_{PP}	μ	SPP	ρ	χ^2_{v1}/d.o.f	χ^2_{v2}/d.o.f
51 B16 -1.0 V1	1455	56	410	292 ± 23	118 ± 23	0.201 ± 0.015	2.105 ± 0.307	-0.48	1.63	0.14
51 B12 -1.0 V2	1455	70	412	282 ± 23	130 ± 23	0.194 ± 0.015	1.862 ± 0.251	-0.47	0.99	0.09
51 B10 -1.0 V1	1455	56	411	235 ± 22	176 ± 31	0.161 ± 0.014	3.147 ± 0.348	-0.50	0.37	0.05
51 B10 -1.0 V2	1455	70	412	272 ± 23	140 ± 25	0.187 ± 0.015	1.998 ± 0.259	-0.49	0.51	0.02
51 B16 -0.5 V1	1455	56	410	292 ± 23	118 ± 23	0.201 ± 0.015	2.105 ± 0.307	-0.48	1.63	0.14
51 B12 -0.5 V2	1455	70	412	282 ± 23	130 ± 23	0.194 ± 0.015	1.862 ± 0.251	-0.47	0.99	0.09
51 B10 -0.5 V1	1455	56	411	235 ± 22	176 ± 31	0.161 ± 0.014	3.147 ± 0.348	-0.50	0.37	0.05
51 B10 -0.5 V2	1455	70	412	272 ± 23	140 ± 25	0.187 ± 0.015	1.998 ± 0.259	-0.49	0.51	0.02

Table E.5: Table of results for the 8 variants for λ slice 51

Histogram Variant Name	N_{sig}	N_{PP}	N_{Data}	F_{Sig}	F_{PP}	μ	SPP	ρ	χ^2_{v1}/d.o.f	χ^2_{v2}/d.o.f
53 B16 -1.0 V1	3801	165	1273	710 ± 40	563 ± 57	0.187 ± 0.010	3.415 ± 0.217	-0.53	1.03	0.10
53 B12 -1.0 V2	3801	208	1273	657 ± 38	615 ± 56	0.173 ± 0.010	2.958 ± 0.173	-0.52	0.91	0.11
53 B10 -1.0 V1	3801	165	1273	694 ± 40	579 ± 58	0.183 ± 0.010	3.508 ± 0.222	-0.54	1.06	0.07
53 B10 -1.0 V2	3801	208	1273	641 ± 39	632 ± 57	0.169 ± 0.010	3.040 ± 0.178	-0.54	0.46	0.06
53 B16 -0.5 V1	3801	165	1273	710 ± 40	563 ± 57	0.187 ± 0.010	3.415 ± 0.217	-0.53	1.03	0.10
53 B12 -0.5 V2	3801	208	1273	657 ± 38	615 ± 56	0.173 ± 0.010	2.958 ± 0.173	-0.52	0.91	0.11
53 B10 -0.5 V1	3801	165	1273	694 ± 40	579 ± 58	0.183 ± 0.010	3.508 ± 0.222	-0.54	1.06	0.07
53 B10 -0.5 V2	3801	208	1273	641 ± 39	632 ± 57	0.169 ± 0.010	3.040 ± 0.178	-0.54	0.46	0.06

Table E.6: Table of results for the 8 variants for λ slice 53

Histogram Variant Name	N_{sig}	N_{PP}	N_{Data}	F_{Sig}	F_{PP}	μ	SPP	ρ	χ^2_{v1}/d.o.f	χ^2_{v2}/d.o.f
55 B16 -1.0 V1	2748	144	1369	761 ± 43	608 ± 64	0.277 ± 0.015	4.224 ± 0.268	-0.56	2.37	0.19
55 B12 -1.0 V2	2748	195	1369	692 ± 43	677 ± 63	0.252 ± 0.015	3.473 ± 0.208	-0.59	1.84	0.17
55 B10 -1.0 V1	2748	144	1369	716 ± 44	653 ± 68	0.261 ± 0.015	4.532 ± 0.285	-0.60	1.14	0.10
55 B10 -1.0 V2	2748	195	1369	689 ± 43	680 ± 64	0.251 ± 0.015	3.487 ± 0.211	-0.60	0.69	0.04
55 B16 -0.5 V1	2747	144	1368	759 ± 43	609 ± 64	0.276 ± 0.015	4.230 ± 0.269	-0.57	2.61	0.21
55 B12 -0.5 V2	2748	195	1369	692 ± 43	677 ± 63	0.252 ± 0.015	3.473 ± 0.208	-0.59	1.84	0.17
55 B10 -0.5 V1	2747	144	1368	718 ± 44	651 ± 68	0.261 ± 0.015	4.518 ± 0.285	-0.60	1.13	0.10
55 B10 -0.5 V2	2748	195	1369	689 ± 43	680 ± 64	0.251 ± 0.015	3.487 ± 0.211	-0.60	0.69	0.04

Table E.7: Table of results for the 8 variants for λ slice 55

E.2 HistFactory Results For $|\phi_{CS}|$ Regions

Histogram Variant Name	N_{sig}	N_{PP}	N_{Data}	F_{Sig}	F_{PP}	μ	SPP	ρ	χ^2_{v1}/d.o.f	χ^2_{v2}/d.o.f
1 B20 High -1.0 V2	2514	136	631	493 ± 29	138 ± 23	0.196 ± 0.011	1.016 ± 0.143	0.45	0.75	0.18
1 B14 High -1.0 V1	2514	82	631	490 ± 28	141 ± 24	0.195 ± 0.010	1.723 ± 0.224	-0.41	2.25	0.53
1 B14 High -1.0 V2	2514	136	631	481 ± 29	150 ± 24	0.191 ± 0.011	1.101 ± 0.145	0.45	1.19	0.20
1 B12 High -1.0 V1	2514	82	631	478 ± 28	153 ± 26	0.190 ± 0.011	1.869 ± 0.235	-0.43	1.03	0.19
1 B20 High -0.5 V2	2512	130	616	509 ± 30	107 ± 22	0.203 ± 0.011	0.823 ± 0.151	0.51	0.73	0.10
1 B14 High -0.5 V1	2513	81	621	500 ± 28	121 ± 22	0.199 ± 0.011	1.494 ± 0.223	-0.43	1.65	0.14
1 B14 High -0.5 V2	2512	130	616	495 ± 30	121 ± 23	0.197 ± 0.011	0.928 ± 0.154	0.50	1.19	0.11
1 B12 High -0.5 V1	2513	81	621	488 ± 29	133 ± 24	0.194 ± 0.011	1.643 ± 0.237	-0.46	1.06	0.19

Table E.8: Table of results for the 8 variants for $|\phi_{CS}|$ slice 1 high

Histogram Variant Name	N_{sig}	N_{PP}	N_{Data}	F_{Sig}	F_{PP}	μ	SPP	ρ	χ^2_{v1}/d.o.f	χ^2_{v2}/d.o.f
4 B20 High -1.0 V2	9525	1774	5957	950 ± 53	5007 ± 145	0.100 ± 0.005	2.822 ± 0.046	-0.41	3.44	1.35
4 B14 High -1.0 V1	9525	1182	5957	1026 ± 53	4931 ± 165	0.108 ± 0.005	4.172 ± 0.069	-0.39	3.60	0.88
4 B14 High -1.0 V2	9525	1774	5957	931 ± 53	5026 ± 145	0.098 ± 0.006	2.833 ± 0.047	-0.42	4.22	1.58
4 B12 High -1.0 V1	9525	1182	5957	1013 ± 53	4944 ± 165	0.106 ± 0.005	4.183 ± 0.069	-0.39	3.75	0.94
4 B20 High -0.5 V2	9470	912	3667	805 ± 57	2862 ± 119	0.085 ± 0.006	3.139 ± 0.080	-0.59	2.71	0.73
4 B14 High -0.5 V1	9472	617	3647	970 ± 58	2677 ± 129	0.102 ± 0.006	4.339 ± 0.114	-0.57	2.59	0.31
4 B14 High -0.5 V2	9470	912	3667	772 ± 58	2895 ± 121	0.081 ± 0.006	3.175 ± 0.081	-0.60	1.69	0.34
4 B12 High -0.5 V1	9472	617	3647	954 ± 57	2693 ± 129	0.101 ± 0.006	4.364 ± 0.114	-0.56	2.53	0.25

Table E.9: Table of results for the 8 variants for $|\phi_{CS}|$ slice 4 high

Histogram Variant Name	N_{sig}	N_{PP}	N_{Data}	F_{Sig}	F_{PP}	μ	SPP	ρ	χ^2_{v1}/d.o.f	χ^2_{v2}/d.o.f	χ^2_{v3}/d.o.f
6 B20 High -1.0 V2	6254	447	2752	948 ± 54	1804 ± 104	0.152 ± 0.008	4.035 ± 0.134	-0.57	2.38	0.75	1.20
6 B14 High -1.0 V1	6254	373	2752	976 ± 53	1776 ± 109	0.156 ± 0.008	4.762 ± 0.157	-0.55	3.23	0.75	1.65
6 B14 High -1.0 V2	6254	447	2752	952 ± 53	1799 ± 104	0.152 ± 0.008	4.025 ± 0.132	-0.56	4.31	1.31	2.28
6 B12 High -1.0 V1	6254	373	2752	900 ± 54	1852 ± 114	0.144 ± 0.008	4.965 ± 0.163	-0.58	3.14	0.83	1.36
6 B20 High -0.5 V2	6233	415	2542	1035 ± 57	1507 ± 95	0.166 ± 0.009	3.631 ± 0.144	-0.62	1.23	0.22	0.64
6 B14 High -0.5 V1	6230	350	2550	1065 ± 56	1485 ± 98	0.171 ± 0.009	4.243 ± 0.166	-0.60	1.81	0.16	1.07
6 B14 High -0.5 V2	6233	415	2542	1037 ± 56	1505 ± 94	0.166 ± 0.009	3.627 ± 0.142	-0.61	1.87	0.16	1.08
6 B12 High -0.5 V1	6230	350	2550	986 ± 57	1564 ± 103	0.158 ± 0.009	4.468 ± 0.172	-0.62	1.11	0.06	0.66

Table E.10: Table of results for the 8 variants for $|\phi_{CS}|$ slice 6 high

Histogram Variant Name	N_{sig}	N_{PP}	N_{Data}	F_{Sig}	F_{PP}	μ	SPP	ρ	χ^2_{v1}/d.o.f	χ^2_{v2}/d.o.f
3 B20 Low -1.0 V2	5819	159	797	586 ± 36	211 ± 33	0.101 ± 0.006	1.329 ± 0.181	0.62	0.48	0.10
3 B14 Low -1.0 V1	5819	109	797	657 ± 34	140 ± 28	0.113 ± 0.006	1.288 ± 0.223	0.56	0.64	0.20
3 B14 Low -1.0 V2	5819	159	797	569 ± 36	228 ± 35	0.098 ± 0.006	1.433 ± 0.188	0.63	0.66	0.10
3 B12 Low -1.0 V1	5819	109	797	654 ± 35	143 ± 28	0.112 ± 0.006	1.312 ± 0.227	0.57	0.15	0.00
3 B20 Low -0.5 V2	5819	158	794	591 ± 36	203 ± 33	0.102 ± 0.006	1.286 ± 0.183	0.63	0.53	0.10
3 B14 Low -0.5 V1	5819	109	797	657 ± 34	140 ± 28	0.113 ± 0.006	1.288 ± 0.223	0.56	0.64	0.20
3 B14 Low -0.5 V2	5819	158	794	574 ± 36	220 ± 35	0.099 ± 0.006	1.393 ± 0.190	0.64	0.64	0.09
3 B12 Low -0.5 V1	5819	109	797	654 ± 35	143 ± 28	0.112 ± 0.006	1.312 ± 0.227	0.57	0.15	0.00

Table E.11: Table of results for the 8 variants for $|\phi_{CS}|$ slice 3 low

Histogram Variant Name	N_{sig}	N_{PP}	N_{Data}	F_{Sig}	F_{PP}	μ	SPP	ρ	χ^2_{v1}/d.o.f	χ^2_{v2}/d.o.f
8 B20 Low -1.0 V2	3937	104	1111	945 ± 45	166 ± 36	0.240 ± 0.011	1.597 ± 0.305	-0.63	0.45	0.05
8 B14 Low -1.0 V1	3937	91	1111	920 ± 44	191 ± 37	0.234 ± 0.010	2.096 ± 0.338	-0.60	0.89	0.02
8 B14 Low -1.0 V2	3937	104	1111	920 ± 45	191 ± 38	0.234 ± 0.011	1.836 ± 0.316	-0.64	0.20	0.01
8 B12 Low -1.0 V1	3937	91	1111	939 ± 44	172 ± 35	0.238 ± 0.010	1.892 ± 0.335	-0.60	0.83	0.05
8 B20 Low -0.5 V2	3937	104	1111	945 ± 45	166 ± 36	0.240 ± 0.011	1.597 ± 0.305	-0.63	0.45	0.05
8 B14 Low -0.5 V1	3937	91	1111	920 ± 44	191 ± 37	0.234 ± 0.010	2.096 ± 0.338	-0.60	0.89	0.02
8 B14 Low -0.5 V2	3937	104	1111	920 ± 45	191 ± 38	0.234 ± 0.011	1.836 ± 0.316	-0.64	0.20	0.01
8 B12 Low -0.5 V1	3937	91	1111	939 ± 44	172 ± 35	0.238 ± 0.010	1.892 ± 0.335	-0.60	0.83	0.05

Table E.12: Table of results for the 8 variants for $|\phi_{CS}|$ slice 8 low

Appendix F

HistFactory Fit Plots

F.1 HistFactory Fits For $\lambda - q_T^2$ Regions

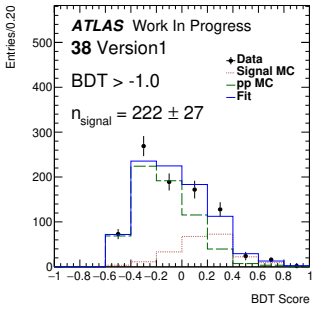

(a) Slice 38 B10 -1.0 V1

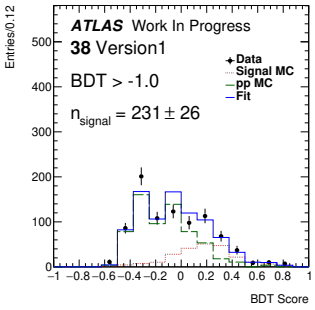

(b) Slice 38 B16 -1.0 V1

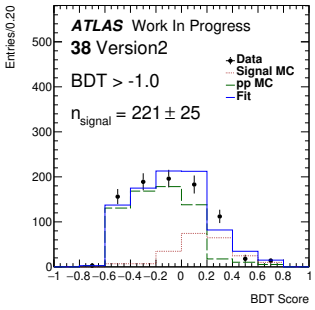

(c) Slice 38 B10 -1.0 V2

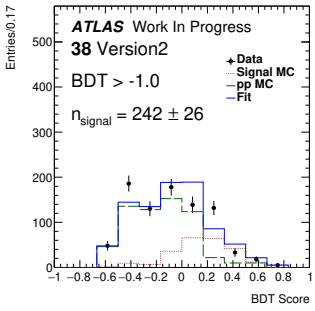

(d) Slice 38 B12 -1.0 V2

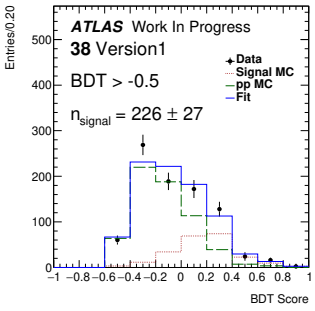

(e) Slice 38 B10 -0.5 V1

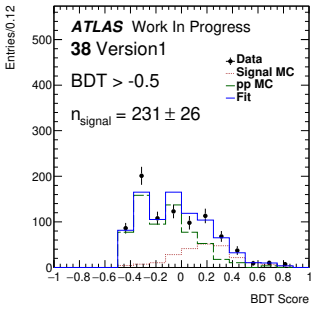

(f) Slice 38 B16 -0.5 V1

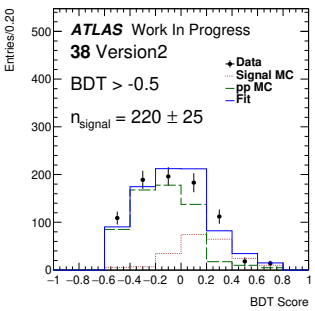

(g) Slice 38 B10 -0.5 V2

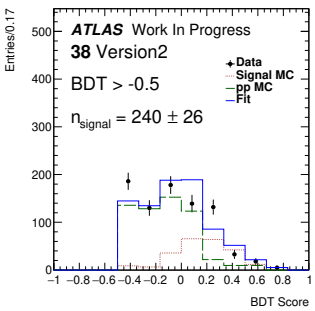

(h) Slice 38 B12 -0.5 V2

Figure F.1: HistFactory fits across the 8 variants for slice 38

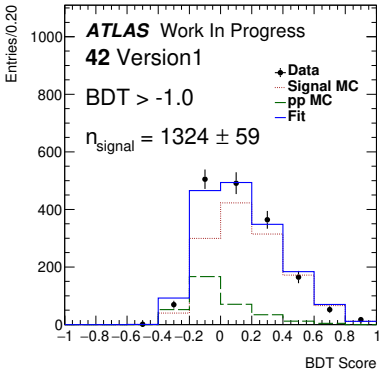

(a) Slice 42 B10 -1.0 V1

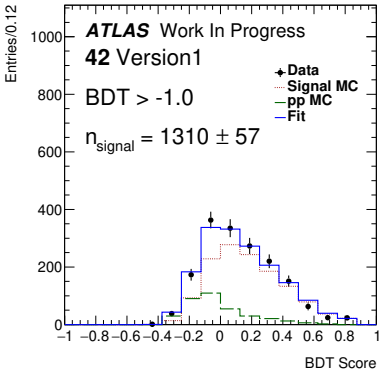

(b) Slice 42 B16 -1.0 V1

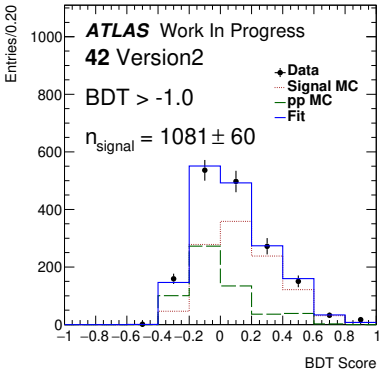

(c) Slice 42 B10 -1.0 V2

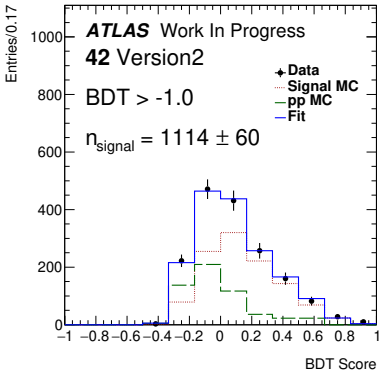

(d) Slice 42 B12 -1.0 V2

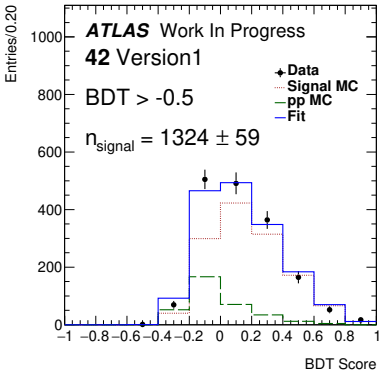

(e) Slice 42 B10 -0.5 V1

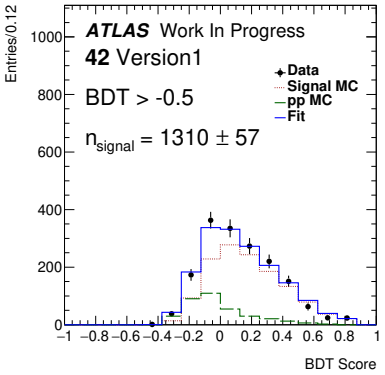

(f) Slice 42 B16 -0.5 V1

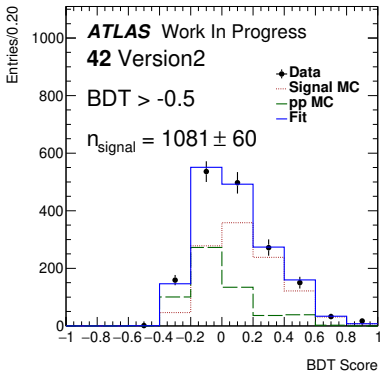

(g) Slice 42 B10 -0.5 V2

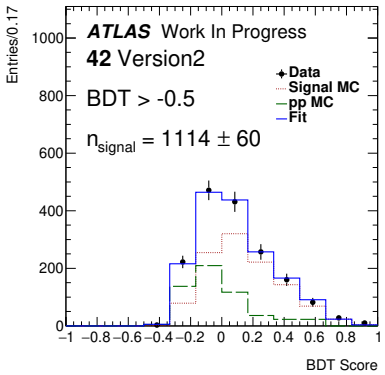

(h) Slice 42 B12 -0.5 V2

Figure F.2: HistFactory fits across the 8 variants for slice 42

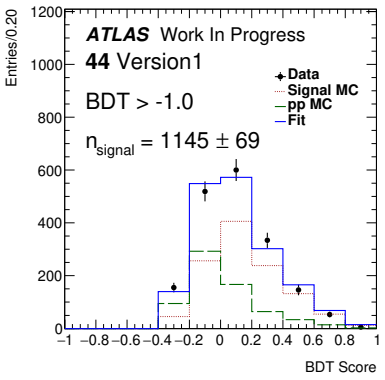

(a) Slice 44 B10 -1.0 V1

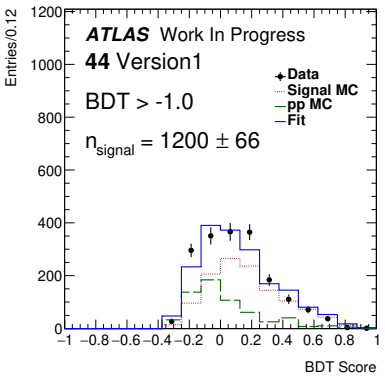

(b) Slice 44 B16 -1.0 V1

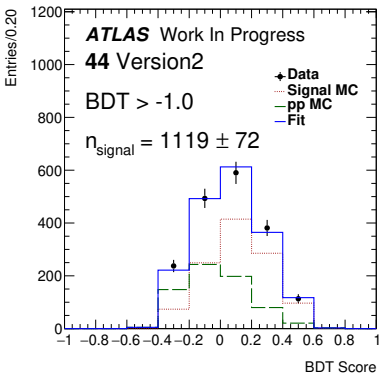

(c) Slice 44 B10 -1.0 V2

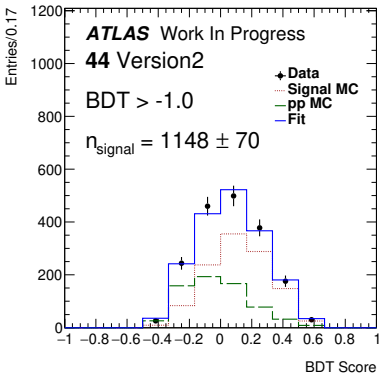

(d) Slice 44 B12 -1.0 V2

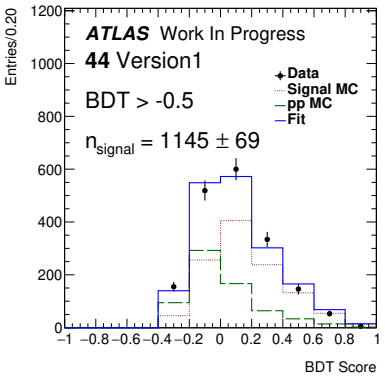

(e) Slice 44 B10 -0.5 V1

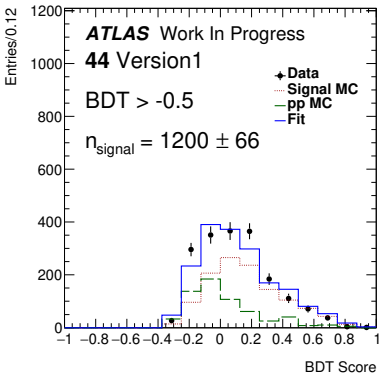

(f) Slice 44 B16 -0.5 V1

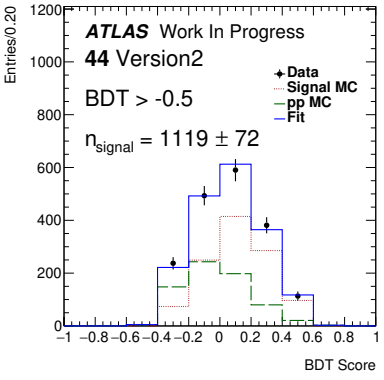

(g) Slice 44 B10 -0.5 V2

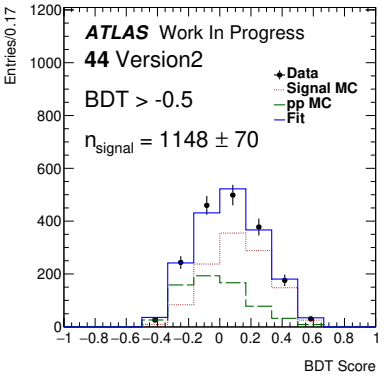

(h) Slice 44 B12 -0.5 V2

Figure F.3: HistFactory fits across the 8 variants for slice 44

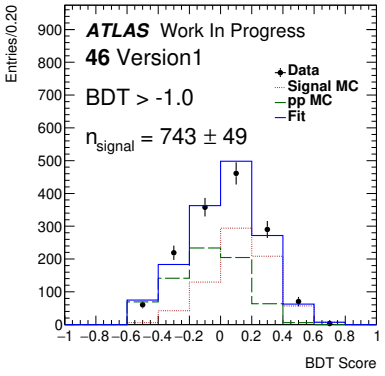

(a) Slice 46 B10 -1.0 V1

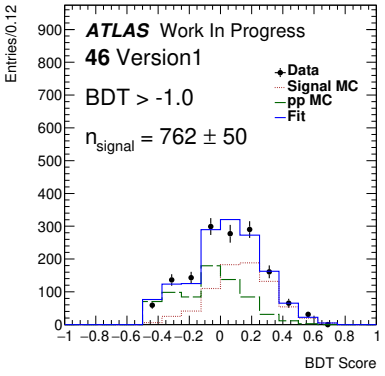

(b) Slice 46 B16 -1.0 V1

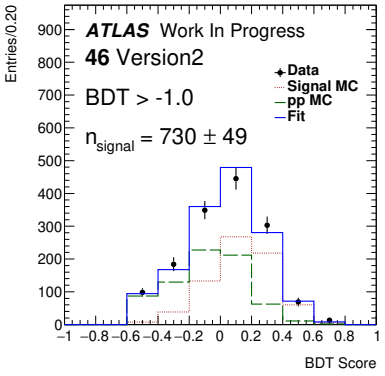

(c) Slice 46 B10 -1.0 V2

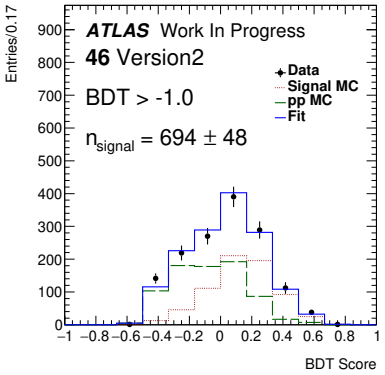

(d) Slice 46 B12 -1.0 V2

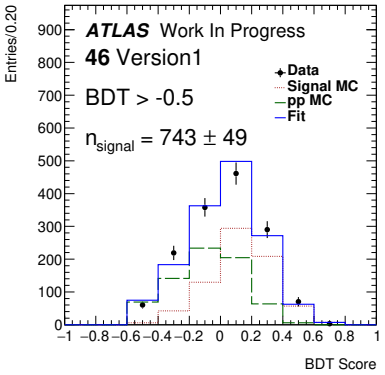

(e) Slice 46 B10 -0.5 V1

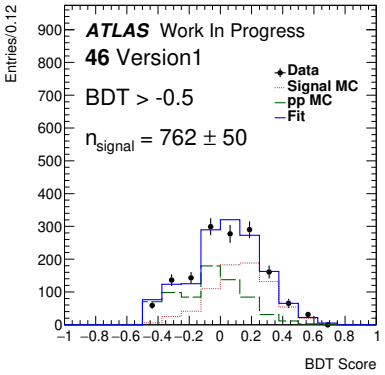

(f) Slice 46 B16 -0.5 V1

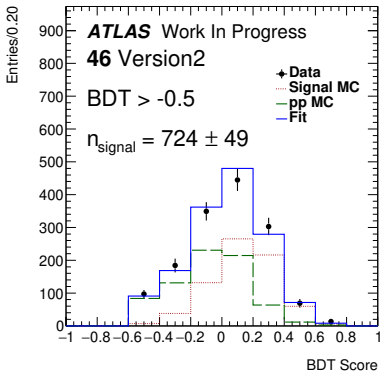

(g) Slice 46 B10 -0.5 V2

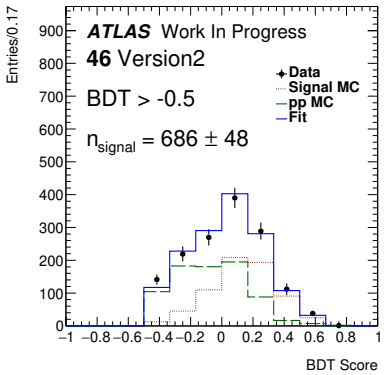

(h) Slice 46 B12 -0.5 V2

Figure F.4: HistFactory fits across the 8 variants for slice 46

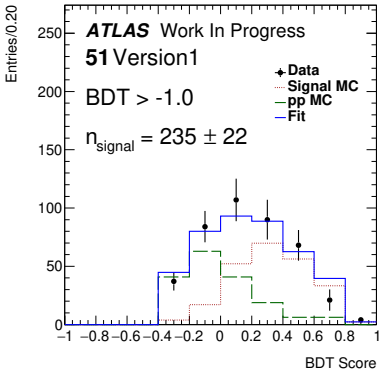

(a) Slice 51 B10 -1.0 V1

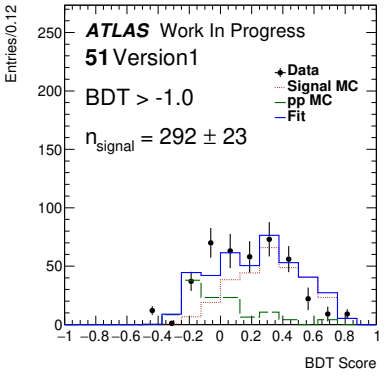

(b) Slice 51 B16 -1.0 V1

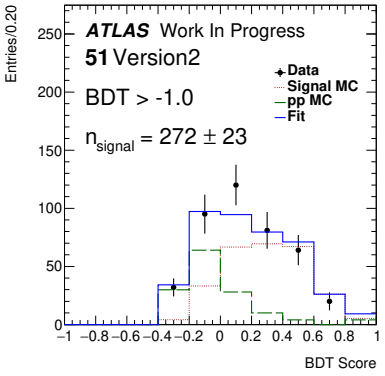

(c) Slice 51 B10 -1.0 V2

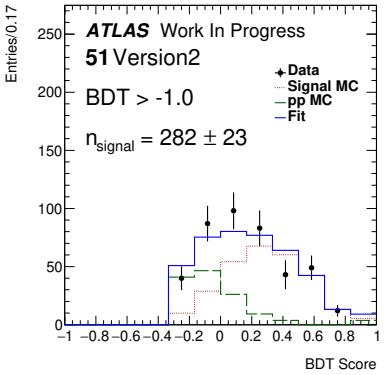

(d) Slice 51 B12 -1.0 V2

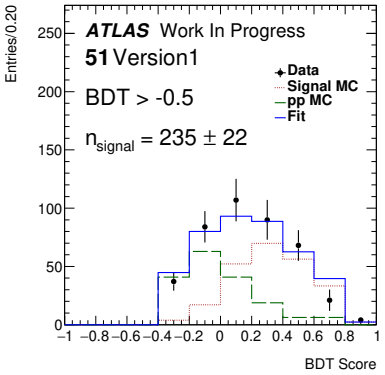

(e) Slice 51 B10 -0.5 V1

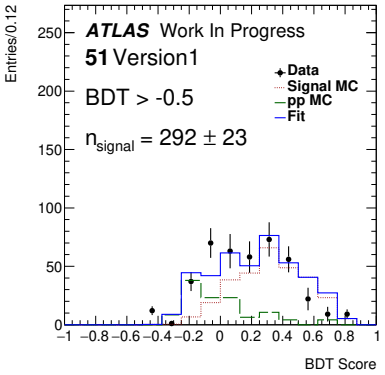

(f) Slice 51 B16 -0.5 V1

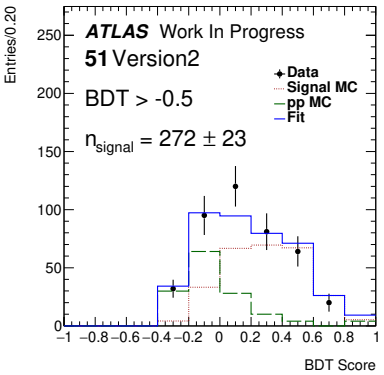

(g) Slice 51 B10 -0.5 V2

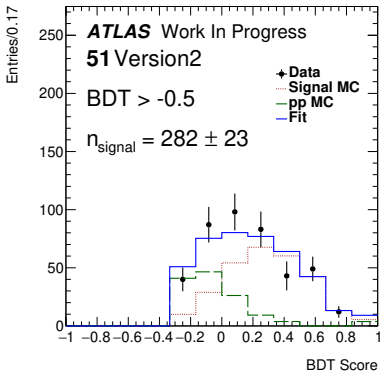

(h) Slice 51 B12 -0.5 V2

Figure F.5: HistFactory fits across the 8 variants for slice 51

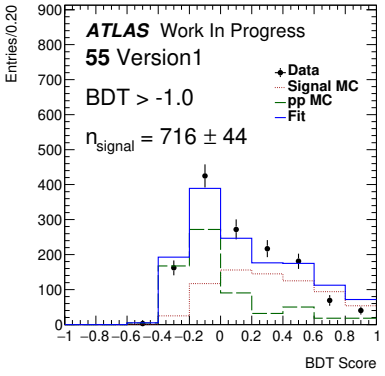

(a) Slice 55 B10 -1.0 V1

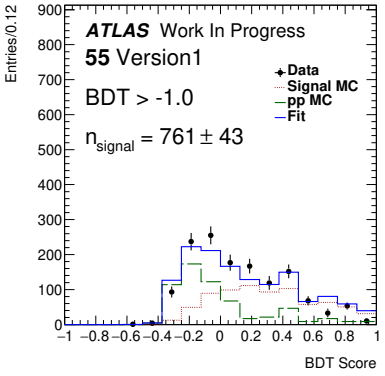

(b) Slice 55 B16 -1.0 V1

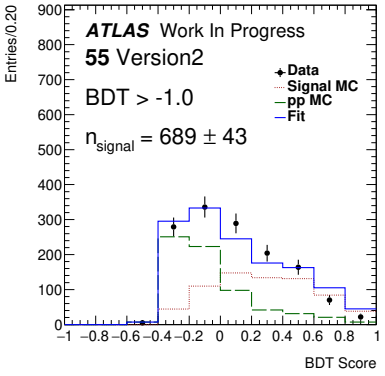

(c) Slice 55 B10 -1.0 V2

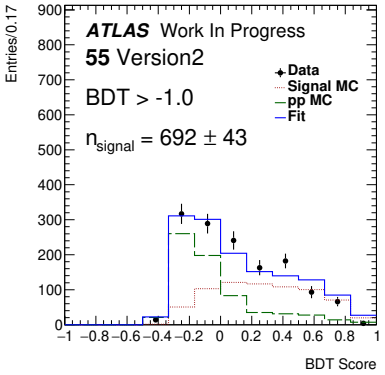

(d) Slice 55 B12 -1.0 V2

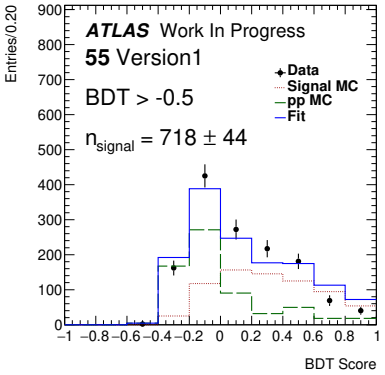

(e) Slice 55 B10 -0.5 V1

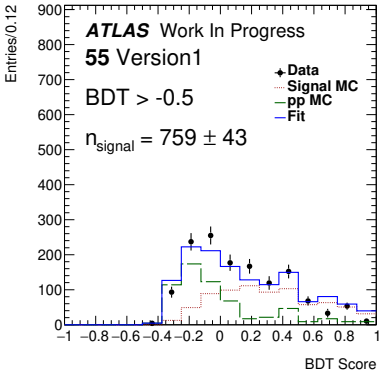

(f) Slice 55 B16 -0.5 V1

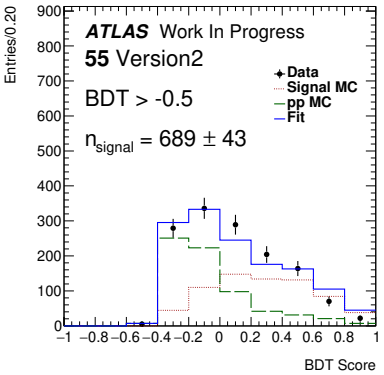

(g) Slice 55 B10 -0.5 V2

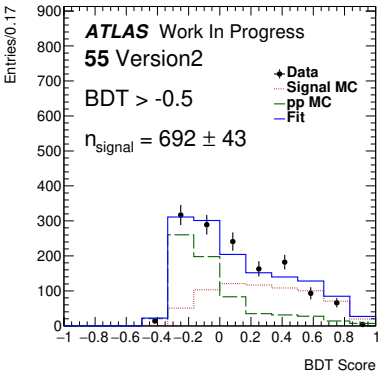

(h) Slice 55 B12 -0.5 V2

Figure F.6: HistFactory fits across the 8 variants for slice 55

F.2 HistFactory Fits For $|\Phi_{CS}|$ Regions

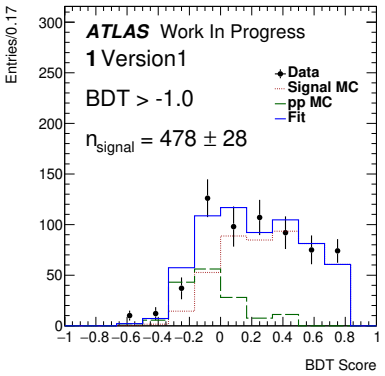

(a) Slice 1 B12 -1.0 V1 High

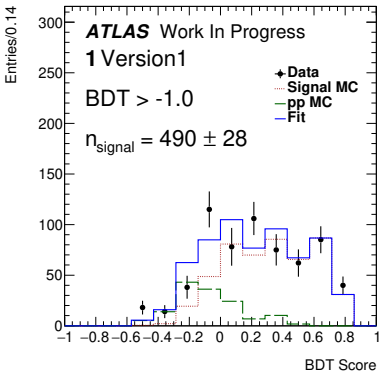

(b) Slice 1 B14 -1.0 V1 High

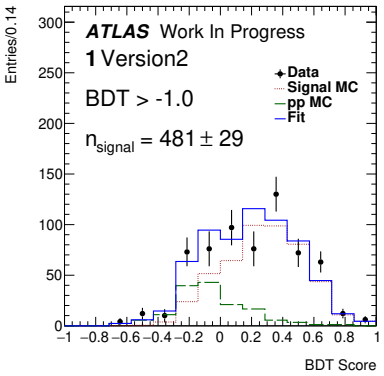

(c) Slice 1 B14 -1.0 V2 High

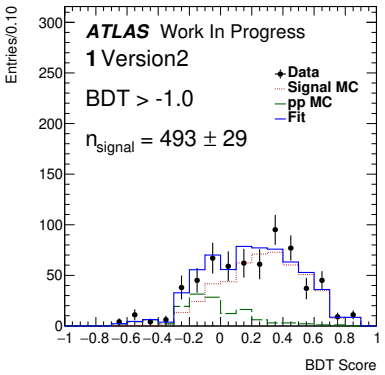

(d) Slice 1 B20 -1.0 V2 High

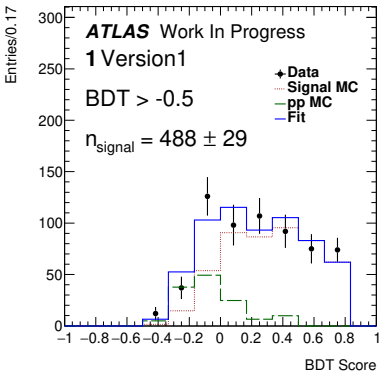

(e) Slice 1 B12 -0.5 V1 High

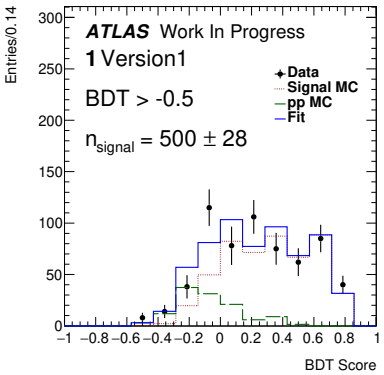

(f) Slice 1 B14 -0.5 V1 High

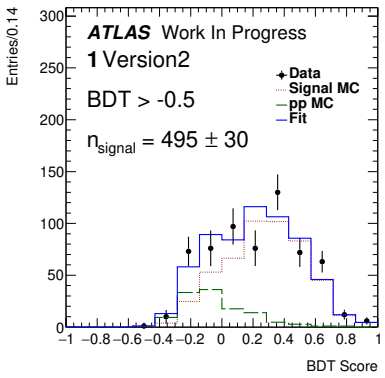

(g) Slice 1 B14 -0.5 V2 High

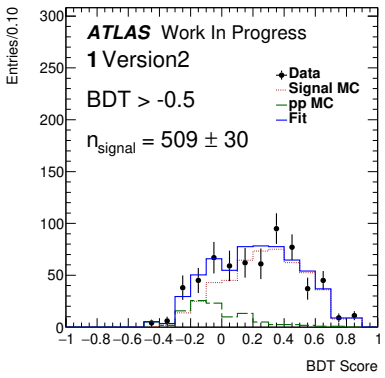

(h) Slice 1 B20 -0.5 V2 High

Figure F.7: HistFactory fits across the 8 variants for slice 1 High

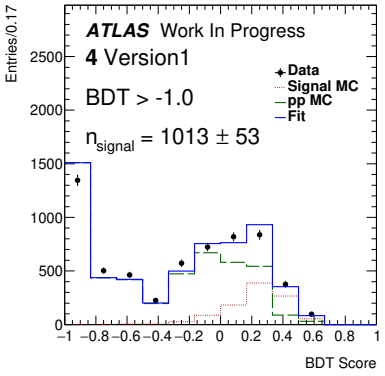

(a) Slice 4 B12 -1.0 V1 High

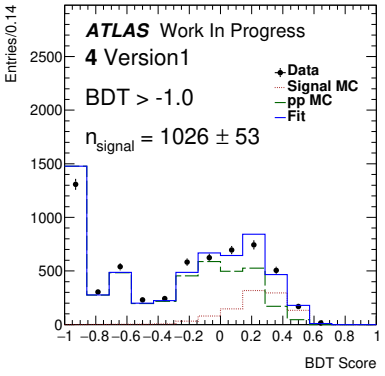

(b) Slice 4 B14 -1.0 V1 High

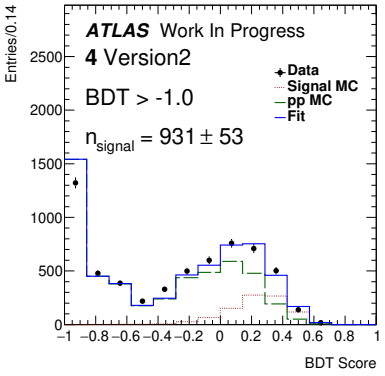

(c) Slice 4 B14 -1.0 V2 High

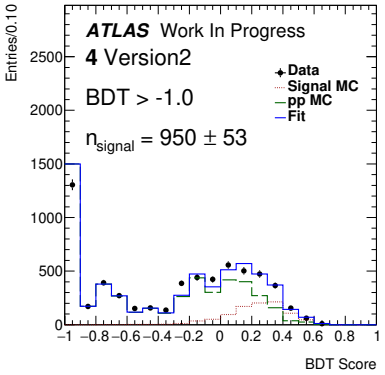

(d) Slice 4 B20 -1.0 V2 High

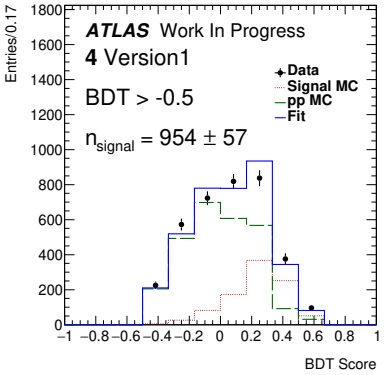

(e) Slice 4 B12 -0.5 V1 High

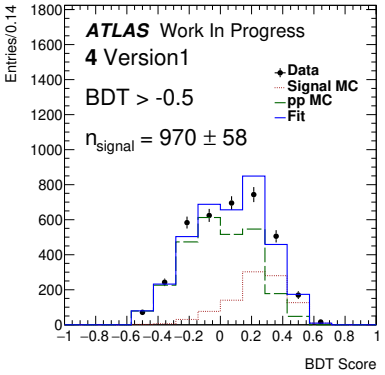

(f) Slice 4 B14 -0.5 V1 High

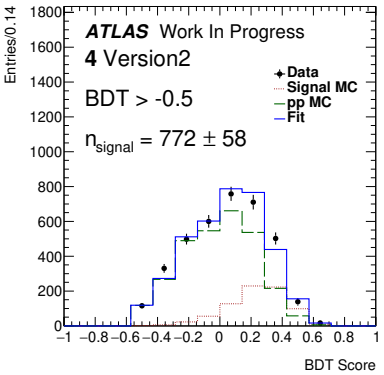

(g) Slice 4 B14 -0.5 V2 High

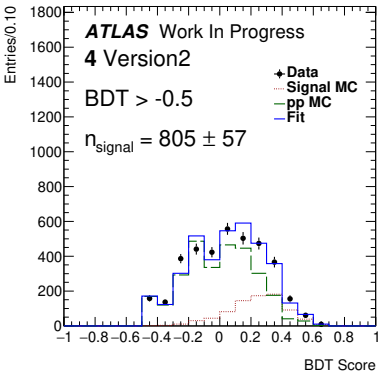

(h) Slice 4 B20 -0.5 V2 High

Figure F.8: HistFactory fits across the 8 variants for slice 4 High

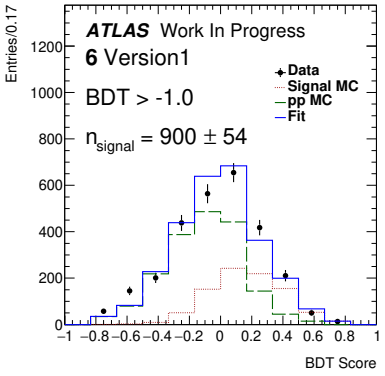

(a) Slice 6 B12 -1.0 V1 High

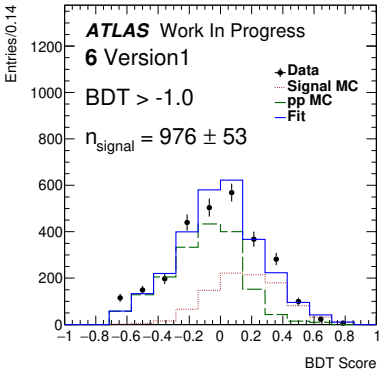

(b) Slice 6 B14 -1.0 V1 High

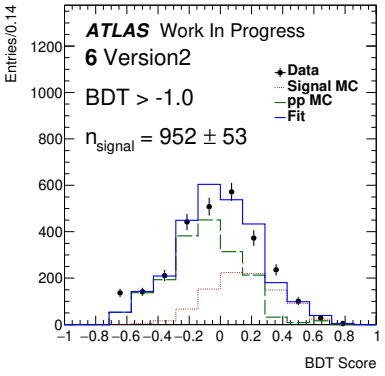

(c) Slice 6 B14 -1.0 V2 High

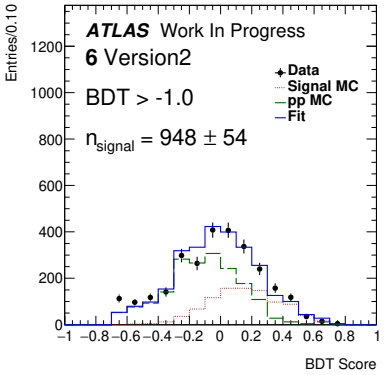

(d) Slice 6 B20 -1.0 V2 High

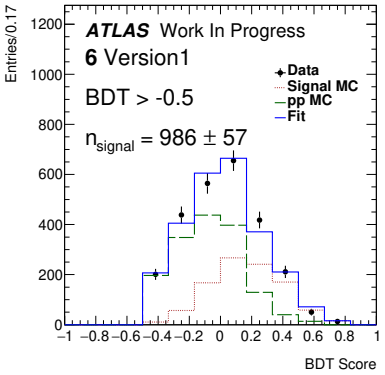

(e) Slice 6 B12 -0.5 V1 High

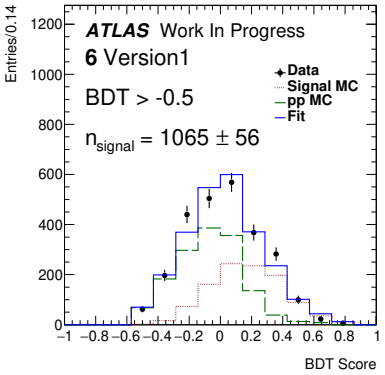

(f) Slice 6 B14 -0.5 V1 High

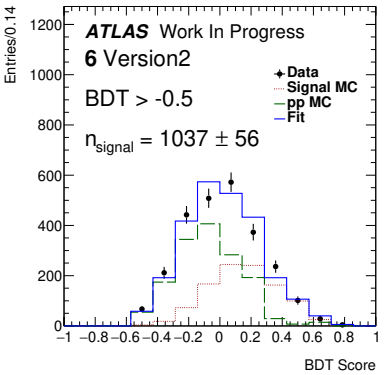

(g) Slice 6 B14 -0.5 V2 High

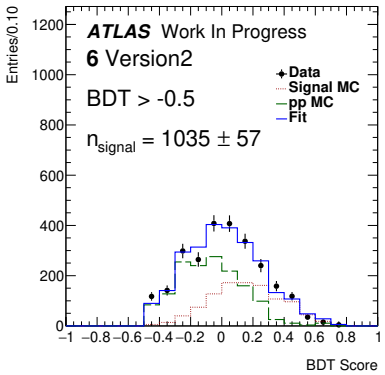

(h) Slice 6 B20 -0.5 V2 High

Figure F.9: HistFactory fits across the 8 variants for slice 6 High

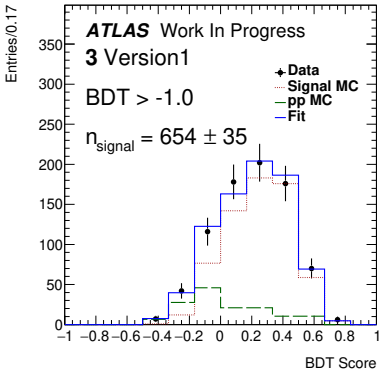

(a) Slice 3 B12 -1.0 V1 Low

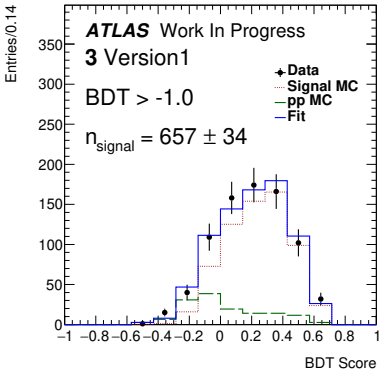

(b) Slice 3 B14 -1.0 V1 Low

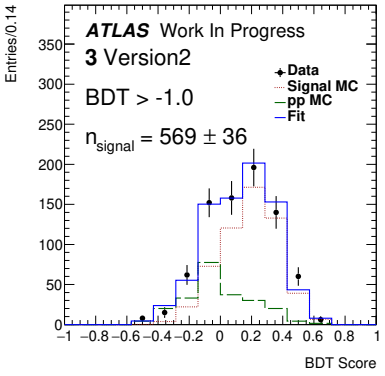

(c) Slice 3 B14 -1.0 V2 Low

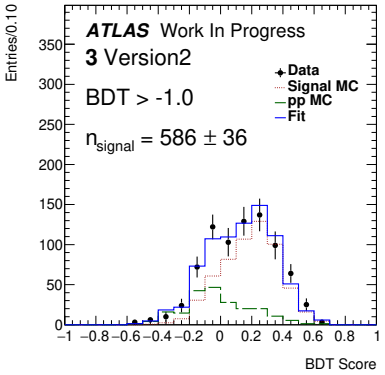

(d) Slice 3 B20 -1.0 V2 Low

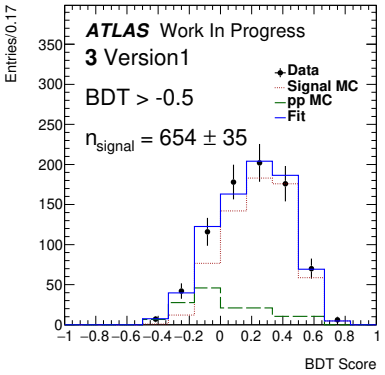

(e) Slice 3 B12 -0.5 V1 Low

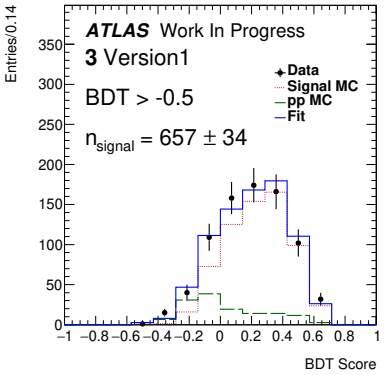

(f) Slice 3 B14 -0.5 V1 Low

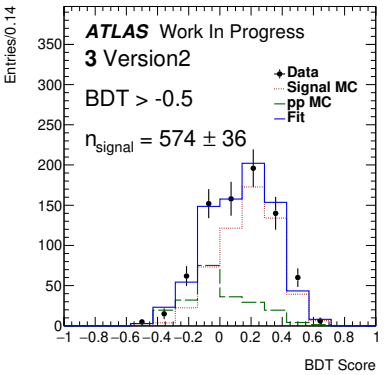

(g) Slice 3 B12 -0.5 V2 Low

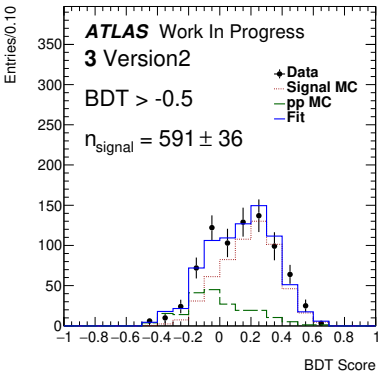

(h) Slice 3 B20 -0.5 V2 Low

Figure F.10: HistFactory fits across the 8 variants for slice 3 Low

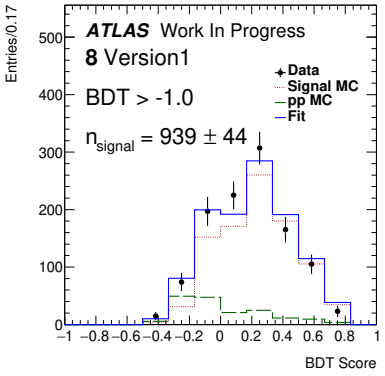

(a) Slice 8 B12 -1.0 V1

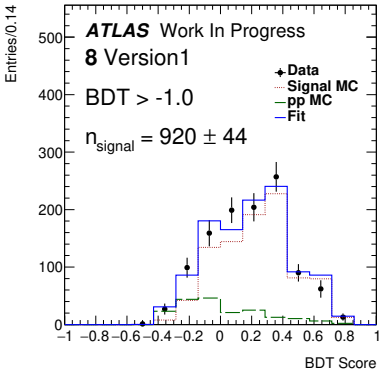

(b) Slice 8 B14 -1.0 V1

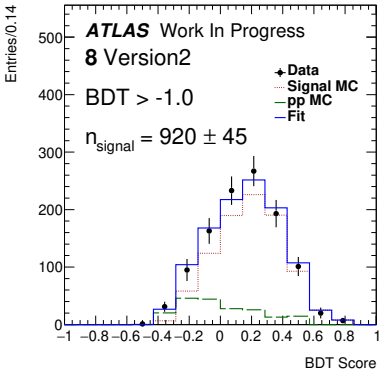

(c) Slice 8 B14 -1.0 V2

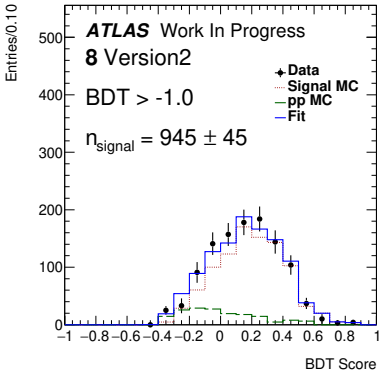

(d) Slice 8 B20 -1.0 V2

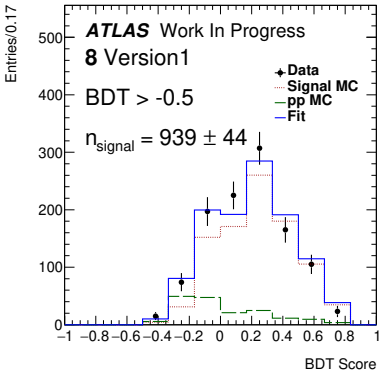

(e) Slice 8 B12 -0.5 V1

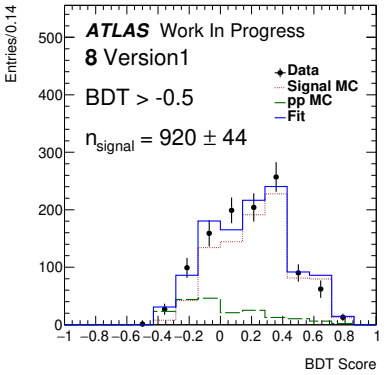

(f) Slice 8 B14 -0.5 V1

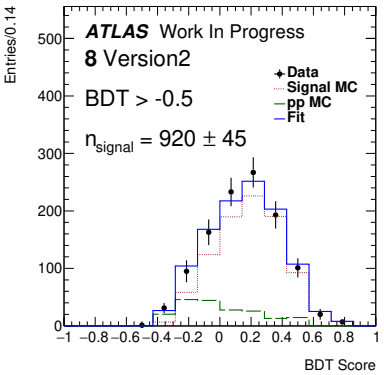

(g) Slice 8 B12 -0.5 V2

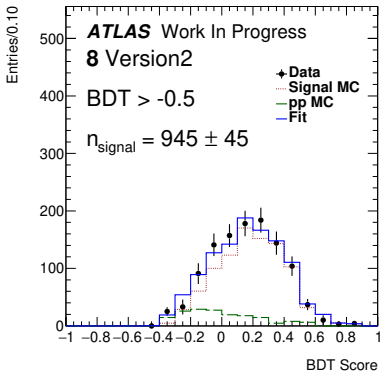

(h) Slice 8 B20 -0.5 V2

Figure F.11: HistFactory fits across the 8 variants for slice 8 Low

Bibliography

[1] G. Aad et al. “The ATLAS Experiment at the CERN Large Hadron Collider”. In: *JINST* 3 (2008), S08003.

[2] Michael Benedikt and Frank Zimmermann. “Proton Colliders at the Energy Frontier”. In: *Nucl. Instrum. Meth. A* 907 (2018), pp. 200–208. eprint: 1803.09723.

[3] S. Chatrchyan et al. “The CMS Experiment at the CERN LHC”. In: *JINST* 3 (2008), S08004.

[4] Jr. Alves A.Augusto et al. “The LHCb Detector at the LHC”. In: *JINST* 3 (2008), S08005.

[5] K. Aamodt et al. “The ALICE experiment at the CERN LHC”. In: *JINST* 3 (2008), S08002.

[6] Esma Mobs. *The CERN accelerator complex - 2019. Complexe des accélérateurs du CERN - 2019*. General Photo. July 2019.

[7] Manuel Guth. “Signal Region Optimisation Studies Based on BDT and Multi-Bin Approaches in the Context of Supersymmetry Searches in Hadronic Final States with the ATLAS Detector”. PhD thesis. Mar. 2018.

[8] Jorg Wenninger. “Operation and Configuration of the LHC in Run 2”. In: (Mar. 2019).

[9] *Luminosity determination in pp collisions at $\sqrt{s} = 13$ TeV using the ATLAS detector at the LHC*. Tech. rep. ATLAS-CONF-2019-021. Geneva, June 2019.

[10] J. Boyd. *The LHC machine in Run-2, and physics highlights from the ATLAS experiment*. June 2018.

[11] *ATLAS magnet system: Technical Design Report, 1*. Technical Design Report ATLAS. Geneva: CERN, 1997.

[12] G. Baccaglioni et al. “Design, Manufacture, and Test of the ATLAS Magnet System Run Down Units”. In: *IEEE Trans. Appl. Supercond.* 16.2 (2006), pp. 561–564.

[13] M. Jackson. “Search for a Standard Model Higgs Boson in the ZH $\to \nu\nu$ bb channel with the ATLAS detector”. PhD thesis. Aug. 2015.

[14] Bartosz Mindur. “ATLAS Transition Radiation Tracker (TRT): Straw tubes for tracking and particle identification at the Large Hadron Collider”. In: *Nucl. Instrum. Meth. A* 845 (2017). Ed. by G. Badurek et al., pp. 257–261.

[15] M Capeans et al. *ATLAS Insertable B-Layer Technical Design Report*. Tech. rep. CERN-LHCC-2010-013. ATLAS-TDR-19. Sept. 2010.

[16] M.S. Alam et al. “The ATLAS silicon pixel sensors”. In: *Nucl. Instrum. Meth. A* 456 (2001), pp. 217–232.

[17] Georges Aad et al. “Operation and performance of the ATLAS semiconductor tracker”. In: *JINST* 9 (2014), P08009. arXiv: 1404.7473 [hep-ex].

[18] Vasiliki A. Mitsou. "The ATLAS transition radiation tracker". In: *8th International Conference on Advanced Technology and Particle Physics (ICATPP 2003): Astroparticle, Particle, Space Physics, Detectors and Medical Physics Applications*. Nov. 2003, pp. 497–501. arXiv: hep-ex/0311058.

[19] Djamel Eddine Boumediene. "ATLAS Calorimeter: Run 2 performance and Phase-II upgrades". In: *PoS* EPS-HEP2017 (2017). Ed. by Paolo Checchia et al., p. 485.

[20] *ATLAS liquid-argon calorimeter: Technical Design Report*. Technical Design Report ATLAS. Geneva: CERN, 1996.

[21] Nikiforos Nikiforou. *Performance of the ATLAS Liquid Argon Calorimeter after three years of LHC operation and plans for a future upgrade*. Tech. rep. arXiv:1306.6756. June 2013.

[22] Ana Maria Henriques Correia. *The ATLAS Tile Calorimeter*. Tech. rep. ATL-TILECAL-PROC-2015-002. Geneva: CERN, Mar. 2015.

[23] A. Hrynevich. "Performance of the ATLAS Tile Calorimeter". In: *JINST* 12.06 (2017). Ed. by Lev Shekhtman, p. C06021.

[24] B Dowler et al. "Performance of the ATLAS hadronic end-cap calorimeter in beam tests". In: *Nucl. Instrum. Meth. A* 482 (2002), pp. 94–124.

[25] R S Orr. "The ATLAS Forward Calorimeter". In: (Sept. 2011).

[26] *ATLAS muon spectrometer: Technical Design Report*. Technical Design Report ATLAS. Geneva: CERN, 1997.

[27] F. Bauer et al. "Construction and Test of MDT Chambers for the ATLAS Muon Spectrometer". In: *Nucl. Instrum. Meth. A* 461 (2001). Ed. by G. Batignani et al., pp. 17–20. arXiv: 1604.02000 [physics.ins-det].

[28] A Polini. *Design and Performance of the ATLAS Muon Detector Control System*. Tech. rep. ATL-MUON-PROC-2011-001. Geneva: CERN, Feb. 2011.

[29] Giordano Cattani. "The resistive plate chambers of the ATLAS experiment: Performance studies". In: *J. Phys. Conf. Ser.* 280 (2011). Ed. by E. Cannuccia et al., p. 012001.

[30] *Technical Design Report for the Phase-II Upgrade of the ATLAS TDAQ System*. Tech. rep. CERN-LHCC-2017-020. ATLAS-TDR-029. Geneva: CERN, Sept. 2017.

[31] ATLAS Collaboration. *Run 2 ATLAS Trigger and Detector Performance*. Jan. 2018.

[32] Michael E. Peskin and Daniel V. Schroeder. *An Introduction to quantum field theory*. Reading, USA: Addison-Wesley, 1995.

[33] Martijn Mulders and Rohini Godbole, eds. *Proceedings, 2nd Asia-Europe-Pacific School of High-Energy Physics (AEPSHEP 2014): Puri, India, November 04–17, 2014*. Vol. 2/2017. CERN Yellow Reports: School Proceedings. Geneva: CERN, Aug. 2017. arXiv: 1805.05281 [hep-ph].

[34] Bernard de Wit. "Introduction to gauge theories and the Standard Model". In: CERN. Geneva: CERN, Oct. 1995.

[35] David J Griffiths. *Introduction to elementary particles; 2nd rev. version*. Physics textbook. New York, NY: Wiley, 2008.

[36] W. Lucha, F.F. Schoberl and D. Gromes. "Bound states of quarks". In: *Phys. Rept.* 200 (1991), pp. 127–240.

[37] Roel Aaij et al. "Observation of $J/\psi\phi$ structures consistent with exotic states from amplitude analysis of $B^+ \to J/\psi\phi K^+$ decays". In: *Phys. Rev. Lett.* 118.2 (2017), p. 022003. arXiv: 1606.07895 [hep-ex].

[38] Roel Aaij et al. "Amplitude analysis of $B^+ \to J/\psi\phi K^+$ decays". In: *Phys. Rev. D* 95.1 (2017), p. 012002. arXiv: 1606.07898 [hep-ex].

[39] Roel Aaij et al. "Observation of $J/\psi p$ Resonances Consistent with Pentaquark States in $\Lambda_b^0 \to J/\psi K^- p$ Decays". In: *Phys. Rev. Lett.* 115 (2015), p. 072001. arXiv: 1507.03414 [hep-ex].

[40] M. Tanabashi et al. "Review of Particle Physics". In: *Phys. Rev. D* 98.3 (2018), p. 030001.

[41] Peter W. Higgs. "Broken Symmetries and the Masses of Gauge Bosons". In: *Phys. Rev. Lett.* 13 (1964). Ed. by J.C. Taylor, pp. 508–509.

[42] F. Englert and R. Brout. "Broken Symmetry and the Mass of Gauge Vector Mesons". In: *Phys. Rev. Lett.* 13 (1964). Ed. by J.C. Taylor, pp. 321–323.

[43] Georges Aad et al. "Observation of a new particle in the search for the Standard Model Higgs boson with the ATLAS detector at the LHC". In: *Phys. Lett. B* 716 (2012), pp. 1–29. arXiv: 1207.7214 [hep-ex].

[44] Serguei Chatrchyan et al. "Observation of a New Boson at a Mass of 125 GeV with the CMS Experiment at the LHC". In: *Phys. Lett. B* 716 (2012), pp. 30–61. arXiv: 1207.7235 [hep-ex].

[45] H. Georgi. *Lie Algebras In Particle Physics. From Isospin To Unified Theories*. Vol. 54. 1982.

[46] R.Keith Ellis, W.James Stirling and B.R. Webber. *QCD and collider physics*. Vol. 8. Cambridge University Press, Feb. 2011.

[47] S. Jiggins. "Search for new resonances decaying to a Standard Model Vector boson (W/Z) and Higgs boson in the $llb\bar{b}$, $l\nu b\bar{b}$ and $\nu\nu b\bar{b}$ channels in pp collisons at $\sqrt{s} =$ 13 TeV with the ATLAS detector". PhD thesis. University College London, 2018.

[48] George Sterman et al. "Handbook of perturbative QCD". In: *Rev. Mod. Phys.* 67 (1 Jan. 1995), pp. 157–248.

[49] Maxim Chernodub. "Background magnetic field stabilizes QCD string against breaking". In: (Jan. 2010).

[50] Tung-Mow Yan and Sidney D. Drell. "The Parton Model and its Applications". In: *Int. J. Mod. Phys. A* 29 (2014), p. 0071. arXiv: 1409.0051 [hep-ph].

[51] Davison E. Soper. "Parton distribution functions". In: *Nucl. Phys. B Proc. Suppl.* 53 (1997). Ed. by C. Bernard et al., pp. 69–80. arXiv: hep-lat/9609018.

[52] C. Bourrely and Jacques Soffer. "Deep inelastic scattering of leptons and hadrons in the QCD parton model and experimental tests". In: (Jan. 2001). Ed. by R. Pike and P. Sabatier, pp. 1565–1581. arXiv: hep-ph/0101195.

[53] M. Breidenbach et al. "Observed Behavior of Highly Inelastic Electron-Proton Scattering". In: *Phys. Rev. Lett.* 23 (16 Oct. 1969), pp. 935–939.

[54] Guido Altarelli and G. Parisi. "Asymptotic Freedom in Parton Language". In: *Nucl. Phys. B* 126 (1977), pp. 298–318.

[55] Eamonn Maguire, Lukas Heinrich and Graeme Watt. "HEPData: a repository for high energy physics data". In: *J. Phys. Conf. Ser.* 898.10 (2017). Ed. by Richard Mount and Craig Tull, p. 102006. arXiv: 1704.05473 [hep-ex].

[56] Jen-Chieh Peng and Jian-Wei Qiu. "The Drell-Yan Process". In: *The Universe* 4.3 (2016), pp. 34–44.

[57] E. W. Hughes and R. Voss. "Spin structure functions". In: *Ann. Rev. Nucl. Part. Sci.* 49 (1999), pp. 303–339.

[58] B.W. Filippone and Xiang-Dong Ji. "The Spin structure of the nucleon". In: *Adv. Nucl. Phys.* 26 (2001), p. 1. arXiv: hep-ph/0101224.

[59] Steven D. Bass. "The Spin structure of the proton". In: *Rev. Mod. Phys.* 77 (2005), pp. 1257–1302. arXiv: hep-ph/0411005.

[60] Masashi Wakamatsu. "Unraveling the physical meaning of the Jaffe-Manohar decomposition of the nucleon spin". In: *Phys. Rev. D* 94.5 (2016), p. 056004. arXiv: 1607.04018 [hep-ph].

[61] Xiang-Dong Ji. "Gauge-Invariant Decomposition of Nucleon Spin". In: *Phys. Rev. Lett.* 78 (1997), pp. 610–613. arXiv: hep-ph/9603249.

[62] B.L.G. Bakker, E. Leader and T.L. Trueman. "A Critique of the angular momentum sum rules and a new angular momentum sum rule". In: *Phys. Rev. D* 70 (2004), p. 114001. arXiv: hep-ph/0406139.

[63] Marco Stratmann and Werner Vogelsang. "Exploring the polarization of gluons in the nucleon". In: *J. Phys. Conf. Ser.* 69 (2007), p. 012035. arXiv: hep-ph/0702083.

[64] Daniel de Florian et al. "Evidence for polarization of gluons in the proton". In: *Phys. Rev. Lett.* 113.1 (2014), p. 012001. arXiv: 1404.4293 [hep-ph].

[65] Wilco J. den Dunnen et al. "Accessing the Transverse Dynamics and Polarization of Gluons inside the Proton at the LHC". In: *Phys. Rev. Lett.* 112 (2014), p. 212001. arXiv: 1401.7611 [hep-ph].

[66] Wilco Johannes den Dunnen. "Polarization effects in proton-proton collisions within the Standard model and beyond". PhD thesis. Vrije U., Amsterdam, 2013.

[67] Andrea Signori. "Flavor and Evolution Effects in TMD Phenomenology: Manifestation of Hadron Structure in High-Energy Scattering Processes". PhD thesis. Vrije U., Amsterdam, 2016.

[68] Cristian Pisano et al. "Extraction of partonic transverse momentum distributions from semi-inclusive deep inelastic scattering and Drell-Yan data". In: *PoS* DIS2017 (2018). Ed. by Uta Klein, p. 237. arXiv: 1709.03324 [hep-ph].

[69] Umberto D'Alesio. "Exploring the transverse spin structure of the nucleon". In: *AIP Conf. Proc.* 1056.1 (2008). Ed. by Sigfrido Boffi et al., pp. 106–113. arXiv: 0809.3162 [hep-ph].

[70] Vincenzo Barone, Alessandro Drago and Philip G. Ratcliffe. "Transverse polarisation of quarks in hadrons". In: *Phys. Rept.* 359 (2002), pp. 1–168. arXiv: hep-ph/0104283.

[71] Vincenzo Barone, Franco Bradamante and Anna Martin. "Transverse-spin and transverse-momentum effects in high-energy processes". In: *Prog. Part. Nucl. Phys.* 65 (2010), pp. 267–333. arXiv: 1011.0909 [hep-ph].

[72] Cristian Pisano et al. "A first determination of the unpolarized quark TMDs from a global analysis". In: *PoS* QCDEV2017 (2018), p. 010. arXiv: 1801.08443 [hep-ph].

[73] Maddie Smith. "Investigating Gluon Polarisation Within the Proton". MA thesis. Lancaster University, 2020.

[74] Daniel Boer et al. "Linearly Polarized Gluons and the Higgs Transverse Momentum Distribution". In: *Phys. Rev. Lett.* 108 (2012), p. 032002. arXiv: 1109 . 1444 [hep-ph].

[75] Jean-Philippe Lansberg et al. "Pinning down the linearly-polarised gluons inside unpolarised protons using quarkonium-pair production at the LHC". In: *Phys. Lett. B* 784 (2018). [Erratum: Phys.Lett.B 791, 420–421 (2019)], pp. 217–222. arXiv: 1710.01684 [hep-ph].

[76] Daniel Boer and Cristian Pisano. "Polarized gluon studies with charmonium and bottomonium at LHCb and AFTER". In: *Phys. Rev. D* 86 (2012), p. 094007. arXiv: 1208.3642 [hep-ph].

[77] S. Chekanov et al. "Measurement of (anti)deuteron and (anti)proton production in DIS at HERA". In: *Nucl. Phys. B* 786 (2007), pp. 181–205. arXiv: 0705.3770 [hep-ex].

[78] Jian-Wei Qiu, Marc Schlegel and Werner Vogelsang. "Probing Gluonic Spin-Orbit Correlations in Photon Pair Production". In: *Phys. Rev. Lett.* 107 (2011), p. 062001. arXiv: 1103.3861 [hep-ph].

[79] J.P. Ma and C. Wang. "QCD factorization for quarkonium production in hadron collisions at low transverse momentum". In: *Phys. Rev. D* 93.1 (2016), p. 014025. arXiv: 1509.04421 [hep-ph].

[80] L.D. Isenhower et al. *Polarized Drell-Yan measurements with the Fermilab Main Injector*. Tech. rep. May 2012.

[81] John C. Collins and Davison E. Soper. "Angular Distribution of Dileptons in High-Energy Hadron Collisions". In: *Phys. Rev. D* 16 (1977), p. 2219.

[82] Jean-Philippe Lansberg, Cristian Pisano and Marc Schlegel. "Associated production of a dilepton and a $\Upsilon(J/\psi)$ at the LHC as a probe of gluon transverse momentum dependent distributions". In: *Nucl. Phys. B* 920 (2017), pp. 192–210. arXiv: 1702.00305 [hep-ph].

[83] Wilco J. den Dunnen et al. "Accessing the Transverse Dynamics and Polarization of Gluons inside the Proton at the LHC". In: *Phys. Rev. Lett.* 112 (21 May 2014), p. 212001.

[84] Isobel Mawby. "Probing Gluon TMDs in Unpolarised Hadron Scattering Experiments". PhD thesis. Lancaster University, 2018.

[85] Torbjörn Sjöstrand et al. "An introduction to PYTHIA 8.2". In: *Comput. Phys. Commun.* 191 (2015), pp. 159–177. arXiv: 1410.3012 [hep-ph].

[86] P.J. Mulders and J. Rodrigues. "Transverse momentum dependence in gluon distribution and fragmentation functions". In: *Phys. Rev. D* 63 (2001), p. 094021. arXiv: hep-ph/0009343.

[87] ATLAS Collaboration. *Performance of the ATLAS muon triggers in Run 2*. Tech. rep. arXiv:2004.13447. Geneva: CERN, Apr. 2020.

[88] *Muon reconstruction and identification efficiency in ATLAS using the full Run 2 pp collision data set at* $\sqrt{s} = 13$ *TeV*. Tech. rep. ATLAS-CONF-2020-030. Geneva: CERN, Aug. 2020.

[89] Morad Aaboud et al. "Measurement of the photon identification efficiencies with the ATLAS detector using LHC Run 2 data collected in 2015 and 2016". In: *Eur. Phys. J. C* 79.3 (2019), p. 205. arXiv: 1810.05087 [hep-ex].

[90] Z. Was, P. Golonka and G. Nanava. "PHOTOS Monte Carlo for precision simulation of QED in decays: History and properties of the project". In: *PoS* ACAT (2007), p. 071. arXiv: 0707.3044 [hep-ph].

[91] S. Agostinelli et al. "GEANT4–a simulation toolkit". In: *Nucl. Instrum. Meth. A* 506 (2003), pp. 250–303.

[92] M. Tanabashi et al. "Review of Particle Physics". In: *Phys. Rev. D* 98.3 (2018), p. 030001.

[93] Pushpalatha C. Bhat. "Multivariate Analysis Methods in Particle Physics". In: *Ann. Rev. Nucl. Part. Sci.* 61 (2011), pp. 281–309.

[94] Andreas Hocker et al. *TMVA - Toolkit for Multivariate Data Analysis*. Mar. 2007. arXiv: physics/0703039.

[95] Morad Aaboud et al. "Measurement of J/ψ production in association with a $W^{\pm}$ boson with *pp* data at 8 TeV". In: *JHEP* 01 (2020), p. 095. eprint: 1909.13626.

[96] Morad Aaboud et al. "Measurement of quarkonium production in proton-lead and proton-proton collisions at 5.02 TeV with the ATLAS detector". In: *Eur. Phys. J. C* 78.3 (2018), p. 171. eprint: 1709.03089.

[97] Georges Aad et al. “Measurement of the differential cross-sections of prompt and non-prompt production of J/ψ and $\psi(2S)$ in pp collisions at $\sqrt{s} = 7$ and 8 TeV with the ATLAS detector”. In: *Eur. Phys. J. C* 76.5 (2016), p. 283. eprint: 1512.03657.

[98] Kyle Cranmer et al. *HistFactory: A tool for creating statistical models for use with RooFit and RooStats*. Tech. rep. CERN-OPEN-2012-016. New York: New York U., Jan. 2012.

[99] Pekka Sinervo. “Definition and Treatment of Systematic Uncertainties in High Energy Physics and Astrophysics”. In: *eConf* C030908 (2003). Ed. by L. Lyons, R.P. Mount and R. Reitmeyer, TUAT004.

[100] *Photon identification in 2015 ATLAS data*. Tech. rep. ATL-PHYS-PUB-2016-014. Geneva: CERN, Aug. 2016.

[101] Morad Aaboud et al. “Measurements of b-jet tagging efficiency with the ATLAS detector using $t\bar{t}$ events at $\sqrt{s} = 13$ TeV”. In: *JHEP* 08 (2018), p. 089. arXiv: 1805.01845 [hep-ex].